

Influence of Lubrication on Tribological Nanoscopic Contact Processes

Dissertation

Simon Stephan

Vom Fachbereich Physik
der Rheinland-Pfälzischen Technischen Universität
Kaiserslautern-Landau
zur Verleihung des akademischen Grades
"Doktor der Naturwissenschaften"
genehmigte Dissertation

Betreuer: Prof. Dr. rer. nat. Herbert M. Urbassek

Zweitgutachter: Prof. Dr. rer. nat. Michael Kopnarski

Datum der wissenschaftlichen Aussprache:

6.12.2023

DE-386

„If we were to name the most powerful assumption of all, which leads one on and on in an attempt to understand life, it is that all things are made of atoms, and that everything that living things do can be understood in terms of the jiggings and wiggings of atoms.“

– Richard P. Feynman

Abstract

Lubricated tribological contact processes are important in both nature and in many technical applications. Fluid lubricants play an important role in contact processes, e.g. they reduce friction and cool the contact zone. The fundamentals of lubricated contact processes on the atomistic scale are, however, today not fully understood. A lubricated contact process is defined here as a process, where two solid bodies that are in close proximity and eventually in parts in direct contact, carry out a relative motion, whereat the remaining volume is submersed by a fluid lubricant. Such lubricated contact processes are difficult to examine experimentally. Atomistic simulations are an attractive alternative for investigating the fundamentals of such processes. In this work, molecular dynamics simulations were used for studying different elementary processes of lubricated tribological contacts. A simplified, yet realistic simulation setup was developed in this work for that purpose using classical force fields. In particular, the two solid bodies were fully submersed in the fluid lubricant such that the squeeze-out was realistically modeled. The velocity of the relative motion of the two solid bodies was imposed as a boundary condition. Two types of cases were considered in this work: i) a model system based on synthetic model substances, which enables a direct, but generic, investigation of molecular interaction features on the contact process; and ii) real substance systems, where the force fields describe specific real substances. Using the model system i), also the reproducibility of the findings obtained from the computer experiments was critically assessed. In most cases, also the dry reference case was studied. Both mechanical and thermodynamic properties were studied – focusing on the influence of lubrication. The following properties were studied: The contact forces, the coefficient of friction, the dislocation behavior in the solid, the chip formation and the formation of the groove, the squeeze-out behavior of the fluid in the contact zone, the local temperature and the energy balance of the system, the adsorption of fluid particles on the solid surfaces, as well as the formation of a tribofilm. Systematic studies were carried out for elucidating the influence of the wetting behavior, the influence of the molecular architecture of the lubricant, and the influence of the lubrication gap height on the contact process. As expected, the presence of a fluid lubricant reduces the temperature in the vicinity of the contact zone. The presence of the lubricant is, moreover, found to have a significant

influence on the friction and on the energy balance of the process. The presence of a lubricant reduces the coefficient of friction compared to a dry case in the starting phase of a contact process, while lubricant molecules remain in the contact zone between the two solid bodies. This is a result of an increased normal and slightly decreased tangential force in the starting phase. When the fluid molecules are squeezed out with ongoing contact time and the contact zone is essentially dry, the coefficient of friction is increased by the presence of a fluid compared to a dry case. This is attributed to an imprinting of individual fluid particles into the solid surface, which is energetically unfavorable. By studying the contact process in a wide range of gap height, the entire range of the Stribeck curve is obtained from the molecular simulations. Thereby, the three main lubrication regimes of the Stribeck curve and their transition regions are covered, namely boundary lubrication (significant elastic and plastic deformation of the substrate), mixed lubrication (adsorbed fluid layers dominate the process), and hydrodynamic lubrication (shear flow is set up between the surface and the asperity). The atomistic effects in the different lubrication regimes are elucidated. Notably, the formation of a tribofilm is observed, in which lubricant molecules are immersed into the metal surface. The formation of a tribofilm is found to have important consequences for the contact process. The work done by the relative motion is found to mainly dissipate and thereby heat up the system. Only a minor part of the work causes plastic deformation. Finally, the assumptions, simplifications, and approximations applied in the simulations are critically discussed, which highlights possible future work.

Kurzfassung

Geschmierte tribologische Kontaktprozesse sind sowohl in der Natur als auch in vielen technischen Anwendungen von großer Bedeutung. Fluide Schmiermittel spielen bei vielen Kontaktprozessen eine wichtige Rolle: Sie verringern die Reibung und kühlen die Kontaktzone. Die grundlegenden Mechanismen auf atomistischer Skala von geschmierter Kontaktprozesse sind jedoch heute noch nicht vollständig verstanden. Ein geschmierter Kontaktprozess ist hier definiert als ein Prozess, bei dem zwei feste Körper, die sich in unmittelbarer Nähe und ggf. in direktem Kontakt befinden, eine Relativbewegung ausführen, wobei das restliche Volumen von einem flüssigen Schmiermittel ausgefüllt ist. Solche geschmierten Kontaktprozesse sind experimentell nur schwer in situ zu untersuchen. Atomistische Simulationen sind eine attraktive Alternative zu klassischen Experimenten, um die Elementarprozesse von Tribokontakten zu untersuchen. In dieser Arbeit wurden Molekulardynamiksimulationen zur Untersuchung der Elementarprozesse geschmierter tribologischer Kontaktprozesse eingesetzt. Zu diesem Zweck wurde in dieser Arbeit ein vereinfachter, aber realistischer Simulationsaufbau unter Verwendung klassischer Kraftfelder entwickelt. Insbesondere wurden die beiden Festkörper vollständig in das flüssige Schmiermittel eingetaucht, so dass das Herausdrücken der Fluidteilchen aus der Kontaktzone realistisch abgebildet wurde. Die Geschwindigkeit der Relativbewegung der beiden Festkörper wurde als Randbedingung aufgeprägt. In dieser Arbeit wurden zwei Fälle betrachtet: i) ein auf Modellsubstanzen basierendes Modellsystem, das eine direkte, aber generische Untersuchung der molekularen Wechselwirkungsmerkmale auf den Kontaktprozess ermöglicht; und ii) reale Stoffsysteme, bei denen die Kraftfelder konkrete reale Stoffe beschreiben. Unter Verwendung des Modellsystems i) wurde auch die Reproduzierbarkeit der aus den Computereperimenten gewonnenen Erkenntnisse kritisch untersucht. In den meisten Fällen wurde auch der trockene Referenzfall betrachtet. Es wurden sowohl mechanische als auch thermodynamische Eigenschaften des Tribosystems untersucht, wobei der Schwerpunkt auf dem Einfluss der Schmierung durch ein Fluid lag. Die folgenden Eigenschaften wurden untersucht: Die Kontaktkräfte, der Reibungskoeffizient, das Versetzungsverhalten im Festkörper, die Spannbildung und die Ausbildung der Furche im Substrat, das Auspressverhalten des Fluids aus der Kontaktzone, die lokale Temperatur und die Energiebilanz des Systems, die Adsorption

von Fluidteilchen an den Festkörperoberflächen sowie die Ausbildung eines Tribofilms. Systematische Untersuchungen wurden durchgeführt, um den Einfluss des Benetzungsverhaltens, der molekularen Architektur des Schmierstoffs und der Schmierpalthehöhe auf den Kontaktprozess aufzuklären. Die Ergebnisse zeigen, dass, wie erwartet, das Vorhandensein eines fluiden Schmiermittels die Temperatur der Kontaktzone reduziert. Darüber hinaus wurde gezeigt, dass das Vorhandensein des Schmierstoffs einen erheblichen Einfluss auf die Reibung und die Energiebilanz des Prozesses hat. Das Vorhandensein eines Schmierstoffs verringert den Reibungskoeffizienten im Vergleich zu einem trockenen Fall in der Anfangsphase eines Kontaktprozesses, während noch Schmierstoffmoleküle in der Kontaktzone zwischen den beiden Festkörpern vorhanden sind. Dies ist auf eine erhöhte Normalkraft und eine leicht verringerte Tangentialkraft in der Anfangsphase des Kontaktprozesses zurückzuführen. Wenn die Fluidmoleküle mit fortschreitender Kontaktlaufzeit aus dem Spalt herausgedrückt sind und die Kontaktzone im Wesentlichen trocken ist, wird der Reibungskoeffizient durch die Anwesenheit eines Fluids im Vergleich zu einem trockenen Fall erhöht. Dies ist auf das Eindringen einzelner Fluidmoleküle in die Festkörperoberfläche zurückzuführen, wozu Energie aufgewendet werden muss. Durch die Untersuchung des Kontaktprozesses bei unterschiedlichen Spalthöhen wird der gesamte Bereich der Stribeck Kurve mit den molekularen Simulationen abgebildet. Dabei werden die drei Haupt-Reibungsregime der Stribeck Kurve und ihre Übergangsbereiche abgedeckt: Grenzreibung (signifikante elastische und plastische Verformung des Substrats), Mischreibung (Verhalten adsorbierter Fluidmoleküle an Feststoffoberflächen dominiert den Prozess) und Flüssigkeitsreibung (Scherströmung im Fluid zwischen den beiden Feststoffoberflächen). Auf der Basis der Computereperimente wurden die Elementarprozesse in den drei Reibungsregimen untersucht. Insbesondere wird die Bildung eines Tribofilms beobachtet, bei dem die Schmierstoffmoleküle in die Metalloberfläche eingedrückt werden. Die Bildung eines Tribofilms hat wichtige Konsequenzen für den Kontaktprozess – insbesondere im Bereich der Grenzreibung. Ferner konnte gezeigt werden, dass die durch die Relativbewegung verrichtete Arbeit größtenteils dissipiert und dadurch das System erwärmt wird. Nur ein kleiner Teil der Arbeit verursacht plastische Verformungen. Abschließend werden die in den Simulationen verwendeten Annahmen, Vereinfachungen und Näherungen kritisch diskutiert, wodurch mögliche zukünftige Arbeiten aufgezeigt werden.

Contents

Abstract	V
Kurzfassung	VII
List of Symbols	XIII
1 Introduction	1
2 Fundamentals	7
2.1 Tribology and Lubrication	7
2.1.1 History and State of the Art	9
2.1.2 The Tribosystem	11
2.1.3 Lubrication	13
2.1.4 The Relevance of Interfaces in Lubricated Tribosystems	17
2.1.5 Tribology on Different Scales	23
2.2 Molecular Simulation	24
2.2.1 Molecular Simulations as Computer Experiments	24
2.2.2 Molecular Dynamics: Simulation Method	25
2.2.3 Structure of Crystals, Fluids, and Interfaces on the Atomistic Scale	30
2.2.4 Molecular Models	35
2.2.5 Computational Tribology on the Atomistic Level	40
2.2.6 Simulation Scenario Used in This Work	43
3 Influence of Solid-Fluid Interaction on Lubrication	47
3.1 Introduction	47
3.2 Methods	49
3.2.1 Molecular Model	49
3.2.2 Simulation Setup	52
3.2.3 Definition of Observables	53
3.3 Results and Discussion	56
3.3.1 Mechanical Properties	56

3.3.2	Energy Balance	62
3.3.3	Temperature Field and Thermodynamic Properties of Lubricant	66
3.4	Conclusions	70
4	Reproducibility of Atomistic Friction Computer Experiments	73
4.1	Introduction	73
4.2	Simulation Scenario and Definition of Observables	76
4.2.1	Force Field and Simulation Setup	76
4.2.2	Statistical Analysis	79
4.2.3	Definition of Observables	80
4.3	Results and Discussion	82
4.3.1	Mechanical Properties	83
4.3.2	Thermodynamic Properties	88
4.4	Conclusions	93
5	Mechanical Effects of Lubrication on the Nanoscale	95
5.1	Introduction	95
5.2	Methods	97
5.2.1	Simulation Setup	97
5.2.2	Molecular Model	98
5.2.3	Definition of Observables	100
5.3	Results and Discussion	101
5.3.1	Forces	101
5.3.2	Dislocations	105
5.3.3	Groove, Chip, and Contact Zone	107
5.4	Conclusions	114
6	Molecular Dynamics Simulation of the Stribeck Curve	117
6.1	Introduction	117
6.2	Methods	120
6.2.1	Simulation Scenario	120
6.2.2	Molecular Model	122
6.2.3	Definition of Observables	124
6.3	Results and Discussion	127
6.3.1	Mechanical Properties	127
6.3.2	Thermodynamic Properties	142
6.4	Conclusions	147
7	Discussion and Outlook	149
7.1	Critical Discussion	149

7.2 Possible Future Work	151
8 Conclusions	155
Literature	159
Appendix	203
A The Lennard-Jones Model System	203
B Details on Statistical Uncertainty Analysis	207
B.1 Calculation of Local Thermodynamic Properties	207
B.2 Comparison of Uncertainty Analysis to Results from Chapter 3	208
C Details on Stribeck Curve Simulations	215
C.1 Model for Solid-Fluid Interactions	215
C.2 Computational Aspects of Simulations	216
C.3 Force Contributions	217
C.4 Temperature and Pressure in the Lubrication Gap	218
Authorship Declaration	219
Supervised Student Theses	223
Curriculum Vitae	225
Acknowledgment	227

List of Symbols

Latin symbols

a, b	parameters
A	area
a	acceleration
b	slip length
b	Burgers vector
c	parameter
d	depth
E	total energy
F	force
F	embedding function
$g(r)$	radial distribution function
h	film thickness
h	height
\hat{H}	Hamilton operator
K	total kinetic energy
k	parameters
k_B	Boltzmann constant
L	dislocation length
L	load
l	length
M	particle mass
N	number of components
N	number of particles
N	number of simulations
n	number of moles
p	pressure
p	momentum
p^s	vapor pressure

Q	heat
q	charge
R	roughness parameter
R	radius
\underline{r}	position vector
r	distance between particles
r_c	cut-off radius
T	temperature
U	internal energy
u	potential energy
v	velocity
V	volume
V	total potential energy
W	work
\underline{x}	composition vector
x	spatial coordinate
y	spatial coordinate
z	spatial coordinate
Z	observable variable

Superscripts

0	friction coefficient offset
0	reference point
F	fluid
I	indenter
i	particle index
i	component index
j	particle index
k	particle index
l	particle index
N	normal
S	substrate
s	interphase
SL	solid-liquid
SV	solid-vapor
T	tangential
VL	vapor-liquid

*	reduced with respect to LJ units system
\sim	solid-fluid interaction
-	arithmetic mean
'	moving coordinate system

Greek symbols

α	contact angle or angle
β	parameter
$\dot{\gamma}$	shear rate
γ	coupling coefficient
γ	surface tension
Γ	phase space
Δ	difference or interval
Δ_Z	significance measure for Z
δ	normalized standard deviation
ε	Lennard-Jones energy parameter
ϵ_0	electric constant
η	shear viscosity
Λ	dimensionless film thickness
ν	kinematic viscosity
μ	coefficient of friction
μ_i	chemical potential of component i
ϕ	angle
ψ	wave function
Ψ	interaction function
ρ	density
$\tilde{\rho}$	electron density
σ	Lennard-Jones size parameter
σ	surface roughness
σ	standard deviation
τ	time
τ	shear stress
θ	angle

Abbreviations

AFM	atomic force microscope
bcc	body centered cubic
BL	boundary lubrication
BZS	Boltzmann-Zuse society
DXA	dislocation extraction algorithm
EAM	embedded atom method
EMD	equilibrium molecular dynamics
fcc	face centered cubic
HL	hydrodynamic lubrication
LJ	Lennard-Jones
LNG	liquid natural gas
MD	molecular dynamics
ML	mixed lubrication
NB	non-bonded
NEMD	non-equilibrium molecular dynamics
NVE	microcanonical ensemble
NVT	canonical ensemble
sc	simple cubic
TraPPE	transferable potentials for phase equilibria

1 Introduction

Tribological processes and the functionality of lubricants in such are of great importance in nature as well as in many technical applications, for example in production processes like cutting and grinding, in machine parts such as bearings and gears, in micro-devices such as micro-pumps, and also in bone joints. Fluid lubricants play a crucial role in such contact processes. The main tasks of lubrication are (a) the reduction of friction and (b) the cooling of the contact zone. The underlying elementary processes in tribological contacts occur on the nanoscale. Today, these elementary processes are still not fully understood. This is, on one hand, due to the fact that a large number of physical effects and mechanisms are relevant in an interrelated and complex way and, on the other hand, due to the fact that contact processes are difficult to study experimentally. The actual contact zone is often very small (on the nanoscale) and experimentally hard to monitor. This is due to the geometrical setup, i.e. two solid bodies enfolding the lubricated contact zone. Moreover, in many applications, extreme conditions prevail in the contact zone regarding pressure and temperature, which makes in situ experiments difficult.

Molecular dynamics simulation are an interesting alternative to classical laboratory experiments for studying processes on the nanoscale. On one hand, they are physically-based and provide great predictive capabilities and, on the other hand, they provide a great level of insight into the studied process. In molecular simulations, matter is modeled on the atomistic level based on the molecular interactions, which are described by mathematical models – so-called force fields. The time evolution of the system, i.e. trajectories of the particles are computed by solving *Newton's* equation of motion. Molecular dynamics simulations have today become an indispensable tool in many scientific disciplines, e.g. physics, chemistry, biology, and material sciences. Molecular dynamics simulations are therein often used to elucidate the inner workings and fundamentals of processes and mechanisms that are hard to study experimentally.

Solving and backtracking the particle motion on the atomistic level provides enormous insights. This is not only due to the fact that the atomistic structure can be analyzed in great detail, but also due to the fact that the motion and interactions of particles on

the atomistic scale are linked to macroscopic properties by statistical mechanics. Hence, molecular simulations provides simultaneous access to both the atomistic structure and macroscopic properties, which is very beneficial for relating the simulation results to laboratory experiment data (usually from the macroscopic level). The benefits of predicting and analyzing atomistic trajectories are reflected in the famous quote of *Richard P. Feynman* stating that a great deal "can be understood in terms of the jiggings and wiggings of atoms." [120]. MD simulation actually provides access to monitoring this 'jiggings and wiggings' of the atoms within different setups and situations, e.g. a tribological system, using relatively few physical assumptions.

Therefore, MD simulation has become a popular tool in tribology¹. Hence, MD simulation has been used for several years for investigating contact processes. However, many of the mechanisms of interest (lubrication, dislocations, local structural change, plastic deformation, topography change, etc.) occur on relatively large length scales compared to the size of atoms. Accordingly, large and computationally demanding simulations (approx. 10^7 - 10^8 particles) are required to capture these properties and phenomena. Furthermore, complex, i.e. computationally intensive interaction models are required for realistically modeling specific substances. For these reasons, molecular simulation that provides a realistic kinematic and kinetic picture of tribological contact processes and captures essential physical features has only been accessible for some years.

There are numerous studies available in the literature, in which processes like nanoindentation and nanoscratching were investigated using MD simulation. Mostly, dry contacts were studied – focusing on mechanical properties. Thermal properties and effects caused by the thermo-mechanical coupling have been only few times studied so far. Most importantly, there are comparatively few MD simulation studies available addressing the influence of lubrication on contact processes. In most studies that consider the presence of a fluid lubricant, only very thin liquid films consisting of a few molecular layers were modeled. Hence, no fluid bulk phase was considered. Yet, this fluid bulk phase is crucial for establishing a physically realistic picture of the behavior of fluid particles in contact processes, e.g. regarding the squeeze-out from the contact zone and its cooling effects. In order to realistically model the fluid flow and the thermal balance (including heat conduction) of a contact process consisting of two solids and a lubricant, the contact must be submersed in a fluid.

In this work, lubricated contact processes were studied by MD simulation, where the contact was fully submersed in a fluid lubricant. This – computationally challenging – simulation setup was used for studying different aspects of lubricated contact processes

¹A detailed literature review on applications of MD simulation in nanotribology is presented section 2.2.5

on the nanoscale such as its cooling capabilities and its influence on the coefficient of friction.

In this work, a simplified scenario is considered, that yet comprises essential features, such that central elementary processes of a lubricated contact process become observable and accessible via the computer experiment. In this simplified scenario, two solid bodies carry out a relative motion (first indentation, then scratching, and eventually retraction) – at constant velocity. The two solid bodies are fully submersed in a fluid lubricant. Both solid bodies are single crystals. The two solids are composed of different materials, the so-called *substrate* is relatively soft, whereas the so-called *indenter* is relatively hard. This terminology is adapted from experimental nanoindentation and atomic force microscopy (AFM) [123] and used throughout this work. The indenter used in this work has a somewhat spherically-curved contact surface (sphere, cylinder, spherical cap), whereas the substrate is atomistically flat.

All three components (substrate, indenter, and fluid lubricant) are atomistically modeled using classical force fields. Two different modeling cases were considered: (a) a simplified yet realistic and generic model system, where all atomistic interactions are modeled by the Lennard-Jones potential; (b) real substance systems, where the atomistic interaction potentials were chosen such that specific components are modeled, e.g. iron for the substrate and decane for the lubricant. Both approaches have different advantages, e.g. the model system is computationally significantly cheaper and more extensive and systematic studies are therefore feasible using this approach. Furthermore, the model system chosen in this work, the so-called *Lennard-Jones model system*, is a widely used system such that a large body of knowledge of the individual elements and properties are available, e.g. on the wetting and adsorption properties of the fluid on the solid surfaces as well as on the thermodynamic properties of the fluid and the solid bulk phases (details on the Lennard-Jones model system are given in Appendix A). Moreover, the insights into the elementary processes obtained from the model system are generic and (with some limitations) generally applicable. These limitations are, however, not a priori exactly known. Hence, the transferability of the results and insights from the model system to a given specific use case has restrictions. The real substance case, on the other hand, is evidently well applicable to the specific use case it is designed for. However, it is in general unfeasible to transfer the results from a specific real substance case modeling specific components to other use cases, since it is not a priori known to what extent certain aspects of the results and findings are a result of specific features of the considered component models. Therefore, the complementary approach, i.e. using in parts a generic model system and in other parts real substance models, is a good compromise between these conflicting objectives. Thus, general insights are obtained in this work from a generic, computationally cheap, and strongly simplified model sys-

tem. And, specific insights are obtained from a selection of real substance systems. This complementary approach additionally enables an assessment of the transferability of the findings obtained from the model system to a given real substance system. Hence, the methodology itself can be assessed by the combination of the approaches.

This work is (in most parts) a cumulative dissertation, which summarizes results from work previously published in scientific peer-reviewed journals [348, 356, 358, 359]. These four papers correspond to the chapters 3 - 6. The Appendix 'Authorship Declaration' provides an overview of the four papers and the corresponding contributions from the author of this thesis. The state of the art and the scope of each study is presented at the beginning of each chapter. Additionally, chapter 2 presents an introduction into both the physical aspects of tribology and lubrication as well as molecular dynamics simulation as a computer experiment method. Moreover, chapter 7 presents a critical discussion on the results and simulation methodology as well as possible future improvements. The chapters 2 and 7 were specifically constructed for this thesis. All references used for the preparation of this thesis are indicated herein.

This work is outlined as follows: Chapter 2 gives an introduction into tribology from a physical perspective, by defining the term *tribosystem* and its elements as well as their individual significance for different tribological properties. The state of the art in tribology research is stated – focusing on nanotribology. Based on this introduction, open research questions that are addressed in this work are defined. Then, the methodology used in this work to address these research questions is introduced, i.e. non-equilibrium molecular dynamics simulation and the atomistic models used therein. The chapters 3 and 4 present the results for the Lennard-Jones model system simulations. The chapters 5 and 6 present the results for the real substance systems simulations. The chapter 7 presents a critical discussion on the assumptions and simplifications applied in the simulations, e.g. regarding the surface topography and the solid body structure. Finally, conclusions are drawn in chapter 8.

In chapter 3, the elementary processes of lubrication are studied using the Lennard-Jones model system. The focus is on the influence of the solid-fluid interaction energy (which determines the wetting state) on the contact process. To gain better understanding of the influence of lubrication on the nanoscale, both dry and lubricated scratching processes in the model system are compared. The entire range between total dewetting and total wetting is investigated by tuning the solid-fluid interaction energy between the lubricant and the solid bodies. The investigated scratching process consists of three sequential movements: A cylindrical indenter penetrates an initially flat substrate, then scratches in lateral direction, and is finally retracted out of the contact with the substrate. The indenter is fully submersed in the fluid in the lubricated cases. The substrate, the indenter, and the fluid are described by suitably parametrized Lennard-Jones model

potentials. The presence of the lubricant is found to have a significant influence on the friction and on the energy balance of the process. The thermodynamic properties of the lubricant are evaluated in detail. Also, the response functions of the fluid at the solid-fluid interfaces in the vicinity of the contact zone are studied. The work done by the indenter is found to mainly dissipate and thereby heats up the substrate and eventually the fluid. Only a minor part of the work causes plastic deformation of the substrate.

In chapter 4, the reliability and reproducibility of observables sampled from nanoscopic contact process simulations is assessed by means of their statistical uncertainties. Therefore, the computer experiment was carried out not only once, but is repeated eight times, with individual runs that only differ in the initial thermal motion (i.e. particle velocities). This set of replicas enables an assessment of observations for distinguishing reproducible physical phenomena from stochastic coincidence. In this way, a dry and a lubricated nanoscale scratching process are studied – using the same setup as considered in chapter 3. Hence, a cylindrical indenter carries out two sequential movements: It first penetrates a substrate vertically and then scratches laterally, which causes elastic and plastic deformation of the substrate. In the lubricated case, the indenter is fully submersed in the fluid. The substrate, the indenter, and the fluid were described by suitably parametrized Lennard-Jones potentials. Various mechanical and thermodynamic process properties were monitored in all simulation runs. The results are compared and evaluated statistically.

Moreover, the results and insights obtained regarding the influence of the solid-fluid interaction energy (cf. chapter 3) on the contact process observables is assessed regarding the statistical significance. Therefore, the measures obtained from the statistical analysis in chapter 4 were applied to the results from chapter 3. The results of this assessment are presented in the Appendix B.

In chapter 5, a real substance system is studied. Thereby, the effect of the presence of a lubricant on indentation and scratching of an iron surface is studied. By comparing a dry reference case with two lubricated contact processes – differing in the adsorption strength of the lubricant – the effects of the lubricant are identified. The contact process is fully submersed in a lubricant. Moreover, the substrate block was chosen large enough to detect lattice defects and their time evolution. After an initial phase, in which the lubricant is squeezed out of the contact zone, the contact between the indenter and the substrate is essentially dry. The number of lubricant molecules confined in the indenter-substrate gap increases with increasing lubricant adsorption energy. Trapped lubricant particles broaden the indenter area active in the scratching process – mainly on the flanks of the groove – compared to a dry reference case. This leads to a slight increase in the chip height as well as the chip volume and also contributes to the scratching forces.

In chapter 6, real substance systems are studied more systematically. Based on the insights obtained from the results presented in chapter 5, the simulation scenario was refined, i.e. more realistic lubricant fluids are used, the shape and the size of the indenter is chosen more realistically, and the size of the substrate block is decreased (as no significant effect of lubrication on the dislocation evolution was observed in previous works, cf. chapter 5). Moreover, a physically more realistic solid-fluid interaction energy is used that was derived from quantum mechanical simulations taken from the literature. Using this refined setup, lubricated contact processes are studied for determining the entire range of the Stribeck curve. Therefore, the lateral movement of two solid bodies at different gap height is studied. In each simulation, an indenter is moved at constant height above a flat iron surface in a lubricating fluid. Both methane and n-decane are considered as lubricants. The three main lubrication regimes of the Stribeck curve and their transition regions are covered by the study: Boundary lubrication (significant elastic and plastic deformation of the substrate), mixed lubrication (adsorbed fluid layers dominate the process), and hydrodynamic lubrication (shear flow is set up between the surface and the asperity). The formation of a tribofilm in which lubricant molecules are immersed into the metal substrate surface is found – not only in the case of scratching, but also for boundary lubrication and mixed lubrication. The formation of a tribofilm is found to have important consequences for the contact process. Moreover, the two fluids are found to show distinctly different behavior in the three lubrication regimes. Moreover, it is found that the nature and structure of the tribofilm strongly depends on the molecular architecture of the lubricant.

2 Fundamentals

In this chapter, first the fundamentals and state of the art of tribology and lubrication – and nanotribology in particular – are discussed by elaborating the physical fundamentals of these processes. This is done by discussing first a bigger picture of the physical effects and properties relevant for lubricated contact processes. From this bigger picture, the main physical features are derived that are considered and studied in this work. Then, molecular dynamics simulation is introduced as a computer experiment tool. Therein, the focus is on the physical modeling and abstraction applied for the description of lubricated contact processes studied in this work.

Hence, this chapter does not only introduce the background and methodology, but puts the simulations carried out within this dissertation in a broader context of the field of tribology and modeling approaches. This broader context is used to emphasize the simplifications and abstractions applied in the model development such that the results and insights obtained from the MD simulations can be critically assessed. The applicability of the model simplifications with respect to reality are then critically assessed in chapter 7, which also proposes possible future work based on that evaluation.

2.1 Tribology and Lubrication

Tribological contact processes play an important role in different fields of technology and nature, e.g. in bearings, in manufacturing processes, between roughness asperities of two macroscopic technical surfaces, in hard disk drives, during earth quakes, and in bone joints, but also in daily life. Hence, tribology is not only relevant in engineering, but also geology, biology, and informatics [140, 251, 289, 341]. Accordingly, the motivation for understanding the physical fundamentals of tribology and lubrication comes from many different disciplines.

The field of tribology comprises the topics of friction, lubrication, wear (and others). Despite the fact that every child has experienced friction and heard the term 'friction' and is aware that it is related to physics, the definition of the word is surprisingly

somewhat unsettled. The Cambridge dictionary states that friction is "the force which makes it difficult for one object to slide along the surface of another or to move through a liquid or gas" [54]. *Bauer*, on the other hand, states that "friction is a process and causes a conversion of mechanical energy into (predominantly) thermal energy" [24]. In one case, friction is defined as a force and, in the other case, friction is defined as a process/energy conversion. Frequently, also more vague definitions are found. This illustrates that the field of tribology, friction, lubrication etc. is richly layered and allows different perspectives. In this work, the focus is on the physical fundamentals and elementary processes of lubrication.

The purpose of lubrication is to reduce friction, reduce wear, and provide a cooling of the contact zone. For multiple reasons, lubricated contact processes are a particularly interesting and challenging type of process to investigate: i) lubricated contacts can in general be in very different (lubrication) states, which differ significantly (discussed in detail in section 2.1.3); ii) in many applications, extreme conditions prevail in lubricated tribosystems, e.g. pressures up to several GPa (cf. section 2.1.2 for details); iii) a large number of elementary processes occur simultaneously; iv) many physical effects and elementary processes are superimposed and, eventually, affect each other [42, 286]; iv) multiple length scales are involved. In particular, many of these elementary processes interact with each other – often in a complex way and on different scales – such that a holistic picture of lubrication has to be considered. Despite the fact that friction and lubrication are a very old research topics, they are still relatively poorly understood, e.g. regarding the atomistic elementary processes, the coupling of elementary processes, and the coupling of different length scales.

This section is structured as follows, first a brief overview is given on the history and state of the art (section 2.1.1) in tribology and lubrication – focusing on the relevance of atomistic modeling and simulation therein. Then, the 'tribosystem' and related terms are introduced (section 2.1.2). Moreover, the tribosystem studied by atomistic simulations in this work is put in context with different real world tribosystems. Subsequently, the current state of the art and understanding of the physical fundamentals of lubrication are discussed (section 2.1.3). Since interfaces play a dominant role in lubricated contacts, their relevance is discussed in detail (section 2.1.4). Finally, the fact that many tribological processes occur on different length scales simultaneously is discussed (section 2.1.5), which is in particular relevant to critically assess the modeling approach used in this work (cf. chapter 7).

2.1.1 History and State of the Art

The field of tribology is highly interdisciplinary and highly relevant in different disciplines. Accordingly, a large number of seminal text books address tribology or aspects of tribology from different perspectives [35, 42, 83, 251]. Also the history of tribology, friction, and lubrication has been comprehensively discussed in the literature, e.g. Refs. [42, 96, 285, 289]. However, these take in most parts a phenomenological perspective. The advent on the physical fundamentals of tribology, friction, and lubrication provided by atomistic simulations in the past three decades has on the other hand less systematically been reviewed. Therefore, a brief summary on the computational physics aspects and tribology on the atomistic scale is given in this section. This also comprises the question, how insights from computational atomistic simulations and phenomenological aspects have so far been brought together.

For a long time, tribology (not named as such until the mid of the last century¹) was a field primarily driven by engineers taking a macroscopic and phenomenological perspective on the topic [46]. Hence, a prime aim was to develop models that describe the macroscopic behavior of a tribological system, which was in most cases done by (semi)empirical models. A first principle modeling and understanding in the sense of *Feynman's* 'jiggling and wiggling' [120] only became feasible with the availability of advanced laboratory equipment providing insights to smaller scales and computers in the second half of the last century. Yet, a comprehensive understanding of the atomistic level tribology has still not been established to date.

However, it was early acknowledged that material properties and the behavior of materials on the level of the building blocks of matter, i.e. the atomistic scale, are fundamentally important for friction and lubrication [42, 46]. For example, *Lagmuir and Blodgett* [42, 46, 216, 217] discovered in the 1920s that even a monolayer of lubricant molecules can have an important influence on the contact process. Moreover, it was early recognized that thermal processes and dissipation plays an important role in tribology and lubrication by locally appearing hot spots [46]. It was also early understood that one of the fundamental mechanisms of friction is that mechanical work is converted (dissipated) to thermal energy and the temperature of the participating bodies increases [46, 96]. It should also be mentioned that, as a consequence of the central role of dissipation, for many technical processes, the attempt to reduce (and understand) friction also has a strong economical motivation [83, 251].

In general, laboratory experiments or computer experiments may be carried out to study a given physical problem. The focus of this work is on (atomistic) computer exper-

¹the term 'tribology' occurred in 1966 and was proposed by *H.P. Jost* [187]. The very first appearance is attributed to *D. Tabor* naming his research group 'Tribophysics' [251].

iments. However, to enable an assessment of the adequacy of a simulation model, a profound understanding of what is known from laboratory experiments on small (nanoscopic and mesoscopic) scale tribological effects and mechanisms is a prerequisite.

Today, tribological experiments can be carried out not only on the macroscopic level [84] (e.g. using tribometers [23]), but also on the nanoscopic level (e.g. using atomic force microscope – AFM). In classical macroscopic friction and lubrication experiments, a large number of effects (from different length scales) are superimposed and studying elementary processes is difficult. Moreover, interfering variables such as dirt, air humidity etc. are present. However, physical elementary processes on the atomistic scale became in general accessible to laboratory experiments by advanced equipment such as the AFM in the 1980s [39]. Using such equipment, nanoscale friction experiments can be carried out [42, 57, 58, 58, 280]. The AFM method was for example used for elucidating the stick-slip motion on the atomistic level [184, 251, 313, 384].

With the advent of computer methods, an attractive alternative route to laboratory experiments became available, namely atomistic computer experiments. Starting with the ground-breaking work of *Metropolis* and co-workers [262], *Alder and Wainwright* [6] and *Rahman* [296], a new access route to the prediction of material properties and modeling nanoscopic processes based on 'first principles' became available. This starting point actually gave access to survey and monitor *Feynman's* "jiggings and wiggings of atoms" [119, 120] in different situations. This route can be favorably used for elucidating the fundamentals and elementary processes of for example friction, lubrication, and wear. With increasing availability and speed of computers, it was, however, only in the 1990s that computer experiments were applied for elucidating the fundamentals of friction and lubrication [108, 127, 129, 214, 215, 340, 384–386] by the pioneers *Thompson, Landman, Robbins* and co-workers. In particular, computer experiments allowed a more isolated assessment of individual elementary processes and situations as well as coupling of few specific elementary processes. The downside of this is that a somewhat artificial situation blinding out certain aspects is looked at in a computer experiment, e.g. mostly (unrealistically) atomistically flat substrate surfaces are considered for studying the influence of the lattice orientation on friction [131, 133, 203]. Moreover, the modeling goes in hand with various assumptions and simplifications.

Hence, a critical discussion of the modeling approach is a crucial aspect of atomistic tribology simulations. In recent years, atomistic computer experiments for studying tribological contacts have become a well-established approach [49, 95, 128, 140, 301, 304, 374, 375, 397].

The two perspectives of tribology, i.e. the top-down (phenomenological) and the bottom-up (physical model and simulation driven) have not yet been brought together in a satisfactory way [251]. This is, on one hand, due to the fact that experimental

methods on contact processes are inherently difficult due to the accessibility of the process and the fact that effects from multiple scale levels are relevant that require different laboratory equipment. On the other hand, the computer experiment route still suffers from a limitation of computer time and lack of throughout reliable and realistic material models (e.g. for the solid-fluid interactions).

2.1.2 The Tribosystem

According to *H. Czichos* [82], a tribosystem is "an entity with a structure of *interacting components in relative motion* to perform a technical function.". This comprises at least two solid bodies, called triboelement A and triboelement B² and eventually an intermediating component. A comprehensive introduction into the 'tribosystem' concept is given in Refs. [24, 83]. The technical function of a tribosystem is out of the scope of this work. The interest lies in investigating the physical principles and dominating atomistic effects of the 'interacting components in relative motion' of a tribosystem. The definition of the tribosystem is hereafter refined such that a setup of three components is considered, namely two solid bodies and a fluid lubricant. The two solid bodies are termed 'substrate' and 'indenter'.

In this work, tribosystems on the nanoscopic level are studied for investigating fundamental mechanisms of lubrication. Therefore, a generic tribosystem on the nanoscopic scale is considered, which does *not* aim to model a specific macroscopic tribosystem for a specific technical application. However, it is evidently relevant to address the question, what the nanoscopic computer experiment setup resembles on a macroscopic (real world) level. Fig. 1 shows abstraction routs relevant for this work. Interestingly, the scenario considered in the computer experiments of this work (bottom of Fig. 1) can be considered an abstraction of three very different macroscopic laboratory tribosystems (top of Fig. 1). In the computer experiment tribosystem, an indenter that is fully submersed in a lubricant carries out a motion with respect to a substrate (which is eventually elastically and plastically deformed). This can be considered a model for an atomic force microscope experimental setup, a single asperity contact of a technical tribosystem, and a manufacturing machining process (top line of Fig. 1 - left to right, respectively).

It is eminent to discuss that the abstraction applied in these modeling approaches is significant, i.e. what simplifications are in general applied in the model setup. The most crucial simplifications are: (a) the substrate surface is initially atomistically flat; (b) the substrate is initially a single crystal without any defects; (c) the substrate and indenter surface is clean, i.e. no oxide, dirt, adsorbed gases etc. on the solid body

²In German usually called 'Grundkörper' and 'Gegenkörper' [83].

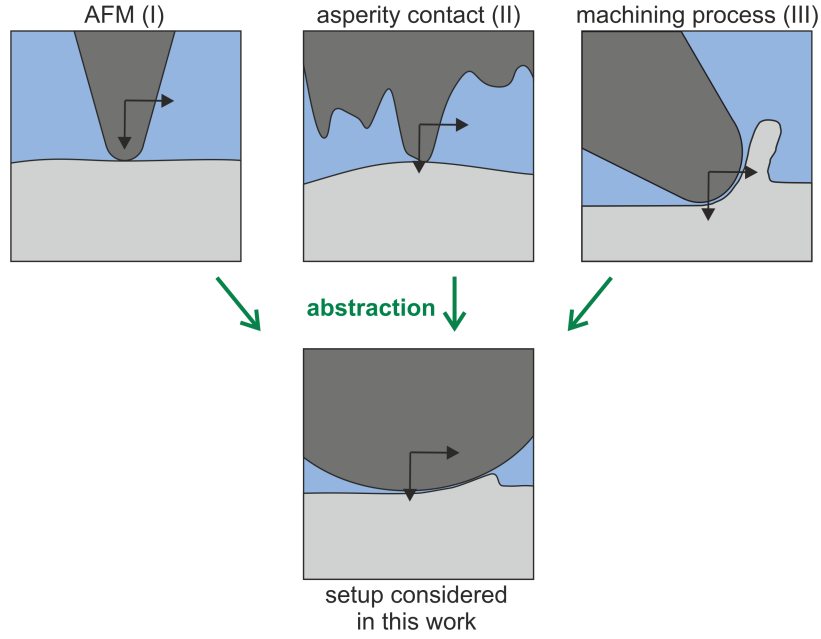


Figure 1: Abstraction routes relevant in this work. Top: Real world lubricated contact processes from different applications (left to right: Atom force microscope (AFM) experiments, single asperity contact from technical surfaces, and machining processes). Bottom: Generalized and simplified setup considered in the computer experiments in this work. Green arrows indicate the model abstraction. Black arrows indicate the process kinematics. The principal features (two solid bodies in direct contact, exhibiting a relative motion, and submersed in a fluid lubricant) of all three applications are covered by the simulation scenario used in this work.

surfaces are considered; and (d) the relative motion is of the order of magnitude of 10^1 m/s as contact velocity³.

The simplification (a) is potentially an influential simplification. It is well-known that surfaces are not atomistically flat even for polished finishing [36, 51]. Rather, a complex surface topography is usually present [36, 139, 224, 292]. Also, the simplification (b) is potentially influential as solid bodies have (in most applications) defects, cf. section 2.2.3 for details. Also, the material structure in the surface area is often modified (cf. section 2.1.5). Likewise, the simplification (c) is critical as in technical application tribosystems, the surfaces of the solid bodies are in general not 'clean'. Rather, thin layers of adsorbed 'dirt' and oxide films cover the surface [1, 27]. These layers usually have a thickness of at least some molecules. This has been already acknowledged in the seminal monograph of *Bowden and Tabor* [46] (they also found that a rigorous removal of these adsorbed layers yields an increasing coefficient of friction, which is indirectly relevant for this work). The simplifications (a)-(c) may be to some extent less critical for the abstraction route I, where the model setup resembles an AFM experiment, as in such

³Lower contact velocities are practically not accessible via atomistic computer experiments [128, 140], see section 2.2 for details.

sensitive equipment, very well prepared, i.e. clean, defect free etc., probes may be used. This does however, not hold for the abstraction routes II and III (cf. Fig. 1), where these attributes usually differ significantly between the real world experiment and the model setup. On the other hand, the contact velocity used in the computer experiment setup is in good agreement with cutting speeds and contact velocities applicable in the processes from the abstraction routes II and III depicted in Fig. 1. Yet, the contact velocities in AFM experiments are some orders of magnitude smaller. Hence, the simplification (d) is well justified for the abstraction route II and III, but problematic for I.

2.1.3 Lubrication

Lubrication is the usage of a third component between the two solid bodies of a tribosystem to improve the tribocontact. The aim of lubrication is to reduce friction, reduce the energy dissipation, and reduce the wear. Here, only fluid lubrication is considered, i.e. no solid lubricants. It is known for a long time that the presence of a lubricant reduces the temperature in the contact zone, e.g. *Bowden and Tabor* describe the reduction of temperature hot-spots by the presence a liquid lubricant [46]. Moreover, the presence of a lubricant has an important influence on the friction forces. Lubrication has been extensively studied in the field of engineering in the past decades and significant process has been made, i.e. empirical insights into which modifications of a tribosystem yield performance improvements [83, 248, 388]; for example elongated lubricant molecules situated on surfaces reducing friction [114, 333, 388]. The *physics of lubrication*, however, are today not as well-understood, i.e. the causality relations between the physical elementary processes and the macroscopic performance of the system.

Lubrication is an intriguing topic, as the presence of a fluid in a tribosystem has very different effects – depending on the state of the system. The different lubrication regimes are reflected in the *Stribeck curve* [244], which characterizes different lubrication states. The Stribeck curve is attributed to *R. Stribeck*, a German engineer, who published his results on different lubrication regimes in 1902 [368]. Fig. 2 schematically shows the typical slope of the Stribeck curve. Depending on the lubrication conditions between the two solid bodies, different lubrication states are established [245, 341, 424].

The Stribeck curve describes the coefficient of friction μ as a function of the so-called 'dimensionless film thickness ratio' Λ , i.e.

$$\mu = \mu(\Lambda) . \tag{1}$$

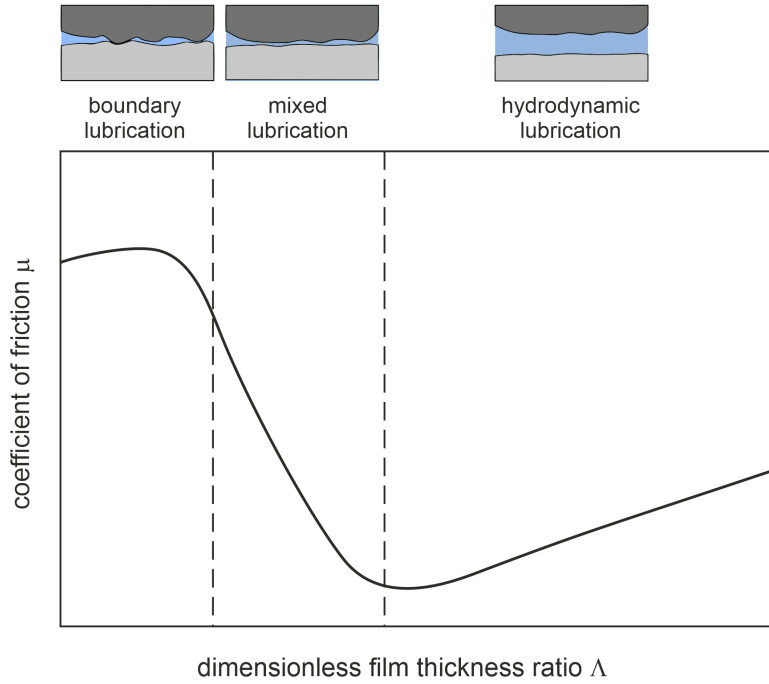


Figure 2: Scheme of the *Stribeck* curve and main lubrication regimes and a scheme of the corresponding configuration of the tribosystem. Slope of Stribeck curve adapted from Refs. [417].

The coefficient of friction μ is defined (using *Amontons-Coulomb* law [251]) as

$$\mu = \frac{F_t}{F_n}, \quad (2)$$

where F_n indicates the normal (load) force and F_t indicates the tangential (friction) force on the indenter. The coefficient of friction is a measure for the resistance of two bodies (here called indenter and substrate) that are in contact and experience a relative motion. Yet, it is important to emphasize that the coefficient of friction is not a material property, but rather characterizes the contact process in a holistic way. The dimensionless film thickness ratio Λ (abscissa in the *Stribeck* curve) is usually defined as [417]

$$\Lambda = \frac{h}{\sigma} \quad \text{with} \quad h = \frac{\eta v}{L}, \quad (3)$$

where h indicates the fluid film thickness, η the viscosity of the fluid, and v the velocity. The surface roughness is indicated by σ and the load is given by $L = F_n/A$, where A indicates the contact area. It should be noted that sometimes, different definitions for Λ are used [83, 233, 244] (in chapter 6 of this work, only the dependency of μ on the film thickness h is considered). The Stribeck curve (cf. Fig. 2) can be divided into characteristic sections describing the main lubrication regimes [338], namely hydrodynamic lubrication (HL), mixed lubrication (ML), and boundary lubrication (BL). In the hydrodynamic lubrication (HL) regime, the two solid bodies are fully separated by the fluid

and the load is carried by the fluid pressure [373]. The relative motion between the solid bodies establishes a shear flow in the fluid and viscous friction dominates the system. As the two solid bodies are not in contact in the HL regime, there is only little wear. In the mixed lubrication (ML) regime, the two solid bodies are in close proximity such that both elastic and plastic deformation of the solid bodies may occur. The friction is influenced by a large number of mechanisms in the ML regime, e.g. the distortion of the adsorbed fluid layer, viscous friction, and plastic deformation. In the boundary lubrication (BL) regime, the solid bodies are in contact and the friction is dominated by the elastic and plastic deformation and wear in the solid bodies [175]. A more detailed discussion on the lubrication regimes is given in Refs. [83, 388, 417].

The Stribeck curve addresses the lubrication state of a tribosystem – especially historically – primarily from a macroscopic phenomenological perspective. The atomistic configurations, structure, and dynamics of the fluid in the contact zone and the physical elementary processes of the different lubrication regimes are today not fully understood. This is also due to the fact that it is difficult to study the influence of individual contact process parameters individually [42] – in both experiment and computer experiments. Many contact process parameters are linked, e.g. the dissipation and wear. Moreover, many contact process parameters, at the same time, influence the contact process and are influenced by the contact process, e.g. the temperature. An important focus of this work is on contributing to the understanding of lubrication – in particular of the fluid behavior in the direct vicinity of the contact zone. This includes the fluid molecules' squeeze-out behavior, the fluid adsorption behavior at the solid surfaces, the formation of a tribofilm, and the influence of structural properties of the fluid molecules.

The *Amontons-Coulomb* law (2) can be generalized as [91, 99–101, 114, 399, 414]

$$F_t = F_t^0 + \mu F_n , \quad (4)$$

where the term μF_n reflects *Amontons-Coulomb* law describing the load controlled friction and F_t^0 a load-independent friction force offset, which is a result of the adhesive forces. This offset was first proposed by *B. Derjaguin* [91] and is accordingly called *Derjaguin-offset*. Therein, both μ and F_t^0 are parameters characterizing a given tribosystem. Evidently, Eq. (4) reduces to *Amontons-Coulomb* law (2) for $F_t^0 \rightarrow 0$. It was reported that non-vanishing values for F_t^0 occur for systems, where a disordered fluid phase exists between the two solid bodies with rough surfaces [399]. Equation (4) can be further generalized as [128, 399]

$$F_t = F_t^0 + \tau A_{\text{cont}} + \mu F_n , \quad (5)$$

where τA_{cont} is the so-called *Bowden-Tabor* term [46], which reflects the influence of the

contact area dependence on the load $A_{\text{cont}} = A_{\text{cont}}(F_n)$ and the shear stress characterizing adhesion-controlled friction [99]. In this work, the coefficient of friction is taken as a simple observable well-defined by Eq. (2). This is justified not only by the fact that F_t^0 is negligible in the scratching simulations considered in this work, but also supported by the fact that adhesive and non-adhesive contributions cannot be separated in a simple way on the atomistic level [134]. Moreover, in an exemplaric simulation based on the setup used in chapters 3 and 4, the influence of the *Derjaguin-offset* was estimated to be around 0.5% and, therefore, negligible compared to the force contributions that stem from the plastic and elastic deformation of the substrate and the friction at the solid-solid-fluid contact. The employed coefficient of friction definition, cf. Eq. (2) (often referred to as ploughing friction) is unambiguous, consistent, and well-defined. Most of all, it is based on a well-defined measurement quantity that is applicable in both experiment and simulation.

The focus of this work is on the boundary lubrication regime, which is studied in chapters 3 - 5. Yet, in chapter 6, the entire range of the Stribeck curve is studied. It was already described by *Bowden and Tabor* [46] that the interactions between the fluid and the solid particles at the solid interfaces play a decisive role for the lubrication, e.g. chemisorbed oxygen yields a lower friction compared to nitrogen. To get a better understanding for the underlying friction mechanisms, the influence of the solid-fluid interactions on the contact process was studied in detail in this work (cf. chapters 3 and 5).

The viscosity of the lubricant is evidently an important tribological property, not only for the behavior of the *Stribeck* curve (cf. Eq. (1) and (3)), but also for the squeeze-out behavior of the fluid from the contact zone. The viscosity quantifies the resistance of the fluid to imposed shear forces. Thereby, the viscosity is introduced as

$$F_t = \eta A \frac{v}{z}, \quad (6)$$

where F_t indicates the drag force required to move a top layer with the area A of a fluid with the thickness z at a velocity v . More general, the viscosity η is the linear coefficient between the shear stress τ and the shear rate $\dot{\gamma} = \frac{\partial v}{\partial z}$, i.e.

$$\tau = \eta \dot{\gamma}. \quad (7)$$

Often, instead of the (dynamic/ shear) viscosity η , the so-called kinematic viscosity ν is used, which is simply given as

$$\nu = \frac{\eta}{\rho}, \quad (8)$$

where ρ indicates the density. The viscosity of a pure component is a function of the

temperature and pressure. For small shear rates, the viscosity is described by Eq. (7), which is called Newtonian behavior. For high shear rates $\dot{\gamma}$, however, shear thinning can occur for many lubricants and the viscosity decreases. Then, the viscosity (of a pure substance) does not follow Eq. (7), but becomes a more complex function

$$\eta = \eta(T, p, \dot{\gamma}) , \quad (9)$$

where T indicates the temperature and p the pressure.

2.1.4 The Relevance of Interfaces in Lubricated Tribosystems

Interfaces between bulk phases play a decisive role in tribological processes [42, 51, 251]. In tribosystems, multiple types of interfaces occur, cf. Fig. 3. On an atomistic level, the boundary between two bulk phases will always be in fact a transition region in which the properties change (also due to thermal fluctuations) somewhat continuously from one bulk phase to the other [1, 178]. This continuous transition is most pronounced for fluid-fluid interfaces, but also present for solid-fluid interfaces and solid-solid interfaces.

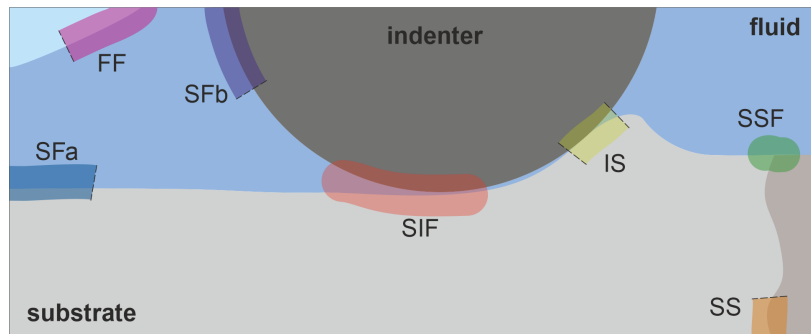


Figure 3: Scheme of the tribosystem on the nanoscale and examples of relevant interfaces at which two or more bulk phases are separated by an interphase. The abbreviation nomenclature is based on the three bulk phase bodies, i.e. substrate (S), indenter (I), and fluid (F). The substrate consists here of two grains (light and dark). The fluid consists of a liquid and a vapor phase, dark and light blue, respectively. The indenter is here a single crystal. The transparently colored strips indicate the interphase regions, where the particles experience interactions specific to a given interface that differ from those of the bulk phases.

The interfacial region is at times called interphase, emphasizing it being a spatial three-dimensional region between (in latin 'inter') two 'phases'. This is opposite to the term 'interface', which suggests a two-dimensional boundary between the phases. The term interface suggests that the two bulk phases are in contact at the interface⁴. This is,

⁴Oxford dictionary: "interface: (..) where two subjects, systems, etc. meet and affect each other." [281]

however, not the case in reality, i.e. the two bulk phases do not meet, but are separated by a layer, which establishes the transition between the two phases. The term interphase [76], on the other hand, correctly suggests that the two bulk phases are separated by an 'intermediate phase' that indirectly connects the bulk phases. The term interphase correctly emphasizes that a special region of matter exists that has neither properties of the adjacent bulk phases. Hence, the term 'interphase' captures the physics better. This physical picture is also reflected by the *Gibbs* adsorption equation characterizing the interphase of a system with N components at a given constant temperature T from a rigorous thermodynamic perspective [138] as

$$\sum_{i=1}^N n_i^s d\mu_i + Ad\gamma = 0 , \quad (10)$$

where μ_i indicates the chemical potential of component i , n_i^s the number of moles in the interphase s , A the surface area, and γ the surface energy (a.k.a. surface tension). Eq. (10) can be re-written as

$$\sum_{i=1}^N \Gamma_i d\mu_i = -d\gamma \quad \text{with} \quad \Gamma_i = \frac{n_i^s}{A} , \quad (11)$$

where Γ_i indicates the adsorption of component i in the interphase with respect to a reference system (which can be a position and/ or a reference component) [138, 150, 178]. Accordingly, the adsorption Γ_i is a measure for the mean composition of the heterogeneous interphase. Hence, the interphase is a spatial region, where the material properties (including the molecular interactions) deviate from the bulk phase properties. Yet, the two terms interphase and interface are often – and also in this thesis – used in a synonymous way.

The particles in the interfacial region experience different mean interactions compared to particles in the two adjacent bulk phases. Thereby, particles in interphases exhibit a change/ gradient of the external potential. This has important consequences for the properties of these interphases and for the behavior of the tribosystem (cf. Fig. 3) they are part of. A bulk phase, on the other hand, is defined as a collection of particles that do not experience a direct or indirect influence of an interfacial region and have on average homogeneous isotropic interactions.

Different types of interphases are relevant for tribosystems as schematically shown in Fig. 3. Their physical nature and relevance for tribosystems are briefly discussed in the following. It should be noted that a three-phase interphase can not be considered a contact *line* on an atomistic level – opposite to the classical view from the macroscopic level. This is due to the fact that the size of such interfacial regions is not negligible in comparison to the size of the contact zone, which will be shown in the results parts of

this work (cf. chapters 3 - 6). Hence, two different types of interphases are discerned for a tribosystem (cf. Fig. 3): The interfacial regions connecting two phases having a layer-like shape and the interfacial region connecting three bulk phases having a tube-like shape:

- solid-fluid interphases between the fluid lubricant and the solid bodies (either fluid-substrate or fluid-indenter interphase, cf. SFa and SFb in Fig. 3, respectively)
- solid-solid interphases between the two solid bodies (often different material) in the case of a direct contact of the two (indenter-substrate interphase, cf. IS in Fig. 3)
- solid-solid interphases of grain boundaries within one of the solid bodies (either substrate-substrate or indenter-indenter interphase, cf. SS in Fig. 3)
- vapor-liquid interphases in the case that cavitation occurs in the fluid lubricant (fluid-fluid interphase, cf. FF in Fig. 3)
- solid-solid-fluid interphase connecting the indenter, the substrate, and the fluid in the vicinity of the actual contact zone (substrate-indenter-fluid interphase, cf. SIF in Fig. 3)
- solid-solid-fluid interphase, where the interfacial regions connecting fluid adsorption layers on the solid bodies are in contact with an interfacial region connecting two grain boundaries (fluid-indenter-substrate interphase, cf. SSF in Fig. 3)

The above list is not exhaustive, but illustrates the complexity of the physical system. More types of interphases can occur and become relevant, e.g. a gas cavity gets in contact with a solid surface establishing a classical wetting situation (solid-vapor-liquid) etc.

The thickness of interphases – quantified here for simplicity in number of atoms/particles – strongly varies for the different types of interphases (yet this can not be taken as a measure for their significance). The number of particles experiencing significant anisotropic interactions and thereby constituting the interphase is in most cases at least approximately five (ballpark estimate). This is due to the fact that interaction potentials have a range of significant interaction of approximately 2.5 times the particle size. The particles in the center of an interphase, which experience strongest deviations from the bulk phase structure, pass the effects of the heterogeneity indirectly on within a layer thickness of at least five particles. This holds for practically all types of interfaces applicable in tribosystems, see list above. Yet, fluid-fluid interphases can have a larger thickness – they even approach infinite thickness upon approaching a critical point [303].

In general, different types of properties of interphases are important for tribological contact processes – in particular transport resistivities, e.g. the transport coefficients

for heat transfer and mass transfer. It should be noted that, at interfaces, different transport resistivities compared to the bulk phases apply. Moreover, not only the heat conductivity of the interphase itself, but an additional transfer resistance applies for heat transfer across interfaces (the so-called *Kapitza* resistance [192, 325]). Moreover, the atomistic structure of the interphases is important for the kinetics of the contact process. Also, classical properties – usually used in the context of bulk phases – are crucial for the overall system behavior such as the density, the compressibility, and the heat capacity of the interphases as well as the particle mobility (for example described by the diffusion coefficient).

Three types of interfaces are discussed in more detail in the following as these are of particular importance for the simulation systems studied in this work:

Solid-fluid interphase

The solid-fluid interphases between the fluid bulk phase and either the substrate or the indenter are of central importance for tribological contacts. Various properties of these interphases are important for the process such as the wetting behavior, the adsorption behavior, and the transport resistivities. The wetting behavior determines the contact angle of fluid droplets as well as capillary effects in the lubrication gap. The *Young* equation establishes the link between the contact angle α and the interfacial tensions of the vapor-liquid, solid-vapor, and solid-liquid interfaces, γ_{VL} , γ_{SV} , and γ_{SL} , respectively. For a planar solid surface it can be written as [178]

$$\cos \alpha = \frac{\gamma_{SV} - \gamma_{SL}}{\gamma_{VL}} . \quad (12)$$

For rough surfaces or chemically heterogeneous surfaces, the *Young* equation has to be modified, e.g. via the *Wenzel* model [178] as

$$\cos \tilde{\alpha} = R \cos \alpha , \quad (13)$$

where $\tilde{\alpha}$ indicates the contact angle on a structured wall, R indicates the ratio between the actual and projected solid surface area, and α is the contact angle for a planar wall. In the simulations carried out in this work, initially, the substrate has a planar surface, whereas a rough and chemically heterogeneous surface exists after the contact process. For solid-fluid interphases, also the adsorption behavior is important. It describes the amount and configuration of fluid particles adsorbed on the solid surfaces and thereby constituting the fluid side of the interphase. The adsorption is usually quantified as the number of fluid particles of component i per surface area Γ_i (cf. Eq. (10) and (11)). It is in general a function of many variables for a solid-fluid interphase, in particular

$$\Gamma_i = \Gamma_i(R, \varepsilon_{SF}, \sigma_F, T, p, \underline{x}) , \quad (14)$$

where ε_{SF} indicates the interaction energy between fluid and solid particles, \underline{x} the composition, and σ_{F} the size of the fluid molecules. In adsorption layers, the fluid particles exhibit a strong structuring compared to the relatively stochastic structure in the fluid bulk phase. The adsorption layer has an important influence on the cooling capabilities of the lubricant, as the heat removed via the fluid has to pass through the adsorption layer. Moreover, properties of the fluid adsorption layers are in particular important for the friction behavior in the mixed lubrication regime, cf. Fig. 2. The mobility of fluid particles in the direction parallel to the interface is important for the friction process and the squeeze-out of particles out of the lubrication gap (also in the boundary lubrication regime). The adsorption layer can act as the slip plane of the relative motion of the two solid bodies. On the atomistic scale, a slip velocity of the fluid at the solid surface v_s in a flow field exists, which can be characterized by

$$v_s = b \frac{\tau_s}{\eta}, \quad (15)$$

where η indicates the viscosity, τ_s the shear stress, and b the slip length, which characterizes the deviation from the no-slip condition [178, 251]. Moreover, the solid particles in the solid-fluid interphase and their properties (e.g. hardness and vibrations) play an important role for the formation of the tribofilm [1]. A large number of properties of solid-fluid interfaces have been individually comprehensively studied in the literature for different types of systems – both real substance [90, 329, 406] and model systems [26, 56, 92, 161, 162, 219, 325]. This comprises both equilibrium properties [26, 56, 56, 162, 219] and dynamic properties [90, 92, 325, 329, 406]. Yet, their role in tribosystems (cf. Fig. 3) is not as well-explored today.

Solid-solid interphase

The solid-solid interface between the indenter and the substrate (cf. Fig. 3) is evidently of central importance for the contact process [1, 7, 237, 415, 420]. Yet, in the case of lubricated contact processes – as focused on in this work – it is not a priori clear that the two solid bodies actually come in direct contact and a solid-solid interphase forms or a fluid film remains between the two solid bodies. If a solid-solid interphase forms, very high load and stress is expected in that interfacial region. Moreover, the contact and relative motion will cause the formation and evolution of crystal defects in the solid bodies – primarily in the softer solid body. For dry contact processes, a wealth of studies is available on the structure and evolution of the structure in the solid-solid interphases [8, 95, 134, 205, 237, 304, 304, 415]. Yet, for lubricated situations, the amount of available studies is scarce.

Solid-solid-fluid interphase

The solid-solid-fluid interfacial region between the indenter, the substrate, and the fluid

is decisive for the squeeze-out of fluid particles out of the actual contact zone. Also, this interphase plays an important role for the slip behavior of the system. The mass flux of particles squeezed out of the contact zone have to pass through parts of the solid-solid-fluid interfacial region. Hence, not only the fluid viscosity in that small region, but also the simultaneous adsorption behavior of the fluid particles on two adjacent solid surfaces is important. Moreover, it should be noted that the solid-solid-fluid interphase region backsides of the indenter can be a source for the formation of vapor phase bubbles, i.e. cavitation (cf. Fig. 3). This was in fact observed in some simulations carried out in this work, cf. chapter 6.

A special case of interphase is the so-called tribofilm. A tribofilm forms in tribological contacts as a transformation of one or multiple of the participating phases [83, 93, 103, 235, 237, 320, 339, 405, 420, 425]. The tribofilm often has a thickness larger than classical interphases and comprises to some extent chemical reactions. A tribofilm can have a thickness on the micrometer range. The formation and properties of tribofilms on the atomistic level are today relatively poorly understood.

Since interphases are highly relevant for tribosystems due to their physical properties, they also play a decisive role in the modeling of tribosystems using MD simulations. The interactions of the particles are – by definition – anisotropic in these heterogeneous interfacial regions. This poses additional challenges to the atomistic interaction models employed in the simulations – especially for modeling solid-fluid interactions and solid-solid interactions between different components, i.e. cross-interactions. The cross-interaction models applied in a simulation dominate several interfacial properties (see above). However, the molecular modeling of solid-fluid interactions is still in its infancy compared to bulk phase interaction modeling. This is discussed in more detail in section 2.2.4.

Interfaces play a crucial role in lubricated contact processes. Despite the fact that this seems to be well-accepted today [74], there have been so far surprisingly little systematic atomistic studies carried out on the role of interfaces in such, e.g. the relevance of the interfacial *Kapitza* heat transfer resistance on the thermal balance, the behavior of fluid adsorption layers of the solid bodies in the three-phase contact, and the formation of a tribofilm. A systematic study of the role of interfaces in tribosystems is also out of the scope of this work (but an interesting topic for future research). Yet, the physical effects discussed above are in fact observed and highly relevant for the computer experiments carried out in this work (cf. chapters 3 - 6). The results from this work further emphasize the relevance of interfacial properties in tribosystems.

2.1.5 Tribology on Different Scales

Tribology is not only a highly interdisciplinary topic, also aspects from multiple length scales are relevant. Thus, effects on the macro scale, the meso scale, and the nanoscale level influence the overall behavior of a tribosystem. Fig. 4 gives an overview of selected aspects relevant to the different length scales in tribology. The focus of this work is on the nanoscopic scale, where matter is built of atoms and molecules. Accordingly, this field of tribology is usually called *nanotribology* [37, 140, 375]. Nevertheless, physical effects and mechanisms on the meso scale and macro scale level influence the nanoscale level. For example, the temperature field and the heat fluxes into the bulk bodies on the macro scale can be considered boundary conditions on the nanoscale. Also, the surface topography and structure on the meso scale has important consequences for the model design. A detailed discussion of the role of scale effects and their coupling in tribology is given in Refs. [41, 42, 83, 395].

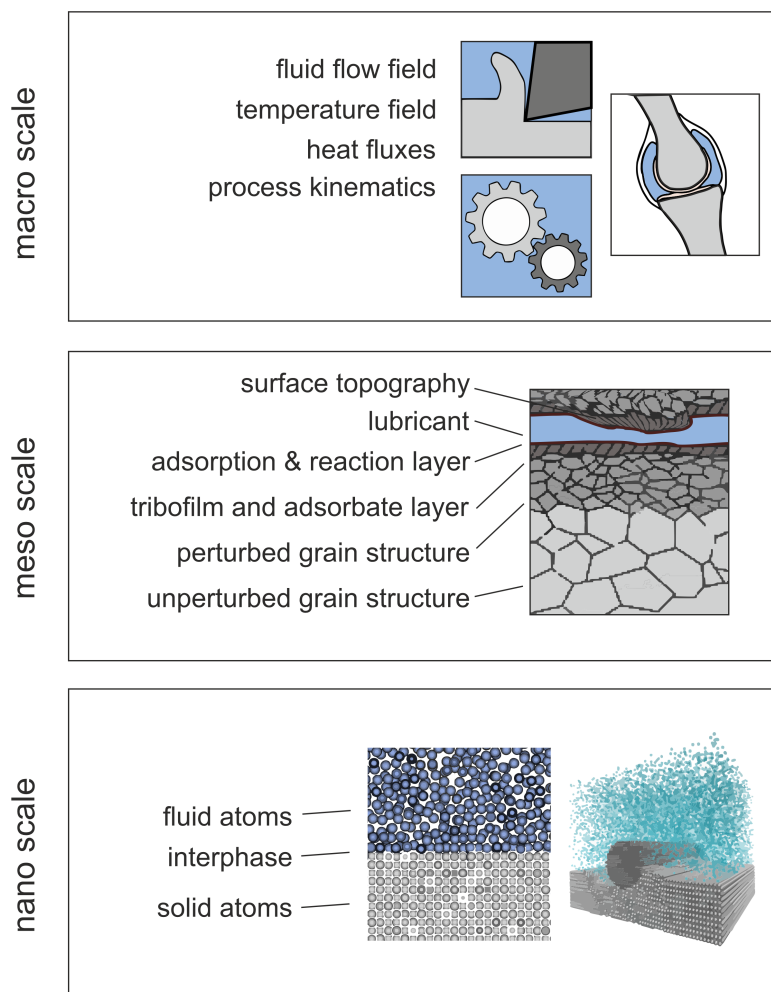


Figure 4: Overview of aspects relevant to tribology on different length scales. In parts adapted from Ref. [24, 83].

2.2 Molecular Simulation

Molecular dynamics (MD) simulation based on classical Newtonian force fields has, since the 1950s [6, 296], become an indispensable tool in many scientific disciplines, such as physics, chemistry, biology, and engineering. In MD simulations, matter is modeled on the atomistic scale based on molecular interactions, which are described by so-called force fields. Molecular simulations can be applied for two types of tasks: (a) the prediction of material properties and (b) the modeling of nanoscale processes. In this work, nanoscale processes are considered, i.e. lubricated contact processes. The challenges of MD simulations lie on the one hand in the fact that a large number of particles has to be simulated over a long time, which requires significant computational resources, and, on the other hand, in the techniques that are required for determining macroscopic properties from the atomistic simulations.

There is a large number of introductory literature on MD simulations available today, e.g. Refs. [9, 125, 297]. These give a comprehensive introduction into the simulation technique. In this chapter, only the physical key aspects of the simulation method relevant for the simulations carried out in this work are discussed. This comprises a brief discussion on the reliability of the results obtained from molecular simulation computer experiments and what general sources of error are to be expected (section 2.2.1), an introduction of the physical kernel of the simulation method (section 2.2.2), a brief summary on the structure of matter in different phases and interphases on the atomistic level (section 2.2.3), a discussion on molecular models used in the simulations for describing matter (section 2.2.4), a literature review on MD simulations in tribology and the physical insights obtained from that (section 2.2.5), and an introduction of the basics of the MD simulation scenario used in this work (section 2.2.6).

Besides molecular dynamics simulations, other modeling approaches exist that are frequently used in the literature for the simulation of tribological systems [259, 267]. Most of them are based on continuum approach and can therefore inherently not provide insights into the atomistic nature of the elementary processes. In this work, the sole focus is on molecular modeling and simulation, i.e. the atomistic scale.

2.2.1 Molecular Simulations as Computer Experiments

The importance of computer simulations based on physical models – and molecular simulations in particular – is highlighted by the fact that they are often considered as a third pillar of science, together with theory and laboratory experiments, and are, accordingly, often referred to as *computer experiments* [140, 230]. Analogue to laboratory

experiments, there are several sources of error in computer experiments. However, some important differences have to be noted between laboratory experiments and computer experiments. Evidently, in computer experiments, the model design used for 'simulating the physics' [119] has an important influence on the credibility of the results. The model design in molecular simulation has multiple levels such as (i) the overall layout of the simulation box and the applied boundary conditions (addressed in more detail in section 2.2.5); and (ii) the choice of the molecular interaction models (addressed in more detail in section 2.2.4). Additionally, the sources of error well-known from laboratory experiments also apply to computer experiments such as statistical errors and systematical errors.

Statistical errors are relatively easy to quantify and assess in molecular simulations. Systematical errors, on the other hand, are more difficult to deal with. They are directly related to the reproducibility of the simulation results. A general reproducibility of the findings is a well-accepted basic requirement for any scientific method. For laboratory experiments, the reproducibility is accepted as an important goal. For computer experiments, it is common to assume implicitly that results can be reproduced exactly [170]. However, this standpoint has been criticized, and there is a broad discussion about the reproducibility crisis induced by the complexity of computer simulations [2, 18, 188, 229, 231, 241, 261, 383]. Some limitations of the reproducibility of molecular simulation results have been recently demonstrated – even for simple simulation tasks [319, 361]. Despite this, in practically all applications of molecular simulations, only statistical uncertainties are considered and reported, while systematical uncertainties are not taken into account. The reproducibility of computer experiments and systematic errors depend on many factors, including physical and numerical algorithms, program codes, compilers, hardware, and, finally, the entire work flow including errors induced by human interaction. In this work, the reproducibility of molecular simulation computer experiments is explicitly addressed in chapter 4 – focusing on statistical errors in complex in-stationary and non-equilibrium MD simulation setups.

2.2.2 Molecular Dynamics: Simulation Method

Fig. 5 schematically shows the simulation pipeline of an MD simulation. As a starting point, the simulation task has to be specified, by choosing the geometrical setup (e.g. the size of an indenter and the substrate thickness) and by choosing the molecular models for describing the interactions during the simulation (e.g. the force field of the fluid and the substrate). Based on these principle specifications, an initial configuration is created that comprises the positions \underline{r}_i and velocities (or corresponding momenta \underline{p}_i) of all particles $i = 1..N$ at the beginning of the simulation. This defines a point in the

$6N$ -dimensional phase space [256]

$$\Gamma = \Gamma(\underline{r}_i, \underline{p}_i) . \quad (16)$$

The initial particle positions and momenta have to be chosen carefully to avoid a strong and unfavorable overlap of interaction sites that would yield extreme forces in the first time step and usually cause an 'explosion' of the simulation setup. Since the equilibrium distribution functions of the chosen substances and molecular models at the given thermodynamic conditions are not a priori known, simplistic assumptions are used for building the initial configuration, e.g. using a regular lattice also for initializing fluid phases. The initial velocities are less crucial and are usually specified according to the desired temperature such that a *Maxwell*-distribution is obtained, i.e. [256]

$$f(v) \, dv = 4\pi \left(\frac{M}{2\pi k_B T} \right)^{3/2} v^2 \exp\left(-\frac{Mv^2}{2k_B T}\right) \, dv, \quad (17)$$

which describes the fraction of particles with the velocity between v and $v + dv$ at a given temperature T . In Eq. (17), M indicates the particle mass and $v = \sqrt{v_x^2 + v_y^2 + v_z^2}$.

The simulation itself is split in two phases: (A) an equilibration phase and (B) a production phase (cf. Fig. 5 - left). During the equilibration phase, equilibrium distribution functions for the configurations and velocities are established that reflect the behavior of the chosen molecular models at the given thermodynamic conditions. During the production phase, the properties of interest are sampled under the influence of boundary conditions that reflect the macroscopic situation of interest, i.e. primarily the relative motion of two solid bodies in this work.

During both the equilibration and the production phase, the time evolution of the system, i.e. the trajectories of the particles, are computed by solving *Newton's* equation of motion in combination with the evaluation of the force fields describing the interactions, cf. Fig. 5 - right. In MD simulations, *Newton's* equation of motion are solved numerically, i.e. the time coordinate is discretized. By iteratively computing the forces and force balances for all particles and subsequent configurations by integrating *Newton's* equations of motion, the trajectories of the particles are predicted (in *Feynman's* sense of 'simulating physics with computers'). Additionally, different properties of the system are computed such as the instantaneous temperature, pressure etc. A large (but limited) amount of data is written to the hard drive. Once the desired amount of time steps was computed, the simulation ends and post-processing of the data is applied.

In the MD routine, the forces \underline{F}_i on a given particle i are computed from the potential energy of the force field u

$$\underline{F}_i = -\nabla_{\underline{r}_i} u(\underline{r}_1, \underline{r}_2, \dots, \underline{r}_N) , \quad (18)$$

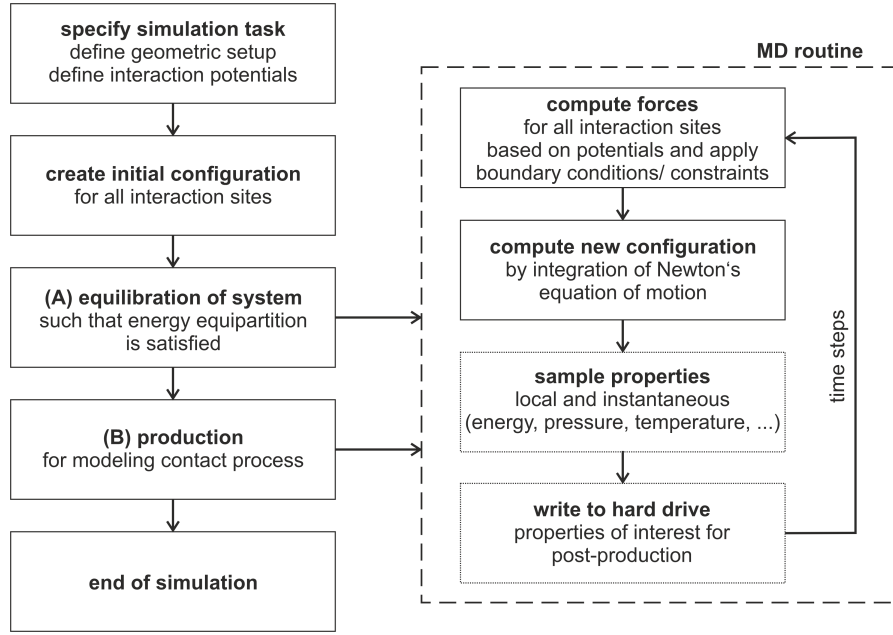


Figure 5: Molecular dynamics simulation algorithm.

where \underline{r}_i indicates the position of a particle (or interaction site) $i = 1..N$. Hence, for a given atomistic configuration, the net forces acting on a given particle depend on all neighboring particles (within a certain cut-off range). Newton's equation of motion

$$\underline{F}_i = M_i \underline{a}_i , \quad (19)$$

where \underline{a} indicates the acceleration and M the particle mass, can then be solved by numerical time integration. There is a large number of MD integrators available today [9, 125]. One of the most simplest ones, the *Verlet* algorithm [9, 398] is used here for illustration, which computes the particle positions at a time $\tau_0 + \delta\tau$ based on the positions at the time τ_0 and $\tau_0 - \delta\tau$. It can be derived from a *Taylor* expansion about \underline{r}_i

$$\underline{r}_i(\tau_0 + \delta\tau) = \underline{r}_i(\tau_0) + \delta\tau \underline{v}_i(\tau_0) + \frac{1}{2} \delta\tau^2 \underline{a}_i + \dots \quad (20)$$

$$\underline{r}_i(\tau_0 - \delta\tau) = \underline{r}_i(\tau_0) - \delta\tau \underline{v}_i(\tau_0) + \frac{1}{2} \delta\tau^2 \underline{a}_i - \dots , \quad (21)$$

where \underline{v}_i indicates the particle velocities and $\delta\tau$ the time step. The summation of Eqs. (20) and (21) yields

$$\underline{r}_i(\tau_0 + \delta\tau) = 2\underline{r}_i(\tau_0) - \underline{r}_i(\tau_0 - \delta\tau) + \delta\tau^2 \underline{a}_i , \quad (22)$$

which allows the computation of the particle positions (conceding a numerical error [9]) and makes the method deterministic. It should be noted that different time integrators differ in their numerical accuracy and computational efficiency.

Macroscopic observables such as the temperature and pressure can be computed from the particle trajectories and forces using statistical mechanics [168, 256]. Therefore, time averaged values $\langle X \rangle$ of instantaneous values are computed for a given property X [125]. The instantaneous temperature can for example be computed (in the canonical ensemble) as

$$T = \frac{1}{3Nk_B} \sum_{i=1}^N \frac{|\underline{p}_i|^2}{M_i} , \quad (23)$$

where \underline{p} indicates the momentum, N the number of atoms, and k_B the Boltzmann constant [9]. Eq. (23) holds for an equilibrium situation. In a case, where a flow field is present and particles in a given region \hat{r} exhibit a net directional motion with the mean velocity $\underline{v}_{\text{flow}}$, the instantaneous local temperature is computed as [107, 312]

$$T = \frac{1}{3Nk_B} \sum_{i=1}^N M_i [\underline{v}_{i,\text{therm}} - \underline{v}_{\text{flow}}(\hat{r})]^2 . \quad (24)$$

The two terms in Eq. (24) reflect the fact that the instantaneous velocity of a particle has two contributions

$$\underline{v} = \underline{v}_{\text{therm}} + \underline{v}_{\text{flow}} , \quad (25)$$

where $\underline{v}_{\text{therm}}$ indicates the contribution of the stochastic thermal motion and $\underline{v}_{\text{flow}}$ indicates the contribution of a net flow field. In an equilibrium situation, no flow exists and $\underline{v}_{\text{flow}} = 0$.

In statistical mechanics, matter can be simulated using (at least) eight different ensembles [143]. An ensemble indicates the entity of configurational states (i.e. points in the phase space) that yield the same macro state. Considering a pure component at a homogeneous equilibrium state, the macro state can be described by different sets of thermodynamic variables, e.g. number of particles N , volume V , and temperature T , which establishes the so-called *canonical ensemble*. On the atomistic level, these variables define the overall boundary conditions the system has to meet in a given ensemble. Hence, in the canonical ensemble, the atomistic system (configurational states) has a constant number of particles, constant volume, and constant temperature (which corresponds to the mean velocity of the particles). The natural ensemble in MD simulation is the NVE ensemble, where the total energy is constant (and the temperature exhibits fluctuations). Thus, a simulation box with N particles and constant volume V that is studied with a given (energy conserving) time integrator yields constant total energy. The total energy E is the sum of the kinetic energy of the particles in the system K and the potential energy of the particles V , i.e.

$$E = K + V . \quad (26)$$

The potential energy term is obtained from the evaluation of the force field of the system (cf. section 2.2.4) at a given time step. To obtain other ensembles in MD simulations, different boundary conditions can be imposed to the system, e.g. a thermostat [9, 125, 297] that re-scales the particle velocities each time step enforcing a constant temperature T , which establishes an NVT ensemble. A thermostat can also be applied selectively in a simulation such that only particles in a specific spatial region are affected (which is particularly relevant for this work). The simulation box is then, strictly speaking, neither NVE nor NVT . Moreover, it should be noted that, in this work, non-equilibrium MD (NEMD) simulations were carried out, which do strictly not establish a statistical mechanical ensemble.

Another type of boundary condition is required in MD simulations, i.e. the actual spatial boundary of the simulation box. Fig. 6 shows three types of boundary conditions that are relevant for this work. Fig. 6 a) shows the classical periodic boundary conditions (in four directions in a plane) [9]; Fig. 6 b) shows a reflective wall; and Fig. 6 c) shows a boundary condition implemented by fixating the positions of two layers of particles.

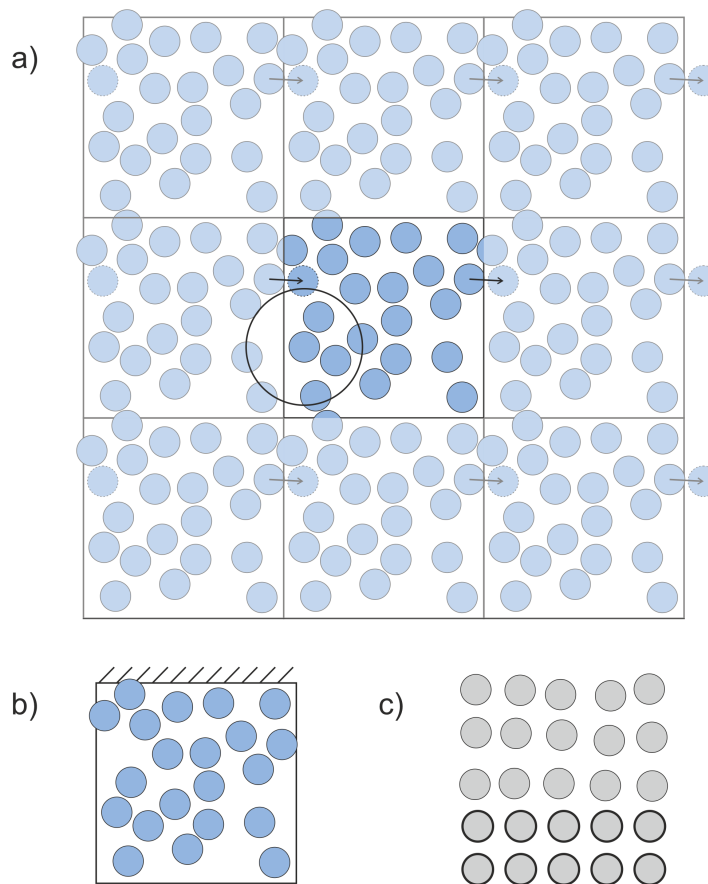


Figure 6: Illustration of different types of boundary conditions: a) periodic boundary conditions, b) repulsive wall boundary conditions, and c) constraint atom position boundary conditions. In parts adapted from Ref. [9].

2.2.3 Structure of Crystals, Fluids, and Interfaces on the Atomistic Scale

Molecular dynamics simulations is an excellent tool for studying the fundamentals of the structure of phases and interphases as well as their relation to macroscopic properties and their evolution during processes on the nanoscale. MD simulation provides a great depth of insights into their inner workings. In particular, matter can be present in four types of phases, i.e. vapor, liquid, solid, and plasma (the latter is, however, not captured by classical force field models and not further considered here). For the tribological contacts studied in this work, the structure of phases and interphases is crucial. In this section, first, the structure of different types of bulk phases is discussed. For solids, also different types of defects are briefly discussed. Then, the atomistic structure at interfaces relevant for this work is discussed.

For a given thermodynamic state, the molecular force field model fully determines the atomistic equilibrium structure. For a homogeneous phase, the structure is usually quantified using distribution functions [9, 154]. The most frequently used and simple distribution function is the radial distribution function (RDF), which is defined as [256]

$$g(r) = \frac{\rho_{\text{local}}(r)}{\rho_{\text{bulk}}} \quad \text{with} \quad \rho_{\text{local}} = \frac{dN}{4\pi r^2 dr} , \quad (27)$$

where r indicates the distance between particles, $\rho_{\text{local}}(r)$ the local density, and ρ_{bulk} the mean bulk phase density. Hence, $g(r)$ is a measure for the probability to observe other molecules in a distance range dr around a given 'central' molecule. Therefore, the RDF must converge to unity for $r \rightarrow \infty$.

Fig. 7 schematically shows examples for the RDF of a gas, a liquid, and a solid phase (top to bottom). For the gas phase, no significant structuring is observed besides the maximum of $g(r)$ that is a result of the dispersive attraction of the particles. For the liquid phase, a strong local structuring is observed. Thus, a given particle has at a specific short distance a high number of neighbors surrounding the particle. For the solid phase, a strong short and long distance structuring is observed, i.e. the particles are on lattice positions, but exhibit some thermal motion.

For solid phases, different lattice structures may be present at equilibrium [14, 201] (amorphous solid phases are not considered here). Fig. 8 schematically shows unit cells of the most common crystal structures, i.e. the *simple cubic* (sc) structure, the *face centered cubic* (fcc) structure, the *body centered cubic* (bcc) structure, and the *hexagonal closest packed* (hcp) structure.

In this work two substrate materials are considered: The Lennard-Jonesium (details

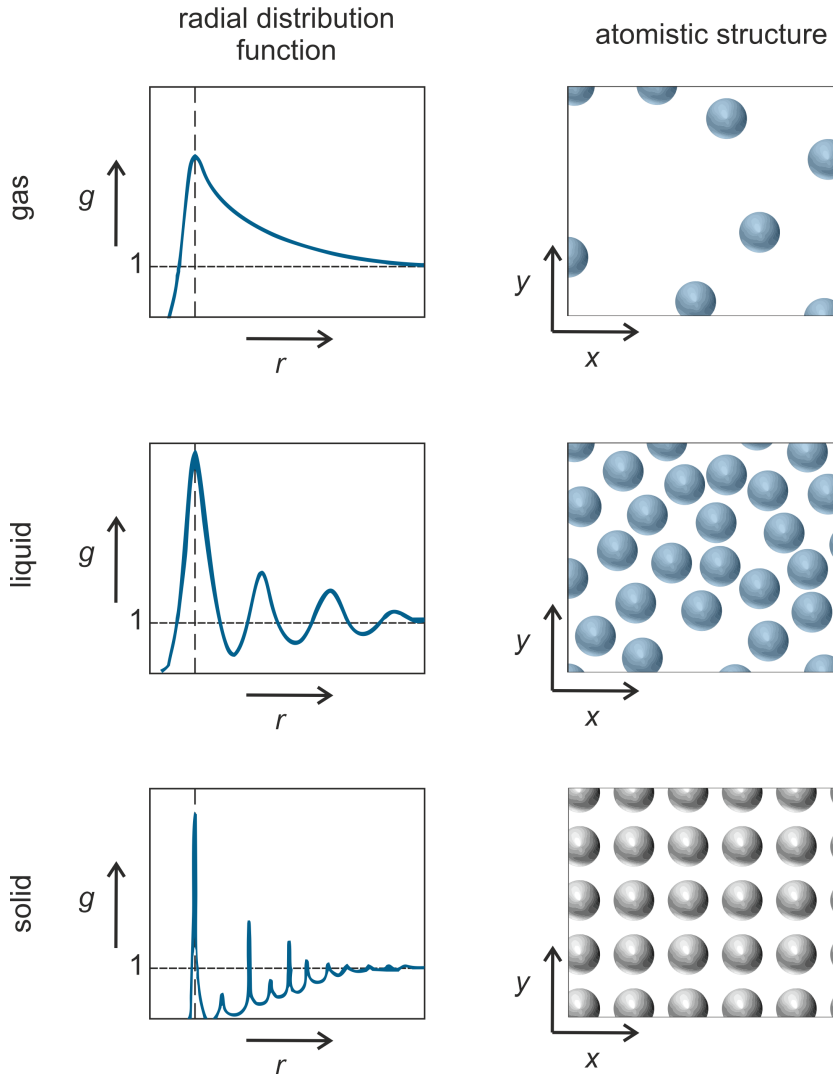


Figure 7: Structure of bulk phases on the atomistic scale for a gas, a liquid, and a (crystalline) solid phase (top to bottom). Left: Schematic radial distribution functions (cf. Eq. (27)). Right: Schematic snapshot of atomistic configuration. In parts adapted from Ref. [9].

given in the Appendix A) and iron. The Lennard-Jonesium material has different equilibrium structures depending on the (thermodynamic) state point [327, 389]. At very low temperatures, the hcp structure exists. At moderate and high temperatures, the fcc solid phase is energetically more favorable for the Lennard-Jones material [327, 389]. In this work, the fcc structure Lennard-Jones material (and corresponding thermodynamic states) are considered. Also, iron has different equilibrium lattice structure phases for different thermodynamic conditions [43, 155, 270]: At moderate temperatures and pressure, the equilibrium structure of iron is bcc, which is also used in this work.

In a perfect crystal, the material consists purely of periodically repeating unit cells, cf. Fig. 8. In a real crystal, irregularities occur that distort the symmetry of the lattice locally. These irregularities are called crystal defects [14, 201]. Fig. 9 schematically

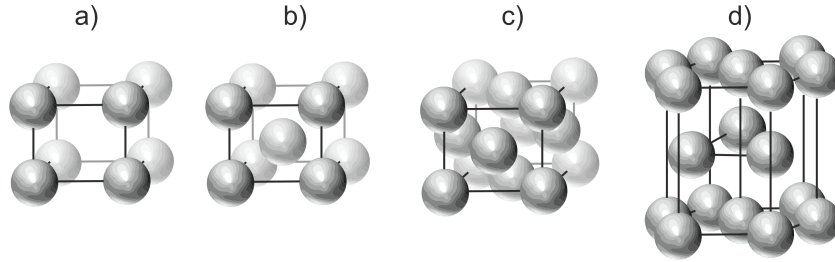


Figure 8: Unit cells of the principal crystal structures: a) simple cubic – sc; b) body centred cubic – bcc; c) face centered cubic – fcc; and d) hexagonal closest packed – hcp. Inspired by Ref. [201].

shows different types of defect structures, i.e. point defects (zero-dimensional), line defects (one-dimensional), and plane defects (two-dimensional). Due to the atomistic interactions, lattice defects affect the particles in the neighborhood of the actual defect. Hence, the lattice structure exhibits perturbations in the vicinity of a lattice defect. Formally, also three-dimensional defects exist, which can be porous structures of the material (not considered here).

Fig. 9 a) - c) shows three types of zero-dimensional defects: a) vacancy point defect; b) interstitial point defect (both self-interstitial and impurity interstitial); and c) substitutional point defect. Hence, particles of a second component can take interstitial or substitutional lattice points for point defects, which is important for the formation of tribofilms (cf. chapter 6).

Fig. 9 d) and e) show the two principal line defect types (also called dislocations). Fig. 9 d) shows an edge dislocation, where a half plane of atoms is inserted and the end line of the half plane forms the line dislocation. Fig. 9 e) shows a screw dislocation, where two atom planes are sheared against each other. Often, combinations of edge and screw dislocations as well as joints of dislocations occur such that the dislocation lines and dislocation networks can become complex geometries.

Different types of two-dimensional (plane) defects exist, such as grain boundaries, free surfaces (to a vacuum), and crystal interfaces to fluid phases. Fig. 9 f) and g) show two types of plane defects. Fig. 9 f) shows a plane defect, where two cubic crystal phases (with different lattice constants) are in contact. Fig. 9 g) shows a plane defect, where two different crystalline phases are tilted. The latter type of plane defect can also occur between two phases of the same crystal type, which is often called grain boundary. Most real materials are polycrystalline with a distribution of grain sizes and relative orientations [76, 147]. Yet, in this work, monocrystalline (single crystal) materials are studied as model systems and the focus is on the influence of lubrication of the tribosystem.

At interfaces, not only crystalline phases experience a perturbation, but also fluid

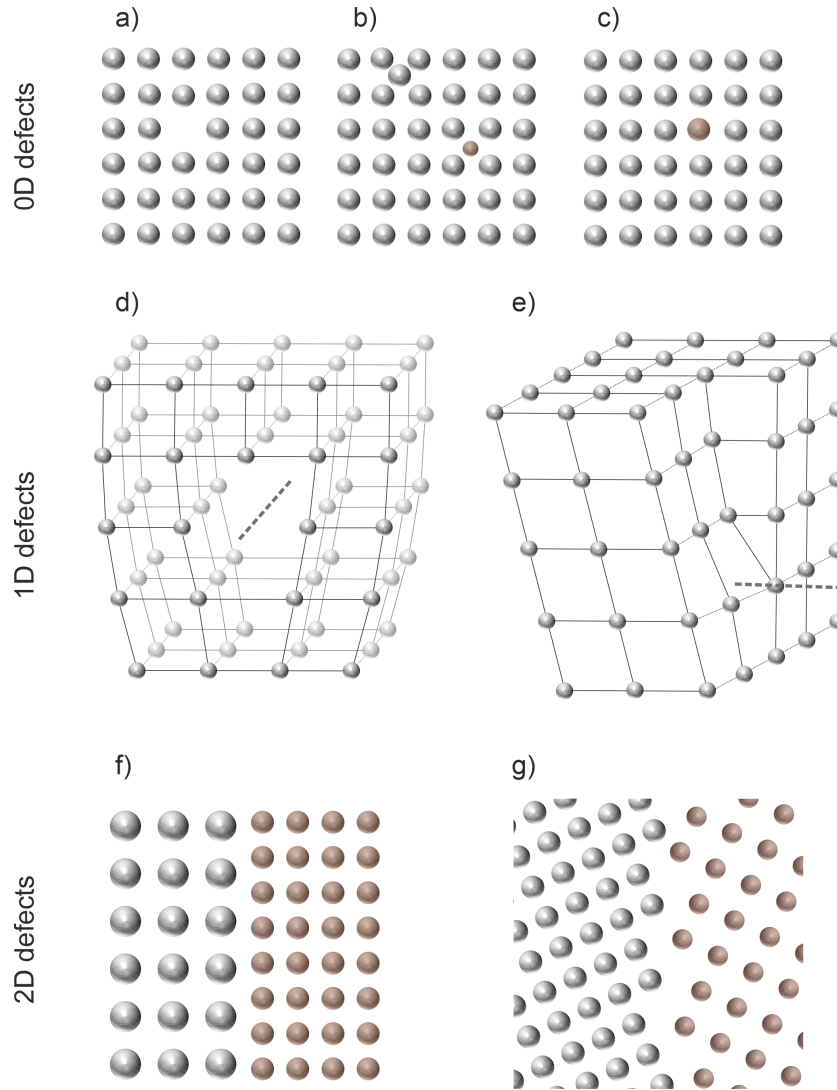


Figure 9: Schematic examples for 0D (point), 1D (line), and 2D (plane) crystal defects. The white and the red balls indicate particles of different materials. See text for details. Inspired by Refs. [14, 201].

phases are strongly affected by interfaces. The behavior of fluids at interfaces is of central importance for studying lubrication on the atomistic scale. Fig. 10 schematically shows different types of interface structures. The left column shows the density profiles, i.e. number density ρ_i of a component i as a function of the coordinate z , which is normal to the interface. The right column shows a snapshot of an exemplaric atomistic configuration.

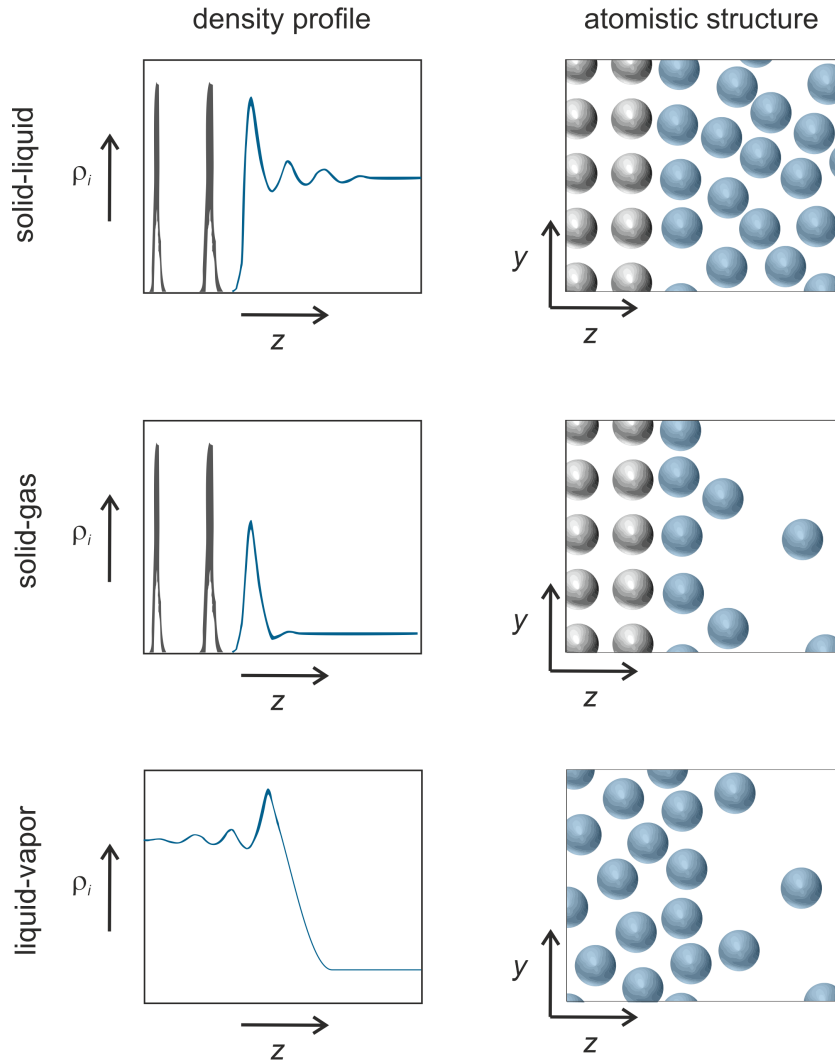


Figure 10: Structure of interfaces between different types of bulk phases⁵ on the atomistic scale (top to bottom). Left: Schematic density profiles as a function of the coordinate normal to the interface. Right: Schematic snapshot of the atomistic configuration. Inspired by Refs. [178, 345].

Fig. 10 - top shows the structure of a solid-liquid interface, where the solid and the liquid phase are two different components. For the solid phase side, the density profile in the interphase is a direct result of the RDF of the corresponding solid phase. Yet, the fact that the particles at the interface experience heterogeneous interactions causes deviations from the density profile at the interface compared to that in the bulk phase (yet too small to be seen in the schematic figure), which is fully in line with the physical picture of plane defects. For the liquid phase side at the solid-liquid interface (cf. Fig. 10 - top), more prominent differences between the bulk material and the material at the interface are observed. The solid phase acts as an external field, which causes a strong layering of the liquid phase particles at the interphase – resembling a solidification of the

⁵The term 'gas' phase is used for indicating a homogeneous gas phase at a given T, p , whereas the term 'vapor' phase is used for indicating a gas phase that co-exists with a liquid phase at a given T , i.e. a vapor-liquid equilibrium.

first layer(s). The details of these adsorption structures, e.g. the thickness and number of adsorbed particles, depend on many factors such as the two participating materials (solid and liquid) as well as the cross-interactions and the thermodynamic conditions [26, 160, 162]. For solid-liquid interfaces (cf. Fig. 10 - top), the mean density of the adsorption layer is similar to that of the liquid bulk phase, but the adsorbed particles are less mobile [40, 45, 113, 219], i.e. stick (to some extent) to the solid particles. The influence of the degree of this 'stickyness' on the tribocontact is studied in chapters 3 and 5.

A similar situation is observed for solid-gas interfaces, cf. Fig. 10 - middle. Again, the fluid particles experience an external field from the solid particle lattice structure and an adsorption layer forms. For solid-gas interfaces (cf. Fig. 10 - middle), the mean density of the adsorption layer is often significantly higher than the bulk fluid density and particles in the adsorption layer are less mobile than those in the bulk phase. This is due to the attractive adsorption interaction between solid and fluid particles as well as the dispersive attractive interactions of other neighboring fluid particles in the adsorption layer.

Nevertheless, for both a solid-liquid and a solid-gas interface, a flux of fluid particles entering and leaving the adsorption layer into and out of the bulk fluid phase exists. At equilibrium, these two fluxes are equal, which establishes a so-called *dynamic equilibrium*. The tendency of fluid particles to leave a position in the adsorption layer is crucial for the squeeze-out behavior of the fluid in the lubrication gap. This behavior depends on many factors such as the solid-fluid interaction model, the shearing conditions, and the thermodynamic condition (e.g. temperature and pressure).

For completeness, also a vapor-liquid interface is depicted in Fig. 10 - bottom, which is relevant for lubrication if cavitation occurs (cf. Fig. 3). Also at vapor-liquid interfaces, the particles experience an external field regarding their interactions – simply due to the heterogeneity of the system. The heterogeneity at fluid-fluid interfaces can cause similar adsorption layering effects as observed for solid-fluid interfaces, but to a significantly smaller extent (exaggerated in the scheme in Fig. 10 - bottom).

2.2.4 Molecular Models

Molecular interactions can in general be modeled using first principle quantum mechanics. Therefore, the *Schrödinger* equation is used for describing the state of a molecular system. The stationary *Schrödinger* equation can be written as

$$\hat{H}\psi = E\psi , \quad (28)$$

where \hat{H} indicates the Hamilton operator (energy operator), ψ is the wave function, and E the energy of the system. Eq. (28) is an eigenvalue problem, where ψ is the eigenfunction and E the eigenvalue. For a stationary molecular system, the (absolute squared) wave function characterizes the probability for a particle to be localized at a given point. By determining E for different molecular structures (with respect to the nuclei positions), the intramolecular and intermolecular interactions can be determined [118].

Yet, this direct ab initio simulation approach is computationally too expensive for describing many particle systems required in nanotribology for studying lubricated contact processes. Therefore, molecular simulations based on classical force fields are widely used today for such applications. The total potential energy of an N -particle system can in general be written as

$$u_{\text{total}} = u_{\text{total}}(\underline{r}_1, \underline{r}_2, \dots, \underline{r}_N) , \quad (29)$$

which is a function of the distance and orientation of atoms. These interaction potentials provide a relatively simple, yet robust, approximation of the 'true' molecular interactions. Hence, classical force fields have become the 'working horse' of molecular simulation. Accordingly, a large number of force fields and classes of force fields, i.e. approaches for formulating Eq. (29), is available today [9, 190]. For the modeling of molecular fluids and for the modeling of solid metals, two different approaches are mostly used: For molecular fluids, so-called transferable force fields [102, 190, 321] and for solid metals, potentials based on the embedded atom method (EAM) [88, 89, 182, 225].

In many cases, only pairwise interactions are considered in the potential functions such that the total interaction potential can be simplified as

$$u_{\text{total}}(\underline{r}_1, \underline{r}_2, \dots, \underline{r}_N) = \sum_{i=1}^N \sum_{j>i}^N u_{ij} , \quad (30)$$

where u_{ij} indicates the pair interaction between two interaction sites i and j ; the sum of $j > i$ is used to avoid double counting of pairs. Pairwise interactions proved sufficient and a good approximation for fluid systems, whereas they are a crude simplification for solid phases, especially metals. Hence, for solid metals, (more expensive) multi-body interaction potentials need to be used to accurately capture the material features.

In transferable force fields for fluids, both intramolecular and intermolecular interactions are explicitly modeled in a generalized way. A transferable force field is a generalized chemical construction plan for substance classes, e.g. characterizing the interaction between specific atom types. Therefore, based on a transferable force field construction plan, a large number of component-specific force fields can be constructed.

Fig. 11 gives an overview of the different interaction types applicable in transferable force fields. The intermolecular interaction potentials lie at the heart of the model. They are mostly modeled by the Lennard-Jones or the generalized Mie potential that

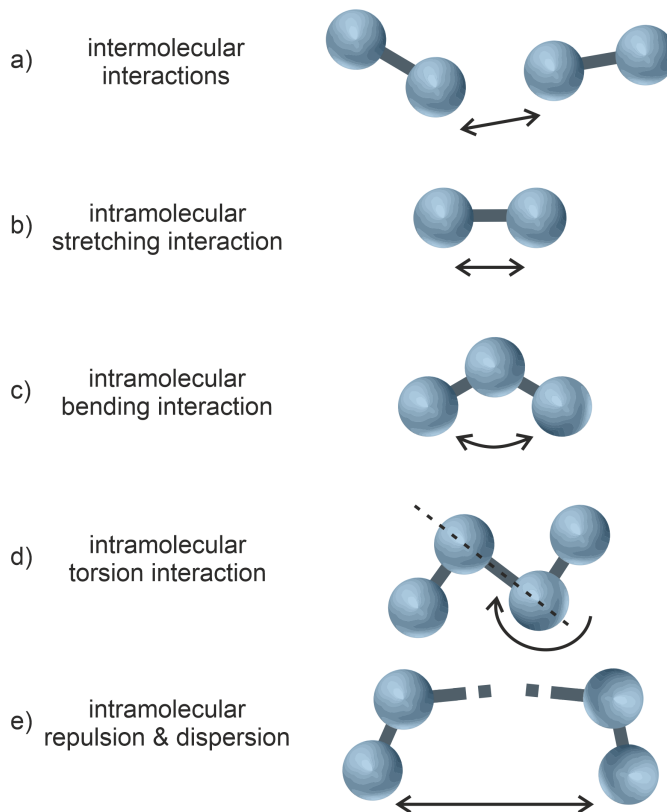


Figure 11: Scheme of the molecular interactions modeled in fluid force fields: a) intermolecular interactions; b) - e) intramolecular interactions. Inspired by Ref. [223].

are eventually superimposed by point charges [9, 190, 353]. There are three main types of transferable force fields, namely (i) all-atom; (ii) united-atom; and (iii) coarse grain. The degree of abstraction of the force fields increases from (i) to (iii), which also increases the computational efficiency as less details are included. However, the accuracy for predicting macroscopic thermophysical properties does not in general correlate with the degree of abstraction [322, 331]. Usually, the ability to extrapolate to state regions that were not considered in the parametrization decreases with increasing the degree of abstraction. In all-atom force fields, all atoms are modeled by an individual interaction site. In united-atom force fields, on the other hand, groups of atoms are fused to an interaction site. For example, methyl or methylene groups are fused to a single interaction site and hydrogen atoms are not explicitly modeled. In coarse grain force fields, larger sections of molecules (or even multiple molecules) are modeled as an interaction site. A large number of transferable force field construction plans have been developed in the past decades, e.g. DREIDING [253], AMBER [79], PCFF8 [372], TraPPE-UA [65, 66, 249, 250, 369, 411], OPLS-AA [79, 86, 185, 186, 410], Potoff [20, 265, 290, 291],

and CVFF [87]. Among these transferable force fields, the TraPPE model is probably the most popular one for modeling alkanes. TraPPE is a united-atom force field. It was developed for modeling vapor-liquid phase equilibria; accordingly named 'Transferable Potentials for Phase Equilibria – TraPPE'. Today, it is frequently used in tribological MD simulation studies, e.g. Refs. [110, 243, 322, 430, 431]. It was therein reported several times that it provides a good representation of alkane molecules. For modeling long chain alkanes, the TraPPE force field was used in this work. For modeling methane, the united-atom force field model from Ref. [402] (part of the *Boltzmann-Zuse society* – BZS force field framework [353]) was used.

The TraPPE force field as used in this work (and other transferable force fields) [66, 249, 250] can be written as

$$U_{\text{TraPPE}} = u_{\text{torsion}}(\phi_{ijkl}) + u_{\text{bend}}(\theta_{ijk}) + u_{\text{stretch}}(r_{ij}) + u_{\text{NB}}(r_{ij}) + u_{\text{inter}}(r_{ij}) \quad (31)$$

$$= c_0 + \sum_{i=1}^6 [c_i \cos(i\phi)] \quad (32)$$

$$+ \frac{k_\theta}{2} (\theta - \theta_{\text{eq}})^2$$

$$+ \frac{k_l}{2} (l - l_0)^2$$

$$+ u_{\text{NB}} + u_{\text{LJ}} + u_{\text{elec}} ,$$

where the last two terms u_{LJ} and u_{elec} indicate the intermolecular interactions $u_{\text{inter}}(r_{ij})$. The intramolecular interactions are given by the torsion potential, the bending potential, the stretching potential, and the non-bonding (NB) potential (cf. Fig. 11 b) - e)). The latter contains the information on the intramolecular interaction potentials between an interaction site and its n^{th} neighbor with $n > 4$. For modeling these intramolecular interactions, scaled intermolecular potentials (in most cases by a factor of 0.5) are used. In Eq. (32), ϕ indicates the torsion angle between four neighboring sites, θ the bending angle between three neighboring sites, and l the distance between two neighboring sites. The intramolecular potential parameters are indicated by c_0 , c_i , k_θ , and k_l .

The intermolecular interactions are described by the Lennard-Jones potential (modeling dispersive and repulsive interactions) and the *Coulomb* potential (modeling electrostatic interactions). The Lennard-Jones potential u_{LJ} can be written as

$$u_{\text{LJ}} = 4\varepsilon \left[\left(\frac{\sigma}{r} \right)^{12} - \left(\frac{\sigma}{r} \right)^6 \right], \quad (33)$$

where ε , σ , and r indicate the energy parameter, the size parameter, and the distance between two particles, respectively.

In most force fields, electrostatic interactions resulting from polarities of the charge

distribution of the (electronic) wave function are modeled by simple point charges, which interact via *Coulomb's* law

$$u_{\text{elec}} = \frac{q_i q_j}{4\pi\epsilon_0 r_{ij}} , \quad (34)$$

where q indicates the charge magnitude of two interaction sites i and j and ϵ_0 the electric constant.

For modeling interactions of different types of interaction sites (also within a pure component), e.g. between a methyl group and a methylene group, the TraPPE force field uses the *Lorentz-Berthelot* combination rules [34, 242] formulated as

$$\sigma_{ij} = \frac{1}{2}(\sigma_{ii} + \sigma_{jj}) \quad \& \quad \epsilon_{ij} = (\epsilon_{ii}\epsilon_{jj})^{1/2} , \quad (35)$$

where σ_{ij} and ϵ_{ij} indicate the Lennard-Jones cross-interaction parameters.

For modeling solid metals, simple interaction potentials such as the Lennard-Jones potential provide an only poor approximation. This is due to the fact that the delocalized electron cloud is not captured by simple models such as the Lennard-Jones potential and that directional bonds between atoms in lattice structures are not covered by spherically symmetric potentials. A more realistic potential for solid metals is the EAM potential. It can be written as

$$u_{\text{EAM}} = F\left(\sum_{j \neq i} \tilde{\rho}(r_{ij})\right) + \frac{1}{2} \sum_{j \neq i} \Psi(r_{ij}) , \quad (36)$$

where F indicates the embedding energy function modeling the effect of the electron cloud on the considered atom, $\tilde{\rho}$ indicates the locally uniform electron density, and Ψ indicates a pair-wise interaction function [88, 89, 182, 225]. The EAM potential is – opposite to most state of the art fluid models – a multi-body potential, since the electron cloud density $\tilde{\rho}(r_{ij})$ is a function of multiple atom positions. Hence, a pure component material is described within an EAM model by three functions and their parameters, i.e. the embedding energy function, the pair-wise interaction function, and the electron cloud contribution function.

Molecular force field models are based on point interaction sites with point masses, i.e. no spatial extension. The spatial extension is implicitly granted by the interaction potentials that exhibit a soft(!) repulsion, i.e. differentiable functions. However, in visualizations, interaction sites are (also in this work) represented by spheres, for example Fig. 11, resembling billiard balls. Hence, these visualizations provide a strongly simplified, may be even misleading, representation. The billiard ball-type visualization suggests hard sphere interactions at a given contact. This does not reflect the reality of the models, where interactions occur on a continuous (differentiable du/dr) basis. This should be kept in mind upon interpreting atomistic configuration visualizations presented in this work.

In this work, real substance systems were studied, where the fluid was modeled using united-atom force fields using either the TraPPE or the BZS framework. The metal solids were modeled using an EAM potential and the diamond indenter using a *Tersoff* potential. This modeling approach is overall computationally relatively expensive. Therefore, a simple model system – the Lennard-Jones model system – was used for systematic studies for elucidating the influence of different model parameters. The concept of the Lennard-Jones model system is introduced in the Appendix A.

2.2.5 Computational Tribology on the Atomistic Level

A large variety of scenarios has been considered for focusing on different aspects of tribology and lubrication [11, 112, 134, 251, 300, 301, 301, 356, 395]. From that, seven principal approaches used by the tribology community can be distilled. Fig. 12 a) - g) gives an overview of these principal MD scenarios.

In the simplest MD simulation scenario used in tribology, a homogeneous bulk phase is considered for determining the atomistic structure and macroscopic properties of bulk phases relevant for tribological applications (cf. Fig. 12 a)). In particular, MD simulations are frequently used for the prediction of thermophysical bulk properties of lubricants [115, 206, 240, 255, 322], but can also be used for homogeneous solid phases. Simulations of lubricants usually aim at predicting transport properties, in particular the viscosity, as well as the heat conductivity, the density, the heat capacity, and the compressibility at a given pressure and temperature. Hence, classical equilibrium molecular dynamics (EMD) are carried out. In such EMD simulations, the *Green-Kubo* formalism or the *Einstein* formalism [144, 148, 149, 180, 211, 287, 305, 307] can be used for determining transport coefficients. In these approaches, transport coefficients are obtained from response functions using fluctuation theory [107, 144, 211]. This very simple scenario has great practical importance in tribology as it enables the prediction of lubricant properties at extreme conditions (that are not accessible by laboratory experiments). Yet, this scenario does not capture the shear dependency of the viscosity, has limitations at extreme pressures and also for studying long chain molecules.

For modeling the shear dependency of fluid properties, the scenario b) is often used. It can be configured with a solid wall (as shown in Fig. 12 b)), but also without, i.e. solely studying a sheared fluid phase. If solid walls are used, also the influence of adsorbed layers on the shear flow and the slip length can be studied. The pressure in the fluid phase can be specified by prescribing a force on the upper solid wall, while the lower solid wall has a fixed position. The scenario b) is a classical non-equilibrium molecular dynamics (NEMD) setup. In particular, the scenario b) can be considered a simple, yet representative model for hydrodynamic lubrication. This MD scenario has been

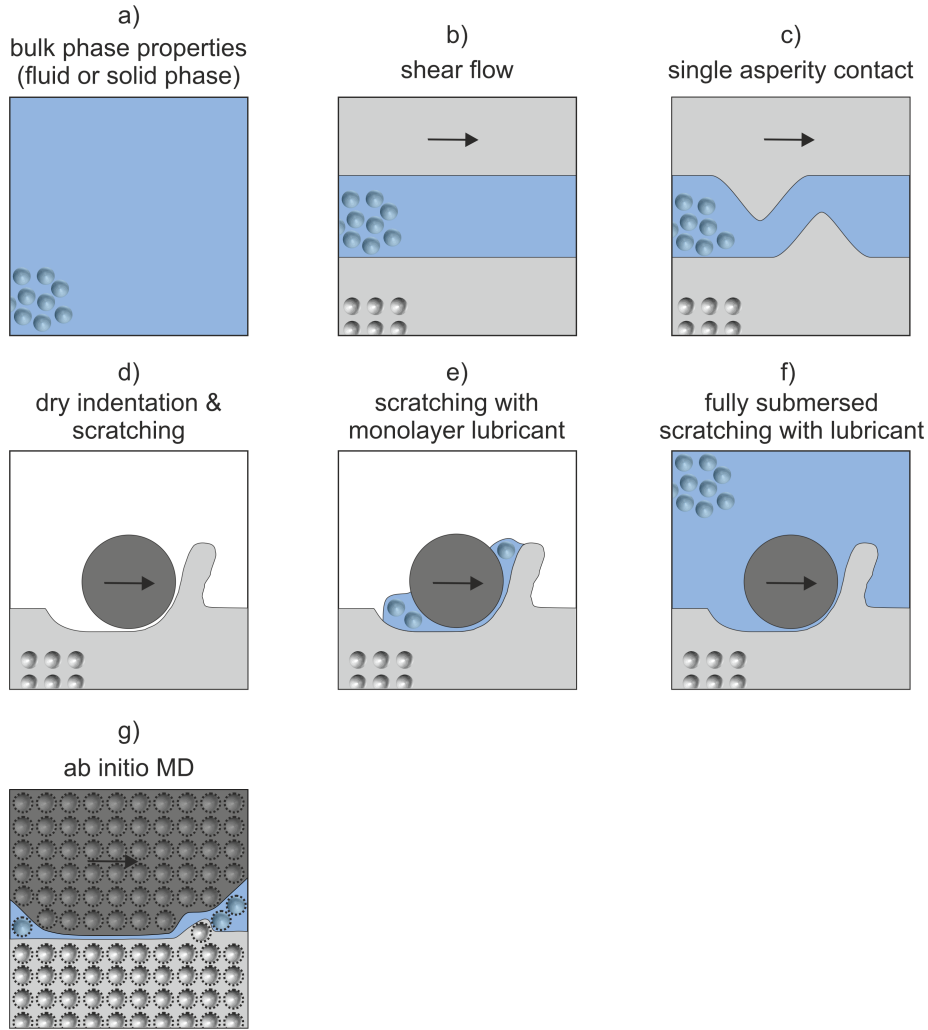


Figure 12: Scheme of different simulation scenarios used in molecular dynamics computational tribology. All matter in the simulation sketches consists of atoms – to avoid visual clutter only insinuated.

applied many times in the literature, e.g. Refs. [5, 31–33, 107, 109, 111, 113, 114, 121, 127, 130, 167, 207, 208, 218, 254, 314–316, 332, 333, 392] and Ref. [112] for a recent review. The scenario b) has also been used for studying viscous dissipation in fluid flows [33, 109]. The scenario enables a good sampling since a continuous stationary process is established. Yet, no actual contact process, i.e. boundary lubrication or mixed lubrication can be modeled based on the scenario b).

For establishing an actual contact process, the scenario b) can be modified in a way such that not two planar walls are used, but two solid bodies with a single asperity tip. This approach is shown in Fig. 12 c) and has been used at times in the literature for studying different types of lubricants [114, 129, 405, 421, 430]. This comes with the drawback that a single event process is studied, which brings difficulties for the sampling of statistically meaningful observables. Moreover, the asperity tip/ indenter is mostly relatively small compared to what is used in AFM experiments and expected for real

material asperities. Also, no significant elastic and plastic deformation of bulk material is captured in this modeling approach, which is required for studying the evolution of crystal defects and the formation of a tribofilm. The scenario c) has also been extended such as multiple asperities are positioned on the solid body surfaces [114, 431]. Yet, this does not change the basic features of the scenario.

For studying the time evolution of crystal defects in tribology, a different principal setup is usually used, cf. Fig. 12 d). Therein, an indenter (that is not attached to the boundaries of the simulation box) carries out a movement that brings it into contact with a substrate material. The latter has in two directions the same dimensions as the simulation box. Hence, the indenter is usually significantly smaller than the substrate. Yet, the indenter shape can be designed such that it provides a realistic picture of experimental setups [268, 374, 375]. The setup d) has been extensively used for studying dry contact processes [3, 204, 205, 246, 268, 278, 304, 340, 375, 397, 432], e.g. regarding the influence of the shape of the indenter [7, 132], substrate materials [8, 134, 416], indentation depth [134, 135], cutting direction in relation to the lattice orientation [131, 133], grain boundaries [136], surface roughness [420, 427], alloys [236], coatings [13], and temperature [131].

For studying lubricated contact processes, a natural choice is to extend the scenario d) such that a lubricant is present in the contact zone. The resulting scenario is depicted in Fig. 12 e), which has been frequently used in the literature. Mostly due to computational restraints, only a relatively small number of fluid particles was used – often a monolayer of adsorbed fluid molecules. This simulation approach has been for example used for studying the influence of the chain length of lubricant molecules [430, 431], the surface roughness [310, 335, 365], different adsorbates [11, 62, 68, 69, 183, 227, 299, 328, 377, 419], the squeeze-out of thin molecule layers [335, 378], and the surface chemistry [85, 366]. In most of these studies, lubrication was only considered by single adsorbed layers of fluid molecules on the substrate surface in the simulation. Hence, in the scenario d), the lubricant does not serve as a heat sink for cooling of the contact zone and also does not provide a realistic back pressure of a fluid bulk phase for the squeeze-out. Moreover, fundamental problems arise from a thermodynamic perspective by modeling the fluid without a bulk phase, but at the same time in contact with a vacuum. Thereby, no meaningful equilibrium state of the fluid is established, i.e. evaporation is prevented by the relatively strong adsorption interactions such that no vapor phase and vapor-liquid equilibrium is established.

Studies in which the contact is truly submersed in a fluid (cf. Fig. 12 f)) are still scarce, e.g. Refs. [220, 221, 300, 323, 324]. Hence, lubricated contact processes, where two solid bodies are in direct contact under the influence of a fluid have not been investigated as systematically. In the scenario f), a fluid bulk phase exists such that a cooling heat

flux from the contact zone into the fluid can be established and studied. Moreover, the behavior of the fluid particles in the gap can be modeled more realistically since the squeeze-out is limited by a fluid bulk phase pressure.

In the setup a) - f), usually systems with a particle number of the order $10^3 - 10^7$ are studied for capturing different properties and effects. In these simulations, usually classical force fields are used (cf. section 2.2.4). A different atomistic simulation approach that should be mentioned for completeness is the so-called ab initio MD approach [156, 189, 212, 213, 274]. Therein, the molecular interactions are – usually at certain time intervals – computed using first principle quantum mechanics. This provides in particular a more realistic description of the cross-interactions, i.e. the solid-fluid (between fluid-indenter and fluid-substrate) and the solid-solid (between indenter-substrate) interactions. This approach is, however, computationally significantly more expensive such that usually system sizes with only about $10^2 - 10^3$ particles can be considered.

MD simulation has been applied for various tasks and research questions in tribology. However, there are practically no studies on the interaction of the dissipation behavior, the thermal balance, and dislocations as well as their dependence on different process parameters in lubricated contact processes. Moreover, the behavior of the fluid in the contact zone in a scenario with a bulk fluid phase has been studied surprisingly little in the past.

2.2.6 Simulation Scenario Used in This Work

The focus of this work was on the influence of the fluid on the contact process and on elucidating the dominating nanoscopic effects caused by the presence of a lubricant fluid. Therefore, a fluid bulk phase was considered in the model that established interphases to the solid substrate and indenter. Therefore, the scenario f) (cf. Fig. 12) was used for the simulations carried out in this work.

Fig. 13 schematically shows the simulation setup used for all four studies carried out in this work (cf. chapters 3 - 6). The main features of the setup were the same in all four studies such as the boundary conditions and principal process kinematics. The indenter was fully submersed in the lubricant fluid and initially positioned above the substrate surface. After an equilibration of the system, the indenter carried out three sequential movements: (i) indentation, during which the indenter moves in $-z$ -direction normal to the surface and penetrates into the substrate; (ii) scratching, during which the indenter moves in $+x$ -direction forming a groove in the substrate; and (iii) retraction in $+z$ -direction, during which the indenter is moved out of the contact. The retraction was only considered in chapters 3 and 5.

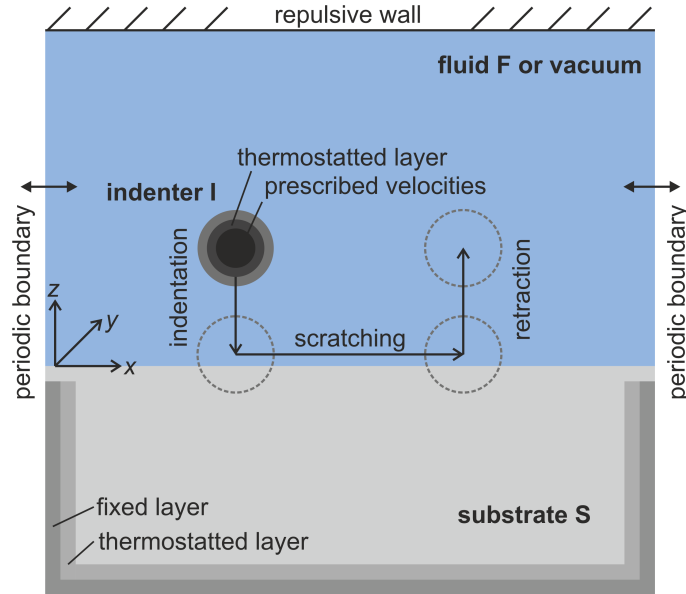


Figure 13: Scheme of simulation setup and boundary conditions used in this work. The simulation setup consists of a solid indenter I, a solid substrate S, and a fluid F lubricant (or dry reference cases a vacuum).

In all four studies, the substrate was a single crystal with an atomistically flat surface (using different material models). The indenter was in all cases significantly smaller than the substrate block and fully submersed in the fluid. The indenter had in all cases a contact surface with a spherical shape. In two studies, the indenter was a cylinder (chapters 3 and 4); in one study, the indenter was a sphere (chapter 5); and in one study, the indenter was a spherical cap (chapter 6). For the fluid, both simple spherically shaped molecules as well as elongated chains were considered. In all cases, the fluid was initially in a classical subcritical liquid state. In three studies (chapters 3 - 5), also a dry reference case was considered.

Also, the main features of the boundary conditions used in the four studies (cf. chapters 3 - 6) were the same. The substrate was fixed in the box by fixing some layers of substrate atoms at the bottom and next to the box margins in x - and y -direction (cf. Fig. 13). In x - and y -direction periodic boundary conditions were applied – essentially only relevant for the fluid phase. The simulation box was confined at the top by a soft repulsive wall. The position of this wall was, moreover, used for prescribing the fluid bulk pressure. For the indenter, the atom positions were prescribed as boundary conditions for defining the kinematics of the process. In some cases (cf. chapter 6), the indenter had additionally a layer of atoms that was temperature controlled and a layer of atoms that was subject to Newton’s equation of motion and classical force balances. In all cases, a layer of atoms in the substrate was also temperature controlled by a thermostat. The thermostats removed dissipated heat from the system. For the thermostating, the *Berendsen* algorithm was used [29] in this work. Thereby, the motion of

the particles in the thermostat region is coupled to an external heat bath. This is done by a simple velocity re-scaling in the *Berendsen* algorithm [29]. Hence, the equation of motion (19) are modified as

$$M_i \underline{a}_i = \underline{F}_i + M_i \gamma \left(\frac{T_0}{T} - 1 \right) \underline{v}_i, \quad (37)$$

where T_0 is the imposed temperature of the heat bath, T is the instantaneous temperature, and γ is a coupling coefficient. Thereby, the velocities of the particles are scaled at a given time step from \underline{v} to $\lambda \underline{v}$, where λ is given by [29]

$$\lambda = \left[1 + \frac{\Delta\tau}{\tau_T} \left(\frac{T_0}{T} - 1 \right) \right]^{1/2}, \quad (38)$$

where τ_T is a parameter of the algorithm that has to be chosen conveniently.

In the case of the Lennard-Jones model system simulations, the setup was furthermore simplified such that a quasi-two-dimensional system was considered. Therefore, the indenter was a cylinder. This provided a significantly simpler fluid flow field and better sampling of the fluid properties in the adsorption layers as well as better statistics for determining the squeeze-out characteristics. The simulation box had a significant elongation in the direction of the cylinder axis to further improve the statistics of the sampling.

In this work, molecular dynamics simulations were used to address the following research questions: How do the cooling capabilities of a lubricant manifest on the atomistic level? How does the presence of a lubricant reduce the friction on the atomistic scale? How does the contact zone on the atomistic level look like, i.e. how does a fluid behave in the contact zone? How are the physical elementary processes on the atomistic level interrelated? Which of the atomistic physical effects are the dominating ones for lubrication? This is not a priori known. Hence, the question, where to put the emphasis in the model design is not easy to address. The system size of the simulations are required to be relatively large anyway (in comparison to simulations used for predicting thermophysical properties of simple bulk phases). Hence, this work also contributes to the question, how to choose the ratio of the number of particles used for the modeling of the indenter, the substrate, and the fluid (and the particles constituting the interfaces) at a given total number of interaction sites used in the simulation. And, this work contributes to the understanding, which material property and therefore material (force field) model is dominating the accuracy of the results.

3 Influence of Lubrication and the Solid-Fluid Interaction on Thermodynamic Properties in a Nanoscopic Scratching Process

3.1 Introduction

Tribological processes are of fundamental importance in many technical applications, but also in nature. It is well-known that using liquid lubricants entails two main advantages: The reduction of friction and the cooling of the contact zone. However, the origin of these phenomena is yet not fully understood on an atomistic level [95, 283, 304, 375]. The region in which two solid bodies interact directly under the influence of a lubricant is extremely small and practically inaccessible for experimental studies, so that only little is known on the phenomena in that zone. Molecular simulation provides an attractive tool to elucidate such processes [11, 112, 134, 300, 301, 356, 395]. The results from molecular simulations of a given scenario are obtained by solving Newton's equation of motion and depend solely on the force field that describes the molecular interactions. If these interactions are reasonably described, the method has strong predictive capabilities [9, 125].

There are many studies on dry nanoindentation and scratching processes, e.g. Refs. [205, 246, 278, 375, 397]. For example, the influence of the shape of the indenter [7, 132], substrate materials [8, 134, 416], indentation depth [135], cutting direction in relation to the lattice orientation [133], grain boundaries [136], surface roughness [427], alloys [236], coatings [13], and temperature [131] were investigated. Also, shear flow friction simulations, where two solid bodies are separated by a fluid, have been extensively investigated in the literature, e.g. Refs. [5, 31–33, 109, 111, 113, 114, 121, 167, 207, 207, 208, 254, 314–316, 392].

Lubricated scratching processes, where two solid bodies are in direct contact under

the influence of a fluid, on the other hand, have not been investigated as systematically. Results on the influence of the chain length of the lubricant molecules [430, 431], the surface roughness [335, 365], adsorbates [11, 62, 68, 69, 183, 227, 299, 328, 377, 419], the squeeze-out of lubricant molecules [335, 356, 378], and the surface chemistry [85, 366] have been reported in the literature. In most of these studies, lubrication was only considered by single adsorbed layers of fluid molecules on the substrate surface in the simulation, while studies in which the contact is truly immersed in a liquid are still rare [220, 221, 300, 356]. Also, small systems with state of the art ab initio MD [156, 212, 213, 274] have been reported recently. None of these studies systematically addresses the question of the influence of the lubricant on the thermal balance of the system, i.e. its cooling capability or the behavior of the fluid due to the dissipation in the vicinity of the contact zone.

Also, to the best of our knowledge, no systematic study has been performed yet that addresses the influence of the solid-fluid interaction energy on nanoscopic scratching processes, where two solid bodies are in direct plastically deforming contact and are fully immersed in a liquid. The solid-fluid interaction energy determines the adsorption and the wetting behavior of the lubricant on the solid surfaces [26, 30, 173]. *Becker et al.* [26] have investigated liquid droplets on solid surfaces in Lennard-Jones systems and determined the influence of the solid-fluid interaction energy on the contact angle.

In this chapter, results of molecular dynamics simulations of a three-stage nanoscopic contact process consisting of indentation, scratching, and retraction of a cylindrical indenter on an initially atomistically flat single crystal substrate are reported. All three components (substrate, indenter, and fluid) are described by the Lennard-Jones potential, which puts the present study in line with that from *Becker et al.* [26]. The Lennard-Jones potential is often used in molecular physics as it is known to describe the thermodynamic properties of simple fluids very well [9, 26, 172, 306, 353, 357, 361, 402] and still gives a reasonable model for some solid crystals [153, 381, 429]. The Lennard-Jones potential is computationally cheaper than more realistic EAM potentials [258], and facilitates a systematic investigation of the influence of the solid-fluid interaction energy on the scratching process. The Lennard-Jones potential has been widely used for studying fundamentals in nanotribology, e.g. for the modeling of dispersive and repulsive interactions of simple spherically shaped fluid molecules [166, 167, 254, 300, 314, 356] as well as such interactions between chain molecules [62, 314–316, 430, 431], the modeling of the solid-fluid interactions [11, 69, 114, 299, 300, 314–316, 328, 356, 377, 392, 430, 431], and also the modeling of solid-solid interactions [220, 221, 356].

Nevertheless, the simplicity of the chosen model limits the applicability and transferability to real systems. Evidently, a Lennard-Jones sphere is not a good representative for oils and fats often used in cutting processes to reduce friction. Also, it is well-

accepted that the Lennard-Jones potential does not capture the plasticity and elasticity of real solid materials accurately. A further crude simplification compared to a real system is that the substrate surface is atomistically flat and the substrate block is a single crystal without grain boundaries that are known to influence contact processes [28, 136]. Also, the negligence of surface chemistry effects is a strong simplification. Hence, the present work does not aim at modeling the cutting process of a certain real system, but instead at describing a simplified yet representative system in a generalized approach. This concept study of an idealized model provides insight into the mechanisms of a fully immersed cutting process on the nanoscale.

The focus of this work lies on the investigation of thermal effects in scratching processes, like grinding and polishing of microstructures [205, 246, 326, 330]. The cooling of both the workpiece and the tool, the overall energy balance as well as the local temperature are crucial process parameters in such machining processes [70, 80, 147, 200, 222, 269, 294], but often not accessible by experiments – especially the local temperature field. Models used to estimate and predict these process parameters in engineering applications, i.e. estimating the dissipation and the distribution of the heat in a machining process are mostly empirically motivated, cf. Refs. [61, 70, 80, 298] and little is known regarding the underlying molecular processes. This work investigates the thermal and mechanical behavior of a simplified machining process and thereby contributes to a better understanding of high precision machining processes [81, 326] on the nanoscale.

Despite the simplicity of the model system, the results are also applicable to technical applications such as liquid methane in cryogenic pumps for LNG (liquid natural gas) processes [15, 38, 174, 413] and for the next generation of rocket engines [77, 191] or liquid nitrogen (N_2) [55] as metal working fluid in cryogenic machining processes [50, 181, 422], as well as in pumps in air separation units [60, 337] for the production and purification of argon and nitrogen.

The work is organized in two parts: In the first part, the simulation method and scenario are introduced and the observed properties are defined. In the second part, the results are presented and discussed.

3.2 Methods

3.2.1 Molecular Model

Fig. 14 shows the simulation setup, which consists of a cylindrical indenter (I), a substrate (S), and eventually in the lubricated cases, a fluid (F). All three components are

modeled with the Lennard-Jones potential, which is truncated and shifted at $r_c = 2.5\sigma$:

$$u_{\text{LJ}}(r) = 4\varepsilon \left[\left(\frac{\sigma}{r} \right)^{12} - \left(\frac{\sigma}{r} \right)^6 \right] \quad \text{and} \quad (39)$$

$$u_{\text{LJTS}}(r) = \begin{cases} u_{\text{LJ}}(r) - u_{\text{LJ}}(r_c) & r \leq r_c \\ 0 & r > r_c, \end{cases} \quad (40)$$

with u_{LJ} being the full Lennard-Jones potential and u_{LJTS} the truncated and shifted potential. The parameters ε and σ are the potential energy and size parameter, respectively. The distance between two particles is r . The cut-off radius is $r_c = 2.5\sigma$ throughout this work, except for the indenter-substrate (IS), which is kept purely repulsive by setting $r_c = 2^{1/6}\sigma$. This setting was also used in a case study in which the adsorption of the fluid on the indenter and the substrate was suppressed.

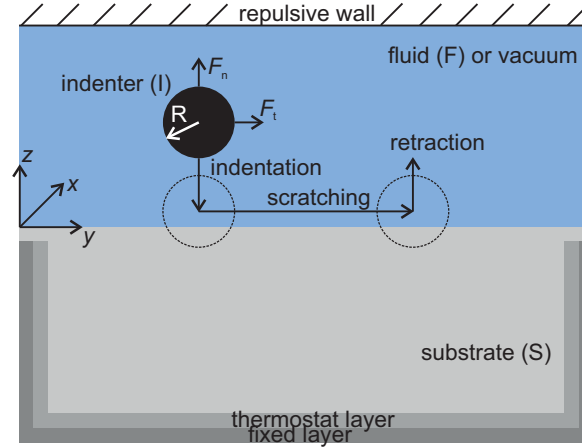


Figure 14: Setup of the simulation box for the indentation, scratching, and retraction of the indenter – not true-to-scale. The indenter is either in a vacuum environment (dry case) or fully immersed in fluid (18 different lubricated cases differing in the energy of the interaction between the fluid and the solids (substrate and indenter) $\tilde{\varepsilon}^*$).

Throughout the present work, all physical properties are reduced [9] using the Lennard-Jones potential parameters of the fluid $\varepsilon = \varepsilon_{\text{F}}$, $\sigma = \sigma_{\text{F}}$, and the molecular mass M , as well as the Boltzmann constant k_{B} . The reduced properties are labeled with an asterisk, e.g. the temperature $T^* = T/(\varepsilon/k_{\text{B}})$, the density $\rho^* = \rho/(1/\sigma^3)$, the pressure $p^* = p/(\varepsilon/\sigma^3)$, the internal energy $U^* = U/\varepsilon$, the work $W^* = W/\varepsilon$, the heat $Q^* = Q/\varepsilon$, the force $F^* = F/(\varepsilon/\sigma)$, the time $\tau^* = \tau/(\sigma\sqrt{M/\varepsilon})$, lengths and distances $l^* = l/\sigma$ (where l can be the radius R , the depth d , or dimensions x, y and z), the volume $V^* = V/\sigma^3$, and the velocity $v^* = v/\sqrt{\varepsilon/M}$. The simulations were performed with the open-source code LAMMPS [288].

For convenience, the size parameter σ of the Lennard-Jones sites of the indenter, the substrate, and the fluid are identical. The same holds for the masses M . The dispersion

energies ε are chosen so that the three components represent realistic materials. The dispersion energy of the fluid ε_{F} is chosen such that it describes methane employing the parameters proposed by *Vrabec et al.* [402]. The dispersion energy of the substrate is adopted from *Halicioglu et al.* [153] such that it models iron energetically. The indenter is a rigid body, with its particles placed on a diamond lattice. The diamond lattice constant of the indenter is 1.55σ .

In the present study, one dry simulation (no fluid present) is compared to 18 different lubricated cases. The latter ones differ only in the energy of the solid-fluid interaction. The solid-fluid interaction energy in each of the lubricated simulations is the same for the indenter-fluid (IF) and the substrate-fluid (SF) interaction and is denoted by a tilde $\tilde{\varepsilon}^*$ throughout this work, i.e. $\tilde{\varepsilon}^* = \varepsilon_{\text{IF}}^* = \varepsilon_{\text{SF}}^*$. The parameter of the solid-fluid interaction energy $\tilde{\varepsilon}^*$ was varied between 0 and 1.7 with an increment of 0.1. For the simulation with $\tilde{\varepsilon}^* = 0$, the fluid only exhibits repulsive interactions with the indenter and the substrate (employing the WCA potential [408], which has $r_c = 2^{1/6} \sigma$). The 18 lubricated simulations cover the entire range of total wetting to dewetting [26]. *Becker et al.* [26] reported that total wetting in Lennard-Jones systems, i.e. a contact angle of 0° , is found for approximately $\tilde{\varepsilon}^* \geq 0.75$ at approximately $T^* = 0.8$. The solid-fluid interaction energy $\tilde{\varepsilon}^*$ is also directly related to the so called *slip length* at solid-fluid interfaces, as reported from shear flow friction simulations for a large number of real substances [32, 40, 167, 209, 314, 316, 363, 386] and Lennard-Jones systems [113, 254].

Table 1 summarizes choices that were made for the interactions in the form of a matrix of all three components (S, I, F) and their cross-interactions with respect to the dispersion energy of the fluid. The self interactions are denoted as the diagonal components, the cross-interactions as the off-diagonal components in Table 1.

Table 1: Pairwise interaction energies employed in the present study; all interaction energies are reduced by the interaction energy of the fluid $\varepsilon^* = \varepsilon/\varepsilon_{\text{F}}$.

	substrate (S)	indenter (I)	fluid (F)
substrate (S)	^(a) $\varepsilon_{\text{S}}^* = 34$	^(b) WCA	^(c) $\tilde{\varepsilon}^* = 0, 0.1 \dots 1.6, 1.7$
indenter (I)	-	rigid body	^(c) $\tilde{\varepsilon}^* = 0, 0.1 \dots 1.6, 1.7$
fluid (F)	-	-	^(d) $\varepsilon_{\text{F}}/k_{\text{B}} = 175.1 \text{ K}$

^(a)Lennard-Jones solid – iron [153];

^(b)*Weeks-Chandler-Andersen* potential [408];

^(c)18 cases differing in the solid-fluid interaction energy;

^(d)Lennard-Jones fluid – methane [402].

3.2.2 Simulation Setup

The indenter carries out three sequential movements during the simulation, cf. Fig. 14: (i) indentation, during which the indenter penetrates into the substrate in $-z$ -direction normal to the unpenetrated substrate surface; (ii) scratching, during which the indenter moves laterally through the surface in $+y$ -direction, forming a groove; and (iii) retraction in $+z$ -direction, which brings the indenter out of the contact. The indentation is carried out between $0 < \tau^* < 142$, the scratching between $142 < \tau^* < 625$, and the retraction between $625 < \tau^* < 809$.

The movement of the rigid indenter is fully prescribed. Its velocity is constant at $v^* = 0.066$ in all three sequential movements. The depth of the indentation is set to $d^* = 4$ and kept constant during the scratching phase. The surface of the substrate lies in the xy -plane. The origin of the Cartesian coordinate system is defined as follows: $z^* = 0$ for the initial unpenetrated surface of the substrate and $x^* = 0$ and $y^* = 0$ in the corner of the simulation domain, cf. Fig. 14. The size of the substrate block is $\Delta x^* = 37.3$, $\Delta y^* = 274.2$, $\Delta z^* = 139.6$. It consists of 1.5×10^6 atoms.

The rigid cylindrical indenter has a radius of $R_1^* = 8.1$ and consists of 8.2×10^3 atoms. The length of the cylinder corresponds to the width of the substrate and the width of the simulation domain in x -direction. The substrate block is fixed in the simulation domain by constraining the positions of three atom layers next to the box margins at the bottom and in both positive and negative y -direction. The substrate is initialized as an fcc single crystal, which is the equilibrium lattice for the Lennard-Jones potential at the chosen state point [389]. The substrate has an initial density of $\rho_s^* = 1.07$. The substrate surface has a (100) orientation. The scratching direction is in $[0 \bar{1} 1]$. The indenter is fully submersed in the fluid in all lubricated cases. The fluid consists of 9.0×10^5 molecules, with an initial temperature of $T^* = 0.8$ and an initial pressure after the equilibration (see below) of about $p^* = 0.014$. Also, the substrate has an initial temperature of $T^* = 0.8$. Periodic boundary conditions are applied in both x - and y -direction, whereas a soft repulsive wall confines the simulation box at $z^* = 251.3$ at the top. The soft repulsive wall was implemented by a harmonic potential membrane. The time step was $\Delta\tau^* = 0.0008$.

All atoms in the simulation domain were equilibrated for 1×10^6 time steps before the three sequential movements of the indenter are carried out. The initial temperature was imposed to the entire system – except the indenter – during the equilibration. This temperature was also imposed to four atom layers between the substrate and the fixed layer (cf. Fig. 14) during the indentation, the scratching, and the retraction via velocity scaling. This was done to extract dissipated heat from the system, which models the heat flux into the bulk body of the substrate.

3.2.3 Definition of Observables

Different observables were computed from the simulation data and used for comparison of the studied dry and lubricated cases. Their definitions are given in the following.

The total tangential force F_t^* and normal force F_n^* on the indenter are evaluated as the sum of all interactions acting on the indenter in y - and z -direction, respectively. The total forces, therefore, stem from the indenter-substrate (IS) and the indenter-fluid (IF) interactions:

$$F_t^* = \sum_{i=1}^m \left(F_{y,i}^{\text{IS}^*} + F_{y,i}^{\text{IF}^*} \right), \quad (41)$$

$$F_n^* = \sum_{i=1}^m \left(F_{z,i}^{\text{IS}^*} + F_{z,i}^{\text{IF}^*} \right), \quad (42)$$

where m is the total number of atoms of the indenter. Also, the indenter-fluid (IF) forces, i.e. only the first terms in Eq. (41) and (42), are computed and compared to investigate the influence of the lubricant. The COF is calculated as

$$\mu = F_t^*/F_n^*, \quad (43)$$

during the scratching.

The energy balance of the system is

$$\Delta U_S^* + \Delta U_F^* = Q_{\text{Th}}^* + W_I^* + \delta E_{\text{err}}^*, \quad (44)$$

where ΔU_S^* and ΔU_F^* are the changes of the total energy (kinetic energy + potential energy) of the substrate and the fluid, respectively. They are averaged in a time interval $\Delta\tau^*$. Q_{Th}^* is the total heat removed from the system by the thermostat. W_I^* is the work done by the indenter on the system. ΔU_S^* , ΔU_F^* , and Q_{Th}^* are simulation results. δE_{err}^* is a remaining numerical error. W_I^* is computed by numerical integration of the respective total force on the indenter

$$W_I^*(\tau^*) = \int_{\text{indentation}} F_n^*(\tau^*) dz + \int_{\text{scratching}} F_t^*(\tau^*) dy + \int_{\text{retraction}} F_n^*(\tau^*) dz, \quad (45)$$

where the forces F_n^* and F_t^* are defined according to Eq. (41) and (42). All energies and forces were computed every 1,000 time steps. The main cause for the remaining numerical error δE_{err}^* in the global energy balance in Eq. (44) is the numerical integration in Eq. (45).

The temperature, the density, and the pressure of the fluid were computed locally

during the three-stage scratching process. All three properties were computed as per-atom values by averaging the respective property over the atoms within the cut-off radius of each atom. The average aligned velocity from each per-atom collective was subtracted from the total average kinetic energy for the computation of the local temperature by the thermal motion. The fluid region was divided into bins with the size $\Delta y^* = \Delta z^* = 1.34$ and reaching over the entire box width in x -direction, cf. Fig. 15. The fluid properties were computed bin wise, i.e. averaged over all molecules in a bin over 5,000 time steps. The resulting temperature, density, and pressure profiles were computed every 5,000 time steps.

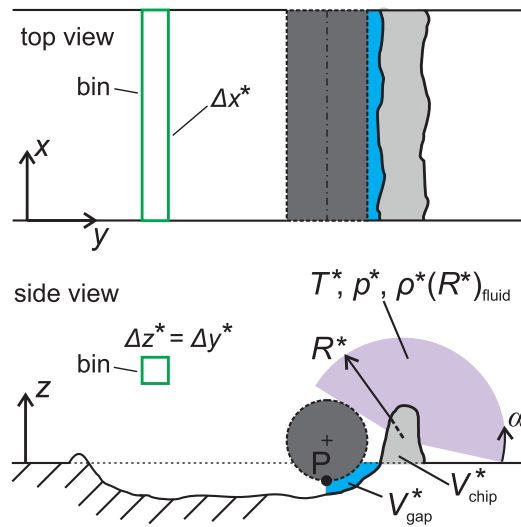


Figure 15: Schematic (not true-to-scale) for the definition of observables used for the investigation of the nanoscopic contact process. The chip is defined as the substrate material above the unpenetrated substrate surface and ahead of the indenter in scratching direction. The thermodynamic state of the fluid is calculated as a function of the distance from the chip surface and averaged over the angle α (purple shaded area). The radial averaging is carried out with respect to the center of mass of the chip. The blue shaded area indicates the lubrication gap presumed for the calculation of the fluid molecules trapped in it. The green rectangle indicates the shape of one of the averaging bins for the computation of the temperature, pressure, and density fields in the simulation box.

The thermodynamic state point (temperature, density, and pressure) of the fluid is furthermore evaluated around the chip that is formed by the substrate. As the scratching quickly becomes a quasi-stationary process, the computation of the state point was only carried out in that stationary phase of the scratching $335 < \tau^* < 625$ (see results). The thermodynamic state point was computed instantaneously every 10,000 time steps. The temperature, density, and pressure of the fluid were computed as a function of the distance R^* from the chip surface as indicated in Fig. 15. The fluid properties were averaged radially around the chip. The instantaneous chip surface was computed using

an alpha shape algorithm [98]. In this way, profiles showing the decay of the fluid temperature, density, and pressure in the vicinity of the chip surface into the fluid bulk are obtained, i.e. $T^*(R^*)$, $\rho^*(R^*)$, $p^*(R^*)$, where R^* is the distance to the chip surface. Details of the computation of the functions $T^*(R^*)$, $\rho^*(R^*)$, $p^*(R^*)$ are given in the Appendix B.

The decay of the temperature, the density, and the pressure of the fluid from the chip surface into the bulk fluid is modeled here by an exponential function:

$$T_i^* = T_i^{*\text{bulk}} + (T_i^{*\text{wall}} - T_i^{*\text{bulk}}) \cdot \exp(-R^*/\beta^T), \quad (46)$$

$$\rho_i^* = \rho_i^{*\text{bulk}} + (\rho_i^{*\text{wall}} - \rho_i^{*\text{bulk}}) \cdot \exp(-R^*/\beta^\rho), \quad (47)$$

$$p_i^* = p_i^{*\text{bulk}} + (p_i^{*\text{wall}} - p_i^{*\text{bulk}}) \cdot \exp(-R^*/\beta^p). \quad (48)$$

The three parameters β^k , with $k = T^*$, ρ^* , p^* , were fitted to all lubricated simulation results simultaneously. Hence, the decay term $\exp(-R^*/\beta^k)$ is assumed to be independent of the solid-fluid interaction energy. The temperature, density, and pressure in the *bulk* fluid and at the *wall* are adopted from each simulation individually. The normalized decay functions ΔT^* , $\Delta \rho^*$, and Δp^* are defined as

$$\Delta T^* = (T_i^* - T_i^{*\text{bulk}})/(T_i^{*\text{wall}} - T_i^{*\text{bulk}}), \quad (49)$$

$$\Delta \rho^* = (\rho_i^* - \rho_i^{*\text{bulk}})/(\rho_i^{*\text{wall}} - \rho_i^{*\text{bulk}}), \quad (50)$$

$$\Delta p^* = (p_i^* - p_i^{*\text{bulk}})/(p_i^{*\text{wall}} - p_i^{*\text{bulk}}), \quad (51)$$

where $i = 1 \dots 18$ stands for the 18 lubricated cases and $T^{*\text{bulk}}$, $\rho^{*\text{bulk}}$, $p^{*\text{bulk}}$, $T^{*\text{wall}}$, $\rho^{*\text{wall}}$, $p^{*\text{wall}}$ for the temperature, density, and pressure in the bulk fluid and directly at the solid-fluid interface, respectively.

The *gap* between the indenter and the substrate is defined as indicated by the dark blue shaded area in Fig. 15 as the volume between the indenter and the substrate at $z^* < 0$ and $y^* > y_{\text{p}}^*$ (cf. Fig. 15), i.e. ahead of the indenter in the scratching direction. The number of trapped fluid molecules N_{gap} in this gap is computed from this definition. The contact between the indenter and the substrate can either be dry (no fluid molecules in the gap) or lubricated (fluid molecules in the gap). The substrate and the indenter surface is analyzed with an alpha shape algorithm [98] from the simulation trajectories and a surface profile line is calculated parallel to the yz -plane.

The chip temperature T_{chip}^* is simply defined as the mean temperature of the chip, where the chip constitutes by all substrate atoms whose positions satisfy the conditions $z^* > 0$ and $y^* > y_{\text{p}}^*$ (cf. Fig. 15). The number of fluid molecules in the gap N_{gap} , the chip temperature T_{chip}^* , and the surface profile line were computed every 10,000 time steps.

3.3 Results and Discussion

3.3.1 Mechanical Properties

Fig. 16 shows the total forces on the indenter in normal (a) and tangential direction (b) for the dry and all lubricated cases during the entire contact process as well as the resulting coefficient of friction (c) during the scratching. The color scale is related to the energy of the solid-fluid interaction $\tilde{\epsilon}^*$, i.e. the wetting behavior of the fluid.

In the dry case, the total normal and tangential force F_n^* and F_t^* are zero in the first part of the indentation and in the last part of the retraction in which the indenter is not in contact with the substrate. F_n^* and F_t^* fluctuate around zero in these phases in the lubricated cases, which is due to viscous friction of the fluid. It is shown in chapter 5 that the amplitude of these fluctuations is related to the energy of the solid-fluid interaction, which is due to the lateral mobility of the fluid molecules on the indenter surface during the movement through the bulk fluid. This lateral mobility of fluid molecules decreases with increasing energy of the solid-fluid interaction, which can also be expressed by the *slip length* [386], as shown in shear flow simulations studies [167, 363, 385, 404].

The total normal force on the indenter F_n^* (cf. Fig. 16 a)) increases during the indentation, which is due to elastic and plastic deformation of the substrate when the indenter penetrates into the substrate. The normal force on the indenter reaches a maximum at the end of the indentation and then decreases at the beginning of the scratching as the contact area between the indenter and the substrate decreases. F_n^* then reaches a steady state until the end of the scratching process. The total normal force F_n^* on the indenter quickly decreases to zero during the retraction when the indenter moves out of the contact with the substrate. The most evident influence of the fluid and the energy of the solid-fluid interaction is observed at the beginning of the indentation. The fluid acts as a precursor between the indenter and the substrate during the so-called *squeeze-out* of fluid particles between the approaching solid bodies [142, 335, 378]. Hence, the total normal force starts increasing in the lubricated cases before both solids actually get into direct contact. This ability of the fluid clearly increases with increasing energy of the solid-fluid interaction. The bump in the normal force at approximately $\tau^* = 50$ in lubricated cases with particularly high energies of the solid-fluid interaction is due to the squeeze-out of a second layer of adsorption molecules on the indenter and the substrate surface. The bump in the normal force occurs when this second adsorption layer is squeezed out of the contact zone (see inset of Fig. 16).

The presence of a lubricant decreases spikes in the normal force during the indentation that are due to the formation of dislocations in the substrate. This dampening

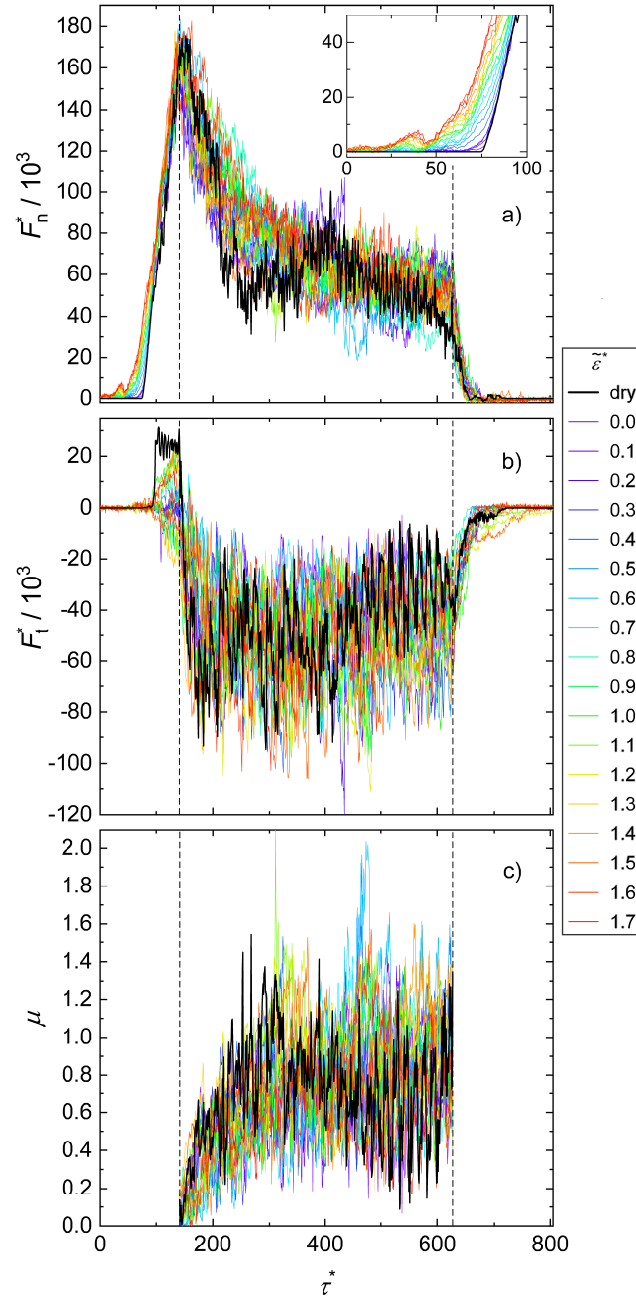


Figure 16: Total normal (a) and tangential (b) forces on the indenter during the entire contact process and coefficient of friction (c) during the scratching. The black line indicates the dry reference case. The colors of the other lines are coded by the energy of the solid-fluid interaction $\tilde{\varepsilon}^*$. The dashed lines indicate the beginning and the end of the scratching phase. The inset in (a) highlights the starting phase of the indentation.

phenomenon is discussed in more detail in chapter 5.

The tangential force F_t^* (cf. Fig. 16 b)) in the dry case makes a jump when the indenter comes into contact with the substrate, which is due to the atomistic nature of the contact [74] between the indenter and the substrate atoms in y -direction. The fact that the jump in the tangential force in the dry case is in positive y -direction is

therefore random and due to the stochastic thermal motion of the particles, which also holds for the lubricated cases. However, the corresponding jump in the lubricated cases is significantly damped due to the presence of fluid atoms acting as springs between the indenter and the substrate. The tangential force F_t^* increases rapidly as the chip starts forming at the beginning of the lateral movement. As for the normal force on the indenter, the tangential force reaches a steady state during which it strongly fluctuates around a mean value of approximately $F_t^* = -47,000$.

At the beginning of the scratching, the coefficient of friction (cf. Fig. 16 c)) increases quickly as the lateral movement starts until it reaches approximately a steady state. The steady state is reached at about $\tau^* = 300$. This holds for the dry case as well as the lubricated cases. Evidently, the coefficient of friction in the lubricated cases is lower than in the dry case at the beginning of the scratching. Vice versa, the coefficient of friction shows a tendency to be lower in the dry case than in the lubricated cases in the steady state phase. The reduction of the coefficient of friction in the lubricated cases in the starting phase is a result of an alteration of the normal and the tangential forces likewise, i.e. the normal force is increased and the tangential force decreased by the presence of a fluid. The increase of the coefficient of friction in the lubricated cases during the steady state phase, on the other hand, is mainly a result of an increased tangential force. This is due to additional viscous friction in the lubricated cases and individually stamped fluid molecules into the substrate surface [37, 356].

The average forces and coefficient of friction during the two characteristic phases are summarized in Fig. 17 a), b), and c), respectively, as a function of the energy of the solid-fluid interaction with respect to the dry case. Two regimes are distinguished: The lubricated phase ($142 < \tau^* < 335$), during which fluid molecules are present in the gap and the steady state phase ($335 < \tau^* < 625$), during which the contact zone is essentially dry.

The presence of a lubricant significantly decreases the coefficient of friction (27%) during the starting phase of the scratching. Vice versa, the presence of a lubricant increases the coefficient of friction once the contact zone is essentially dry (15%). The decreased coefficient of friction in the starting phase ($142 < \tau^* < 335$) is a consequence of a combination of an increased normal force and a decreased tangential force compared to the dry case. The increased coefficient of friction in the lubricated cases compared to the dry case during the steady state phase ($335 < \tau^* < 625$) on the other hand is mainly a result of an increased tangential force. The energy of the solid-fluid interaction does interestingly not significantly influence the average forces and coefficient of friction. This is in contrast to the well-established strong influence of the solid-fluid interaction on the friction behavior in Couette shear flow systems, cf. Refs. [113, 167, 254, 363, 386, 404].

Fig. 18 a) and b) show the resulting normal and tangential forces between the indenter

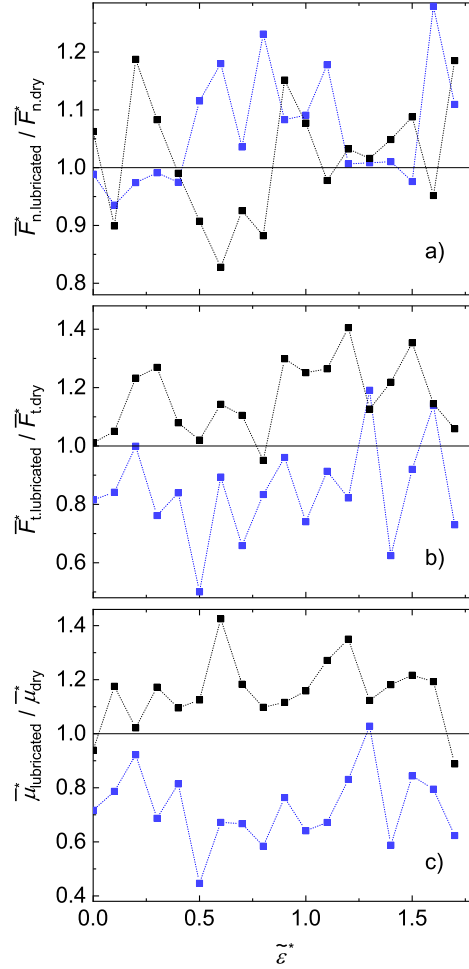


Figure 17: Average forces and coefficient of friction: a) average normal forces, b) average tangential forces, and c) average coefficient of friction as a function of the energy of the solid-fluid interaction $\tilde{\varepsilon}^*$. The average mechanical properties were computed as time averages during the starting phase of the scratching ($142 < \tau^* < 335$) and the steady state of the scratching ($335 < \tau^* < 625$). The results from the dry simulation are taken as reference. The starting phase is indicated by blue symbols, the steady state phase by black symbols. Lines are a guide for the eye.

and the fluid. The normal force is highly correlated with the energy of the solid-fluid

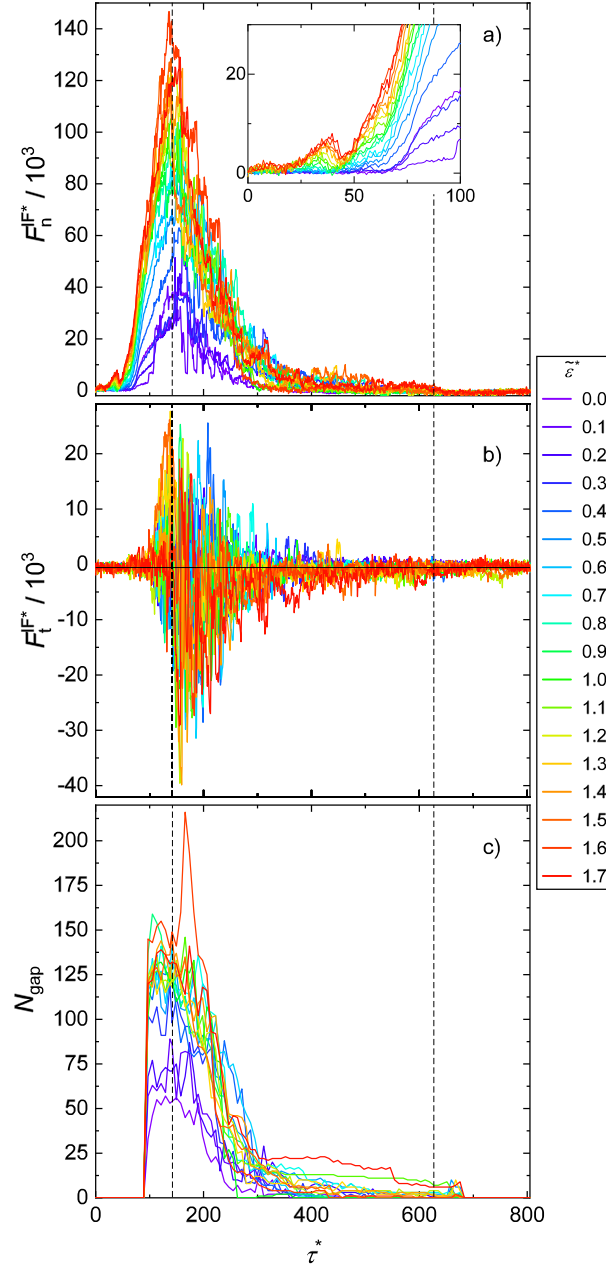


Figure 18: Normal (a) and tangential (b) forces between the indenter and the fluid during the entire contact process. (c) shows the amount of trapped fluid molecules in the gap (as defined in Fig. 15). The color of the lines is coded by the energy of the solid-fluid interaction $\tilde{\varepsilon}^*$. The dashed lines indicate the beginning and the end of the scratching phase from left to right. The inset in (a) highlights the starting phase of the indentation.

interaction $\tilde{\varepsilon}^*$, while the tangential force shows no systematic dependency on the energy of the solid-fluid interaction. This can be attributed to lubricant molecules that are trapped in the gap between the indenter and the substrate during the indentation phase, before they get squeezed out during the steady state phase of the scratching. The amount of trapped fluid molecules remaining in the gap between both solids increases

with increasing energy of the solid-fluid interaction (cf. Fig. 18 c)), which leads to the increasing contribution of the indenter-fluid force to the total force on the indenter in normal direction.

The increase of the normal indenter-fluid force during the indentation is fairly smooth, which is due to a pressure build-up in the lubrication gap. On the contrary, the decay of the normal indenter-fluid force at the beginning of the scratching ($142 < \tau^* < 300$) shows strong fluctuations. Each spike is due to lubricant molecules being abruptly pushed out of the lubrication gap, which is analog to the classical stick-slip behavior [72, 384]. After the squeeze-out of the fluid out of the contact zone, both the normal and the tangential indenter-fluid force exhibit only small fluctuations. The tangential force fluctuates around approximately $F_t^{*IF} = -100$, the normal force around approximately $F_n^{*IF} = 400$. This is in both cases less than 1% of the corresponding total force (cf. Fig. 16). The increase in the total normal force in the lubricated cases compared to the dry case is attributed to the fluid molecules constantly filling the rear edge behind the indenter in moving direction and pushing the indenter upwards. The contribution of the fluid viscous friction can be estimated from the end of the retraction phase, where the indenter only interacts with the fluid. The average normal force due to the viscous friction is therefore approximately $F_n^{*IF} = 200$.

The tangential fluid-indenter forces F_t^{*IF} show very large fluctuations in the starting phase of the scratching ($142 < \tau^* < 300$). Nevertheless, a clear tendency of these fluctuations to negative tangential forces can be observed, cf. Fig. 18 b). This trend is a result of the squeeze-out of fluid molecules out of the lubrication gap, while the large fluctuations stem from lubricant molecules being jammed between the indenter and the substrate. Also from Fig. 18 c), it becomes clear that the squeeze-out time is independent of the energy of the solid-fluid interaction $\tilde{\varepsilon}^*$.

The reduction of the coefficient of friction in the lubricated cases during the starting phase is attributed to the built lubrication layer in the direct vicinity of the contact zone (cf. Fig. 18 c)). The increased coefficient of friction in the lubricated cases during the steady state phase is, on one hand, attributed to viscous friction in the fluid, which is not present in the dry case and, on the other hand, due to individual fluid molecules stamped into the substrate surface [37, 356] (see also chapters 5 & 6).

Fig. 19 shows the number of trapped fluid molecules in the gap, as defined in Fig. 15, at the very end of the indentation ($\tau^* = 142$) as a function of the energy of the solid-fluid interaction $\tilde{\varepsilon}^*$. Starting at no coupling between fluid and solid molecules, i.e. $\tilde{\varepsilon}^* = 0$, the number of trapped molecules increases with increasing energy of the solid-fluid interaction until it reaches a plateau at approximately $\tilde{\varepsilon}^* = 0.75$ where, according to *Becker et al.* [26], total wetting is reached in the investigated Lennard-Jones system. The number of trapped fluid molecules in the gap is, therefore, strongly correlated with

the contact angle that a droplet forms on the substrate [26]. In the regime of energies of the solid-fluid interaction where total wetting is reached, i.e. $\tilde{\varepsilon}^* \geq 0.75$, the amount of trapped fluid molecules does not further increase with increasing energy of the solid-fluid interaction. The intermediary-load of the fluid molecules between the indenter and the substrate during the indentation is limited by the energy of the solid-fluid interaction in the wetting regime of changing contact angle, i.e. $0 < \tilde{\varepsilon}^* < 0.75$. Whereas in the regime of total wetting ($\tilde{\varepsilon}^* \geq 0.75$), the fluid internal pressure becomes the limiting factor, i.e. the fluid's dispersion energy ε_F .

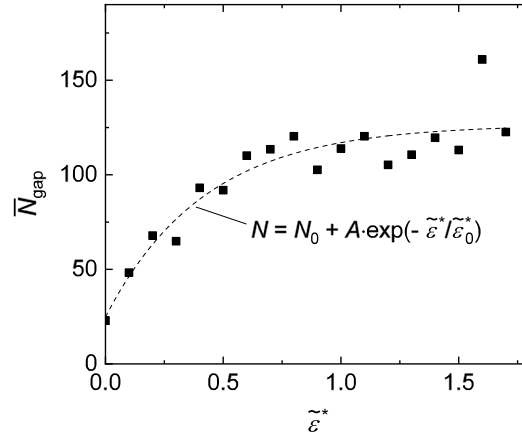


Figure 19: Maximum number of fluid particles in the gap (as defined in Fig. 15) as a function of the energy of the solid-fluid interaction $\tilde{\varepsilon}^*$. The maximum number of fluid particles is time averaged between $142 < \tau^* < 200$ to compensate large fluctuations, cf. Fig 18 c). The dashed line is a best fit of an exponential function with $N_0 = 126.5$, $A = -101.7$, and $\tilde{\varepsilon}_0^* = 0.422$.

3.3.2 Energy Balance

Fig. 20 shows the work done by the indenter until the end of the indentation as a function of the energy of the solid-fluid interaction $\tilde{\varepsilon}^*$. The work done by the indenter in the lubricated cases is given with respect to the work done by the indenter in the dry case. The work done during indentation follows a clear linear trend with increasing energy of the solid-fluid interaction and can be approximated well by

$$W_{\text{I.lub}}^*/W_{\text{I.dry}}^* = a + b \cdot \tilde{\varepsilon}^* . \quad (52)$$

The lubricated case with $\tilde{\varepsilon}^* = 0$ requires slightly more indentation work than the dry case. The remaining offset compared to the dry case can be attributed to the pure squeeze-out (microflow followed by viscous friction and dissipation) of fluid molecules, as no adsorption bonds have to be broken in the case of $\tilde{\varepsilon}^* = 0$. The increasing work done by the indenter with increasing energy of the solid-fluid interaction is mainly due to the

decreasing lateral mobility of the fluid molecules on the solid surfaces [356, 404]. This is due to the fact that the adsorption bonds for $\tilde{\varepsilon}^* > 0$ between the fluid and both solids (indenter and substrate) have to be broken while both solids approach each other, i.e. stick-slip behavior [72, 384]. The work done by the indenter during the scratching does not show such a clear trend due to strong fluctuations of the tangential forces during the scratching (not shown for clarity). The viscous friction in the fluid has a minor influence on the studied contact process.

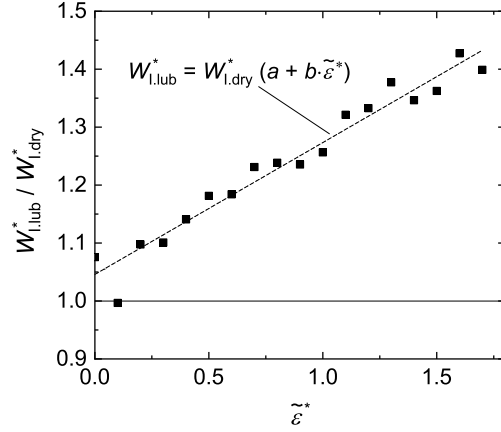


Figure 20: Average work done by the indenter with respect to the dry case until the end of the indentation ($0 < \tau^* < 142$) as a function of the energy of the solid-fluid interaction $\tilde{\varepsilon}^*$. The dashed line is a best linear fit with $a = 1.046$ and $b = 0.228$.

Fig. 21 shows the cumulative energy balance of the entire contact process (cf. Eq. (44)), comparing the dry and the lubricated cases. Since the absolute values of each contribution are mainly due to the kinematics of the process (speed of the indenter, size and shape of the indenter, indentation depth etc.), the relative contribution of the energy partitions are shown and discussed here. All properties of the energy balance W_I^* , ΔU_S^* , ΔU_F^* , and Q_{Th}^* are normalized at each time step during the simulation by the work done by the indenter at the end of the contact process $W_{I,dry}^*$ ($\tau^* = 809$) in the dry case, i.e.

$$\Delta E_{\text{norm}}(\tau^*) = \frac{Z(\tau^*)}{W_{I,dry}^*(\tau^* = 809)} \quad \text{with } Z = W_I^*, \Delta U_S^*, \Delta U_F^*, Q_{Th}^*. \quad (53)$$

This is done for the dry case as well as for all lubricated cases. For clarity, the lubricated cases are combined to the respective color-shaded area. Systematic trends of the energy contributions with varying the energy of the solid-fluid interaction are indicated by arrows. Overall, the energy of the solid-fluid interaction has a minor influence on the energy balance compared to the presence of a fluid in general.

The work done by the indenter corresponds to the energy contribution added to the

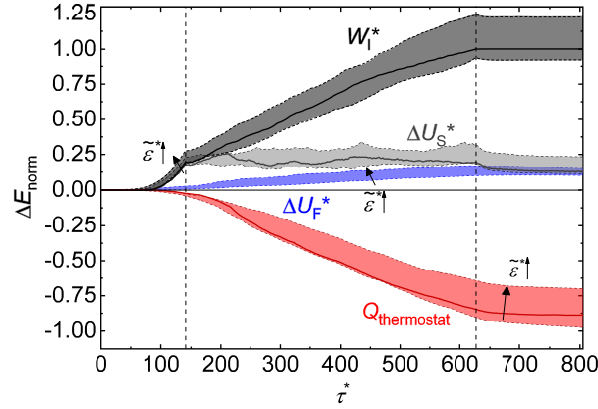


Figure 21: Energy balance of the entire contact process. The solid lines correspond to the dry case, the shaded areas indicate the maximum and minimum of the lubricated cases at each time step. Black corresponds to the work done by the indenter, gray to the internal energy of the substrate, blue to the internal energy of the fluid, and red to the heat removed from the simulation domain via the thermostat layer of the substrate. The vertical dashed lines indicate the beginning and end of the scratching – from left to right.

simulation domain during the contact process. This energy input splits into the heating of the fluid, the heating of the substrate, plastic and elastic deformation of the substrate, and the energy flux into the thermostat layer. The latter describes the heat flux into the bulk material of the substrate.

During the indentation, approximately 81% of the work done by the indenter goes into plastic and elastic deformation of the substrate and its heating up, i.e. the change of the internal energy of the substrate. 6% of the work done by the indenter goes into heating up of the fluid in the lubricated cases and approximately 13% goes into the thermostat layer of the substrate during the indentation.

Throughout the scratching, the internal energy of the substrate fluctuates around an average value, as the average temperature of the substrate quickly reaches a stationary state during the scratching in the applied simulation scenario [221]. The dissipated energy, which is due to the friction in the contact zone, therefore goes either into the thermostat layer of the substrate or into the lubricant, if such is present. The thermal energy removed from the simulation box via the thermostat layer in the dry case exceeds the different lubricated cases during the process at most times – especially at the very end of the contact process. Only in the lubricated case with $\tilde{\varepsilon}^* = 0$, more heat is removed via the thermostat (not shown for clarity), as the thermal coupling between the substrate and the fluid is very weak [192, 195].

The fluid has absorbed between 10 and 15% of the work done by the indenter by the end of the scratching phase – depending on the energy of the solid-fluid interaction. The thermostat layer of the substrate has by then removed 85% of the work done by the

indenter out of the simulation domain in the dry case. The heat flux into the thermostat layer is significantly reduced in the lubricated cases compared to the dry case. In the lubricated cases, the thermostat layer removed approximately 70% of the work done by the indenter out of the simulation domain. This cooling effect of the lubricant thereby significantly reduces the heat impact into the substrate compared to the dry case. The reason for the reduced heat impact on the substrate's thermostat layer by the lubricant is twofold; first, the fluid reduces friction during the scratching and thereby reduces dissipation of energy, cf. the work done by the indenter in Fig. 21. Second, the substrate thermostat removes all dissipated energy from the simulation domain in the dry case, whereas, in the lubricated cases, also the fluid absorbs a portion of the dissipated energy.

The work done by the indenter monotonously increases during the scratching until the beginning of the retraction. At the beginning of the retraction, the substrate does work on the indenter and the total energy of the substrate decreases, as the substrate can relax from its elastic deformation. The energy contained in the elastic deformation can thereby be estimated to be approximately 7% of the total work done by the indenter during the process.

The substrate thermostat layer removed more energy in the dry case compared to most lubricated cases by the end of the contact process. The thermostat layer keeps removing energy from the simulation domain during the retraction of the indenter, as the initial temperature is imposed to this layer. Since the lubricant itself is not temperature controlled and energy keeps being removed via the thermostat layer of the substrate during the retraction, a total heat flux from the fluid to the substrate actually slightly cools the fluid during the retraction.

The energy partition observed here might however change when more realistic systems are investigated, e.g. grain boundaries in the substrate instead of a single crystal [28, 136] and a rough surface instead of an atomistically flat one.

The energy of the solid-fluid interaction $\tilde{\varepsilon}^*$ has only a minor influence on the energy balance of the process. However, some trends are indicated as arrows in Fig. 21 for clarity. The work done by the indenter during the indentation depends on the energy of the solid-fluid interaction (see also Fig. 19). The increase of the internal energy of the fluid during the scratching slightly increases as the energy of the solid-fluid interaction increases. Multiple superimposing phenomena are the reason for this: The *Kapitza* resistance at the substrate-fluid interface decreases with increasing energy of the solid-fluid interaction [21, 192, 325] due to a stronger thermal coupling. This enhances the heat flux from the chip into the fluid with increasing energy of the solid-fluid interaction. Also, the energy of the solid-fluid interaction has an influence on the thermodynamic state point of the fluid close to the chip (see below), which accordingly influences the

thermal conductivity of the fluid and thereby the heat flux. A further phenomenon that influences the heating up of the fluid is the dependency of the lateral mobility of the fluid molecules on the energy of the solid-fluid interaction [356]. Hence, an increasing energy of the solid-fluid interaction leads to an increasing dissipation in the adsorbed fluid layer.

The energy of the solid-fluid interaction $\tilde{\varepsilon}^*$ has a significant influence on the heat input into the bulk substrate, which is modeled by the thermostat layer of the substrate. The heat input into the substrate is reduced by up to 20% for lubricated cases compared to the dry case. The main cause for this reduction is the heating up of the fluid. The reduction of friction due to the presence of a lubricant takes place during the starting phase of the scratching (see the discussed mechanical properties above).

3.3.3 Temperature Field and Thermodynamic Properties of Lubricant

Fig. 22 shows an exemplary snapshot of the temperature, density, and pressure field in the fluid during the simulation towards the end of the scratching ($\tau^* = 554$) in the lubricated simulation with $\tilde{\varepsilon}^* = 1.3$. The temperature field is also shown for the substrate. All three thermodynamic state variables were averaged bin wise during 5,000 time steps. Both the temperature and density profile in the fluid are fairly radial symmetric, which legitimizes the radial averaging as introduced in section 3.2.3. The temperature field, cf. Fig. 22 - top, reveals that the temperature in the substrate decays much faster than in the fluid. This is due to the fact that the heat conductivity in the substrate is about an order of magnitude higher than in the fluid. The maximum temperature is found in the tip of the chip and the adjacent fluid. The pressure is constant in the fluid, except in the direct vicinity of the solid surfaces, i.e. the adsorbed fluid layer. The temperature field in the fluid causes a change in the density compared to the bulk fluid density.

Fig. 23 - top and bottom show the temperature and density of the fluid in the surrounding of the chip as a function of the distance to the chip surface R^* and the energy of the solid-fluid interaction $\tilde{\varepsilon}^*$. Both the temperature and the density field of the fluid weakly depend on the energy of the solid-fluid interaction. Analog to the number of trapped particles (cf. Fig. 19) – the dependency of the temperature field on $\tilde{\varepsilon}^*$ can be distinguished in two regimes: In the range of $0 < \tilde{\varepsilon}^* < 0.75$, the temperature of the fluid in direct contact with the chip is significantly lower than in the range $0.75 < \tilde{\varepsilon}^* < 1.7$. As the indenter and the chip carry out a relative motion through the fluid, the adsorbed fluid layers experience a lateral shear flow on the surfaces of the chip and the indenter. This leads to an additional source of energy dissipation, cf. Refs. [196, 209], as discussed

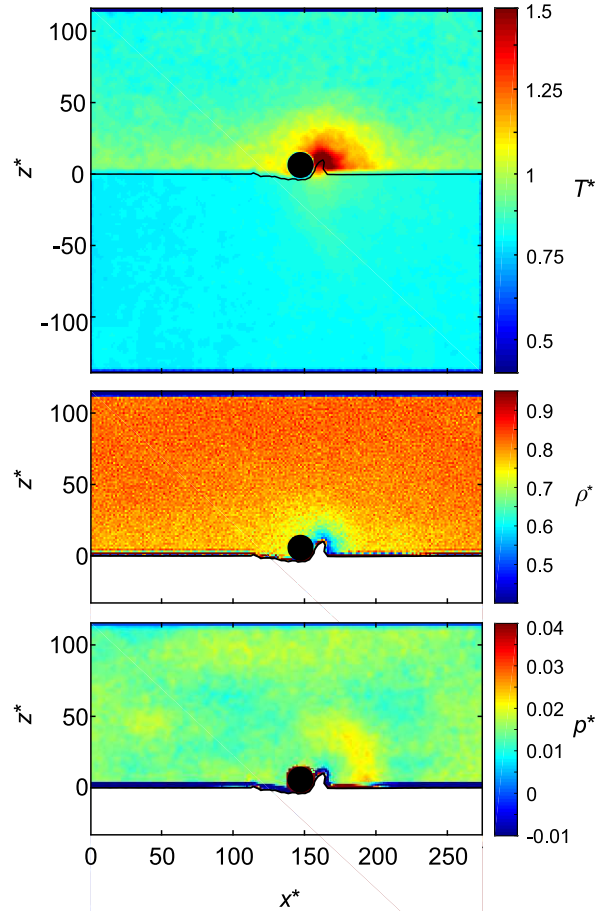


Figure 22: Thermodynamic properties of the fluid: (top) temperature, (middle) density, and (bottom) pressure field at the simulation time $\tau^* = 554$ from the lubricated simulation with the energy of the solid-fluid interaction $\tilde{\varepsilon}^* = 1.3$. Each variable is averaged over the box length in x -direction, cf. Fig. 15.

above. The decreasing lateral mobility of fluid molecules on the solid surfaces with increasing energy of the solid-fluid interaction leads to an increase of this dissipation and generation of heat at the surface, as for example shown by *Kim et al.* [196] and reviewed by *Krim* [209]. This can be observed as the fluid temperature directly at the chip surface increases with increasing energy of the solid-fluid interaction of the fluid $\tilde{\varepsilon}^*$.

Since the simulation scenario is set up in such a way that the entire fluid experiences an isochoric state change, no vaporization of the fluid takes place. But the local state change of the fluid close to the contact zone is not constrained by this boundary condition.

The decay of the temperature, density, and pressure of the fluid from the chip surface into the bulk fluid are reported in Fig. 24. They are normalized – as described in section 3.2.3 – by the corresponding chip surface and bulk value. All lubricated cases show the same decay into the bulk, except some small fluctuations. Therefore, all lubricated cases are plotted as a collective shaded area for clarity. The bulk pressure is reached already at distances of approximately 3σ from the chip surface. The fluid

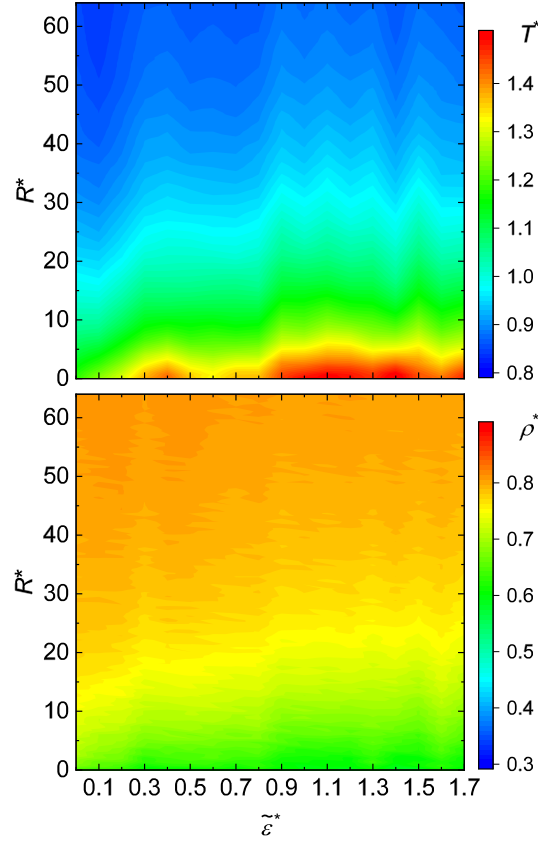


Figure 23: Temperature and density field of the fluid as a function of the distance from the chip surface (cf. Fig. 15) and the energy of the solid-fluid interaction $\tilde{\varepsilon}^*$. (Top) shows the temperature; (bottom) the number density. The properties are averaged during the stationary scratching phase ($335 < \tau^* < 625$) and over the angle α as indicated in Fig. 15 and the Appendix B.

temperature and density, on the other side, converge toward their bulk value at distances of approximately 65σ . The decay of the temperature and the density are almost the same.

The decay of all three state variables can be approximated well with the exponential function as indicated by the solid lines. The temperature and density obey almost perfectly exponential functions, cf. Eq. (49) - (51). The exponential fit function for the pressure profiles agrees within the scattering of the normalized pressure profiles from the different simulations.

Fig. 25 shows the average chip temperature during the scratching process of the lubricated cases with respect to the dry reference case as a function of the energy of the solid-fluid interaction, where the chip is geometrically defined as indicated in Fig. 15. The average chip temperature is slightly decreased compared to the dry case for energies of the solid-fluid interaction $\tilde{\varepsilon}^* < 1$ (with two exceptions), but is increased for energies of the solid-fluid interaction $\tilde{\varepsilon}^* \geq 1$ (one exception). The reduction of the average chip temperature compared to the dry case for $\tilde{\varepsilon}^* < 1$ is a result of the heat flux

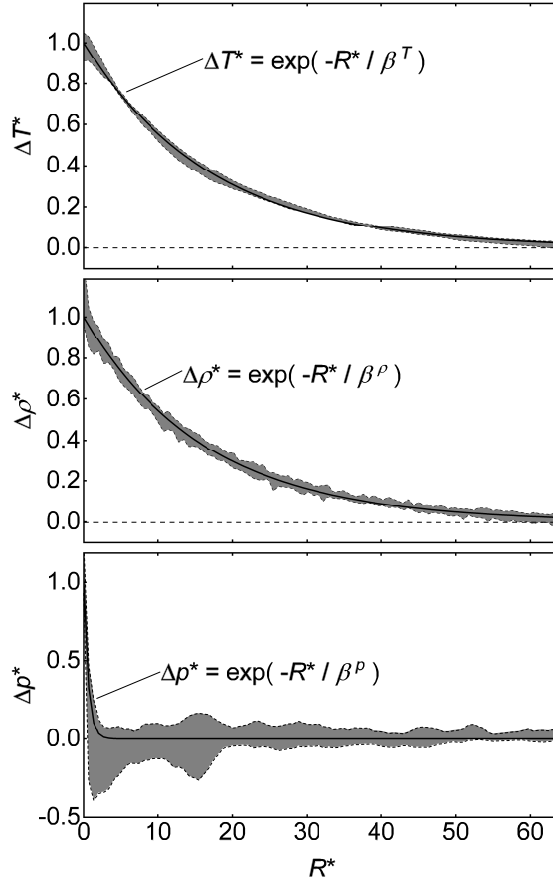


Figure 24: Thermodynamic properties of the fluid as a function of the distance from the chip surface: (top) temperature, (middle) density, and (bottom) pressure averaged during the stationary scratching phase ($335 < \tau^* < 625$) and the angle α as indicated in Fig. 15 and the Appendix B. The shaded areas indicate the maximum and minimum of the different lubricated cases at a given simulation time. The profiles are normalized as defined in Eq. (49) - (51). $R^* = 0$ corresponds to the chip surface and $R^* \rightarrow \infty$ corresponds to the bulk fluid. The exponential decay (black solid lines) is characterized by $\beta^T = 16.96$ for the temperature, $\beta^\rho = 16.43$ for the density, and $\beta^p = 0.59$ for the pressure.

from the chip into the fluid. With increasing energy of the solid-fluid interaction, the average chip temperature increases due to the decreasing lateral mobility of the fluid on the chip surface, which originates from the friction of the adsorbed fluid layers on the chip, cf. [196, 209, 356, 404]. The continuous breaking of adsorption bonds, while the indenter and the chip carry out a relative motion through the fluid, results in an increasing dissipation in the adsorbed fluid layer with increasing energy of the solid-fluid interaction. This leads to an increased average chip temperature for $\tilde{\varepsilon}^* \geq 1$ compared to the dry case.

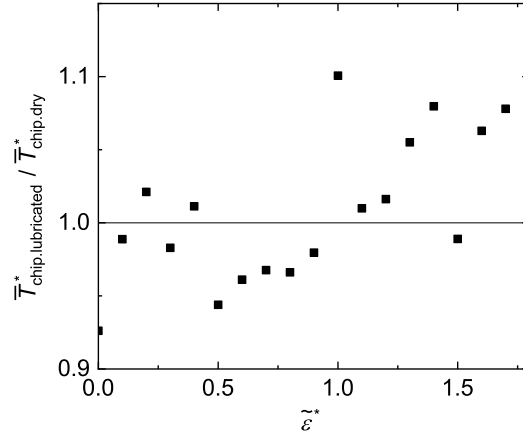


Figure 25: Average chip temperature during the steady state of the scratching ($335 < \tau^* < 625$) with respect to the dry case as a function of the energy of the solid-fluid interaction $\tilde{\varepsilon}^*$. The chip geometry was calculated as defined in Fig. 15.

3.4 Conclusions

The influence of lubrication on a nanoscopic scratching process in a Lennard-Jones model system was investigated by molecular dynamics simulation. Both mechanical and thermal properties were studied. A special focus was on the influence of the energy of the solid-fluid interaction on the dissipation behavior, the resulting heat fluxes, as well as the overall energy balance. This concept study improves the understanding of nanoscopic machining processes in state of the art production processes [81, 326].

The presence of a lubricant reduces the coefficient of friction by about 25% compared to a dry case while lubricant molecules remain between the indenter and the substrate. This is a result of an increased normal and slightly decreased tangential force in the starting phase. Once the fluid molecules are squeezed out and the contact is essentially dry with ongoing scratching, the coefficient of friction is increased by the presence of a fluid compared to a dry case by approximately 15%. The change of the coefficient of friction by the presence of a fluid was found to be independent of the energy of the solid-fluid interaction. The number of trapped fluid molecules during the indentation is in general a function of the energy of the solid-fluid interaction and the pressure. The first is found to be dominating for lower energies of the solid-fluid interaction, while the latter is dominating for cases, where the energy of the solid-fluid interaction is larger than the dispersion energy of the fluid.

The presence of a fluid has a significant influence on the energy balance of the process. The heat impact on the substrate is reduced up to 20% by the presence of a lubricant compared to a dry simulation. This cooling by the fluid is found to be dependent on the energy of the solid-fluid interaction. Two effects contribute to this cooling: First, the

fluid reduces the friction during the starting of the scratching and thereby reduces the amount of dissipated energy in the contact zone. Second, a heat flux from the contact zone to the fluid directly cools the contact zone.

The major part of the work done by the indenter dissipates and is removed from the system via the substrate thermostat. The potential energy of the substrate fluctuates in the stationary phase of the scratching, but does not steadily increase with the ongoing formation of the chip. The energy dissipation dominates the energy balance compared to the energy required for the defect generation and plastic deformation.

The temperature, density, and pressure of the fluid are found to be fairly radial symmetric around the formed chip. The temperature gradient from the chip surface into the bulk fluid is furthermore found to induce a density gradient to maintain local thermodynamic equilibrium as far as possible, whereas the pressure reaches the corresponding bulk value very close to the chip surface. Both temperature and density exhibit the same decay behavior from the chip surface to the bulk fluid. For a future work, it would be interesting to investigate, how far from the thermodynamic equilibrium the fluid around the chip is by comparing the computed state points with those of an equation of state for the Lennard-Jones fluid, for example that proposed by *Heier et al.* [163].

The presence of a lubricant is found to be beneficial for both the mechanical and the thermal behavior of the contact process. Overall, it is found that the energy of the solid-fluid interaction has a surprisingly minor influence on a nanoscopic scratching process, compared to an important influence in shear flow friction simulations [113, 167, 254, 363, 386, 404].

The insight gained from the simplified model system from the present work can be extended in future work by increasing the complexity to also study the effect of chain like lubricant molecules, grain boundaries in the substrate block, and a realistic surface roughness on the contact process properties. In chapter 6 of this work, contact processes with n-decane as lubricant fluid are studied.

4 Reproducibility of Atomistic Friction Computer Experiments: A Molecular Dynamics Simulation Study

4.1 Introduction

The estimation and reporting of statistical uncertainties [226, 412] is a fundamental and widely accepted principle in science. Statistical uncertainties describe the reproducibility of results and are, hence, intrinsically related to the reliability of the results. In laboratory experiments, the quantification of statistical uncertainties is firmly established. Simulation methods based on physical modeling are often referred to as *computer experiments*. Computer experiments and laboratory experiments are complementary and sincerely intertwined [202, 229, 362, 401]. The estimation of uncertainties of computer experiments [194, 309] and thereby their reliability, should in principle have the same role as it has in classical laboratory experiments. However, it is, especially for complex simulation scenarios, presently far from being as well-established as in laboratory experiments.

The question of the quantification of uncertainties in simulations is related to their reproducibility, which has for example been addressed in the fields of climate and weather simulation [193, 342, 380], geology simulations [282], computational fluid dynamics simulations [22, 252], quantum chemistry [177, 228], *Markov* state models [47, 73, 263, 293], and molecular simulations based on classical mechanics [2, 9, 125, 151, 241, 361, 367, 396]. The quantification of statistical uncertainties of equilibrium molecular dynamics (EMD) simulation results has been discussed intensively in the literature [53, 59, 78, 97, 137, 141, 146, 197, 199, 302, 319, 367, 407]. Also, the statistical uncertainties of non-equilibrium molecular dynamics (NEMD) that exhibit a stationary state have been extensively discussed in the literature [107, 247, 387, 400], e.g. for shear flow and

heat transfer [105, 106, 152, 271, 311, 390, 391]. In contrast, there are surprisingly few papers, in which the statistical uncertainties of non-stationary NEMD simulations are addressed in a systematic manner [169, 295]. To the best of our knowledge, no study on the statistical uncertainties in atomistic friction simulations of a scratching process has been carried out yet. Molecular simulations of such atomistic contact processes have become an established tool in the past two decades, studying dry contact processes [13, 131, 132, 134, 136, 204, 236, 246, 416, 427] and the effect of lubrication [5, 11, 62, 68, 69, 109, 111, 112, 178, 183, 220, 221, 227, 277, 299, 300, 323, 328, 333–335, 335, 356, 375, 377, 378, 397, 419, 430, 431].

In general, for a given scientific method, statistical uncertainties can be assessed by carrying out independent repetitions of an experiment. However, the definition of repetition is not unambiguous. We adopt the common standpoint that repetition means using the same equipment and the same methods. If this would be applied in a strict sense to computer experiments, the simulation would be repeated on the same computer with exactly the same input and starting conditions. Then, there is no statistical uncertainty in non-stationary simulations (at least when the numerical machine uncertainty is disregarded). Hence, this strict interpretation is not adequate for the molecular simulations as carried out in the present work. We prefer using a wider interpretation of reproducibility in which we allow for small variations in the input, which, based on physical arguments, should not lead to any significant differences in the results of the observables. Reporting estimates for statistical uncertainties is standard for EMD and stationary NEMD simulations. There, the statistical uncertainty is usually not quantified by running different independent simulations, but rather by using the block averaging method, in which the blocks play the role of the individual experiments and applying evaluation techniques that ensure that there is no bias due to their correlation [9, 107, 125, 367, 396]. Classical block averaging [9] cannot be applied in highly non-stationary NEMD simulations of nanoscopic scratching and plastic deformation processes [295] as considered in the present work. Furthermore, even in apparently steady state phases of such simulations, the fluctuations of observables such as the friction forces and the coefficient of friction cannot be interpreted as statistical uncertainties, as they partially result from the physics of the setup, e.g. the coupling of the kinematics with the crystal structure [384]. At times, statistical uncertainties of complex and non-stationary simulations, as well as statistical uncertainties of simulations for studying rare events, are estimated by performing sets of replicas of a given simulation upon varying the initial configurations in the individual replicas, e.g. in simulations for the determination of transport properties of fluids, grain boundary migration, and properties of bio molecules [10, 48, 59, 78, 210, 295, 317, 428]. Here, this approach is applied to non-stationary scratching simulations.

Hence, in the present work, non-stationary NEMD simulations are used to study nanotribological friction processes with a focus on the statistical uncertainties of the results. Since the main interest was on the effects of lubrication for the tribological scratching system, both a dry and a lubricated case were investigated. A two-stage contact process was studied. The simulation setup and force field was identical to that considered in chapter 3. Therein, an indenter first penetrates in a flat substrate and then carries out a lateral movement scratching the substrate causing elastic and plastic deformation. All three components of this scenario, the substrate, the indenter, and eventually, in the lubricated case, a fluid were described by the Lennard-Jones truncated and shifted potential. The simulations for the dry case as well as those for the lubricated case were repeated eight times each. In each of these replicas, the initial configuration, i.e. the positions of all atoms were identical, but different random seeds were used for initializing the velocities. All simulations were subsequently equilibrated before the movement of the indenter started. The kinematics of the indenter were identical in all cases. Hence, the replicas differ only in the thermal motion. These eight simulations are considered as a *set of replicas* in the following, i.e. we have a "dry set of replicas" and a "lubricated set of replicas". The main interest lies in the reproducibility of the results from the different observables in both a dry and a lubricated contact process. Both mechanical and thermal properties of the process are investigated and averages as well as statistical uncertainties of the results of the sets of replicas for the dry and the lubricated case were determined. The scattering of the results from the simulations of a set of replicas provides a measure for the statistical uncertainty and reproducibility. This provides a sound basis for the comparison of both cases (dry and lubricated) and for assessing the reproducibility of the findings. In contrast, differences between a single dry and a single lubricated run are hard to interpret, as the statistical uncertainty of the results is not known.

It should be noted that besides statistical errors, also systematic errors occur in computer experiments [157, 228, 319, 361]. Systematic errors can be caused by simulation algorithms and methods, hardware architecture etc. Hence, the replica method applied in the present work yields a lower limit of the reproducibility of the considered friction simulations. Systematic errors can be investigated in round robin studies and are not addressed here. *Müser et al.* [278] showed in a contact mechanics round robin study that solutions for a given problem that are addressed by different methods generally agree well, but can differ in parts considerably, which might be caused by statistical and systematic errors. In the present work, only statistical errors due to thermal noise in an atomistic contact process simulation are addressed.

The same simulation scenario as in chapter 3 was used, i.e. same geometry, kinematics, force field etc. (details are given below). The main difference in the setup used in this

chapter compared to chapter 3 is that no retraction phase was considered here, i.e. only indentation and scratching. This is due to the fact that the main phenomena of interest (squeeze-out, lubrication, cooling, etc.) occur during indentation and scratching. In chapter 3, the influence of the solid-fluid interaction energy on different observables was investigated – focusing on thermodynamic and mechanical properties. The resulting different lubricated cases were compared with a dry reference case, cf. chapter 3. It was thereby for example found that the coefficient of friction is significantly reduced by the presence of a lubricant compared to a dry case as long as lubricant molecules remain between the indenter and the substrate. Once the fluid molecules are squeezed out of the contact zone with ongoing scratching, the coefficient of friction was found to be slightly increased by the presence of a fluid compared to a dry case. The number of trapped fluid molecules as well as the thermal balance was found to significantly depend on the solid-fluid interaction energy, cf. chapter 3. This chapter aims at critically assessing the significance and reproducibility of these findings, in which only single simulation runs were compared.

As in the previous chapter, physical properties are conveniently reduced here using the Lennard-Jones potential parameters of the fluid $\varepsilon = \varepsilon_{\text{F}}$, $\sigma = \sigma_{\text{F}}$ and the molecular mass M , as well as the Boltzmann constant k_{B} , e.g. the temperature $T^* = T/(\varepsilon/k_{\text{B}})$, the density $\rho^* = \rho/(1/\sigma^3)$, the pressure $p^* = p/(\varepsilon/\sigma^3)$, the internal energy $U^* = U/\varepsilon$, the work $W^* = W/\varepsilon$, the heat $Q^* = Q/\varepsilon$, the force $F^* = F/(\varepsilon/\sigma)$, the time $\tau^* = \tau/(\sigma\sqrt{M/\varepsilon})$, lengths and distances $l^* = l/\sigma$ (where l can be radii R , the depth d or dimensions x, y and z), the volume $V^* = V/\sigma^3$, and the velocity $v^* = v/\sqrt{\varepsilon/M}$.

4.2 Simulation Scenario and Definition of Observables

4.2.1 Force Field and Simulation Setup

Fig. 26 shows the setup of the simulation, consisting of a cylindrical indenter (I), a substrate (S), and eventually a fluid (F) in the lubricated cases. All three components are modeled with the Lennard-Jones potential truncated and shifted at 2.5σ :

$$u_{\text{LJTS}}(r) = \begin{cases} u_{\text{LJ}}(r) - u_{\text{LJ}}(r_c) & r \leq r_c \\ 0 & r > r_c, \quad \text{and} \end{cases} \quad (54)$$

$$u_{\text{LJ}}(r) = 4\varepsilon \left[\left(\frac{\sigma}{r} \right)^{12} - \left(\frac{\sigma}{r} \right)^6 \right], \quad (55)$$

where u_{LJ} is the full Lennard-Jones potential with ε and σ being the energy and size parameter, respectively. The distance between two particles is denoted by r . The cut-off radius until which molecular interactions are considered is $r_c = 2.5\sigma$ throughout this work, except for the indenter-substrate (IS) interaction, which is purely repulsive by choosing $r_{c,\text{IS}} = 2^{1/6}\sigma$.

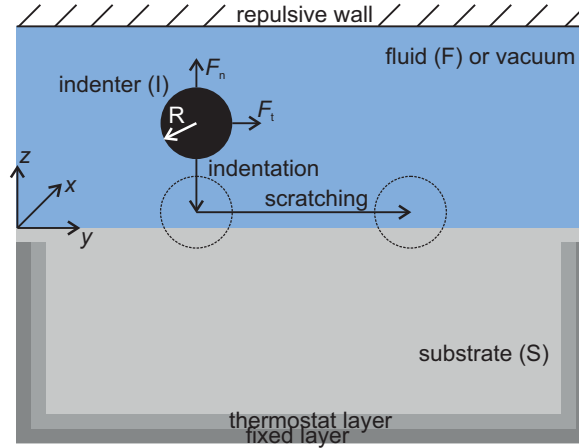


Figure 26: Sketch of the simulation box and the indenter movement (not true-to-scale): Indentation and scratching. Above the substrate, there is either vacuum (dry cases) or a fluid (lubricated cases).

The Lennard-Jones potential is probably the most frequently and thoroughly studied model potential [348, 350, 361]. It describes the thermodynamic properties of simple non-polar fluids very well [102, 353], but is only a crude model for solids [153, 381, 429]. Nonetheless, it is used here for all substances, including the substrate, for two reasons: First, it makes this study consistent with earlier studies investigating the wetting behavior of this model system [26, 92, 351, 357]. Second, it is computationally significantly cheaper than more realistic EAM potentials [258], which is important here, as sets of replicas of simulations had to be performed.

For simplicity, the sites of the indenter, the substrate, and the fluid have the same size σ and the same mass M . Table 2 summarizes the interactions of all components (S, I, F). The self interactions are denoted as the diagonal components, the cross-interactions as the off-diagonal components in Table 2. The dispersion energies were chosen such that the three components represent realistic materials. The parameter of the dispersion energy of the fluid is used throughout this chapter to normalize all molecular interactions. This is indicated by an asterisk. The energy parameter of the fluid was chosen such that it describes methane according to the model proposed by *Vrabec et al.* [402]. The dispersion energy of the substrate was adopted from *Halicioglu et al.* [153] such that it energetically models a pure iron single crystal. The indenter atoms are placed on a diamond lattice with a lattice constant of 1.55σ and are a single rigid body.

The energy of the solid-fluid interaction is the same for the indenter-fluid (IF) and

Table 2: Pairwise interaction energies employed in the present study. The interaction energies are reduced by the interaction energy of the fluid, which is denoted by an asterisk: $\varepsilon^* = \varepsilon/\varepsilon_F$.

	substrate (S)	indenter (I)	fluid (F)
substrate (S)	^(a) $\varepsilon_S^* = 34$	^(b) WCA	^(c) $\tilde{\varepsilon}^* = 0.5$
indenter (I)	-	rigid body	^(c) $\tilde{\varepsilon}^* = 0.5$
fluid (F)	-	-	^(d) $\varepsilon_F/k_B = 175.1$ K

^(a)Lennard-Jones solid – iron [153];

^(b) Weeks-Chandler-Andersen potential [408];

^(c)energy of the solid-fluid interaction[26];

^(d)Lennard-Jones fluid – methane [353].

the substrate-fluid (SF) interactions and denoted by a tilde \sim throughout this chapter, i.e. $\tilde{\varepsilon}^* = \varepsilon_{\text{IF}}^* = \varepsilon_{\text{SF}}^*$. The solid-fluid interaction energy determines the adsorption and the wetting behavior of the lubricant on the solid surfaces [26, 92, 160]. *Becker et al.* [26] have investigated liquid droplets on solid surfaces in Lennard-Jones systems and determined the influence of the solid-fluid interaction energy on the contact angle. The solid-fluid interaction energy was set to $\tilde{\varepsilon}^* = 0.5$ here, which results in a contact angle of approximately 90° for the chosen temperature [26].

In the simulations, the indenter carried out two sequential movements, cf. Fig. 26: (i) indentation during which the indenter penetrated into the substrate in $-z$ -direction normal to the unpenetrated substrate surface, and (ii) scratching, during which the indenter moved laterally through the surface in $+y$ -direction forming a groove. The movement of the rigid indenter was fully prescribed; its velocity was constant at $v^* = 0.066$ during the indentation and scratching. The time step was set to $\Delta\tau^* = 0.0008$. The depth of the indentation was set to $d^* = 4$ and kept constant during the scratching phase. The surface of the substrate lies in the xy -plane.

The rigid cylindrical indenter had a radius of $R_I^* = 8.1$ and consisted of 8.2×10^3 atoms. The length of the cylinder was the same as the width of the substrate and equal to the width of the simulation domain in x -direction, where the periodic boundary conditions were applied. The size of the substrate block was $\Delta x^* = 37.3$, $\Delta y^* = 274.2$, $\Delta z^* = 139.6$; it consisted of 1.5×10^6 atoms. The substrate was initialized as an fcc single crystal, which is the equilibrium lattice for the Lennard-Jones potential at the chosen state point [389]. The substrate surface was perpendicular to the (100) orientation of the lattice. The scratching was carried out in the $[0 \bar{1} 1]$ direction. The indenter was fully submersed in the fluid in the lubricated cases. The fluid consisted of 9.0×10^5 molecules, with an initial temperature of $T^* = 0.8$ and an initial pressure after the equilibration of $p^* = 0.014$ and was therefore in a liquid state and no vapor-liquid equilibrium exists in the simulation box (at $T^* = 0.8$, the vapor pressure of the LJTS fluid is $p^{s*} = 0.012$

[350]). Periodic boundary conditions were applied in both x - and y -direction, whereas a soft repulsive wall confined the fluid in the simulation box at $z^* = 251.3$ at the top. The substrate block was constrained in the simulation domain by fixing the positions of three atom layers next to the box margins in both positive and negative y -direction and at the bottom (cf. Fig. 26).

The system was equilibrated for 1×10^6 time steps. The initial temperature of $T^* = 0.8$ was imposed to the entire system during the equilibration – except for the indenter atoms, which had a prescribed velocity. The same temperature was also imposed to four atom layers between the substrate and the fixed layer (cf. Fig. 26) during the indentation and the scratching via velocity scaling to extract dissipated heat from the system. Hence, only this boundary layer of the substrate block was thermostated during the simulation.

The simulations were performed with the open-source code LAMMPS [288]. The software tool OVITO [370] was used for analyzing the dislocation behavior.

4.2.2 Statistical Analysis

For each set of replica, each simulation setup (dry and lubricated) was carried out eight times. The simulations from a set of replica only differ in the initial thermal motion. The initial configuration of all atoms was identical, but the initial velocities were initialized based on different random seeds within a set of replica. Each simulation was equilibrated as described above. The standard deviation of the results of these eight simulation runs is taken here as a measure for the reproducibility of a given observable. The standard deviation $\sigma_Z(\tau^*)$ of an observable $Z(\tau^*)$ at a time τ^* is defined as

$$\sigma_Z(\tau^*) = \sqrt{\frac{1}{N-1} \sum_{n=1}^N (Z_n(\tau^*) - \bar{Z}(\tau^*))^2}, \quad (56)$$

where N is the number of independent simulations in a set of replica ($N = 8$ here) and $Z_n(\tau^*)$ is the value of an observable of the n^{th} simulation at a specific simulation time τ^* . $\bar{Z}(\tau^*)$ is the arithmetic mean value of the N simulation results at a simulation time τ^* . The mean value and the corresponding standard deviation from a set of replica are thereby computed for each time step of the contact process. The following observables Z were studied: The tangential and the normal force on the indenter F_t^* and F_n^* , respectively, the coefficient of friction μ , the total dislocation length L^* , the chip volume V_{chip}^* , the chip temperature T_{chip}^* , the work done by the indenter W_I^* , the temperature, density, and pressure profile of the fluid T_{fluid}^* , ρ_{fluid}^* , p_{fluid}^* , and the local temperature field in the vicinity of the contact zone $T(z, y)$. Details on their definition and computation are given in the following section.

To compare the reproducibility of the different observables Z , the instantaneous normalized standard deviation $\delta_Z(\tau^*)$ is introduced as

$$\delta_Z(\tau^*) = \frac{\sigma_Z(\tau^*)}{Z^{\max} - Z^{\min}}, \quad (57)$$

where Z^{\max} and Z^{\min} are the maximum and minimum values of an observable Z during the entire simulation time and from all simulations of the set of replica. For brevity, the numeric values of δ_Z are labeled *statistical uncertainties* of a given observable Z .

Small values of $\delta_Z(\tau^*)$ well below unity indicate that trends of the respective quantity Z can be reliably observed despite the statistical uncertainties. Values of $\delta_Z(\tau^*)$ close to unity, on the other hand, indicate that the statistical uncertainties exceed the entire range of values observed for a property Z . In this case, trends of the respective quantity Z can not be discerned reliably.

4.2.3 Definition of Observables

The total tangential force F_t^* and normal force F_n^* on the indenter were computed as the sum of all pair interactions (indenter-substrate (IS) and the indenter-fluid (IF)) on the indenter in y - and z -direction, respectively:

$$F_t^* = \sum_{i=1}^m \left(F_{y,i}^{\text{IS}^*} + F_{y,i}^{\text{IF}^*} \right), \quad (58)$$

$$F_n^* = \sum_{i=1}^m \left(F_{z,i}^{\text{IS}^*} + F_{z,i}^{\text{IF}^*} \right), \quad (59)$$

where m is the total number of atoms of the indenter. The coefficient of friction was calculated as

$$\mu = F_t^* / F_n^*, \quad (60)$$

during the scratching.

During the indentation and the scratching, lattice defects are generated in the substrate. They are quantified by the total dislocation length L^* . The dislocations were identified using DXA [371].

The energy balance of the simulation box is written here as

$$Q_{\text{Th}}^* + W_{\text{I}}^* = \Delta U_{\text{S}}^* + \Delta U_{\text{F}}^* + \delta E_{\text{err}}^*. \quad (61)$$

In Eq. (61), ΔU_{S}^* and ΔU_{F}^* are the changes of the total energy (kinetic energy + potential energy) of the substrate and the fluid, respectively, in a time interval $\Delta\tau^*$. The term

Q_{Th}^* indicates the heat removed from the system by the thermostat; W_{I}^* is the work done by the indenter on the system. ΔU_{S}^* , ΔU_{F}^* , and Q_{Th}^* are simulation results.

The work W_{I}^* is computed by numerical integration of the respective total force on the indenter

$$W_{\text{I}}^*(\tau^*) = \int_{\text{indentation}} F_{\text{n}}^*(\tau^*) dz + \int_{\text{scratching}} F_{\text{t}}^*(\tau^*) dy, \quad (62)$$

where the forces F_{n}^* and F_{t}^* are defined according to Eq. (58) and (59). The energy conservation law is Eq. (61) without the term δE_{err}^* and not fulfilled exactly by the simulation results due to the numeric nature of the simulation. Therefore, the term δE_{err}^* is introduced, which is a measure for the numeric error. This remaining numerical error δE_{err}^* in the global energy balance Eq. (61) is mainly a result of the numerical integration applied in Eq. (62).

To characterize the fluid in the vicinity of the chip, the temperature, density, and pressure profile of the fluid was computed as a function of the distance R^* from the chip surface as schematically shown in Fig. 27. The fluid properties were averaged radially around the chip in a coordinate system that is moving with the indenter during the stationary phase of the scratching such that the results do not depend significantly on the simulation time. To characterize the reproducibility of the thermodynamic properties of the fluid (temperature, density, and pressure), the statistical uncertainty δ_Z was computed individually for each property and distance to the chip surface, i.e. $Z = T^*(R^*), \rho^*(R^*), p^*(R^*)$.

The chip volume and chip temperature were computed following the geometric definition of the chip in Fig. 27, i.e. the substrate atoms ahead of the indenter in the scratching direction and with $z^* > 0$ constitute the chip. The chip surface was analyzed with an alpha shape algorithm [98]. The chip temperature T_{chip}^* was defined as the mean temperature of the substrate atoms in the chip.

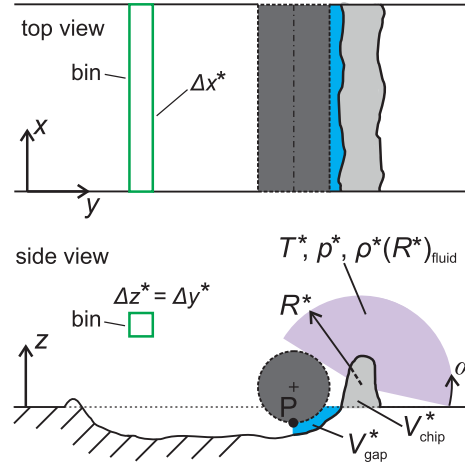


Figure 27: Schematic definition of observables (not true-to-scale) used for characterizing the atomistic contact process. The chip is characterized by its volume and temperature. The thermodynamic state of the fluid is calculated as a function of the distance from the chip surface and averaged over the angle α during the scratching. The radial averaging is carried out with respect to the center of mass of the formed chip. The green rectangle indicates the shape of one of the averaging bins for the computation of the temperature, pressure, and density profiles in the simulation box.

4.3 Results and Discussion

The following discussion is focused on the statistical uncertainties of the results of nanoscopic contact process simulations; the related physical phenomena are only briefly addressed. The simulation scenario that was studied in this chapter in replicas was studied chapter 3 with single simulation runs. The main features of the studied process are as follows: During the indentation (i), the indenter is lowered, gets into contact with the substrate and penetrates it. The indentation phase (i) ends at $\tau^* = 142$. Then, the lateral scratching (ii) begins. In that phase, first the substrate is deformed elastically and then plastically and a chip builds up. In particular, the starting phase ($142 < \tau^* < 335$) of the scratching is highly non-stationary. We refer the reader to chapter 3 for a more comprehensive discussion of the physical phenomena. In this chapter, the focus is on the issues of reproducibility and statistical significance. A detailed discussion of the relation between the results of the influence of the wetting behavior on the tribological properties presented in chapter 3 and the results from this work regarding the statistical significance is given in the Appendix B.

4.3.1 Mechanical Properties

Fig. 28 shows the tangential force on the indenter F_t^* in the set of replicas of the dry and the lubricated cases (top) and the corresponding statistical uncertainty $\delta_{F_t^*}$ (bottom). The tangential force in the dry cases exhibits a jump with a plateau during the indentation in all eight simulations. This plateau during the indentation is a result of misfitting lattices from the substrate and the indenter (cf. chapter 3), i.e. the atomistic nature of the contact process. The thermal motion evidently has an influence on the peak, but nevertheless, the peak is present in all eight dry simulations. At the beginning of the scratching, the lubricated set of replicas has a clearly decreased tangential force compared to the dry set of replicas. Hence, the decrease (cf. chapter 3) is reproducible and can be attributed to the presence of the lubricant. During the stationary phase of the scratching, the absolute value of the tangential force in the lubricated set of replicas shows a tendency to be slightly increased compared to the dry set of replicas. This effect of the presence of a lubricant on the tangential force has also been reported and discussed in chapter 3. The statistical uncertainty of the tangential force $\delta_{F_t^*}$, cf. Eq. (57), increases during the indentation and at the beginning of the scratching, until it reaches a steady level at approximately $\tau^* = 200$. This corresponds well with the steady state of the tangential force itself. The fact that the statistical uncertainty converges is an important indication that there are no systematic differences between the different simulations from a set of replicas. The differences among the simulations from a set of replicas $\delta_{F_t^*}$ due to the differences of the thermal motion reach a steady state (instead of building up with ongoing simulation time), during which a property-specific statistical uncertainty can be estimated. In the case of the tangential force this average statistical uncertainty is approximately $\overline{\delta_{F_t^*}} = 0.1$.

Fig. 29 shows the normal force on the indenter F_n^* in both sets of replicas (top) and the corresponding statistical uncertainties $\delta_{F_n^*}$ (bottom). For the normal force, the deviations among the simulations of a set of replicas are comparatively small during the indentation. The increase of the normal force during the indentation due to the presence of a lubricant, which has been reported previously [348, 356], is also found here and is therefore clearly physical and not an artifact. The same holds for the beginning of the scratching, during which the normal force of the lubricated simulations tends to exceed that in the dry simulations. This lasts until approximately $\tau^* = 300$. For larger simulation times, the results from the dry and the lubricated set of replicas agree within their corresponding uncertainties, which is a result of the differences of the thermal motion in the simulations among a set of replicas. The distinction in a starting phase and an approximate steady state phase can be attributed to the fact that fluid molecules are trapped between the indenter and the substrate at the beginning of the scratching and are subsequently squeezed out until the contact is essentially dry, which

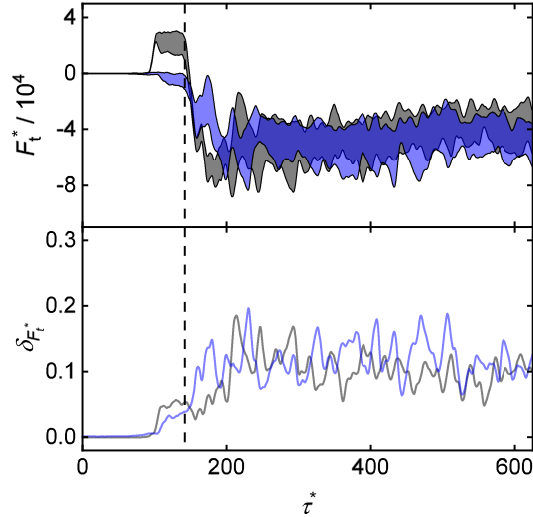


Figure 28: Tangential force on the indenter during the contact process (top) for the lubricated and the dry cases. Results obtained from a set of replicas (eight simulations) for each case. Top: Results for the tangential force; the shaded areas are bands of the width of the standard deviation (cf. Eq. (56)) around the arithmetic mean – computed at each time step individually. Bottom: Normalized standard deviation as defined in Eq. (57). Grey indicates the dry simulation set of replicas, blue (with a 50% transparency) the lubricated one. The dashed vertical line indicates the beginning of the scratching phase.

is the case after about $\tau^* = 335$ in the simulations presented in chapter 3. After this, dry and lubricated simulations practically do not differ in the normal force. As for the tangential force, the statistical uncertainty of the normal force (cf. Fig. 29 - bottom) steadily increases during the indentation and the beginning of the scratching until it reaches a steady level. The statistical uncertainty of the normal force in this steady state phase is about $\overline{\delta_{F_n^*}} = 0.06$, which is approximately half the value found for the tangential force.

The coefficient of friction μ and its statistical uncertainty δ_μ are shown in Fig. 30. It has been shown in chapter 3 that the considered nanoscopic scratching process can be divided into a starting phase (presence of lubricant reduces the coefficient of friction) and a main phase (presence of lubricant slightly increases the coefficient of friction). The coefficient of friction in the lubricated cases is slightly increased during the main phase compared to the dry cases, as most of the fluid molecules are squeezed out of the gap and only individual fluid particles are stamped into the substrate [37, 348, 356]. Both phenomena are clearly confirmed by the statistical analysis of the present work. Since the coefficient of friction is computed from the ratio of the tangential and the normal force, the statistical uncertainty of the coefficient of friction δ_μ is higher than that from the tangential or normal force individually. The average statistical uncertainty of the coefficient of friction in the stationary phase is approximately $\overline{\delta_\mu} = 0.12$. Interestingly,

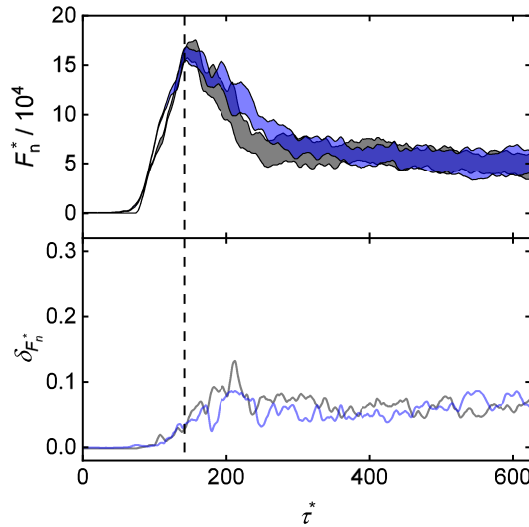


Figure 29: Normal force on the indenter during the contact process (top) for the lubricated and the dry cases. Results obtained from a set of replicas (eight simulations) for each case. Top: Results for the normal force; the shaded areas are bands of the width of the standard deviation (cf. Eq. (56)) around the arithmetic mean – computed at each time step individually. Bottom: Normalized standard deviation as defined in Eq. (57). Grey indicates the dry simulation set of replicas, blue (with a 50% transparency) the lubricated one. The dashed vertical line indicates the beginning of the scratching phase.

the statistical uncertainty of the coefficient of friction in the dry set of replicas clearly exceeds that of the lubricated set of replicas during $200 < \tau^* < 300$, which is likely due to a dampening effect of the trapped fluid particles [356].

The total dislocation length in the substrate L^* and its statistical uncertainty δ_{L^*} from the dry and the lubricated set of replicas are shown in Fig. 31. The total dislocation length increases during the indentation and at the beginning of the scratching until approximately $\tau^* = 200$. Subsequently, the total dislocation length does not increase significantly any more: It fluctuates around a fairly stationary value during the scratching. The comparison with Figs. 28 - 30 shows that the results for the dislocations are not as reproducible as the results for the forces on the indenter and the coefficient of friction. The thermal motion has a significant influence on the initiation and progressive motion of the dislocations. While the results for the dislocations obtained in the set of replicas agree reasonably well during the build-up of the dislocations ($0 < \tau^* < 200$), the results for the dislocation length observed in the scratching phase show large differences, as can be seen from the wide width of the bands in Fig. 31 - top. The corresponding statistical uncertainty reaches values up to $\delta_{L^*} = 0.2$. With ongoing scratching, the statistical uncertainties δ_{L^*} in the lubricated set of replicas is larger than in the dry set of replicas. This is likely due to the influence of individual fluid molecules being stamped

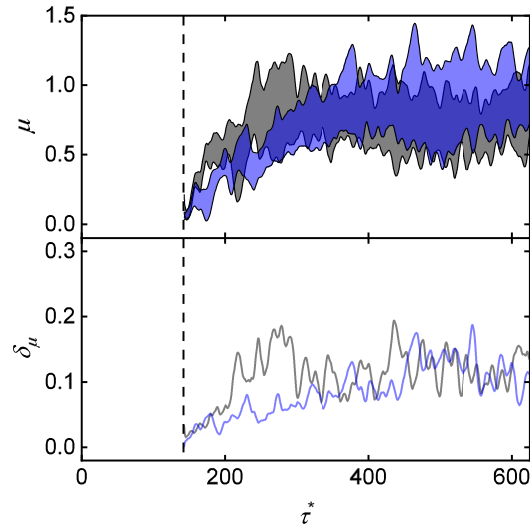


Figure 30: Coefficient of friction during the contact process (top) for the lubricated and the dry cases. Results obtained from a set of replica (eight simulations) for each case. Top: Results for the coefficient of friction; the shaded areas are bands of the width of the standard deviation (cf. Eq. (56)) around the arithmetic mean – computed at each time step individually. Bottom: Normalized standard deviation as defined in Eq. (57). Grey indicates the dry simulation set of replica, blue (with a 50% transparency) the lubricated one. The dashed vertical line indicates the beginning of the scratching phase.

into the substrate surface [37, 356], which can cause dislocations. This imprinting of fluid particles into the surface depends strongly on the thermal motion, which increases the statistical uncertainty of the total dislocation length in the lubricated set of replicas compared to the dry set of replicas. The nucleation of dislocations in an originally defect-free crystal has features of chaotic dynamics in which small differences of the particle positions among simulations of a set of replicas may give rise to different behavior regarding the nucleation and advance of dislocations. Similar arguments pertain to the processes occurring when dislocations meet and react.

Fig. 32 shows the results for the volume of the chip V_{chip}^* as defined in Fig. 27 in both sets of replicas and the corresponding statistical uncertainty $\delta_{V_{\text{chip}}^*}$. The chip starts to form during the scratching (after a short phase of elastic deformation of the substrate) and its volume then increases linearly during the scratching [348, 356]. The statistical uncertainty obtained from the set of replicas for the chip volume is fairly constant once the chip has started forming and has a mean value of approximately $\overline{\delta_{V_{\text{chip}}^*}} = 0.08$. The dry set of replicas has an increased statistical uncertainty of the chip volume compared to the lubricated set of replicas, which might be due to a stabilizing effect by the presence of the fluid around the chip.

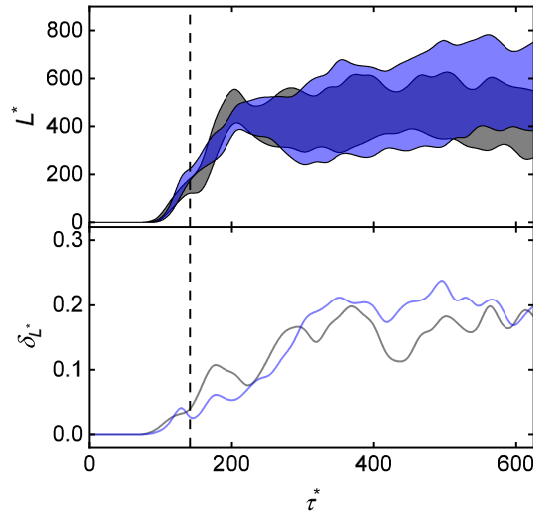


Figure 31: Total dislocation length during the contact process (top) for the lubricated and the dry cases. Results obtained from a set of replicas (eight simulations) for each case. Top: Results for the total dislocation length; the shaded areas are bands of the width of the standard deviation (cf. Eq. (56)) around the arithmetic mean – computed at each time step individually. Bottom: Normalized standard deviation as defined in Eq. (57). Grey indicates the dry simulation set of replicas, blue (with a 50% transparency) the lubricated one. The dashed vertical line indicates the beginning of the scratching phase.

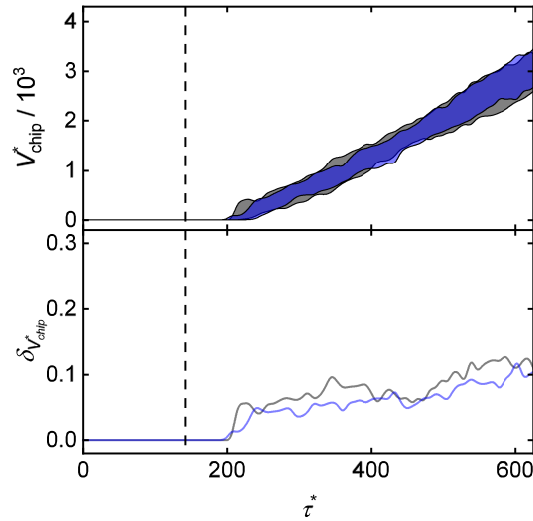


Figure 32: Chip volume as defined in Fig. 27 during the contact process (top) for the lubricated and the dry cases. Results obtained from a set of replicas (eight simulations) for each case. Top: Results for the chip volume; the shaded areas are bands of the width of the standard deviation (cf. Eq. (56)) around the arithmetic mean – computed at each time step individually. Bottom: Normalized standard deviation as defined in Eq. (57). Grey indicates the dry simulation set of replicas, blue (with a 50% transparency) the lubricated one. The dashed vertical line indicates the beginning of the scratching phase.

4.3.2 Thermodynamic Properties

Fig. 33 shows the chip temperature (as defined in Fig. 27) determined in the dry and lubricated set of replicas and the corresponding statistical uncertainty. The chip temperature quickly increases once the first substrate atoms are pushed out of the initially flat substrate surface and subsequently, the chip temperature reaches a plateau on which it fluctuates strongly without a significant change of the average value. The chip temperature increases earlier in the simulations of the lubricated set of replicas than in the dry cases, since the chip starts forming earlier due to adsorbed fluid layers [356]. The statistical uncertainty of the chip temperature jumps to a maximum value when the chip starts to form and falls to a lower level around which it continues to fluctuate. This is due to the fact that the chip itself consists of very few atoms at the beginning of the scratching, which leads to poor statistics within a set of replicas. With ongoing scratching, the chip consists of more and more atoms, which increases the statistical weight and thereby decreases the statistical uncertainty of the chip temperature.

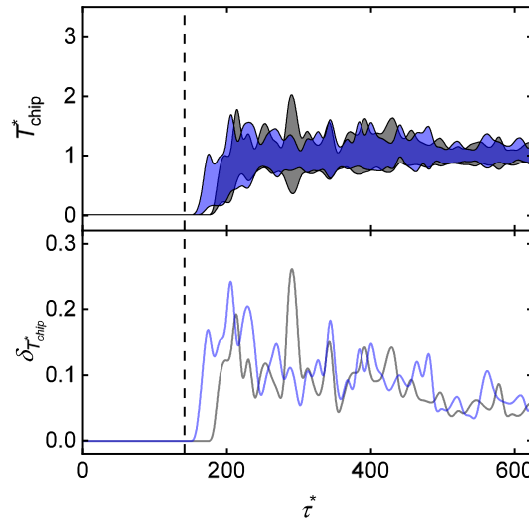


Figure 33: Chip temperature as defined in Fig. 27 during the contact process (top) for the lubricated and the dry cases. Results obtained from a set of replicas (eight simulations) for each case. Top: Results for the chip temperature; the shaded areas are bands of the width of the standard deviation (cf. Eq. (56)) around the arithmetic mean – computed at each time step individually. Bottom: Normalized standard deviation as defined in Eq. (57). Grey indicates the dry simulation set of replicas, blue (with a 50% transparency) the lubricated one. The dashed vertical line indicates the beginning of the scratching phase.

The results for the energy fluxes during the process of the dry and lubricated set of replicas are shown in Fig. 34 - top. The results for the statistical uncertainty shown in the bottom plot of Fig. 34 are those obtained for the work done by the indenter $\delta_{W_I}^*$.

A detailed discussion of this type of thermal balance was given in chapter 3 – in

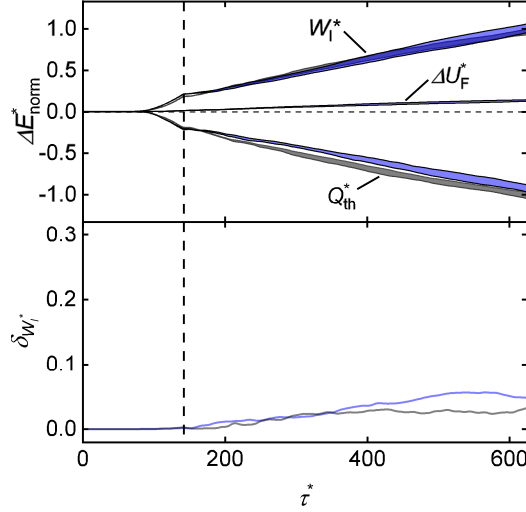


Figure 34: Cumulative energetic observables (work done by the indenter W_I^* , heat removed by the thermostats and change of the internal energy of the substrate Q_{Th}^* , and change of the internal energy of the fluid ΔU_F^*) during the contact process (top) for the lubricated and the dry cases. Results obtained from a set of replicas (eight simulations) for each case. Top: Results for the energetic properties; the shaded areas are bands of the width of the standard deviation (cf. Eq. (56)) around the arithmetic mean – computed at each time step individually. The energetic properties are normalized with respect to the work done by the indenter by the end of the contact process. Bottom: Normalized standard deviation as defined in Eq. (57) – only shown for the work done by the indenter. Grey indicates the dry simulation set of replicas, blue (with a 50% transparency) the lubricated one. The dashed vertical line indicates the beginning of the scratching phase.

particular regarding the influence of the solid-fluid interaction energy. The work done by the indenter increases the internal energy of the substrate and, in the lubricated cases, also that of the fluid. In the simulation, heat is removed by the thermostated layers of the substrate. That heat is plotted here together with the results for the increase of the internal energy of the substrate, as in a larger scenario or a macroscopic system, most of this heat would contribute to increasing the internal energy of the material. The energetic properties W_I^* , ΔU_F^* , and Q_{Th}^* are normalized during the simulation by the total work done by the indenter at the end of the scratching $W_{\text{I,dry}}^*(\tau^* = 625)$ in the dry cases:

$$\Delta E_{\text{norm}}(\tau^*) = \frac{Z(\tau^*)}{W_{\text{I,dry}}^*(\tau^* = 625)} \quad \text{with } Z = W_I^*, \Delta U_F^*, Q_{\text{Th}}^*. \quad (63)$$

This is done for both sets of replicas.

The fluid has a significant cooling capability (cf. chapter 3), i.e. it reduces the internal energy increase in the substrate by up to 15%, which also becomes clear from comparing the dry and the lubricated set of replicas (cf. results for Q_{Th}^* in Fig. 34). The internal energy of the fluid agrees very well among the simulations of the lubricated

set of replicas – throughout the entire contact process. The work done by the indenter and the change of the internal energy of the substrate also agree very well among the simulations from the set of replicas. However, the statistical uncertainty of the work done by the indenter slightly increases during the scratching, cf. Fig. 34 - bottom. Nevertheless, the statistical uncertainty of the work done by the indenter $\delta_{W_I^*}$ is very small compared to the properties discussed above. Especially during the indentation and at the beginning of the scratching, the simulations from a set of replicas agree almost perfectly for both the dry and the lubricated cases. This is due to the fact that the work done by the indenter as well as the entire energy balance is based on the trajectories of many particles in the simulation. The statistical uncertainty of the work done by the indenter only increases up to $\delta_{W_I^*} = 0.05$, cf. Fig. 34 - bottom. The lubricated set of replicas has mostly a higher statistical uncertainty during the scratching than the dry set of replicas, which is likely due to the strong dependency of the trapping and squeeze-out of fluid molecules between the indenter and the substrate on the thermal noise.

The temperature, density, and pressure profile of the fluid in the vicinity of the chip in the lubricated set of replicas and the corresponding statistical uncertainties are shown in Fig. 35. The fluid state point is computed as a function of the distance from the chip surface, as defined in Fig. 27. The temperature gradient is a direct result of the energy dissipation in the direct vicinity of the contact zone; the density gradient is then a consequence of the temperature gradient to maintain local thermodynamic equilibrium (cf. chapter 3). The pressure profile reaches the bulk fluid pressure already very close to the chip surface. All three thermodynamic variables of the fluid (temperature, density, and pressure) agree well among the simulations from the set of replicas. The statistical uncertainties are highest directly at the chip surface, since only few molecules contribute to the averaging. The amount of fluid molecules contributing to the averaging increases with increasing radial distance from the chip surface for geometric reasons, which results in a decaying statistical uncertainty (cf. Fig. 27 - bottom). The statistical uncertainty of the temperature profile of the fluid decays smoothly with increasing distance to the chip surface, starting from approximately $\delta_{T^*} = 0.09$. The statistical uncertainty of the density and pressure profile of the fluid on the other hand reach a mean value of $\overline{\delta_{\rho^*}} = 0.01$ and $\overline{\delta_{p^*}} = 0.03$ already close to the chip surface.

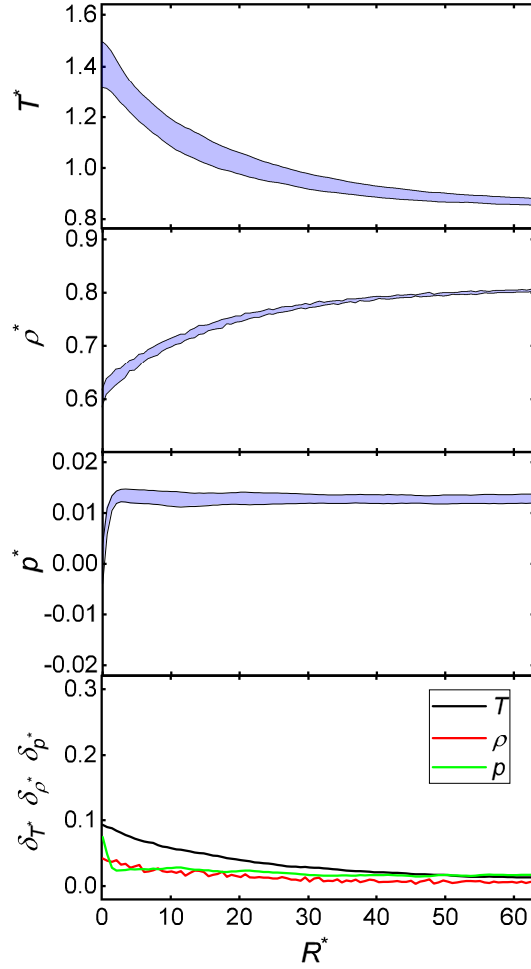


Figure 35: Fluid state point in the surrounding of the formed chip as defined in Fig. 27. Top to bottom shows the fluid temperature, density, and pressure and the corresponding statistical uncertainties, respectively. The fluid state point is computed as a function of the distance from the chip surface R^* . The shaded area indicates the range between the positive and negative standard deviation among a set of replicas at each time step as defined in Eq. (56). The statistical uncertainty δ_{T^*} , δ_{ρ^*} , and δ_{p^*} is computed from Eq. (56) and (57), but using the distance from the chip surface R^* instead of the simulation time τ^* .

Fig. 36 shows the temperature field at three time steps from one dry and one lubricated simulation (one simulation chosen from each set of replicas). High temperatures are mainly observed in the vicinity of the contact zone, the formed chip, and the surrounding fluid in the lubricated cases. Fig. 37 shows the standard deviation of the temperature field at the same three time steps as shown in Fig. 36 among the simulations from the dry (left) and lubricated (right) set of replicas. The temperature in each bin is considered as an observable Z in the sense of Eq. (56) and (57). The temperature of the chip strongly differs among the simulations from a set of replicas – in both the dry and the lubricated cases. This corresponds to the relatively large statistical uncertainty of the dislocation length obtained from a set of replicas. Hence, the differences in the thermal motion among the simulations from a set of replicas yield significant differences in the dislocation nucleation behavior, which results in important differences in the energy dissipation behavior in the substrate in the vicinity of the contact zone. The temperature field in the bulk substrate, on the other hand, agrees well among the simulations of a set of replicas, as the standard deviation of the temperature is low in that region. The same holds for the temperature of the bulk fluid in the lubricated set of replicas.

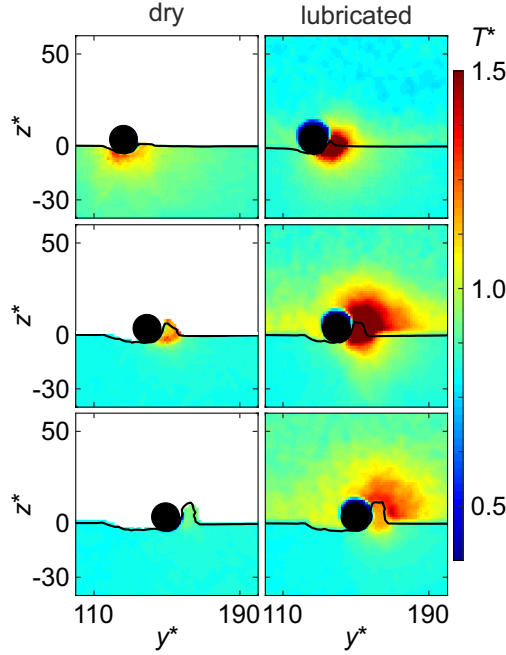


Figure 36: Temperature profiles of one of the simulations at three different time steps of each set of replicas: Dry (left) and lubricated (right).

Table 3 summarizes the normalized mean statistical uncertainties of all investigated observables during the stationary phase of the scratching ($300 < \tau^* < 625$). No systematic difference in the statistical uncertainties of the dry set of replicas and the lubricated set of replicas is observed.

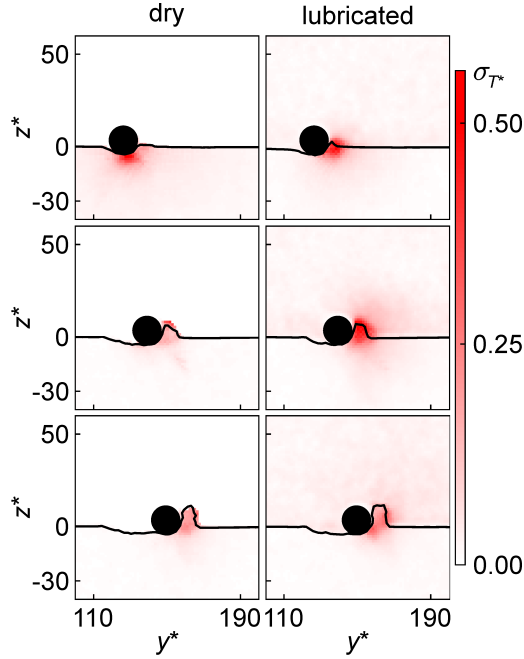


Figure 37: Standard deviation of the temperature profiles among the simulations from the dry (left) and lubricated (right) set of replicas at three different time steps (same as depicted in Fig. 36). Each averaging bin (cf. Fig. 27) is considered as an individual observable Z , i.e. the shown standard deviation $\sigma_T(z, y)$ is computed from the corresponding bin values from the eight simulations among a set of replicas. The standard deviation is therefore computed for each bin individually.

4.4 Conclusions

The statistical uncertainty and thereby the lower limit of the reproducibility of different physical phenomena in nanoscopic friction simulations was quantified in the present work. The standard deviation of a set of replicas, which solely differ in the initial thermal motion is normalized for each observable so that the reliability of the findings derived from different properties can be compared. The statistical uncertainty of all investigated observables was found to converge quickly during the scratching, i.e. differences among the simulations of a set of replicas do not build up with the simulation time.

Large differences among different observables regarding the statistical uncertainties were found. As expected, the more particles contribute to the calculation of a given observable, the lower the statistical uncertainty, e.g. the energetic observables of the overall thermal balance of the system have a very small statistical uncertainty, whereas the local temperature has a very large statistical uncertainty. The local dissipation of energy in the direct vicinity of the contact zone was found to depend strongly on the thermal noise. The energetic observables of the thermal balance of the process as well as the fluid state point around the machined chip exhibit relatively small statistical uncer-

Table 3: Average normalized standard deviation $\overline{\delta_Z}$ during the main phase of the scratching ($300 < \tau^* < 625$). The last three rows indicate the normalized standard deviation of the temperature, density, and pressure profile during the scratching and also averaged between $0 < R^* < 65$.

Z	$\overline{\delta_Z}$	
	dry	lubricated
F_t^*	0.1	0.12
F_n^*	0.06	0.06
μ	0.12	0.11
L^*	0.17	0.2
V_{chip}^*	0.09	0.07
T_{chip}^*	0.07	0.08
ΔE_{norm}^*	0.03	0.04
T_{fluid}^*	-	0.04
ρ_{fluid}^*	-	0.01
p_{fluid}^*	-	0.03

tainties. Interestingly, the normal force is found to have significantly smaller statistical uncertainties than the tangential force.

Particularly high statistical uncertainties were observed for the total dislocation length of crystal defects formed during the indentation and the scratching. Also here, the relatively small number of atoms that constitute these structural defects lead to a large statistical uncertainty. In addition, the chaotic nature of the defect generation and defect reaction processes in the substrate adds to their statistical uncertainty. Finally, in contrast to the thermodynamically locally equilibrated state of the fluid, the crystal defects are in strong thermodynamic non-equilibrium, in the sense that they would never form by themselves in equilibrium; their potential energy strongly exceeds their kinetic energy such that large forces are needed to generate the defects. All these influences explain why dislocations – here quantified by the total length of the formed dislocation lines – have relatively large statistical uncertainties.

No systematic differences regarding the reproducibility were found between the dry and the lubricated contact process. Only for some observables, the lubricated case exhibits a higher statistical uncertainty than the dry case due to the strong dependency of the stamping of fluid molecules into the substrate surface on the thermal noise.

5 MD Simulation Study of Mechanical Effects of Lubrication on a Nanoscale Contact Process

5.1 Introduction

The small zone in which two solid bodies interact directly in a contact process is highly important, e.g. for high precision machining and tribological processes. Unfortunately, the nanoscopic contact zone is practically inaccessible by experiment so that only little is known on the phenomena occurring in that zone. Molecular dynamics simulations are attractive for providing such information.

Dry nanoindentation and dry scratching processes have been studied in detail with different focuses [204, 246]. For example there are studies on the influence of the shape of the tool [7, 132], substrate materials [8, 134, 416], indentation depth [134], cutting direction in relation to the lattice orientation [131], grain boundaries [136], surface roughness [427], alloys [236], coatings [13], and temperature [131].

For an introduction into lubricated contact processes in general, we refer to the literature [178, 277, 375, 397] and chapter 2 of this work. The influence of different variables on lubricated contact processes has been studied on the atomistic scale: The chain length of the lubricant molecules [430, 431], the surface roughness [335], adsorbates [11, 62, 68, 69, 183, 227, 299, 328, 377, 419], and the surface chemistry [85]. There have also been attempts to link atomistic simulation with experiments in that field [75, 145, 279, 330]. In most of these studies, lubrication was only considered by including adsorbed layers of fluid molecules on the substrate in the simulation, while studies in which the contact is truly immersed in a liquid are rare [220, 221, 300]. An interesting finding is the squeeze-out of the lubricant from the contact zone, which has been observed both in simulations in which the lubricant was only a thin adsorbed fluid layer [335, 378], as well as in previous works from our group in which the indenter was

immersed in the lubricant [220, 221]. In some studies, the solids were modeled by only a few atom layers [335, 378]. Cross-interactions resulting from the simultaneous presence of the bulk fluid phase and the bulk substrate have to the best of our knowledge only been investigated by *Rentsch et al.* [300] and in previous (preliminary) studies of our group [220, 221]. Also, the influence of the solid-fluid interaction energy on the lubricated nanoscopic contact process has not yet been investigated systematically.

In the present study, molecular dynamics simulations of a three-stage nanoscopic contact process consisting of indentation, scratching, and retraction of an indenter on a substrate are reported. The contact process is set up by an iron-like solid substrate, a rigid spherical indenter, and a purely dispersively interacting fluid methane modeled by a Lennard-Jones potential. The Lennard-Jones potential [9] is used here to investigate the influence of a simple fluid and due to its generic importance in soft matter physics. Also, liquid methane in contact processes is important for technical applications, e.g. in cryogenic pumps for LNG (liquid natural gas) processes [15, 38, 174, 413] and the next generation of rocket engines [77, 191]. Furthermore the simple Lennard-Jones fluid is a realistic model for liquid nitrogen (N_2) [55], which has become an important cutting fluid for cooling in cryogenic machining processes [50, 422].

Three cases of the contact process are compared: A dry reference case and two lubricated cases in which the indenter is fully immersed in the liquid lubricant. The two cases differ in the solid-fluid interaction energy, which determines the adsorption strength of the lubricant on the indenter and substrate surface. *Becker et al.* [25, 26] investigated how, for Lennard-Jones systems, the solid-fluid interaction energy correlates with the wetting state, e.g. the contact angle formed between a liquid droplet on a solid surface. The solid-fluid interaction energy is not set here such as to match the actual contact angle of liquid methane on pure iron, which is not known for atomistically flat single crystals. Rather, it is chosen to obtain a fully wetted state (strong attraction) and a state with a finite contact angle of about 71° (weak attraction).

The influence of the lubrication on various properties of the contact process is examined in this work: The normal and tangential forces, the coefficient of friction (COF), the chip formation, the roughness of the created groove surface, and the development of dislocations in the substrate. It is found that after a simulation time in which the lubricant is squeezed out, the contact between the indenter and the substrate is essentially dry. Nevertheless, effects of lubrication are present and depend on the solid-fluid interaction energy.

The article is organized in two parts: In the first part, the potential model, simulation method and scenario are introduced and observation variables are defined. In the second part, the results are presented and discussed.

5.2 Methods

5.2.1 Simulation Setup

Fig. 38 shows the simulation setup. It consists of the rigid spherical indenter with a radius of $R = 5$ nm, the solid substrate, and (in two simulations) a lubricant into which the indenter and the substrate are immersed. The size of the substrate block is 52.5 nm, 62.6 nm, 27.2 nm in x -, y - and z -direction, respectively. The substrate surface is in the xy -plane. The indenter conducts three sequential movements: (i) indentation, during which the indenter penetrates into the substrate in $-z$ -direction normal to the surface, (ii) scratching, during which the indenter moves in $+y$ -direction through the substrate forming a groove, and (iii) retraction in $+z$ -direction. The movement of the indenter is prescribed, its velocity is 20 m/s throughout all three phases of its movement (i)-(iii). The indentation depth is 3 nm and kept constant during the scratching phase (ii). The origin of the Cartesian coordinate system is defined as follows: $z = 0$ for the initial unpenetrated surface of the substrate and $x = 0$, $y = 0$ for the initial position of the center of the indenter.

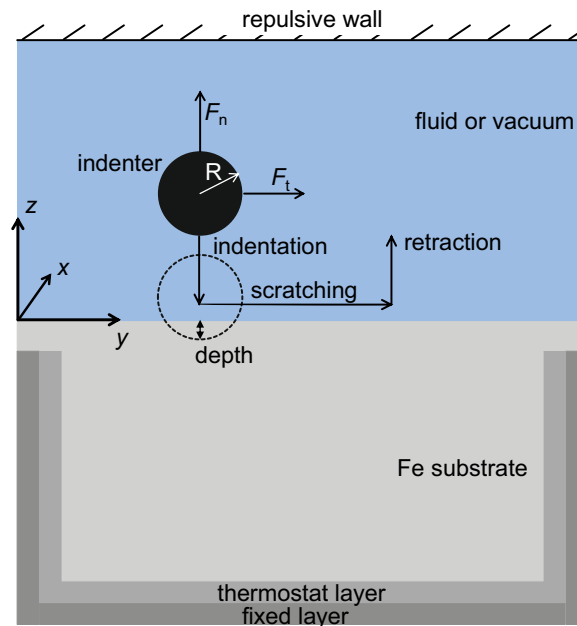


Figure 38: Setup of the simulation box for the indentation, scratching, and retraction of the indenter. The indenter is either in a vacuum environment (dry case) or immersed in fluid (two lubricated cases).

The substrate was fixed in the box by fixing three layers of substrate atoms next to the box margins in x - and y -direction and at the bottom. In x - and y -direction, periodic boundary conditions were applied. The simulation box was confined at the top at $z_{\text{wall}} = 28.2$ nm by a soft repulsive wall. The initial temperature was set to 100 K,

which is above the melting temperature of the lubricant. This temperature was imposed to the entire system during the equilibration. Furthermore, this temperature was imposed to four atom layers between the substrate and the fixed layers, as indicated as *thermostat layer* in Fig. 38. The temperature of this layer was imposed by velocity scaling [29] throughout the indentation and scratching simulation. The latter temperature controlling extracts dissipated energy from the simulation box.

The fixed thermostated layers of the substrate end eight atom layers below the substrate surface. The number of atoms is about 9.2×10^4 for the indenter, 1.5×10^6 for the lubricant, and 7.7×10^6 for the substrate.

5.2.2 Molecular Model

Table 4 shows the symmetric interaction matrix of all three substances (substrate, indenter, and lubricant) and their cross-interactions. The diagonal entries of the matrix indicates the interactions within each substance. The off-diagonal entries indicate unlike interactions.

Table 4: Interaction types employed in the present study.

	substrate	indenter	lubricant
substrate	EAM ^(a)	WCA ^(b)	LJTS-wetting ^(d)
indenter	-	rigid body	LJTS-wetting ^(d)
lubricant	-	-	LJTS-lubricant ^(c)

^(a)embedded atom model [258];

^(b)*Weeks-Chandler-Andersen* potential [408];

^(c)Lennard-Jones truncated and shifted fluid [402];

^(d)wetting behavior of LJTS-fluid [26].

The substrate is a bcc iron single crystal. Initially, its surface is atomically flat. The substrate-substrate interaction is described by the iron embedded atom model (EAM) of *Mendeleev et al.* [258]. The crystal has a (100) surface; the scratching was performed in $[0 \bar{1} \bar{1}]$ direction, which is aligned with the y -axis.

The indenter atoms were placed on a regular diamond lattice, which has a lattice constant of 0.3567 nm. The indenter is a rigid sphere with a radius $R = 5$ nm with fully prescribed velocities to move the indenter in the respective simulation phase (i)-(iii).

The lubricant-lubricant interaction is modeled by single Lennard-Jones truncated and shifted (LJTS) [402] interaction sites, cf. 'LJTS-lubricant' in Table 4. The LJTS po-

tential is defined by [9]

$$u_{\text{LJ}}(r) = 4\varepsilon \left[\left(\frac{\sigma}{r} \right)^{12} - \left(\frac{\sigma}{r} \right)^6 \right] \quad \text{and} \quad (64)$$

$$u_{\text{LJTS}}(r) = \begin{cases} u_{\text{LJ}}(r) - u_{\text{LJ}}(r_c) & r \leq r_c \\ 0 & r > r_c. \end{cases} \quad (65)$$

with u_{LJ} as the full Lennard-Jones potential and ε and σ being the energy and size parameter, respectively. The distance between two particles is denoted by r .

The Lennard-Jones potential is truncated at the cut-off radius $r_c = 2.5\sigma$ and shifted. The parameters for the lubricant-lubricant interaction are those, which have been reported for methane by *Vrabec et al.* [402] ($\varepsilon_{\text{F}} = 0.0151 \text{ eV}$ and $\sigma_{\text{F}} = 3.7241 \text{ \AA}$). The lubricant has an initial density of 0.4389 g/cm^3 .

The off-diagonal entries in Table 4 indicate the cross-interaction between sites of different substances, i.e. indenter-substrate, lubricant-substrate, and indenter-lubricant. The indenter-substrate interaction is purely repulsive. It is modeled by a Lennard-Jones potential [19] that is cut-off at the minimum of the potential [7, 131, 136], i.e. the *Weeks-Chandler-Andersen* potential (WCA) [408].

Lubricant sites interact with substrate and indenter sites in both lubricated scenarios in the same way via the LJTS potential. This is referred to as 'LJTS-wetting' in Table 4 as the lubricant-substrate and lubricant-indenter adsorption energy determines the lubricants wetting state [26]. To study the influence of the wetting state on the indentation and scratching process, two different solid-fluid dispersion energies are considered in the present work: A weak solid-fluid interaction energy of $\varepsilon_{\text{weak-ads.}} = 0.00503 \text{ eV}$ resulting in a contact angle of $\alpha = 71^\circ$ and a stronger solid-fluid interaction energy of $\varepsilon_{\text{strong-ads.}} = 0.01723 \text{ eV}$ resulting in a totally wetting state [26].

The size parameter for the solid-fluid interaction $\sigma_{\text{ads.}}$ is equal to that of the lubricant model. For the sake of brevity the two lubricated cases are denoted as *weak-* and *strong adsorbing case* in the following.

The simulations were performed with the open-source code LAMMPS [288]. The dislocation extraction algorithm (DXA) [371] was used to identify the dislocations, to determine their *Burgers* vectors, and to measure the total length of the dislocation lines L . The free software tools ParaView [165], VisIt [71], and OVITO [370] were employed for visualizing the atomistic configurations.

5.2.3 Definition of Observables

Different observables were extracted from the simulation data and used for comparison of the three studied cases. The tangential force F_t and the normal force F_n on the indenter are evaluated as the sum of all pair interactions acting on the indenter in y - and z -direction. The forces in y -direction are multiplied by -1 for convenience. They stem from the indenter-substrate and the indenter-fluid interactions.

$$F_t = - \sum_{i=1}^m \left(F_{y,i}^{\text{IS}} + F_{y,i}^{\text{IF}} \right) \quad (66)$$

$$F_n = \sum_{i=1}^m \left(F_{z,i}^{\text{IS}} + F_{z,i}^{\text{IF}} \right), \quad (67)$$

where m is the total number of atoms of the indenter. The COF is

$$\mu = F_t / F_n. \quad (68)$$

During the indentation and scratching, lattice defects are generated. They are quantified by the total dislocation length L . The dislocations were identified using DXA [371]. Geometrical properties of the chip and the groove were determined using an alpha shape algorithm [98]. Thereby, the groove and the chip formation are recorded each 30 ps.

The *gap* between the indenter and the substrate is defined as indicated with the blue shaded area in Fig. 39 as the volume between the indenter and the substrate at $z < 0$ and $x > x_P$ (cf. Fig. 39), i.e. ahead of the indenter in the scratching direction. Both, the gap volume and the number of trapped molecules are calculated from this definition. The contact between the indenter and the substrate can either be dry (no fluid molecules in the gap) or lubricated (fluid molecules in the gap). Also the gap and chip volume were determined from the alpha shape algorithm.

We define a *surface enlargement* $A_{\text{real}}/A_{\text{ideal}}$ as the ratio of the real surface of the groove to its ideal surface, cf. Fig. 39. The real surface is again determined using the alpha shape algorithm. The ideal surface is

$$A_{\text{ideal}} = 2\pi R d + 2x_P R \arccos\left(\frac{R-d}{R}\right), \quad (69)$$

where R is the indenter radius, d the indentation depth and x_P the scratching distance, cf. Fig. 39. Eq. (69) assumes a perfect spherical indenter and an ideal groove shape composed of a cylindrical and 2 semi-spherical sections. The surface-site positions are employed to determine A_{real} . The particle size, i.e. size parameter σ , is not considered for A_{real} , which makes the surface enlargement independent from the employed force field and transferable to other problems.

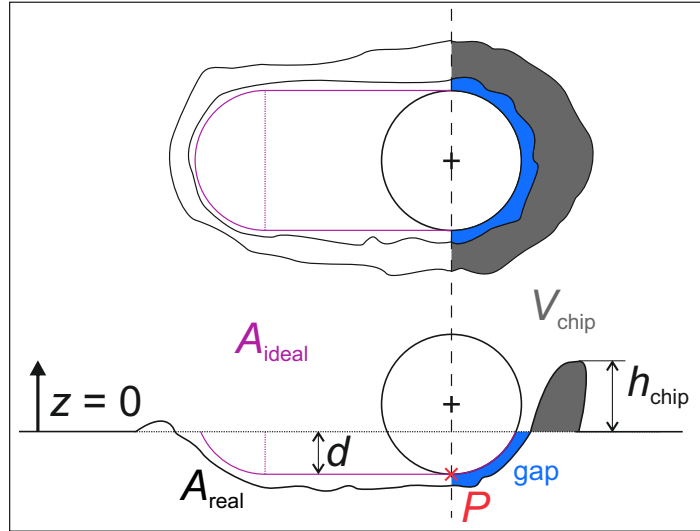


Figure 39: Schematic definition of geometric parameters used for describing the studied process. The chip is characterized by its height and volume, the groove by the ratio of the ideal and the real groove surface. Blue indicates the lubrication gap presumed for the calculation of its volume and the lubricant molecules trapped in it. The point P indicates the bottom point of the indenter.

Also, the chip height h_{chip} and volume V_{chip} were calculated. The chip volume, as indicated in Fig. 39, was calculated from numerical integration of the chip surface area, which is also gained by the alpha shape algorithm. The reference for both is the surface of the unmachined substrate.

5.3 Results and Discussion

5.3.1 Forces

The total normal and total tangential force on the indenter F_n and F_t for all three cases (dry, weak adsorption lubricated, and strong adsorption lubricated) are compared in Fig. 40 a) and b). The average normal and tangential force F_n and F_t are zero in the first part of the indentation and in the last part of the retraction in which the indenter is not in contact with the substrate (0 - 150 ps and 750 - 860 ps). In the lubricated cases, F_n and F_t fluctuate around zero in these phases due to the presence of the lubricant. As shown in the insets in Fig. 40, the fluctuations in the case with strong adsorption are larger than in the case with weak adsorption, due to the weaker interactions.

During the indentation (125 - 300 ps), the normal force F_n rises strongly for all three cases. The rise starts earlier for the case with strong adsorption than for the case with weak adsorption due to the stronger influence of the adsorbed layers. Due to the absence

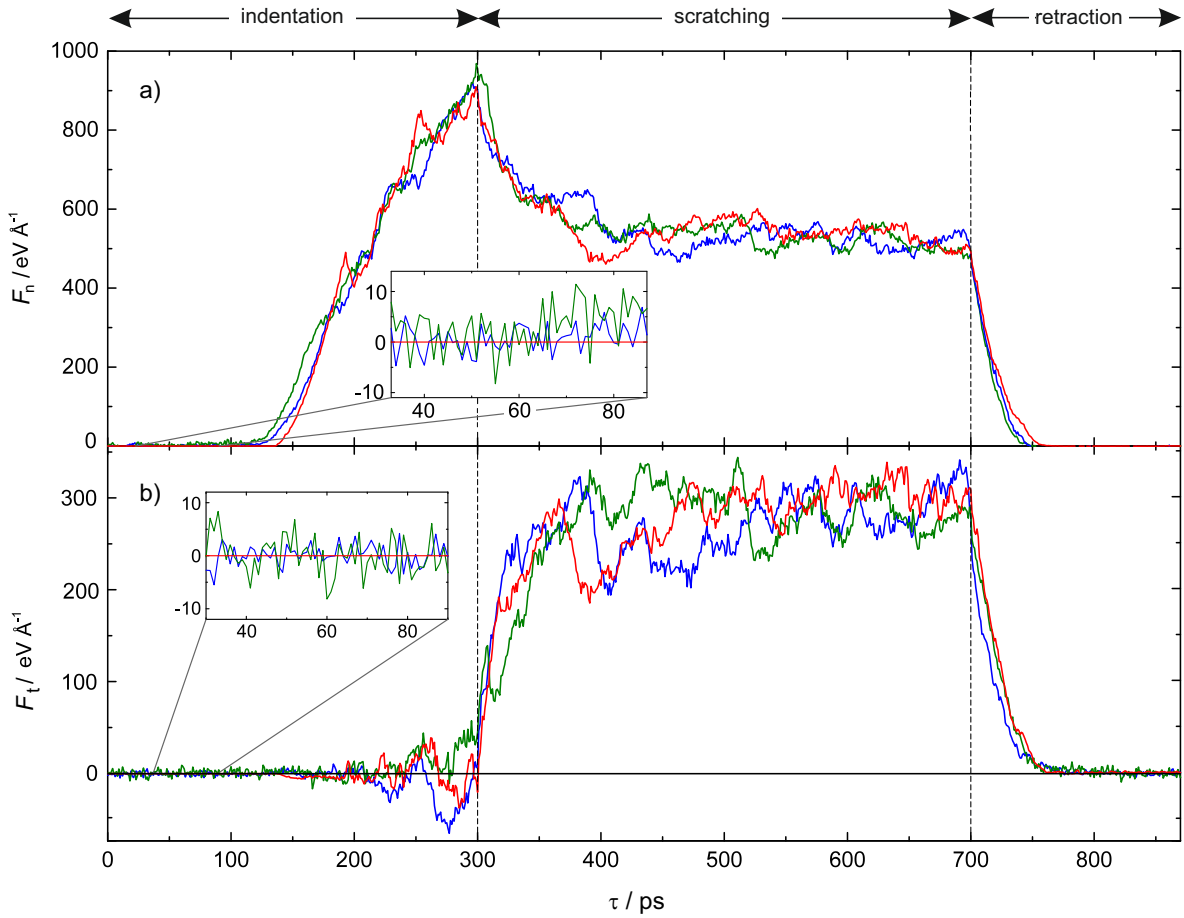


Figure 40: Normal a) and tangential b) forces on the indenter during the entire simulation (indentation, scratching and retraction). The green and blue lines indicate the lubricated simulations, with strong and weak adsorption, respectively. The red line indicates the dry simulation.

of such layers, the rise of F_n starts later in the case without lubricant. There are two important dips in the curve for F_n for the case without lubricant which are due to the start of dislocation movements. This is a common observation, see e.g. Ref. [134]. Smaller dips are also present in the lubricated case with weak adsorption and, to a still lesser extent, in the case with strong adsorption. Hence, the hypothesis can be stated that the lubrication dampens the effects which lead to the start of the movement of dislocations.

Fig. 40 b) shows the results for the tangential force F_t . As long as the indenter is not in contact with the substrate, the observations are essentially the same as for F_n : There are small fluctuations around zero for the two lubricated cases due to the presence of the fluid. Once the indenter gets into contact with the substrate, the fluctuations increase and features of oscillations begin to develop for all three cases. These oscillations are clearly discernible for the dry case and the lubricated case with weak interaction, whereas they are damped for the case with strong interactions.

At the end of the indentation (300 ps), the values for F_n are similar for all three cases. For F_t , they are essentially zero, not counting the deviation for the strongly adsorbing case, which is a result of an asymmetric squeeze-out of fluid, as discussed below in more detail.

After the start of the lateral movement (300 - 400 ps), the tangential force F_t increases rapidly as the chip starts to form, while the normal force F_n decreases as the contact area between the indenter and the substrate decreases. This decrease of contact area is due to the kinematics of the process, which forms a gap between the backside of the indenter and the substrate at the beginning of the lateral motion. This gap then quickly fills with fluid molecules in the lubricated cases as can be seen in Fig. 46. The increase of F_t is slower for the lubricated case with strong adsorption than for the other cases. This is a consequence of the fluid molecules that are trapped in the gap between the indenter and the substrate and are slowly squeezed out as described in more detail below.

After about 400 ps, a steady state with strong fluctuations is reached, for both F_t and F_n , in all three studied cases. The differences between these cases are within the band of the strong fluctuations. Again, oscillatory components are observed in the fluctuating signals for F_t . During the retraction phase, which starts at 700 ps, both F_n and F_t decrease to zero and there is no significant difference between the three cases.

The coefficient of friction $\mu = F_t/F_n$ in the scratching phase is shown in Fig. 41 - top for the three studied cases. Fig. 41 - bottom shows the difference $\Delta\mu$ between the two lubricated cases and the dry case, which is considered as the reference. The results for the three studied cases agree within the band of the strong fluctuations. A steady state is established after 100 ps for which the coefficient of friction is about 0.52 ± 0.1 .

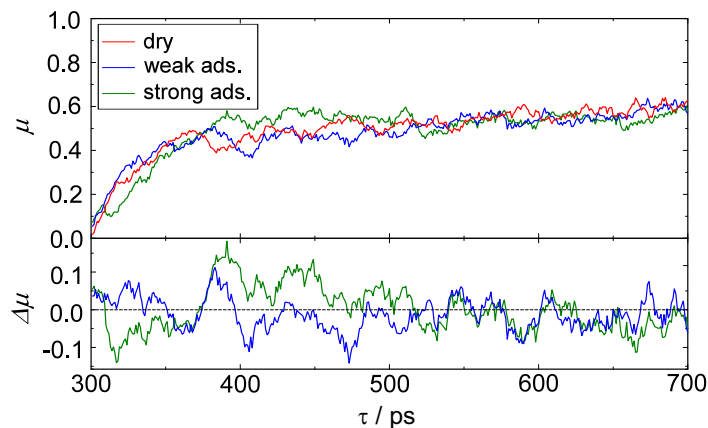


Figure 41: Coefficient of friction μ during the scratching phase for the three studied cases (red: Dry, blue: Weak adsorption, and green: Strong adsorption). In the lower part of the diagram the difference between the two lubricated cases and the dry case is plotted.

The forces on the indenter result from contributions of the indenter-fluid and the

indenter-substrate interactions, cf. Eq. (66) and (67). Fig. 42 shows these contributions to the normal force on the indenter F_n . In the early phase of the indentation, the contribution of the indenter-fluid interaction dominates. Subsequently, its contribution to F_n declines and becomes minor in the stationary phase of the scratching phase. As expected, the contributions of the indenter-fluid interactions are more important for the case with strong adsorption than for the case with weak adsorption. Also the decline is slower for the case with strong adsorption, which is related to the slower squeeze-out of the liquid from the gap between the indenter and the substrate for that case. The corresponding results for the tangential force F_t are shown in Fig. 43. They reveal that F_t is dominated by the indenter-substrate interactions.

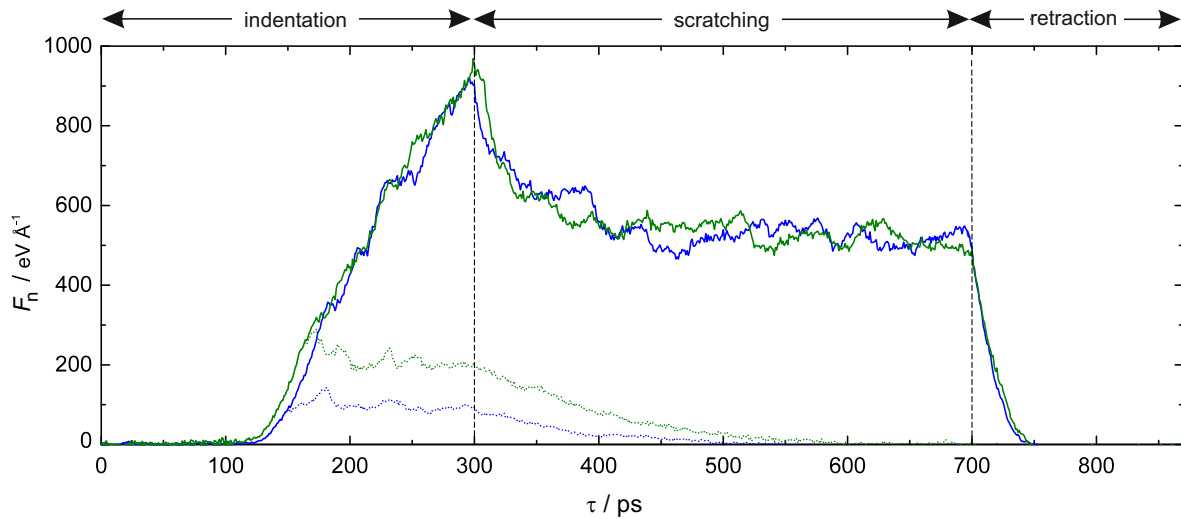


Figure 42: Normal forces between the indenter and the fluid (dotted line) and the total forces on the indenter (solid line) during the simulation. The green and blue lines indicate the lubricated simulations, with strong and weak adsorption, respectively.

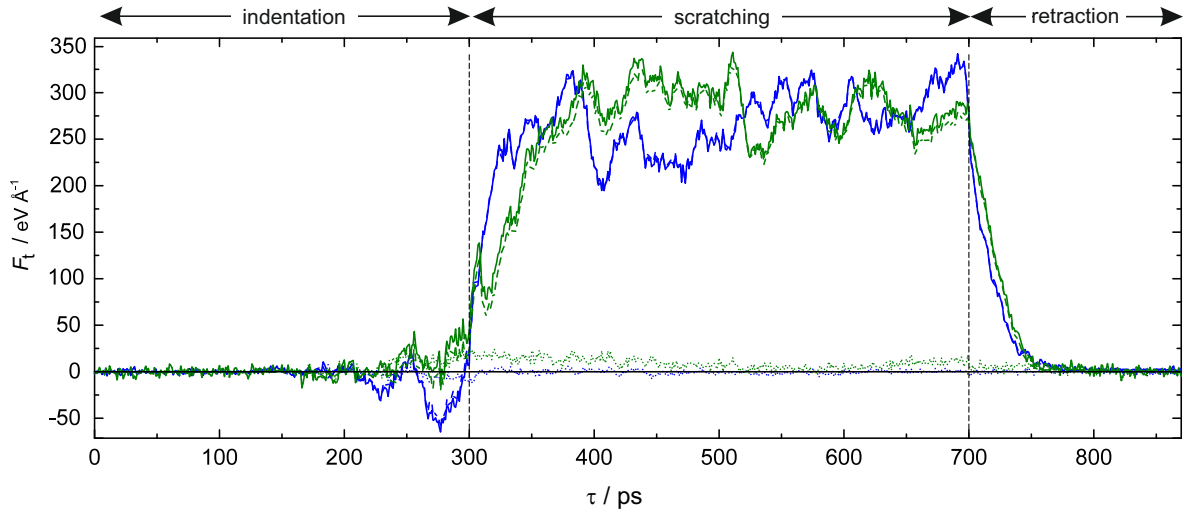


Figure 43: Tangential forces between the indenter and the fluid (dotted line), between the indenter and the substrate (dashed line – very close to solid line), and the total forces on the indenter (solid line) during the simulation. The green and blue lines indicate the lubricated simulations, with strong and weak adsorption, respectively.

5.3.2 Dislocations

During the indentation and scratching, dislocations are formed in the substrate. Fig. 44 shows the evolution of the dislocation network at different stages of the scratching process for the three cases. During the indentation and scratching process, material is removed from the groove. This requires strong plastic deformation that shows up in the form of dislocations. The type of dislocations is identified by their *Burgers* vector b . For bcc iron, there are two important types of dislocations, those with $b = 1/2\langle 111 \rangle$ and those with $b = \langle 100 \rangle$, see Fig. 44. The first one is favored and dominates since it requires less energy to nucleate and move.

The formation of dislocations is characterized by the formation of long semi-loops of $1/2\langle 111 \rangle$ dislocations; these may even detach from the surface and move into the inner of the crystal as prismatic dislocation loops. During the scratching, the dislocation network changes by addition of newly formed dislocations as well as by the reaction of existing dislocations. The most prominent example of such a reaction is the merging of two $1/2\langle 111 \rangle$ dislocations to form a $b = \langle 100 \rangle$ dislocation. Note that the form of individual dislocations is subject to a high amount of stochastic randomness, caused by thermal fluctuations in the generation process (cf. discussion in chapter 4). In view of these fluctuations, the dislocation patterns resulting under the influence of lubrication does not strongly differ from that in the dry contact. Thus, for instance, in all cases after removing the indenter, the dominance of $b = 1/2\langle 111 \rangle$ dislocations is reduced and $b = \langle 100 \rangle$ dislocations become more dominant. This is caused by the high mobility of

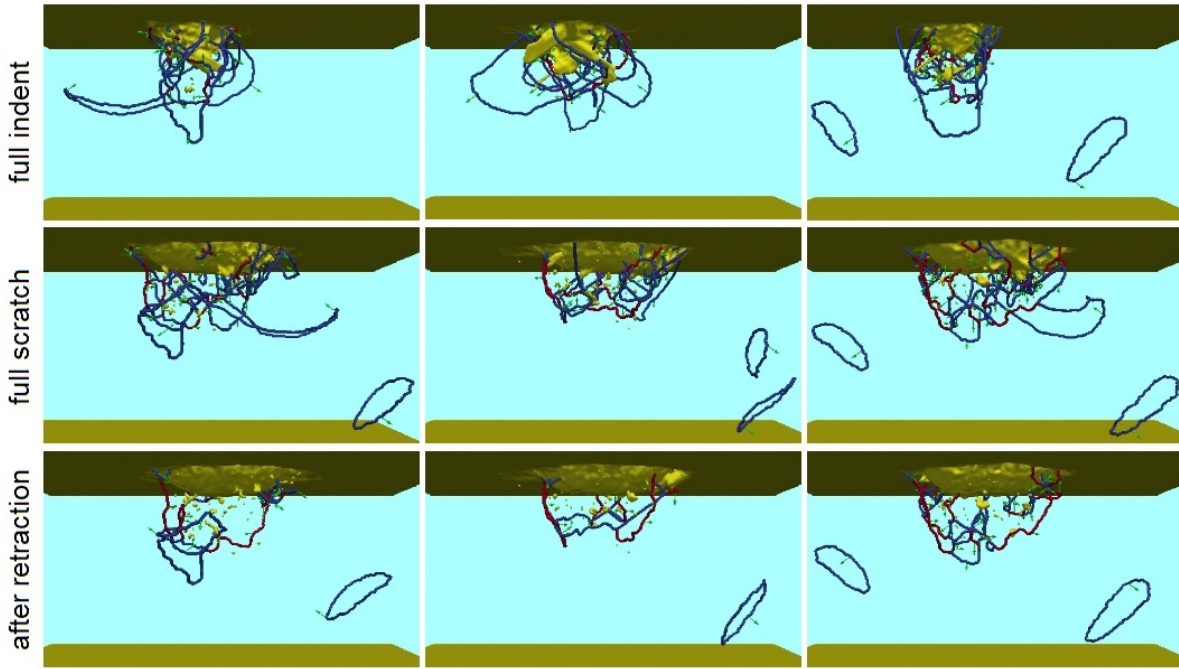


Figure 44: Evolution of the dislocation network created in the penetrated substrate after full indentation (top row), at the end of the scratching (center row), and after the retraction of the indenter (bottom row). The case with the dry contact is shown in the left column; that of weak adsorption in the middle; and the case of strong adsorption is shown in the right column. Yellow indicates the deformed surface and point defects. Dislocation lines with *Burgers* vector $1/2 \langle 111 \rangle$ are shown in blue, those with $\langle 100 \rangle$ in red. Green arrows indicate the direction of the *Burgers* vector.

$b = 1/2 \langle 111 \rangle$ dislocations that retract back to the surface during the removal of the indenter.

The processes of defect formation in the crystal can be quantitatively analyzed by the total dislocation length L , see Fig. 45, during the entire process of indentation, scratching, and retraction. Lubrication affects the first nucleation of dislocation in the indentation stage, where plasticity is generated earlier in the two lubricated cases than in the dry case. This appears evident from the fact that the lubricant can transfer forces from the indenter to the substrate already before the two solids are in direct contact. At the end of the indentation (300 ps), the total dislocation length is somewhat higher for the case with strong adsorption than in the other two cases. This can be understood as an effect of the adsorbed layers leading to an effective increase of the size of the indenter and thereby to more plastic deformation. During the scratching, the total dislocation length increases in the dry case and in the case of the strongly adsorbing lubricant, while almost no increment for the case of weak adsorption lubrication is found. After the retraction, the total dislocation length decreases since some dislocations move to the surface and are annihilated there. During the scratching, the effect of the lubricant

is hardly visible behind the stochastic fluctuations of the dislocation generation and reaction processes. The main effect of the lubrication on the dislocation formation in the material lies in the earlier generation process during the indentation.

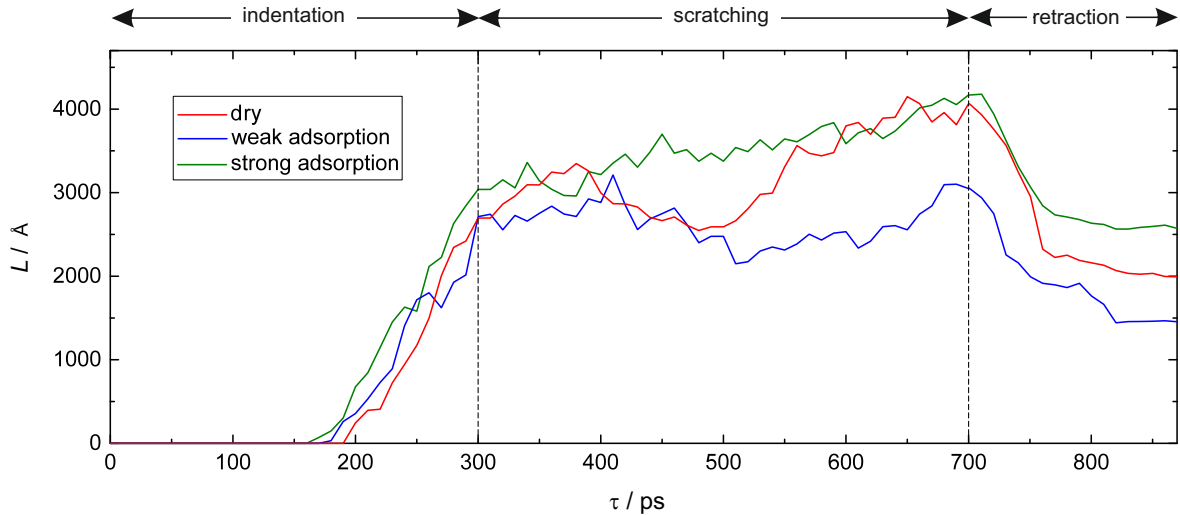


Figure 45: Total dislocation length in the substrate during the simulation (indentation, scratching, and retraction). The green and blue lines indicate the lubricated simulations, with strong and weak adsorption, respectively. The red line indicates the dry simulation.

5.3.3 Groove, Chip, and Contact Zone

Fig. 46 shows screenshots of the contact zone of all three simulations (left: Dry, center: Weak adsorption, right: Strong adsorption) at different simulation times. All indenter atoms are visible and opaque. Lubricant molecules are visible if they are underneath the unpenetrated substrate surface $z = 0$ and substrate atoms are visible if they are above the unpenetrated substrate $z = 0$. The differences between the three simulations are small but visible. The chip formation is similar in all cases until the end of the scratching (700 ps). At this time, the tip of the chip leans against the indenter in the dry case, while in the lubricated cases, the tip of the chip is straight up. This is due to lubricant molecules between the tip of the chip and the indenter, especially in the strongly adsorbed case (not shown for clarity). The lubrication itself, i.e. the number of trapped molecules between the indenter and the substrate, differs between the strong and weak adsorption case. More molecules remain trapped in the strong adsorption case, cf. 300 ps, 390 ps, and 480 ps. But both cases have a dry contact zone (as defined in Fig. 38) after that, i.e. all lubricant molecules are squeezed out of the gap.

Fig. 47 shows the shape of the groove and chip formed. Most notable is the fact that dry and lubricated contacts lead to the same form of groove and chip, although slight

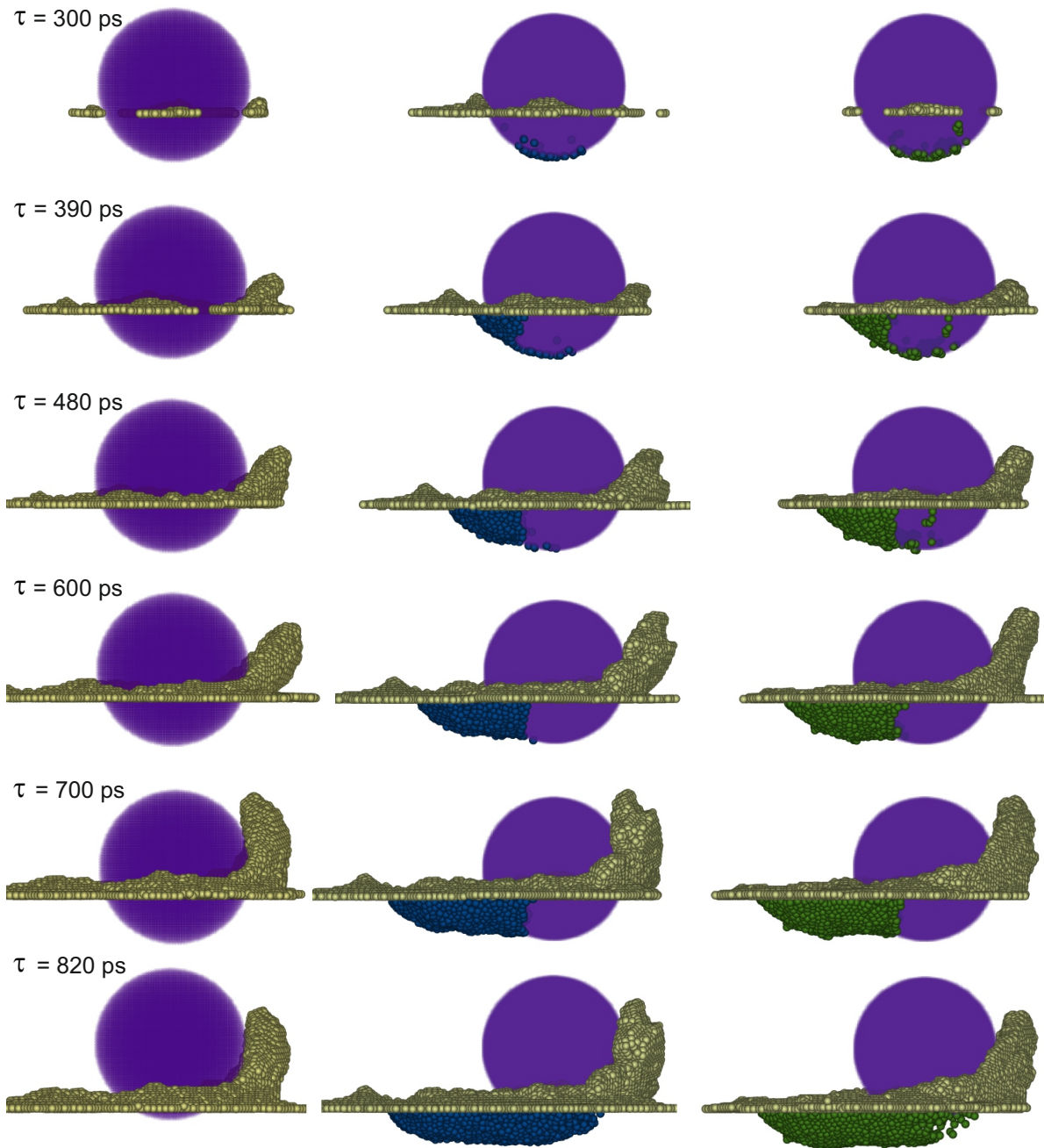


Figure 46: Screenshots of the contact zone for all three simulations (left: Dry; middle: Weak adsorption; right: Strong adsorption). Each row corresponds to the same simulation time. Only the substrate atoms with $z > 0$ and the lubricant molecules with $z < 0$ are visible for clarity. Yellow atoms indicate the substrate, blue and green the lubricant in the weak and strong adsorption case respectively. The spherical indenter is purple.

differences are present. The chip in the weak adsorption case has a somewhat broader chip in y -direction than the other two cases.

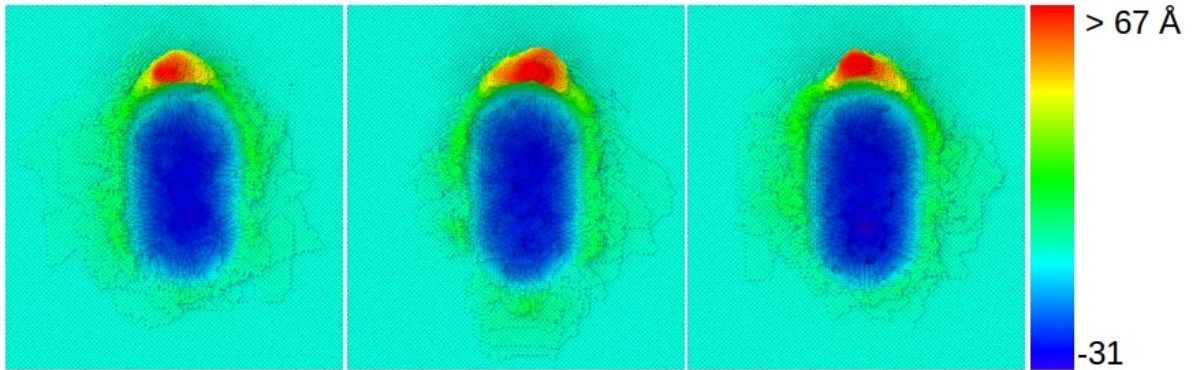


Figure 47: Top view of the chip and groove formed after the retraction of the indenter for the case of a dry contact (left), weak adsorption (middle), and strong adsorption (right). The color indicates the distance to the reference plane with coordinate $z = 0$. The absolute values are given in the legend on the right hand side.

The chip volume and maximum chip height is plotted in Fig. 48 a) and b), respectively. The chip volume increases in all three simulations steadily after the beginning of the lateral movement of the indenter. The increase continues at the beginning of the retraction (700 - 750 ps), because the substrate relaxes elastically and thereby lifts the chip. While the three cases hardly differ in the chip volume at the beginning of the scratching (300 - 500 ps), they differ at the end of the scratching (500 - 700 ps). The chip volume of the strong and weak adsorption case is increased about 10% and 20%, respectively, compared to the dry case. This is mainly based on a mechanical coupling of the indenter and the chip, not only straight in front of the indenter where the chip is highest, but also sideways in x -direction of the spherical indenter (cf. Fig. 47). In this flank of the groove, the adsorbed lubricant molecules widen the indenter from the substrate point of view. The fact that the weakly adsorbed fluid leads to an even stronger increasing chip volume than the strongly adsorbed fluid is due to a better lateral mobility of lubricant molecules along the indenter and substrate surface [386, 423]. This leads to a better inflow to the newly formed chip-indenter-fluid contact.

The same argument holds for the maximum chip height h_{chip} . It behaves similarly in between the three simulations until approximately 500 ps of the simulation time. Subsequently, the maximum chip height for the two lubricated cases lies about 10% above the corresponding dry simulation, although the two lubricated scenarios differ less in the chip height than the chip volume. The center of the chip is therefore less affected by the presence of a lubricant than the flanks of the chip and the flanks of the groove, cf. Fig. 47. The chip is mainly formed in the front of the groove, due to the scratch direction in $[0 \bar{1} \bar{1}]$ and slip along $[1 \bar{1} \bar{1}]$. This is a consequence of the slip

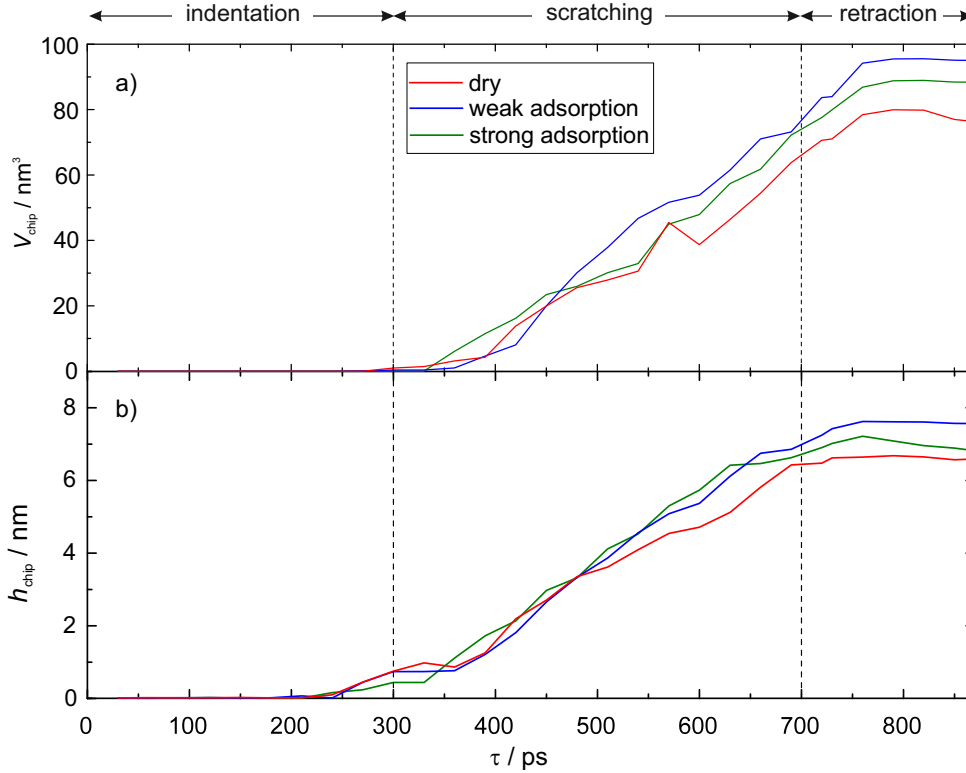


Figure 48: Characterization of the chip evolution during the simulation: a) chip volume; and b) maximum chip height.

systems activated in the single crystal: In bcc crystals, slip occurs on the $\{110\}$ – and to a lesser degree also $\{112\}$ planes – in the close-packed $\langle 111 \rangle$ directions. Sideways slip is also generated, but it is not so prominent. This feature is typical for spherical indenters, but may change for other indenter shapes, see Ref. [7].

Fig. 49 shows the surface enlargement $A_{\text{real}}/A_{\text{ideal}}$ as defined in section 5.2.3. A constant $A_{\text{real}}/A_{\text{ideal}}(\tau)$ implies a linearly increasing surface area, cf. Eq. (69). The surface enlargement differs strongly from unity at the beginning (300 - 400 ps) of the scratching and converges to a constant value slightly above unity. This is not only a result of the comparison of an atomically resolved surface with an ideal one, but also due to the definition of A_{ideal} , which does not take the atom's size into account, e.g. σ_{IS} . The decay of $A_{\text{real}}/A_{\text{ideal}}$ at the beginning of the scratching (300 - 500 ps) is a result of the elastic relaxation of the spherical part of the groove that the indenter leaves behind. The slope of $A_{\text{real}}/A_{\text{ideal}}(\tau)$ is similar in all three simulations, although throughout the scratching process, the strong adsorption case has a higher surface enlargement than the dry case. The weak adsorption case does not differ significantly from the dry case. The surface enlargement lies in the strong adsorption case on average 0.08 above the dry one. This is due to a stamping of single or clustered lubricant molecules into the substrate during the squeeze-out of lubricant molecules out of the contact zone underneath and aside the indenter. This mechanism was already described by *Bhushan et al.* [37]. At the

solid-liquid interaction energies investigated in this study, the lubricant molecules are individually stamped into the substrate. No covering film is formed. This is shown in Fig. 50 comparing the dry case with the strong adsorption lubricated case. Note how the inclusion of a lubricant renders the machined surface rougher (comparing Fig. 50 a) and b)). The incorporation of lubricant atoms within the outermost atom layer of the substrate, Fig. 50 c) and d), represents the first step of forming a chemically transformed layer, which is denoted as tribofilm in the case that chemically reactive species are employed [364].

The development of the indenter-substrate gap volume (as defined in Fig. 39) is shown in Fig. 51 a). The gap volume is only evaluated for those time steps, when the bottom of the indenter has reached $z = 0$. Since the gap volume is only calculated underneath the unpenetrated surface $z = 0$, the gap volume increases linearly during the indentation. The gap volume remains fairly constant during the scratching. At the beginning of the retraction (700 - 750 ps), the gap volume stays further constant, because the substrate follows the retraction movement of the indenter due to the substrate's elastic relaxation. After the substrate reaches its final plastically deformed groove, the gap volume increases again linearly. The gap volume at $z < 0$ is hardly affected by the presence of a lubricant. However, the difference plot to the dry case in Fig. 51 b) reveals that the strongly adsorbed fluid leads to a slightly increased gap volume, which is due to individually stamped molecules into the substrate, cf. Fig. 50.

The number of trapped lubricant molecules in the gap between the indenter and the substrate (as defined in Fig. 39) during the contact process is shown in Fig. 51 c). Also this evaluation is only applied for those time steps, after the bottom edge of the indenter reaches the ground level of the substrate. The amount of trapped lubricant molecules increases in the strong adsorption case during the indentation, as the lubrication gap

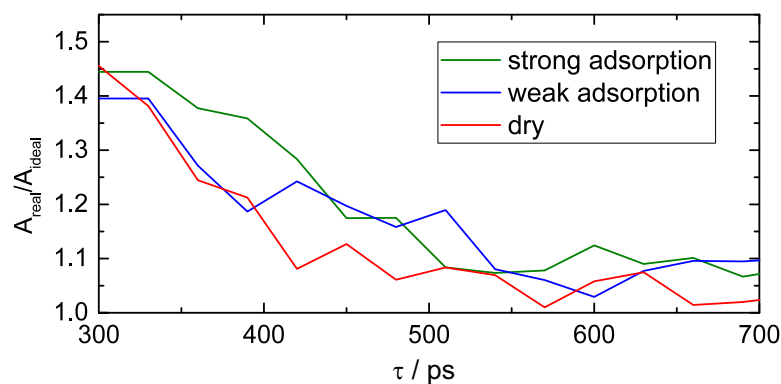


Figure 49: Surface enlargement of the groove area, defined as the ratio of the real surface area A_{real} of the groove in the simulation as sum of finite surface elements and the ideal area A_{ideal} , which corresponds to the groove of a perfect sphere scratching in a substrate.

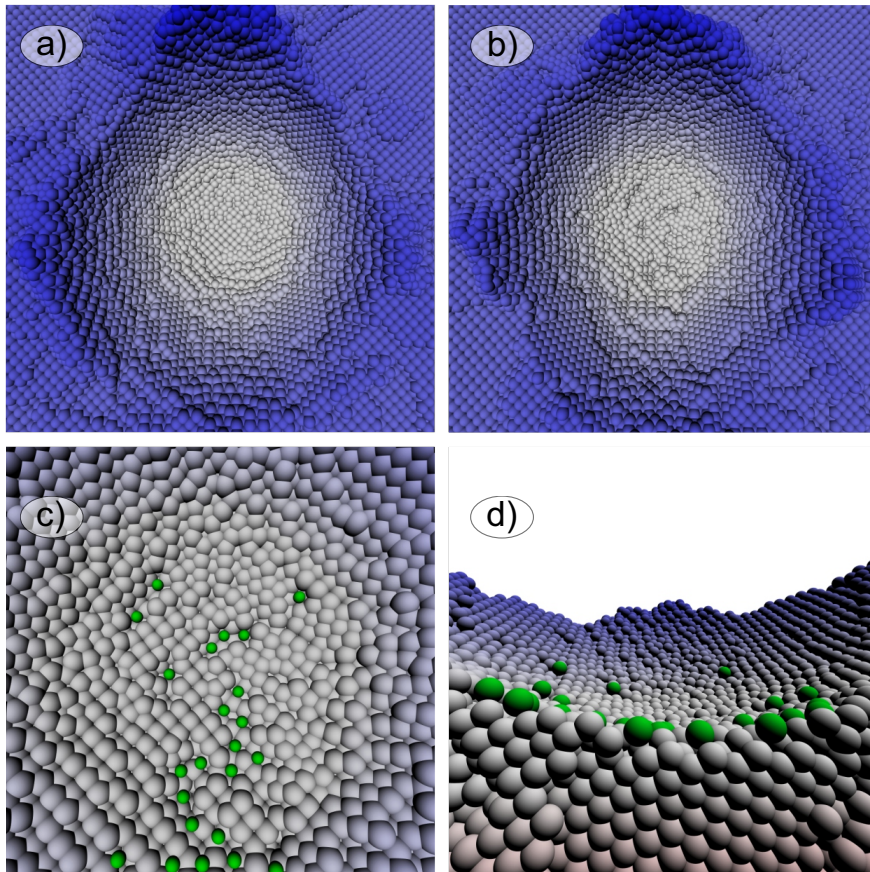


Figure 50: Screenshots of the contact zone at a simulation time 360 ps from the dry case a) and the lubricated case with the strong adsorption energy b), c), and d). The indenter is in all pictures faded out; as is the lubricant in b). Grey and blue atoms indicate the substrate with the z -position as color code: Grey at the bottom of the groove and blue at the top of the chip. a) and b) show the top view in negative z -direction. c) shows a closer zoom to the bottom of the groove from b). d) shows a cut view through a yz -plane at the bottom of the groove in positive x -direction. In both c) and d), the lubricant molecules are faded in and colored green.

is formed. On the contrary, the number of lubricant molecules in the weak adsorption case monotonously decreases already during the formation of the lubrication gap (180 - 300 ps).

The stronger adsorbed fluid remains longer attached to the indenter and the substrate surface, resulting in a slower squeeze-out. The lubricant molecules are squeezed out completely between 450 to 550 ps during the scratching, which is in perfect agreement with the indenter-fluid force converging to zero at this simulation time (cf. Fig. 43). The weakly adsorbed fluid, on the other side, is already partially squeezed out during the indentation and completely pushed out of the gap until circa 520 ps, which is also in very good agreement with the indenter-fluid force, cf. Fig. 43. The number of trapped lubricant molecules is in the strong adsorption case on average about four times the

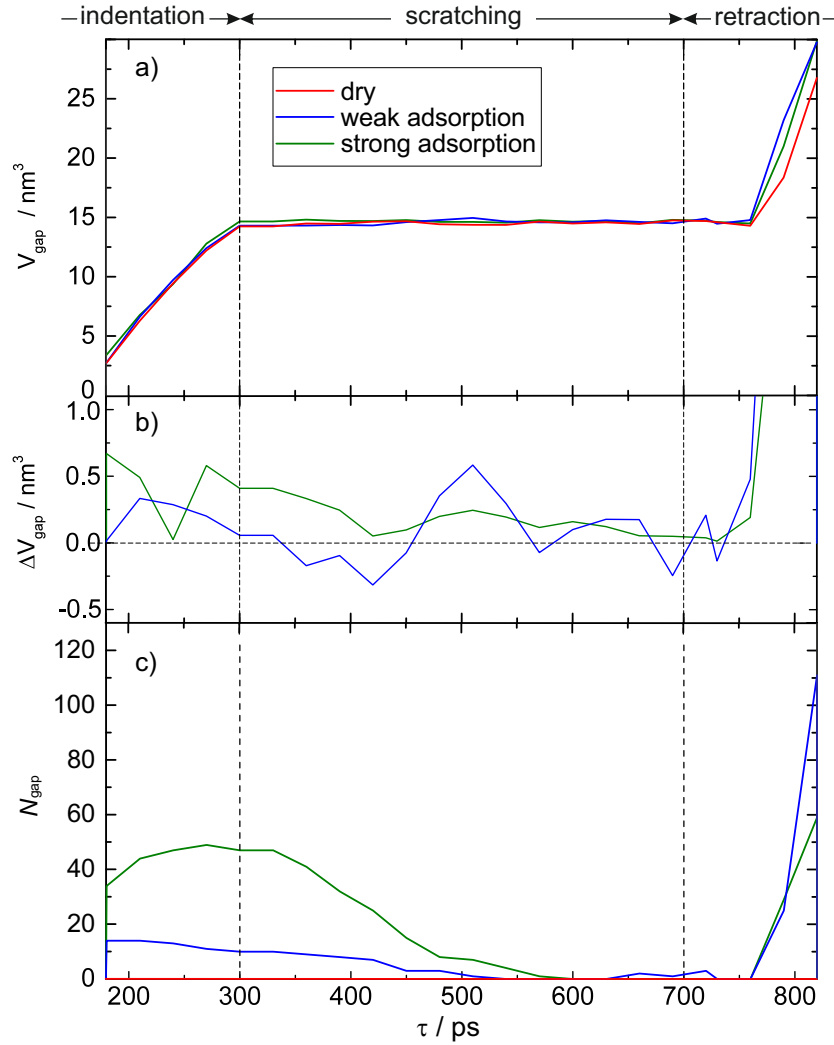


Figure 51: a) shows the gap volume between the indenter and the substrate. b) shows the difference in the gap volume between the dry and the two lubricated cases. c) shows the number of trapped lubricant molecules in the gap (as defined in Fig. 39).

amount in the weak adsorption case. The squeeze-out duration time is, on the other side, hardly affected by the adsorption interaction energy.

The molecule size σ_F has the same order of magnitude as the size parameter of the indenter-substrate interaction. Thus, the fluid molecules fit in the gap between the substrate and the indenter. Vice versa, lubricant molecules only form a mono-layer in the gap at the beginning of the contact process before they are squeezed out (cf. Fig. 46).

Furthermore, an interesting mechanism can be observed during the retraction of the indenter (750 - 820 ps), when the amount of lubricant molecules in the gap increases, since the gap itself increases. Liquid fills this increasing gap. As already mentioned above, the lateral mobility of adsorbed molecules on a wall increases with decreasing

adsorption interaction energy [386, 423]. Therefore, lubricant molecules fill the gap faster during the retraction in the weak adsorption case, which is also clearly visible in the last screenshot in Fig. 46.

5.4 Conclusions

Nanoindentation and nanoscratching in an iron (100) surface of a dry and lubricated contact process were studied by molecular dynamics simulation. The lubricant is modeled as a Lennard-Jones fluid. Two lubricated scenarios, differing in the solid-fluid interaction energy, are compared with a dry one. While the lubricated case with a relatively weak adsorption energy behaves rather similar to the dry case, considerable differences are found between the contact process with a stronger adsorbing fluid compared to the dry case.

The lubricant is found to reduce fluctuations in the time evolution of most examined observables considerably, such as the friction forces, the total dislocation length, and the chip formation – especially in the case of a strong adsorption energy. This reduction increases significantly with the adsorption energy. These effects are likely due to a mechanical coupling between the indenter and the substrate atoms via the lubricant, which balance force peaks.

The normal force acting on the indenter during machining is only mildly affected by the presence and nature of the lubricant, while the tangential force is subject to strong fluctuations during the machining process. A closer look reveals that while the lubricant is still embedded between the indenter and the substrate, the strongly adsorbing lubricant features an enhanced tangential force. This is attributed to an effective enlargement of the indenter size by the lubricant.

The lubricant forms a monolayer in the gap in both investigated lubricated cases, but is squeezed-out of the contact zone quickly during the scratching. The amount of trapped lubricant molecules in the gap correlates with the total normal force between the indenter and the lubricant and increases significantly with the adsorption energy of lubricant molecules. The squeeze-out time is hardly affected and is around 200 ps of the scratching time. Afterwards, the contact zone is dry, i.e. no lubricant molecules are left in the gap.

The chip formation is only slightly influenced by the presence of a lubricant. The chip height is less affected by the presence of a lubricant than its width. The chip volume between the strong and weak adsorption cases and the dry case increases by 10% and 20%, respectively. This is probably a result of the inflow of lubricant molecules in the

constantly newly formed gap between the indenter and the substrate, where material is moved. These lubricant molecules act like a broadening of the indenter – during the indentation in the entire contact zone and during the scratching mainly sideways of the indenter – and thereby lead to increased material removal. The decrease of lateral mobility with an increasing solid-fluid interaction energy becomes also very clear by the fluid inflow during the retraction of the indenter out of the substrate contact.

An increasing adsorption energy of a lubricant has two opposing effects: (1) the lubricant molecules stick stronger in the gap, since more energy is needed to break the adsorption bonds and squeeze them out of the gap between the indenter and the substrate. (2) A weaker adsorption energy on the other hand favors the lateral mobility of lubricant molecules along the indenter and substrate surface, which results in a better inflow to the contact zone during the retraction.

Future work will aim at modeling more complex lubricant fluids, such as oils, and include a study of the influence of the fluid environment on the energy balance in the machining zone. In addition, the question to what extent the roughness of substrate and tool surfaces might enable a continuous inclusion of the lubricant within the indenter-substrate gap will be explored.

6 Molecular Dynamics Simulation of the Stribeck Curve: Boundary Lubrication, Mixed Lubrication, and Hydrodynamic Lubrication on the Atomistic Level

6.1 Introduction

Understanding the fundamental processes of lubrication is critical for many technical applications. In many technical applications, e.g. machining in production processes, gears, and bearings, extreme conditions (pressure and temperature) prevail in the contact. Moreover, the actual contact process and dominating mechanisms occur on very small scales. Therefore, experimental in situ methods for investigating the mechanisms in tribocontacts – in particular on the atomistic level – are presently not feasible. Molecular dynamics (MD) simulations [9, 301] using classical force fields [102, 275, 353] are an attractive tool for studying the fundamental mechanisms in tribological processes, e.g. the mechanisms of the different lubrication regimes of the Stribeck curve. MD provides a great level of insights for a large number of observables. Also, the strong physical basis of the simulation method requires no parametrization on experimental data of the actually studied process. However, the accuracy of the results strongly depends on the correctness of the applied force field describing the molecular interactions and the simulation setup.

Lubrication regimes are usually classified using the Stribeck curve [244]. Thereby, depending on the gap height between two solid bodies, different lubrication conditions and mechanisms dominate the contact process [245, 341, 424] (see also section 2.1.3). Fig. 52 schematically shows the lubrication regimes applicable when the two solid bodies are in close proximity. In the hydrodynamic lubrication (HL) regime, the two solid

bodies are separated by the fluid in a way that a bulk fluid phase exists in the gap. Upon relative motion between the solid bodies, a shear flow is established in the fluid. However, the fluid pressure in the gap may be high enough such that elastic deformation occurs in the solid bodies. Viscous friction dominates the system in the HL regime. In the mixed lubrication (ML) regime, the two solid bodies are in close proximity and the gap height has approximately the thickness of the adsorption layers of the fluid on the solid surfaces. Both, elastic and plastic deformation may occur. The friction is influenced by a large number of mechanisms in the ML regime, e.g. the distortion of the adsorbed fluid layer, viscous friction, and plastic deformation. In the boundary lubrication (BL) regime, the solid bodies are in contact and plastic deformation is caused by the asperity penetrating the substrate. The friction is dominated by the elastic and plastic deformation. For studying the interrelations between bulk phase properties and mechanisms in the direct vicinity of the contact zone, e.g. the interplay of the squeeze-out of the fluid and the formation of a tribofilm, large system sizes have to be considered. In this work, a large-sized MD simulations were carried out to study different lubrication regimes along the Stribeck curve in a model system to elucidate the dominating mechanisms in the different regimes.

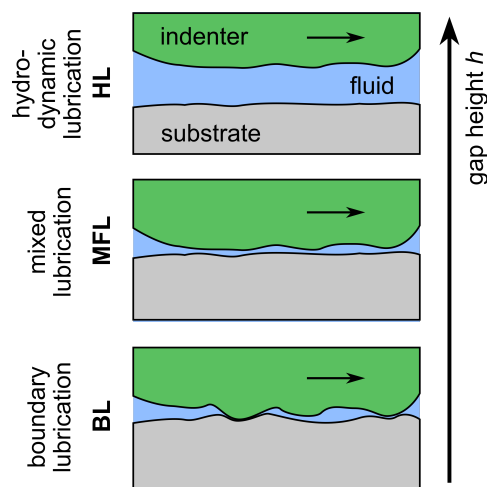


Figure 52: Scheme of lubrication regimes as a function of the gap height h indicating the distance between two solid bodies experiencing a relative motion.

MD simulation has been extensively used in recent years for studying friction on the atomic scale. In particular, the hydrodynamic lubrication regime has been studied many times in the literature using MD simulations, e.g. Refs. [5, 31–33, 107, 109, 111–114, 121, 167, 207, 208, 218, 254, 314–316, 332, 333, 392]. Also, contact processes comprising deformation of the solid bodies of dry contacts have been extensively studied in the past [132, 205, 246, 304, 375, 397, 416]. Lubricated systems with elastic and/ or plastic deformation on the other hand has been less frequently studied using classical MD simulations [11, 62, 129, 214, 220, 221, 299, 323, 328, 335, 348, 356, 430, 431]. Moreover,

lubricated contact processes comprising plastic deformation, where the solid bodies are fully immersed by the fluid such that also a fluid bulk phase exists that exhibits heat conduction, load transfer, back pressure against the squeeze-out etc. has been only rarely investigated [220, 221, 300, 323, 336, 348, 356, 430, 431]. Also, to the best of our knowledge, the transition of the different lubrication regimes has not yet been studied using MD.

In this work, large-sized systems were studied, where the contact process is fully immersed in a fluid to elucidate the interplay of different friction mechanisms (e.g. the formation of tribofilm, break-up of fluid adsorption layers, squeeze-out, elastic and plastic deformation, dissipation and heat conductivity) in the different lubrication regimes. In the system, a spherical indenter (modeling the tip of an asperity) carries out a lateral movement on an atomistically flat substrate. The studied setup is a simplified yet a representative one. The substrate is an iron single crystal and the indenter is a single crystal diamond. The effect of two lubricants is compared: Methane and n-decane (for brevity, referred to as 'decane' in the following). The influence of the lubrication gap height is systematically studied to investigate the three different lubrication regimes BL, ML, and HL along the Stribeck curve. Hence, simulations were carried out in this work at constant gap height, which is different to the usual approach, where the load is prescribed. We consider both a conceptual model system using the simple Lennard-Jones model as lubricant (modeling methane) as well as studying a practically relevant system using decane as lubricant. The Lennard-Jones model system is convenient for studying complex processes and phenomena on the atomistic scale [16, 159, 164, 171, 346, 379] (and studied in detail in chapters 3 & 4). The Lennard-Jones system is very well-understood today regarding its thermophysical properties; not only thermodynamic equilibrium bulk phase properties [348, 350, 361], but also transport [17, 92, 116, 126, 218, 257, 325] and interfacial properties [26, 162, 357] have been systematically investigated in the literature. Also, methane is relevant for tribological applications, e.g. in cryogenic pumps for LNG (liquid natural gas) processes [15, 38, 174, 413]. The second system studied here contains n-decane as a fluid. This is a reasonable – yet simplified – model for lubricants in technical applications.

The kinematics of the indenter are fully prescribed. Hence, the forces on the indenter at a given gap height are a response to the kinematics. A large number of mechanical and thermodynamic properties of the system were studied in detail. For the mechanical properties, the total forces on the indenter, the coefficient of friction, the groove and chip formed on the substrate, the behavior of the fluid in the adsorption layer, and the formation of the tribofilm in the substrate surface are discussed. For the thermodynamic properties, the dissipated energy, the temperature field, and the pressure field of the fluid are studied. This comprehensive concept study enables a systematic assessment of the

fundamental mechanisms in the different lubrication regimes of the Stribeck curve, cf. Fig. 52.

The present work is outlined as follows: Section 6.2 introduces the simulation setup and the observables used to characterize the contact process. The results for both the mechanical and thermodynamic properties are discussed in section 6.3.1 and 6.3.2, respectively.

6.2 Methods

6.2.1 Simulation Scenario

Fig. 53 schematically shows the simulation setup. It consists of a solid spherical cap as indenter, a solid substrate, and a fluid lubricant. Two types of simulations were carried out: One with methane as fluid and one with decane as fluid. For each type, simulations at different gap heights were carried out. The size of the substrate block was 401, 763, and 31 Å in x -, y , and z -direction, respectively. The surface of the substrate was in the xy -plane. The indenter was cap-shaped with a radius of $R = 500$ Å. The height of the indenter cap was 70 Å. It carried out two sequential movements: (i) positioning/indentation, during which the indenter moves in $-z$ -direction normal to the surface; and (ii) lateral movement, during which the indenter moves in $+y$ -direction. To systematically study the three lubrication regimes BL, ML, and HL, the indentation depth was varied systematically. A given indentation depth \tilde{h} yields a certain lubrication gap h between the indenter and the substrate, cf. Fig. 53. The indentation gap \tilde{h} was defined as the distance between the center of the particles of the bottom of the spherical cap and the top of the substrate (cf. Fig. 53). However, the lubrication gap height h was used throughout the study for characterizing the simulations, which was defined as $h = \tilde{h} - 2^{1/6}\sigma_{\text{IS}}$, where σ_{IS} is the size parameter of the interaction potential between the substrate and the indenter. Hence, for $h \leq 0$, the substrate and the indenter would directly interact with each other, even if no fluid was present.

For both fluids, 14 gap height values h were considered. The following values for the lubrication gap were used $h = -7, -6, -5, -4, -3, -2, -1, 0, 1, 2, 4, 6, 8, 12$ Å. Hence, for $h < 0$, elastic and/ or plastic deformation will certainly occur, whereas for $h > 0$, deformation of the substrate may in general occur – depending on the behavior of the fluid in the gap. For a more detailed analysis (see results section), the focus is put on the simulations with $h = -6, -4, -2, 0, 4, 8$ Å. Hence, in total 28 simulations were carried out. The indenter velocity during the vertical positioning was 10 m/s and during the lateral movement 20 m/s. It is a long-standing and often discussed problem that velocities used

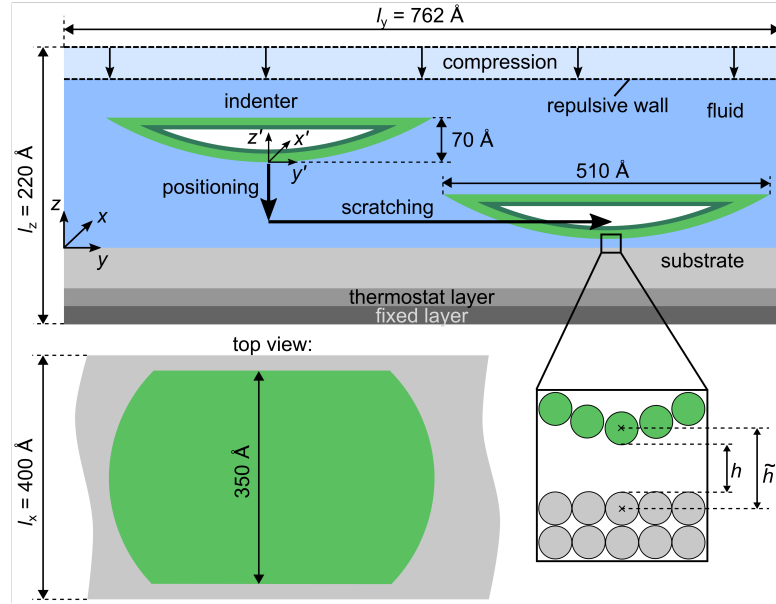


Figure 53: Setup of the simulation box for the lateral movement of the indenter on the substrate surface (not true-to-scale). The indenter was fully submerged in the lubricant fluid. Before the lateral movement, the indenter was positioned at a specified lubrication gap h .

NEMD friction simulations do not comply with those used in classical friction experiments [95, 426]. Accordingly, the speed in most classical friction experiments [94, 234] is significantly smaller than our scratching velocity. However, interestingly, 20 m/s is a realistic cutting speed used in manufacturing processes such as grinding and turning [147].

The simulation time $\tau = 0$ indicates the beginning of the indentation phase, which positions the indenter at a given gap height h . Depending on the gap height h , the positioning phase was between $0 < \tau < 440$ ps and $0 < \tau < 630$ ps. The lateral movement was carried out for 1400 ps. Therefore, the scratching length was 280 \AA .

The origin of the Cartesian coordinate system was defined as: $x = 0$, $y = 0$ in the corner of the simulation domain and $z = 0$ for the initially unpenetrated surface of the substrate, cf. Fig. 53. The substrate consisted of 8×10^5 particles. The substrate was fixed in the simulation box by fixing 3 atom layers at the bottom of the substrate (cf. Fig. 53). Periodic boundary conditions were applied in x - and y -direction. It should be noted that this might in general affect the fluid flow in the system. However, as the simulation box is very large, artifacts from the periodic boundary conditions are probably small.

The motion of the indenter was imposed by prescribing the velocity of the inner core atoms of the indenter, cf. dark green region in Fig. 53. Hence, the outer layer atoms of the indenter moved according to Newton's equation of motion, cf. light green region in

Fig. 53. The indenter consisted of 7×10^5 particles. The radius of the base of the indenter cap was 500 Å. To limit the total number of particles in the box, the cap indenter was trimmed in x -direction to a total width of $\Delta x = 350$ Å, cf. Fig. 53. Hence, the cap indenter had a front and rear face side. However, due to the overall large indenter size, no significant effect of the sideways trimming on the contact process at the bottom of the indenter are expected.

At the top, the simulation domain was confined by a soft repulsive wall. For the initialization, the fluid particles were placed on a regular grid. To establish a liquid state, the soft repulsive wall was lowered such that the fluid particles were compressed. Before the compression, the entire simulation box was equilibrated for 1 ns. This compression was carried out before the movement of the indenter. At the beginning and during the compression, the entire simulation box was thermostatted at T_{equi} . For methane, the temperature was $T_{\text{equi}} = 130$ K and for decane $T_{\text{equi}} = 350$ K. During the compression, the density of the bulk fluid was sampled. The compression was stopped when a prescribed density was reached. For both fluids, this prescribed density value was taken from the NIST database [238] as the liquid state density at $p = 50$ MPa and $T_{\text{equi}} = 130$ K and $T_{\text{equi}} = 350$ K for methane and decane, respectively. During the movement phase of the indenter, three layers of atoms of the substrate at the bottom of the simulation box were thermostatted (cf. Fig. 53) to remove dissipated heat from the system. The thermostating was imposed using classical velocity scaling [52]. It should be noted that, as the substrate block is relatively thin, the heat transfer into the substrate is modeled in a simplified way. In the case of methane as fluid, there were 8.68×10^5 fluid interaction sites and 1.44×10^6 interaction sites in the case of decane. Each methane molecule consists of a single interaction site; each decane molecule consists of 10 interaction sites. The simulation box had in total (indenter, fluid, and substrate) 2.37×10^6 interaction sites in the methane simulation cases and 2.94×10^6 interaction sites in the decane simulation cases.

The time step was 1 fs and 0.5 fs for the methane and decane simulations, respectively. The simulations were carried out with the open-source simulation code LAMMPS [288]. The visualizations were performed using the open-access tools ParaView [4, 165] and OVITO [370].

6.2.2 Molecular Model

Table 5 gives an overview of the symmetric interaction matrix present in the simulations. The diagonal entries of the matrix indicate the interactions between interaction sites of the same substance. The off-diagonal entries in Table 5 specify the cross-interactions between sites of different substances, i.e. indenter-substrate, fluid-substrate, and indenter-

fluid. The substrate and the indenter force field was the same in all simulations. As two different substances (methane and decane) were considered for the fluid, two different force fields were used for their modeling.

Table 5: Interaction potentials employed in the present study.

	substrate	indenter	fluid
substrate	EAM (iron) ^(a)	WCA ^(b)	9-6 LJ ^(c)
indenter	-	<i>Tersoff</i> (diamond) [382]	9-6 LJ ^(c)
fluid	-	-	BZS (methane) ^(d)
	-	-	TraPPE (decane) ^(e)

^(a)Embedded atom model potential [258];

^(b)*Weeks-Chandler-Andersen* potential [408];

^(c)Lennard-Jones potential [232];

^(d)Boltzmann-Zuse society force field [353, 403];

^(e)Transferable potentials for phase equilibria force field [102, 249].

The substrate was an iron bcc single crystal with an initially atomistically flat surface and a lattice constant of 2.855 Å. It should be noted that these are strong simplifications compared to a real system exhibiting a surface roughness [158, 409] and dislocations [136]. The substrate-substrate interactions were prescribed by the iron embedded atom model (EAM) potential proposed by *Mendeleev et al.* [258]. The crystal had a (100) surface orientation and the lateral movement was performed in $[0 \bar{1} 1]$ direction (it should be noted that the lattice orientation with respect to the scratching direction has in general an influence on the process properties [131]).

The diamond indenter was modeled by a *Tersoff* potential [382]. The potential was developed to describe the intermolecular interactions in carbon diamond. The atoms of the indenter were initialized on a diamond lattice with a lattice constant of 3.5667 Å.

Two different fluids were used as lubricants: Methane and decane. Methane was modeled using a BZS force field proposed by *Vrabec et al.* [353, 403]; decane was modeled using a TraPPE force field proposed by *Martin and Siepmann* [102, 249]. Both, the BZS and TraPPE force field are known to describe properties of fluids very well, e.g. for the vapor pressure [276, 403], the saturated densities [276, 403] as well as transport properties such as the viscosity [284] and interfacial properties [276, 403]. Also, this force field class is known to usually yield reasonable extrapolation behavior to state points that were not considered for the parametrization [110, 308].

The indenter-substrate interactions were modeled using the purely repulsive *Weeks-Chandler-Andersen* (WCA) potential [408]. Hence, the classical 12-6 Lennard-Jones potential with a cut-off at the minimum of the potential $r_c = 2^{1/6}\sigma$ was used.

Fluid particles interact with both substrate and indenter atoms. In this work, the solid-fluid interactions were modeled with the (full) 9-6 Lennard-Jones potential. In general, the parameters ε and σ for the solid-fluid interactions can be determined by different routes, i.e. a top-down or a bottom-up approach. In the top-down approach, the interaction parameters are chosen such that the system described by the force field model captures a certain macroscopic behavior, e.g. an experimentally determined contact angle or adsorption isotherm. In the bottom-up approach, the interaction parameters are derived from quantum chemical calculations. In the present work, the bottom-up approach was used. We used the force matching method outlined by *Ercolessi and Adams* [104]. The quantum chemical data was taken from Ref. [418]. Details are given in the Appendix C. It should be noted that the solid-fluid cross-interactions – in particular the solid-fluid interaction energy ε – have an important influence on tribological processes (see also chapter 3) and interfacial properties such as adsorption layers on the surface [92, 162, 325], static and dynamic wetting effects [26, 92], the heat transfer across the interface [325], and accordingly an influence on the thermal balance of tribological processes. Also, the squeeze-out of particles from the lubrication gap is known to depend on the solid-fluid interactions [348, 356].

The chosen molecular models and interaction potentials provide a good trade-off between accuracy and computational efficiency, which is crucial for the large-scale simulation study carried out here.

6.2.3 Definition of Observables

A large number of primary simulation data was sampled and then further post-processed such that multiple aggregated observables became available for the evaluation of the process. Both mechanical and thermodynamic properties were considered. The focus is on the mechanisms occurring in the direct vicinity of the contact zone.

The total tangential force F_t and normal force F_n on the indenter were calculated as the sum of all pair interactions (indenter-substrate (IS) and indenter-fluid (IF)) on the indenter in y - and z -direction

$$F_t = \sum_{i=1}^m \left(F_{y,i}^{\text{IS}} + F_{y,i}^{\text{IF}} \right), \quad (70)$$

$$F_n = \sum_{i=1}^m \left(F_{z,i}^{\text{IS}} + F_{z,i}^{\text{IF}} \right), \quad (71)$$

where m is the total number of interaction sites of the indenter. The tangential force is defined here in positive y -direction (scratching direction) and thereby indicates the

reaction force of the scratching process. The coefficient of friction was computed from the absolute value of the tangential force and the normal force on the indenter

$$\mu = |F_t|/F_n , \quad (72)$$

during the process. The forces on the indenter were written to the hard-drive every 1 ps. The error bars of the forces and the coefficient of friction were calculated as their standard deviation during the quasi-stationary phase of the lateral movement (see below).

The work done by the indenter W was computed by numerical integration of the total force on the indenter

$$W(\tau) = \int_{\text{indentation}} F_n(\tau) dz + \int_{\text{scratching}} |F_t(\tau)| dy , \quad (73)$$

where the forces F_n and F_t were computed according to Eq. (70) and (71). The heat of the thermostat $Q_{\text{thermostat}}$ is defined as the cumulative energy that was added or removed from the particles in the thermostat layer of the substrate (cf. Fig. 53). The heat flux $\dot{Q}_{\text{thermostat}}$ was calculated as the slope of $Q_{\text{thermostat}}(\tau)$ in the quasi-stationary phase. The quasi-stationary phase was from $\tau_{\text{scratch}} \geq 400$ ps to the end of the lateral movement, where $\tau_{\text{scratch}} = 0$ indicates the beginning of the lateral movement.

The temperature and the pressure of the fluid were computed locally during the contact process. The fluid temperature and pressure were computed as per-atom values by averaging the respective property over the atoms within the cut-off radius of each atom. The average aligned velocity from each per-atom collective was subtracted from the total average kinetic energy for the computation of the local temperature. The fluid region was divided into bins in the yx -plane (cf. Fig. 54) over the entire simulation domain. The edge length of the bins was $\Delta x = \Delta y = 4.8 \text{ \AA}$. The fluid properties were computed bin wise, i.e. averaged over all molecules in a bin. Only fluid particles below the indenter were considered, i.e. below the respective z -coordinate of the upper edge of the indenter. These temperature and pressure profiles were computed in block averages every 20 ps. The maximum temperature and pressure difference ΔT^{max} and Δp^{max} were derived from these temperature and pressure fields, respectively, as the difference of the maximum value of all bins and the mean bulk value derived in the area unaffected by any adsorption layers. This was done for all block averages in the quasi-stationary regime. The final value of a given observable and its error bar was calculated as the average and the standard deviation of all values sampled during the quasi-stationary phase.

The substrate and the indenter surface was analyzed using an alpha shape algorithm

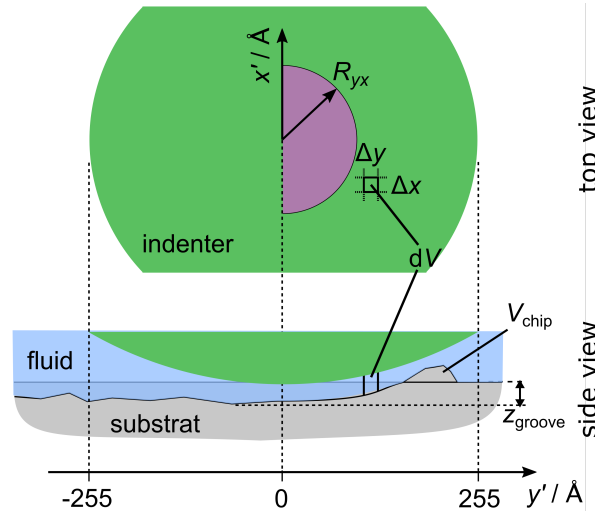


Figure 54: Schematic (not true-to-scale) for the definition of observables used for the sampling. The chip volume V_{chip} is defined as the substrate material above the unpenetrated substrate surface. The purple semicircle with $R = 100 \text{ \AA}$ indicates the region, where particles were counted for N_{gap} . The black rectangle with $\Delta x = \Delta y = 4.6 \text{ \AA}$ and the volume dV indicates the shape of an averaging bin for the computation of the temperature, pressure, and density. The bin represents a grid that is distributed over the entire simulation box.

[98]. Thereby, the bounding hull surface of the indenter and the substrate is obtained. These surfaces are defined by sets of points. Using the alpha shape method, the obtained surfaces capture both convex and concave parts of the solid body surfaces. For determining the particles that constitute the surface, an alpha radius of $1.05 R_{\text{alpha},c}$ was used, where $R_{\text{alpha},c}$ indicates the critical radius [98]. Here, $R_{\text{alpha},c}$ was increased by 5% such that holes and gaps in the deformed surface were avoided. The resulting geometrical bodies were used for further process characterization. The volume of the chip V_{chip} was calculated from the volume bounding hull obtained from the alpha shape method. The chip was defined here as the geometric body formed by substrate particles above the initial height of the surface and ahead of the center of the indenter, cf. Fig. 54. The depth of the groove Δz_{groove} was defined as the difference of lowest z -coordinate of the upper surface of the substrate to its initial surface height. Both observables were evaluated every 20 ps in the quasi-stationary phase. From these block average values, the mean value and its standard deviation was computed. The number of fluid particles (i.e. interaction sites in the case of decane) in the gap N_{gap} and in the tribofilm $N_{\text{tribofilm}}$ were calculated based the alpha shape surface analysis. The evaluation of the number of fluid particles in the gap N_{gap} and in the tribofilm $N_{\text{tribofilm}}$ was carried out at the very end of the contact process. The number of fluid particles in the gap N_{gap} counts all fluid interaction sites below the surface of the indenter and above the substrate surface. Only particles within a radius of $R_{yx} = 100 \text{ \AA}$ from the center of the indenter and in front of the indenter are considered for determining N_{gap} (cf. Fig. 54). The local number of fluid

particles in the tribofilm $\tilde{N}_{\text{tribofilm}}$ counts the number of fluid molecule interaction sites below the substrate surface. Both the total value of $N_{\text{tribofilm}}$ as well as the local number of fluid particles imprinted into the substrate surface $\tilde{N}_{\text{tribofilm}}(z)$ were computed. It should be noted that the computed values for N_{gap} , $\tilde{N}_{\text{tribofilm}}$, and $N_{\text{tribofilm}}$ slightly depend on the alpha shape parameter α , which determines to what degree, concave roughness structures of the deformed substrate surface are captured [98]. The influence of α on the computed indenter surface is negligible since the diamond indenter surface does practically not deform. For N_{gap} , $\tilde{N}_{\text{tribofilm}}$, and $N_{\text{tribofilm}}$, no statistical uncertainty is reported as they were only calculated from the atomistic configuration at the end of the contact process. Moreover, the density profiles of the adsorption layers $\rho(z)$ were calculated from data taken after the equilibration in areas that were unaffected by the indenter.

6.3 Results and Discussion

The results are structured as follows: First, the mechanical properties of the process are discussed, then, the thermodynamic properties. The mechanical properties comprise the kinetics of the process, the mechanical work done by the indenter, the formation of the chip and the groove in the substrate as well as the characterization of the lubrication gap, the adsorption of the fluid on the substrate, and the formation of the tribofilm in the substrate surface. The thermodynamic properties comprise an analysis of the overall dissipated energy as well as the temperature and pressure field of the fluid in the lubrication gap. From the 14 gap heights that were considered in this work, six characteristic gap heights that capture the main characteristics of the Stribeck curve lubrication regimes are discussed in detail in the following.

6.3.1 Mechanical Properties

Kinetics and Coefficient of Friction

Fig. 55 shows the results for the total forces on the indenter during the entire contact process for the exemplarily chosen gap height $h = -4 \text{ \AA}$ for illustration of the overall contact process kinetics. The normal force F_n and the tangential force F_t on the indenter show the characteristic shape for a subsequent indentation and lateral movement process [134, 348, 356]. During the indentation, the normal force exhibits a steep increase as the indenter causes (at the exemplarily chosen h) elastic and plastic deformation on the substrate. Moreover, the bulk fluid phase is squeezed out of the lubrication gap,

which requires work done by the indenter [348]. During the lateral movement, the normal force quickly drops and reaches an approximately constant value. The tangential force fluctuates around zero during the indentation. At the beginning of the lateral movement, the tangential force exhibits a jump and then fluctuates around an approximately constant value, which is due to the formation of the chip. During the lateral movement, the process reaches a quasi-stationary state at approximately $\tau = 1000$ ps. During that quasi-stationary state, observables were averaged to yield height-specific process parameters (see methods section for details).

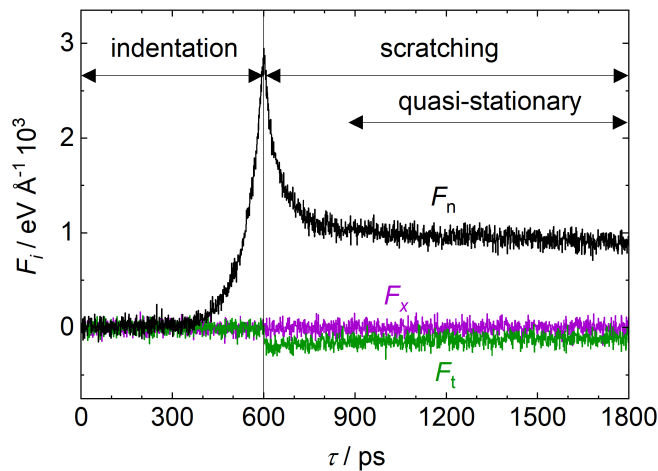


Figure 55: Exemplaric results for the total force on the indenter sampled during the contact process (results shown for the methane simulation at $h = -4 \text{ \AA}$). The three components of the total force, F_N , F_T , and F_x are shown. The *quasi-stationary regime* was taken as $1000 \text{ ps} < \tau < 1800 \text{ ps}$.

Fig. 56 shows mechanical process parameters sampled and averaged during the quasi-stationary phase as a function of the gap height: Fig. 56 a) shows the normal and tangential total force on the indenter; Fig. 56 b) shows the results for the Stribeck curve, i.e. the coefficient of friction; Fig. 56 c) shows the work done by the indenter by the end of the contact process. Results for both the methane and the decane simulations are shown.

At the bottom of Fig. 56, the small arrows indicate the six characteristic simulations ($h = -6, -4, -2, 0, 4, 8 \text{ \AA}$) that are discussed in detail for both the mechanical and thermodynamic properties, cf. Figs. 57, 58, 63, 65, and 66.

Fig. 57 shows screenshots of the visualization of the contact process during the quasi-stationary phase taken at the end of the lateral movement $\tau_{\text{scratch}} = 1200 \text{ ps}$, which provides direct insights into the atomistic mechanisms of the process.

From Fig. 56, it can be seen that the normal total force on the indenter F_n decreases with increasing gap height. This is as expected: As the process kinematics are prescribed, the normal force on the indenter is large at small gap height. Also for the

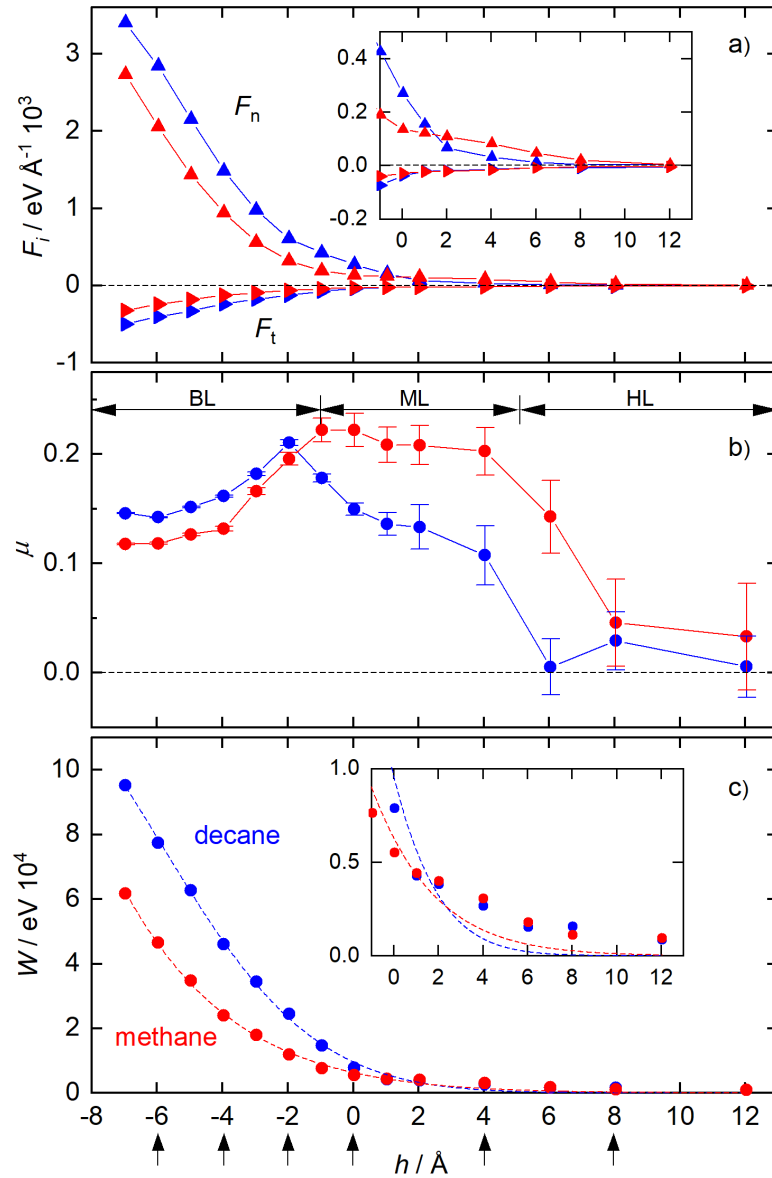


Figure 56: Results sampled in the quasi-stationary regime (cf. Fig. 55) as a function of the gap heights h : Forces on the indenter (top) in z - (up-triangles) and y -direction (right-triangles), coefficient of friction (middle), and work done by the indenter during the contact process simulation (bottom). Results for both lubricated cases: Methane (red) and decane (blue). Solid lines are a guide for the eye. The dashed lines are empirical fits of the form $W/\text{eV} = \exp(a + bh + ch^2)$ with the parameters $a = 8.749$, $b = -0.362 \text{ \AA}^{-1}$, and $c = -0.00468 \text{ \AA}^{-2}$ for methane and $a = 9.17$, $b = -0.493 \text{ \AA}^{-1}$, and $c = -0.0236 \text{ \AA}^{-2}$ for decane. Small arrows indicate the six characteristic simulations ($h = -6, -4, -2, 0, 4, 8 \text{ \AA}$) discussed in detail in the following.

tangential force, the (absolute) value $|F_t|$ obtained during the quasi-stationary phase decreases with increasing gap height. For $h > 0$, the absolute values of the forces $|F_n|$ and $|F_t|$ are significantly smaller since there is no direct contact between the indenter and the substrate and only the fluid shear flow acts as a mediator between the relative

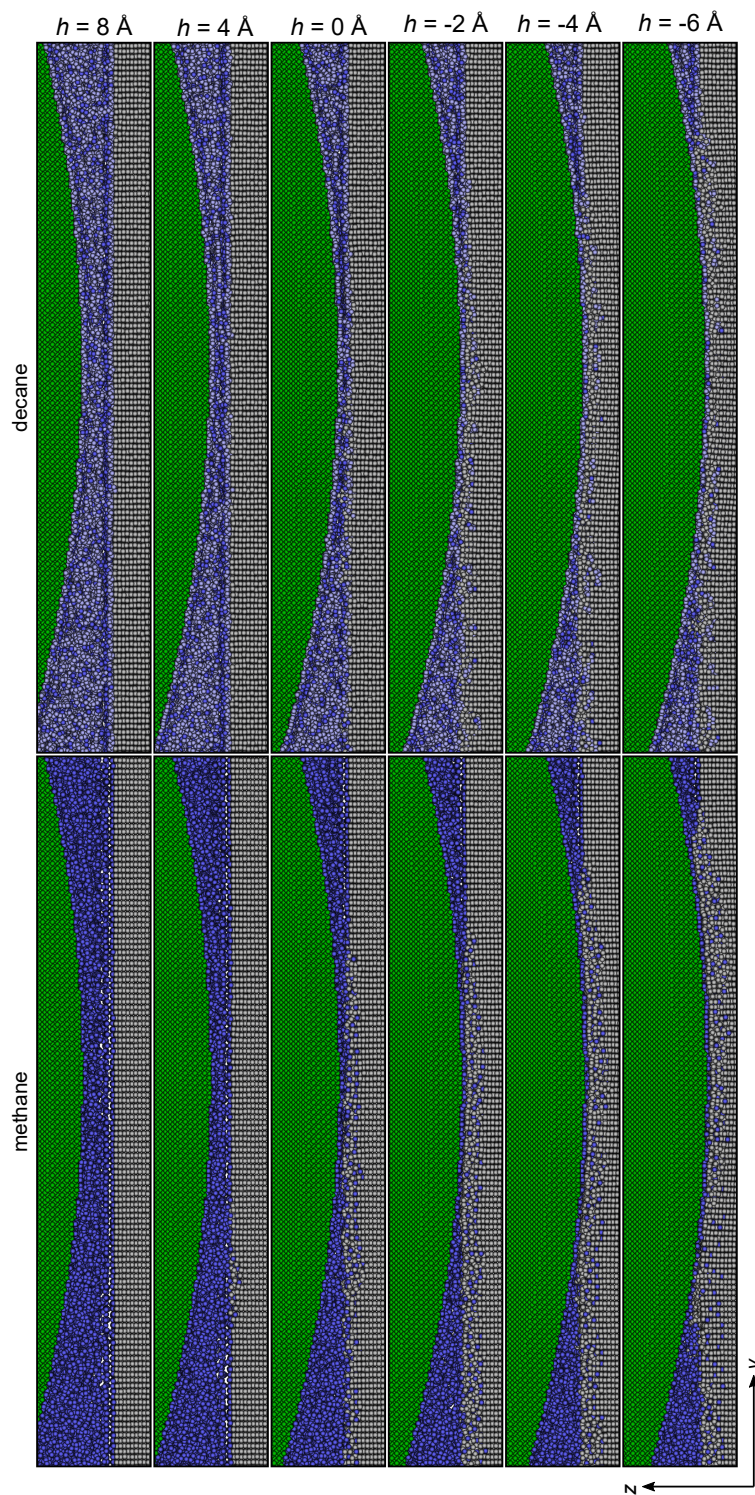


Figure 57: Screenshots of the contact zone. Results shown for $h = 8, 4, 0, -2, -4, -6 \text{ \AA}$. The left column gives the results for the methane simulations; the right column shows the results for the decane simulations. Green particles indicate the indenter; blue particles indicate the fluid; gray particles indicate the substrate. For decane, dark blue indicates the CH_3 interaction sites and bright blue the CH_2 sites. The screenshots were in all cases taken at the simulation time $\tau_{\text{scratch}} = 1200 \text{ ps}$ and at $x = 200 \text{ \AA}$. The perspective is in positive x -direction and the indenter motion was in y -direction.

motion of the bodies. For small (negative) gap heights, i.e. the indenter penetrates the substrate, the normal force is about an order of magnitude larger than the corresponding tangential force. This is mostly due to the indenter geometry, which is relatively flat and therefore has a high contact area with the substrate. The comparison of the results for the methane and the decane simulations shows that, qualitatively, the results for the two fluid cases are similar. Yet, important quantitative differences are observed. For small gap heights $h < 1 \text{ \AA}$, the absolute values of the forces $|F_n|$ and $|F_t|$ in the decane simulation cases exceed those in the corresponding methane cases. Vice versa, for large gap heights $h > 1 \text{ \AA}$, the absolute values of the forces are larger in the methane cases. Interestingly, the cross-over of the methane and decane force occurs for smaller gap height for the tangential force than for the normal force. This transition can also be clearly seen in the behavior of the coefficient of friction, cf. Fig. 56 b).

From the results for the coefficient of friction, the three friction regimes and the typical shape of the Stribeck curve can be clearly identified: For small gap heights values $h < -1 \text{ \AA}$, BL occurs. For intermediate gap heights $-1 \text{ \AA} < h < 4 \text{ \AA}$, ML prevails. For large gap heights $4 < h$, HL occurs. The identification of the three lubrication regimes is also supported by the simulation screenshots depicted in Fig. 57. For $4 < h$, the coefficient of friction is very small, which is due to the fact that the contact process is fully mediated by the hydrodynamic shear flow of the fluid and only very little elastic and plastic deformation is done on the substrate. Hence, HL prevails. In that regime, the fluid bulk phase properties dominate the process behavior. In the BL regime $h < -1 \text{ \AA}$, significant elastic and plastic deformation of the substrate occurs as a result of the penetration of the indenter into the substrate. Moreover, a tribofilm¹ is formed on the substrate surface in the BL regime, cf. Fig. 57. In the BL regime, the coefficient of friction increases with increasing gap height. Moreover, the coefficient of friction in the BL regime is about an order of magnitude larger than that in the HL regime. In the ML regime $-1 \text{ \AA} < h < 4 \text{ \AA}$, a smooth transition occurs from the BL regime to the HL regime. The adsorption layer of the fluid on both solids plays a dominant role in the ML regime as most fluid particles in the gap are part of the adsorption layer (cf. Fig. 57). The coefficient of friction exhibits a maximum at the lower bound of the ML regime and strongly decreases with increasing gap height towards the HL regime. The results for the Stribeck curve obtained in this work from MD simulations (cf. Fig. 56 b)) are in good qualitative agreement with experimental data, e.g. Ref. [233]. Experimental Stribeck curves usually show the evolution of the coefficient of friction with a dimensionless parameter (see section 2.1.3 for details), such as the suitably scaled speed of contact.

¹The term 'tribofilm' is usually associated with chemical reactions between the lubricant and the substrate surface. The term tribofilm is adopted here despite the fact that non-reactive force fields were used since the heterogeneous phase formed from substrate and fluid particles has similar characteristics as tribofilms.

In our case, the contact separation, i.e. gap height h appears, which is usually scaled with the surface roughness. Since the latter vanishes in our case, the choice of such a dimensionless parameter is non-trivial here and we study the Stribeck curve as a function of h .

The three lubrication regimes can moreover be characterized based on the slip in the system. In the HL regime, the shear slip occurs in the bulk fluid phase. In the ML regime, the slip plane lies within the adsorption layer of the fluid molecules on the solid surfaces. The slip in this solid-fluid interfacial region is energetically less favorable and yields an increased coefficient of friction. In the BL regime, the slip lies in parts below the substrate surface, which leads to the formation of the chip and the groove. This slip plane is energetically less favorable and more work has to be done by the indenter.

A detailed evaluation of the force contribution is given in the Appendix C. Therein, it is shown that the substrate-indenter interactions contribute significantly to the total force on the indenter in the BL regime – for both the normal and the tangential force. This is despite the fact that at all studied gap heights, a closed fluid monolayer remains between the two solid bodies, cf. Fig. 57. However, as the indenter-substrate interactions have a larger range than the size of the fluid particle beads, there is a direct interaction between the indenter and the substrate in the simulations in the BL regime.

The comparison of the methane and decane results provides further insights. Interestingly, in the direct vicinity of the cross-over between the methane and the decane results for the coefficient of friction, the results for $\mu(h)$ for both fluid cases exhibit a maximum. It is not clear if this is a coincidence. In the ML and HL regime, the methane simulations yield a higher coefficient of friction than the decane simulations. This is as expected: In the ML regime, the adsorption behavior of the fluid is crucial. Methane, as a simple practically spherical molecule, forms very structured adsorption layers (see details below), which dampens the slip-stick motion. Decane, on the other hand, forms a more unraveled adsorption layer, which enhances the slip-stick motion on the surface. In the HL regime, the fluid bulk phase properties prevail and decane has more favorable tribological properties than methane.

The work done by the indenter throughout the process is depicted in Fig. 56 c). As the tangential force absolute value in the decane simulations exceeds that in the methane simulations at given h , also the work done by the indenter is larger in the decane simulations. This holds for the entire BL regime and for the lower bound of the ML regime. However, in the range $1 \text{ \AA} < h < 6 \text{ \AA}$, more work is done by the indenter in the methane cases. This is due to the fact that the strongly structured adsorbed methane molecules interact energetically unfavorable in the bulk fluid inlet. This also results in a higher pressure increase in the lubrication gap, e.g. at $h = 4 \text{ \AA}$, cf. Fig. 66 below.

Characterization of Chip and Groove

The formation of the chip and the groove in the substrate are characteristic properties of the contact process. Fig. 58 shows the substrate surface at the end of the contact process (view direction is in negative z -direction) for the cases $h = -6, -4, -2, 0, 4, 8 \text{ \AA}$; indenter and fluid particles are not shown. Fig. 59 shows the chip volume V_{chip} and the groove depth Δz_{groove} (cf. section 6.2.3 for the definition of the observables) at the end of the lateral movement as a function of the gap height h . The chip volume decreases monotonously with increasing gap height and approximately with a log-function – especially in the case of decane. Also the groove depth decreases with increasing gap height.

In the HL regime $h > 4 \text{ \AA}$, the magnitude of the groove depth and the chip volume is very small, cf. Fig. 58. Hence, both the elastic and plastic deformation is very small in that regime – as expected. In the ML regime $-1 \text{ \AA} < h < 4 \text{ \AA}$, the adsorbed fluid layers strongly interact with the substrate surface. This causes elastic and plastic deformation and thereby the formation of both a faint chip and a groove in the substrate, cf. Fig. 58. In the BL regime $h < -1 \text{ \AA}$, significant elastic and plastic deformation of the substrate occurs, cf. also Fig. 58. As the indenter has a very flat shape, the chip forms primarily sideways.

For both the chip volume and the groove, important differences are observed for the methane and decane simulations. In the BL regime, the V_{chip} results for the two fluid cases are essentially the same, whereas significant differences are observed in the ML regime. There, at a given gap height, the methane case yields a larger chip formation compared to the decane case. For all three lubrication regimes, the presence of decane molecules as a lubricant causes a deeper groove compared to methane molecules, cf. Fig. 59.

In the case of methane, the groove depth is surprisingly approximately constant in the range $h = -3 \dots -4 \text{ \AA}$ (mostly ML), cf. Fig. 59. This is due to the fact that the adsorbed methane particles (especially the ones adsorbed on the substrate) strongly interact with the substrate surface, cf. Fig. 57. The spherical particles substitute lattice atoms in the substrate, which effectively increases the volume of the substrate. This compensates the volume loss due to the chip formation (cf. Figs. 58 and 59). This contributes also to the fact that the methane simulation results yield a larger coefficient of friction in the ML regime than the decane simulations.

Due to the presence of adsorbed fluid layers on the surfaces in the case of decane, the indenter size is effectively increased, which increases also the groove depth Δz_{groove} at a given gap height h . Therefore, the groove depth Δz_{groove} exceeds the gap height h . This holds for both the BL and the ML regime. On the contrary, for the methane

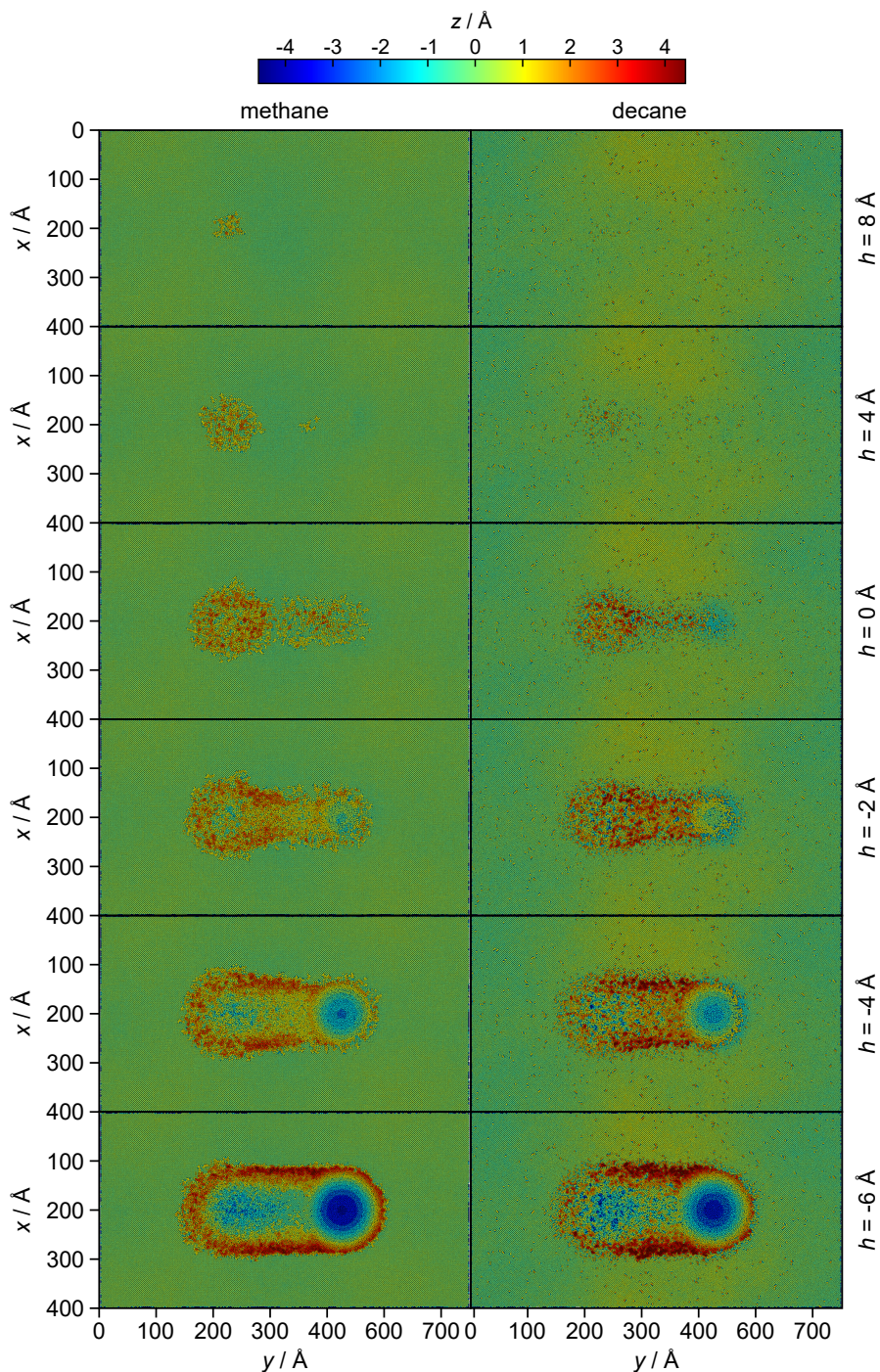


Figure 58: Top view on the substrate and groove formed at the end of the lateral movement of the indenter. Results shown for $h = 8, 4, 0, -2, -4, -6$ Å (top to bottom). The left column shows the results for the methane simulations; the right column those for the decane simulations. The color of the single particles indicates the distance to the reference plane with $z = 0$. Only substrate particles shown.

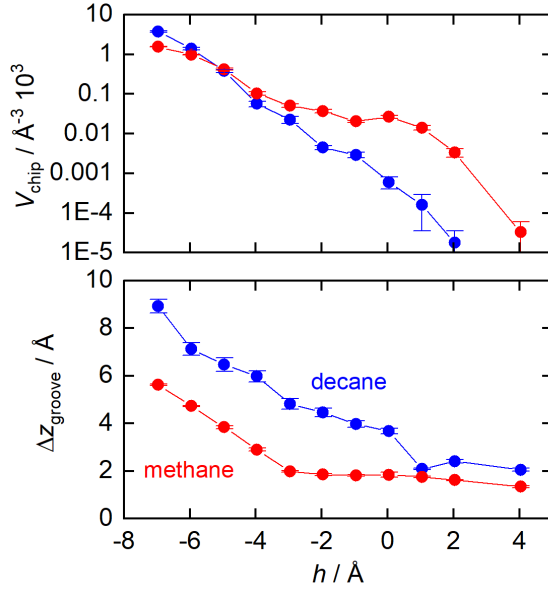


Figure 59: Geometric properties of the machined substrate during the quasi-stationary phase as a function of the gap height h (cf. Fig. 55): Chip volume V_{chip} (top) and groove depth Δz_{groove} (bottom). Lines are a guide for the eye. Results shown for the methane simulations (red) and decane simulations (blue).

simulations, the groove depth Δz_{groove} is smaller than the gap height in the BL regime. This is due to the fact that a significant amount of the methane particles is imprinted into the substrate surface forming a tribofilm. In parts, the methane particles substitute lattice atoms of the substrate (see details below). This effectively increases the volume of the substrate. The fact that we obtain $\Delta z_{\text{groove}} < |h|$ for a given h in the BL regime for the methane simulations is due to the geometric definition of the observables, cf. Fig. 53 and 54.

A detailed analysis of the machined surface (cf. Fig. 58) provides further interesting insights. The groove and the chip formed by the indentation (left part of the trace on the substrate surface) in both the HL and ML regime is more pronounced in the methane cases compared to the decane cases. The fact that the imprint caused by the indentation is significantly more prominent than the groove and chip formed during the lateral movement in the HL and ML regime is due to the squeeze-out behavior of the fluid. For gap heights $h > 0 \text{ \AA}$, a significant amount of fluid particles remains in the gap at the end of the indentation. At the beginning of the lateral movement, more fluid particles are squeezed out of the gap. This decreases the effective size of the indenter and thereby also decreases the groove and chip formed during the lateral movement compared to the indentation.

A further interesting aspect lies in the squeeze-out behavior of the fluid during the lateral movement in the BL regime. For $h = -4 \dots -2 \text{ \AA}$, the width of the groove clearly

decreases during the lateral movement. This is also due to the fact that more fluid particles are squeezed-out of the gap, which effectively decreases the indenter size. At very small gap heights, e.g. $h = -6 \text{ \AA}$, no such transient squeeze-out at the beginning of the lateral movement is observed, i.e. the formed groove and chip pile has a constant width δx during the entire contact process. Overall, in the BL regime, the squeeze-out of the fluid has important consequences for the formed groove and chip – depending on the gap height.

The comparison of the chip formation in the methane and the decane case at $h = -6 \text{ \AA}$ (cf. Fig. 58) reveals that the chip in the decane case is larger (more pronounced and darker red coloring of the chip). This is due to the fact that the decane molecules form a more stable adsorption layer on both surfaces sideways of the indenter. This effectively increases the indenter size sideways. This is consistent with the finding that the chip removal in the decane case requires more work than in the methane case, cf. Fig. 56 - bottom.

Interestingly, the fluid adsorption layer on the indenter surface does not break up (cf. Fig. 57), whereas the adsorption layer on the substrate surface is distorted in the BL regime and in parts of the ML regime. Evidently, the (diamond) indenter has a higher hardness than the (iron) substrate. Therefore, no significant elastic deformation is observed for the indenter, whereas important elastic and plastic deformation is observed for the substrate. These deformations in the substrate surface are probably related to the break-up of the adsorption layer on the substrate surface: When a dislocation occurs on the substrate surface, also the adsorption layer in the direct vicinity of the dislocation experiences a perturbation that can initiate a break-up of the highly structured adsorption layer. A detailed investigation of this interesting phenomenon is out of the scope of this work.

Characterization of Tribofilm and Lubrication Gap

A distinct feature observed in the simulations is the formation of the tribofilm caused by fluid particles being imprinted into the substrate surface. This can be seen from Fig. 58, where the groove shape is not colored smoothly, but with a color scattering. Also, the formation of the tribofilm can be clearly seen in the simulation screenshots depicted in Fig. 57. The mechanism forming the tribofilm in the methane and decane case show important differences. Moreover, the tribofilm properties strongly depend on the gap height h . As the tribofilm formation is directly related to the behavior of the fluid particles in the lubrication gap, the two are discussed in the following corporately. Fig. 60 shows the results of the analysis of number of fluid particles, i.e. interaction sites, in the tribofilm as well as those in the lubrication gap; Fig. 61 provides a detailed

analysis of the unperturbed fluid adsorption layer; Fig. 62 provides additional detailed screenshots illustrating the findings; and Fig. 63 provides a detailed analysis of the formation of the tribofilm.

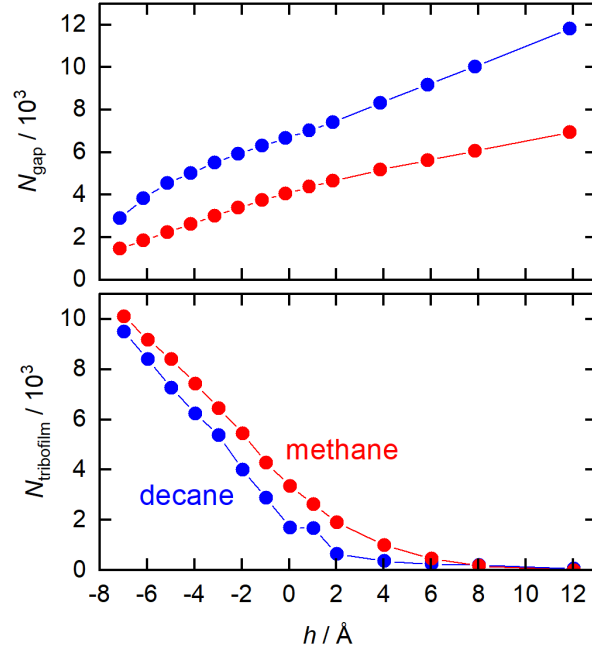


Figure 60: Residence of fluid particle interaction sites during quasi-stationary phase (cf. Fig. 55) as a function of the gap height h . Top: Number of fluid interaction sites in the lubrication gap as defined in Fig. 54; bottom: Number of fluid interactions sites impressed in the substrate surface. Lines are a guide for the eye. Results shown for the methane simulations (red) and decane simulations (blue).

Fig. 60 shows the results for the total number of fluid particle interaction sites in the lubrication gap N_{gap} and in the tribofilm $N_{\text{tribofilm}}$ (cf. section 6.2.3 for the definition of the observables) as a function of the gap height h . With increasing gap height, the number of fluid particle interaction sites in the lubrication gap between the indenter and the substrate surface N_{gap} increases and the number of fluid particle interaction sites in the tribofilm in the substrate surface $N_{\text{tribofilm}}$ decreases. These trends are obtained for both methane and decane. However, important differences are observed for the two fluids: At a given gap height, more decane particle interaction sites than methane particle interaction sites remain in the lubrication gap, whereas more methane particle interaction sites are imprinted into the substrate surface forming the tribofilm. Yet, the differences between the methane and decane results are significantly larger for N_{gap} compared to $N_{\text{tribofilm}}$. A second effect that increases the number of decane particle interaction sites in the lubrication gap in comparison to the methane case lies in the different squeeze-out behavior of the two fluids. The combination of the high pressure in the fluid and the molecular structure of the decane molecules results in a roughening of the substrate surface on the atomistic level in the gap, cf. Figs. 57 and 62. This acts

as a hindrance for the squeeze-out of the decane molecules and more molecules remain in the lubrication gap during the contact process.

The three lubrication regimes can be clearly identified from the behavior of $N_{\text{tribofilm}}(h)$, cf. Fig. 60: In the BL regime, a significant amount of fluid particle interaction sites is imprinted into the substrate surface due to the close contact of the two solid bodies and the high contact forces. The trend of $N_{\text{tribofilm}}(h)$ is approximately linear in the BL regime. In the ML regime, the adsorbed fluid layers are disrupted (cf. Fig. 57) and some fluid molecules are imprinted into the substrate surface; the results for $N_{\text{tribofilm}}(h)$ converge to zero in that regime. In the HL regime, practically no fluid particles are imprinted into the substrate surface and no tribofilm is formed – as expected.

Fig. 61 shows the density profiles of the adsorption layer of the fluid at the unpenetrated substrate surface, i.e. the initial state of the fluid in the gap before the starting of the indentation. In the case of methane, molecules form a strongly structured adsorption layer at the substrate surface.

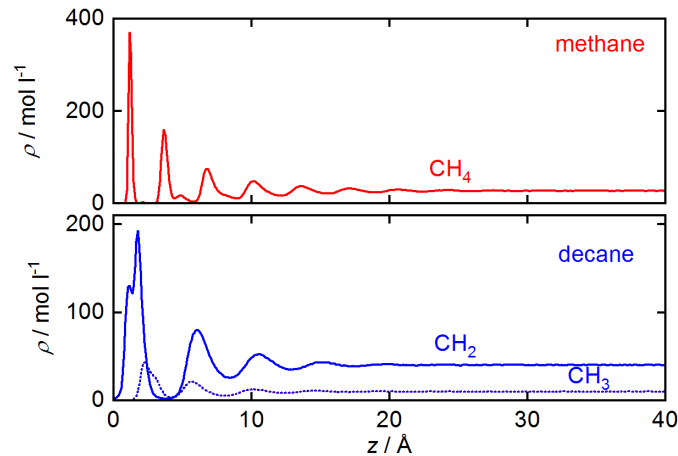


Figure 61: Density profiles of the fluid on the substrate surface sampled after the equilibration before the movement of the indenter. Top: Methane; bottom: Decane. Bulk densities values were $\rho = 0.4397$ g/ml for methane and $\rho = 0.7148$ g/ml for decane. Number of bins used for the sampling was $N_{\text{bins}} = 400$.

The first adsorption layer (cf. Fig. 61) shows a distinct peak followed by a groove, where the local density decreases essentially to zero. Four more distinct adsorption peaks can be observed in the methane density profiles. The distance between these peaks is approximately $\delta z = 2.5 \text{ \AA}$, which is in good agreement to $\sigma/\sqrt{2}$ with σ being the size parameter of the methane particles [403]. Hence, the second layer particles take body centered lattice positions with respect to the first layer. Opposite to the adsorption behavior of methane, a more complex behavior is observed for decane. This

is simply due to the fact that different decane interaction sites can adsorb on the surface. Here, the CH_3 sites and CH_2 sites are distinguished. Due to the force field settings (see Appendix C for details), the CH_2 sites exhibit a stronger adsorption on the substrate surface. Therefore, the first adsorption peak stems from CH_2 sites. Due to the fact that the bond length between CH_2 and CH_3 sites is smaller than the size parameter of the two sites, an overlap of the first CH_2 and CH_3 adsorption peak is observed. With increasing z , only two more distinct peaks are observed in both the CH_2 and CH_3 profile. Also, due to the molecular structure of decane, the depth of the first groove does not decay to zero as observed for methane. Overall, the total fluid density profile in the case of decane shows a smoother transition from the surface into the bulk phase in comparison to methane due to the differences in the molecular structure. This has important consequences for the tribological behavior of the contact process – in particular the stick-slip motion. Thereby, the more disordered adsorption layers in the case of decane contributes to a lower coefficient of friction in the ML and the HL regime compared to the methane case.

Fig. 62 shows detailed screenshots of the tribofilm and the lubrication gap from the atomistic visualization of the rear side of the indenter. The gap heights $h = 8 \text{ \AA}$, 0 \AA , and -6 \AA are exemplarily shown. In the HL regime (cf. Figs. 62 a) and d)), the methane particles form a strongly structured solid-like adsorption layer, whereas the decane molecules form a more disordered adsorption layer. It can be clearly seen that, at $h = -6 \text{ \AA}$ (cf. Figs. 62 c) and f)), the fluid adsorption layer is broken-up and fluid particles are imprinted into the surface. The screenshots shown in Fig. 62 - bottom moreover reveal important differences regarding the formation of the tribofilm during the contact process: During the indentation (left part of the groove), the number of methane particles imprinted into the substrate is high enough such that the substrate lattice structure is broken-up and the tribofilm became amorphous. With ongoing lateral movement (middle and right part of the tribofilm depicted in Fig. 62 c), less methane fluid particles are imprinted into the substrate and the tribofilm remains a crystalline structure. In the case of decane (Fig. 62 f)), the imprinted relatively large and elongated decane molecules cause a semi-amorphous-crystalline structure during the entire contact.

Fig. 63 shows the histograms of the fluid particle interaction sites in the tribofilm as a function of the coordinate z . The origin $z = 0$ lies on the unperturbed substrate surface, cf. Fig. 53. In the HL regime, practically no fluid particles are imprinted into the substrate surface. In the ML regime, the break-up of the adsorption layer in combination with the high contact forces initializes the formation of the tribofilm. In the BL regime, the close contact of the two solid bodies in combination with elastic and plastic deformation of the substrate and the very high contact forces cause the

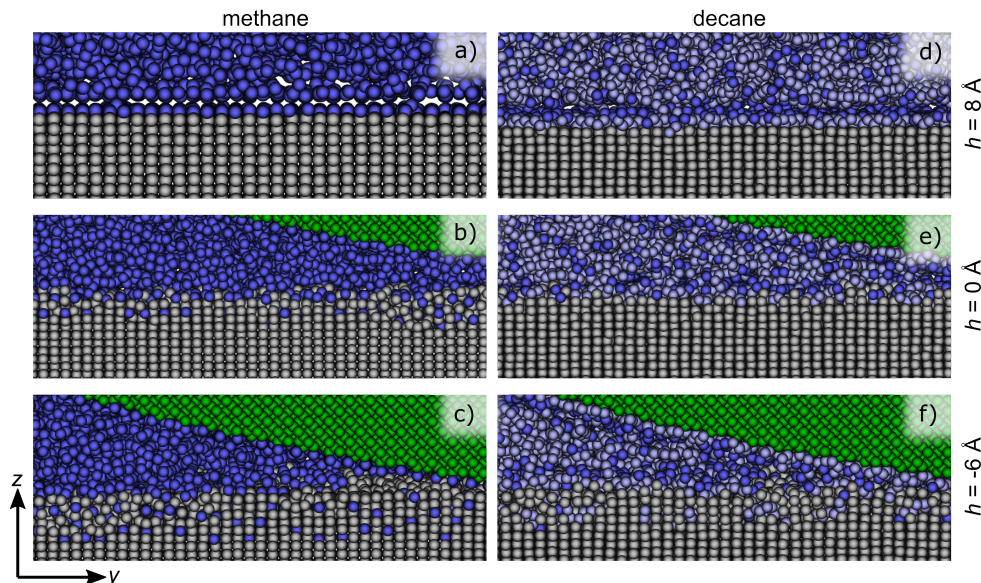


Figure 62: Screenshots of the rear side (in moving direction) of the contact zone for a selection of the simulations. Results shown for $h = 8 \text{ \AA}$ (top), 0 \AA (middle), and -6 \AA (bottom). Left column shows results for the methane simulations; right column those for the decane simulations. Green particles indicate the indenter; blue particles indicate the fluid; gray particles indicate the substrate. For decane, dark blue indicates the CH_3 interaction sites and bright blue the CH_2 sites. The screenshots were in all cases taken at the simulation time $\tau_{\text{scratch}} = 1200 \text{ ps}$ and at $x = 200 \text{ \AA}$. The perspective is in positive x -direction and the indenter motion was in y -direction.

formation of a prominent tribofilm. The formation of dislocations at the substrate surface in conjunction with deformations (formation of groove and chip) makes space for fluid particles. While it is energetically unfavorable for fluid particles to penetrate the atomistically flat surface, it becomes easier to penetrate the surface in the vicinity of a dislocation, i.e. a lattice defect. Hence, the deformation of the substrate increases the amount of energetically favorable locations, where fluid particles can be imprinted into the surface. Moreover, the imprinting of methane particles is energetically evidently less costly compared to the imprinting of elongated decane particles. Thus, methane particles are imprinted at lower gap height h , cf. Fig. 63 - top, compared to decane particles.

In the BL regime, the tribofilm has a thickness of approximately 10 \AA , cf. Fig. 63. Important differences are observed for the methane and the decane cases. At a given gap height, the thickness of the tribofilm is larger in the case of methane. More importantly, the structure of the tribofilm formed by the two fluids differs significantly: In the case of decane, a smooth profile of the number of imprinted fluid interaction sites is observed over the entire thickness of the tribofilm, which exhibits a single maximum slightly below the substrate surface $z = 0$. In the case of methane on the other hand, a profile with

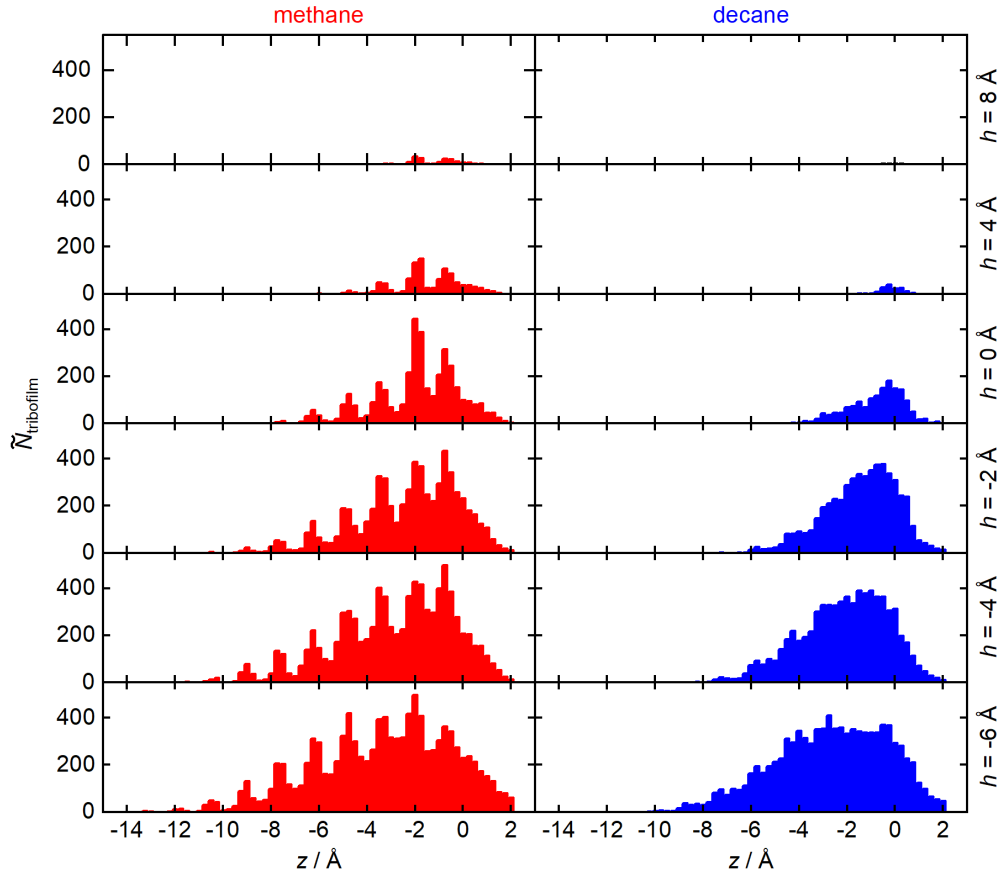


Figure 63: Histogram of fluid particle interaction sites in the tribofilm of the substrate surface. Results shown for $h = 8, 4, 0, -2, -4, -6 \text{ \AA}$ (top to bottom). The left column gives the results for the methane simulations; the right column those for the decane simulations. Data was taken at the end of the scratching.

distinct oscillations is observed indicating that the methane particles substitute lattice atoms of the substrate. This is due to the fact that the methane particles have a similar size as the lattice atoms. This again shows that the substrate surface in the BL regime is strongly distorted in the decane cases, whereas the lattice structure remains more intact in the methane cases – despite the fact that more fluid particles (i.e. interaction sites) are imprinted into the substrate surface, cf. Fig. 60.

The tribofilm comprises particles also at $z > 0 \text{ \AA}$, cf. Fig. 63. This is due to the fact that fluid particles are also imprinted into the chip surface sideways of the indenter, cf. Fig. 58. Moreover, the maximum peak of the tribofilm histogram slightly shifts deeper into the substrate body with decreasing gap height h . This is a result of the formation of the groove in the substrate (cf. Fig. 58). Hence, effectively the substrate surface is pushed to lower z values, but the sampling of $\tilde{N}_{\text{tribofilm}}$ and $N_{\text{tribofilm}}$ remains in the fixed coordinate system. Therefore, this shift is mostly an artifact of the definition of the observable.

Summarizing, for the tribofilm, methane particles substitute lattice atoms in the substrate, whereas decane particles cause a severe distortion of the surface upon being imprinted into the substrate surface. For the lubrication: While the methane adsorption layer is more structured than that of decane, the methane adsorption layer is broken-up more easily. The tribofilm behavior is more relevant in the BL regime; the adsorption layer behavior is more relevant in the ML regime.

6.3.2 Thermodynamic Properties

Fig. 64 shows the heat removed by the thermostat $Q_{\text{thermostat}}$ during the contact process. At the beginning of the lateral movement, some transient processes occur (cf. Fig. 64 - top), which is in accordance with the course obtained for the forces on the indenter (cf. Fig. 55). Then, at approximately $\tau = 900$ fs, the contact process and the heat removed via the thermostat reach a quasi-stationary state, cf. Fig. 64 - top. This holds for all studied gap heights for both the methane and the decane simulations. Fig. 64 - bottom shows the mean heat flux $\dot{Q}_{\text{thermostat}} = dQ_{\text{thermostat}}/d\tau$ during the quasi-stationary regime as a function of the gap height. The comparison of Fig. 56 - bottom and Fig. 64 - bottom shows that 80 ... 95% of the work done by the indenter dissipates into heat that is then removed by the thermostat. In the BL regime, the plastic deformation of the substrate for the formation of the groove and the chip as well as the formation of the tribofilm causes large dissipation of heat in comparison to the ML and HL regime. In the HL regime, the heat flux $\dot{Q}_{\text{thermostat}}$ removing the dissipated heat from the system is about two orders of magnitude smaller compared to the BL regime. In the HL regime, the dissipated heat hardly depends on the gap height. This is as expected, as viscous friction dominates the system in that regime. The comparison of the methane and the decane cases regarding the heat removed from the system provides further interesting insights. In the BL regime, more energy dissipates in the decane cases compared to the methane cases. This is due to the fact that the imprinting of decane molecules and the formation of the amorphous tribofilm requires more energy compared to the methane case. In the ML regime, more dissipated energy is removed from the system in the methane cases compared to the decane cases. For $h \approx 2 \text{ \AA}$, the dissipated heat in the case of methane is about twice that in the case of decane. This is due to the dominance of the adsorbed fluid layers and their break-up, which is more energy intense for the strongly structured methane particles (cf. Fig. 61). Moreover, for the methane simulations in the thin film regime, a tribofilm formation already takes place (cf. Fig. 57), which also requires energy.

Figs. 65 and 66 show the fluid temperature and pressure field, respectively, averaged over the entire quasi-stationary part of the simulations. Results for $h = -6, -4, -2, 0, 4, 8 \text{ \AA}$

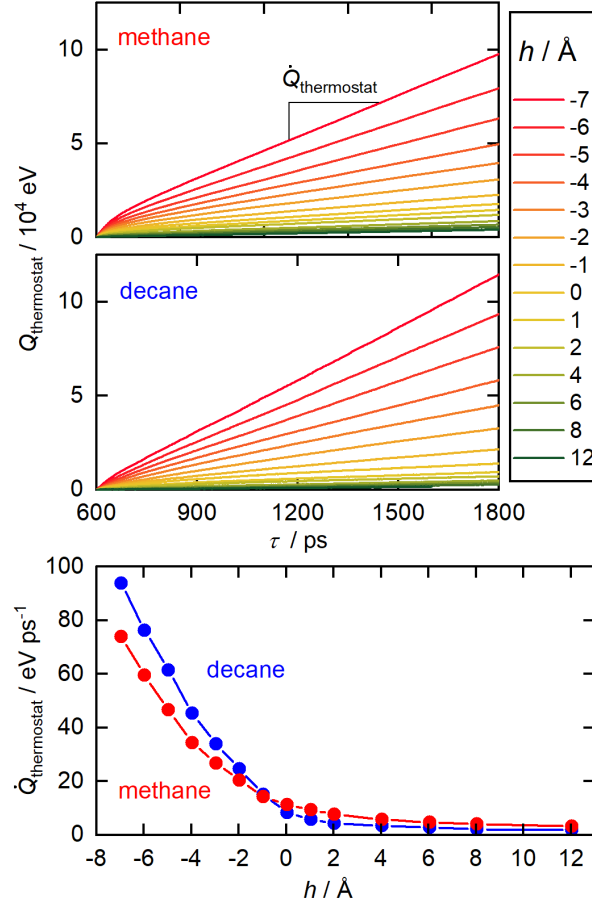


Figure 64: Total energy removed by the thermostat as a function of the simulation time (top) and energy removal rate during the quasi-stationary phase of the lateral movement of the indenter as function of the gap height (bottom). Lines are a guide for the eye (for the bottom plot).

are shown for both methane and decane. The temperature and the pressure field were computed with respect to the initial bulk values. The temperature field shows an elliptic shape, whereas the pressure field is more complex and unsymmetric. This confirms predictions from mesoscopic modeling approaches [198, 239]. The pressure profile is strongly influenced by the differences between the fluid inlet and outlet flow. Both the temperature and pressure fields reflect the shape of the indenter, i.e. the fluid flow passing through the constriction underneath the indenter. Overall, both the fluid temperature and pressure in the gap increases with decreasing gap height h . The pressure profiles are primarily influenced by the obtained normal force F_N at a given gap height, cf. Fig. 56 a). The temperature profiles are primarily influenced by the dissipation behavior of the system and the work done by the indenter and thereby by the tangential force F_T at a given gap height, cf. Fig. 56 a) and c). For both the temperature and pressure fields, the center of the pattern is shifted slightly in positive y' -direction, i.e. is located slightly towards the front side of the indenter.

In the HL regime, practically no temperature increase ΔT is observed for the fluid

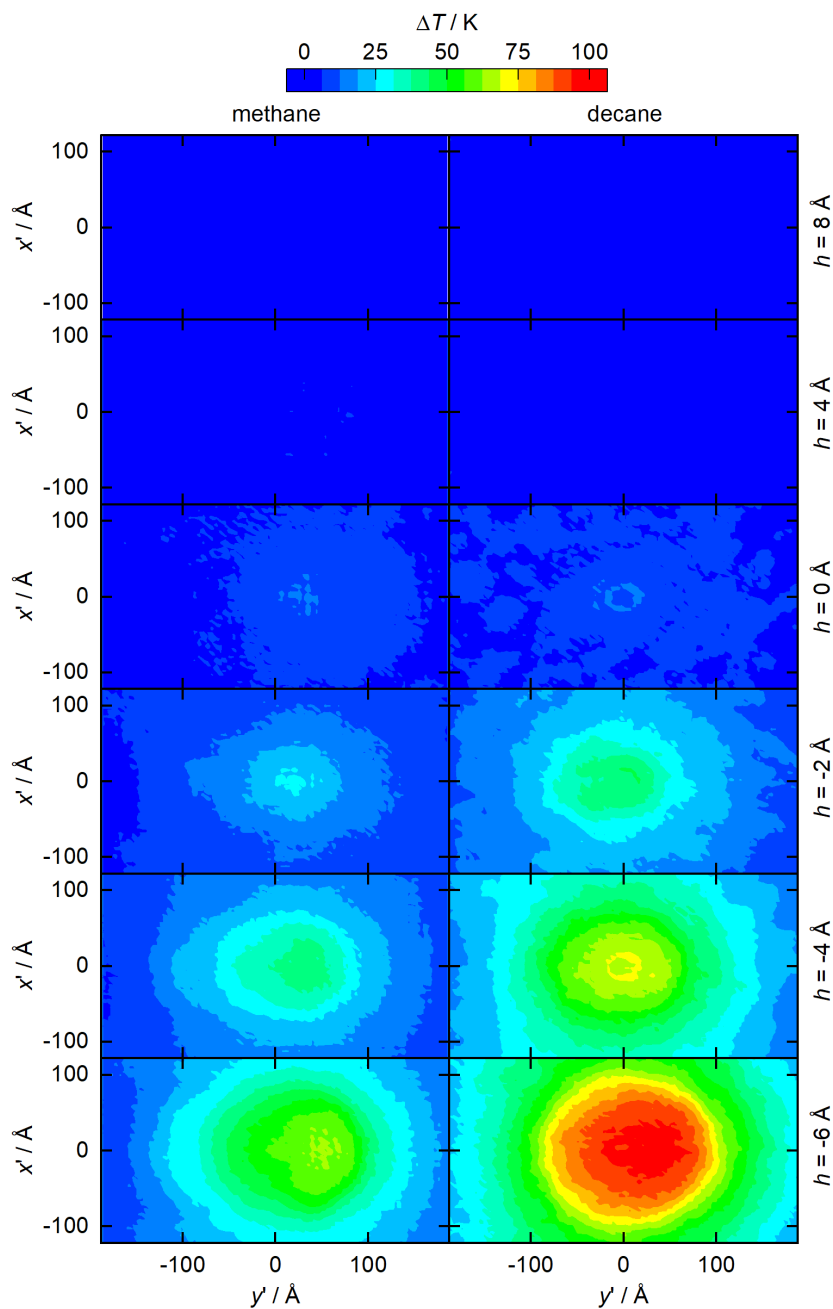


Figure 65: Temperature field of the fluid in the lubrication gap with respect to the moving coordinate system (cf. Fig. 53). The lubrication gap was determined by the slit between the alpha shape surface of the indenter and the substrate. Results shown for $h = 8, 4, 0, -2, -4, -6 \text{ \AA}$ (top to bottom). The left column shows the results for the methane simulations; the right column those for the decane simulations. Data was sampled during the quasi-stationary phase ($\tau_{\text{scratch}} \geq 400 \text{ ps}$). The color code is the same for all shown plots.

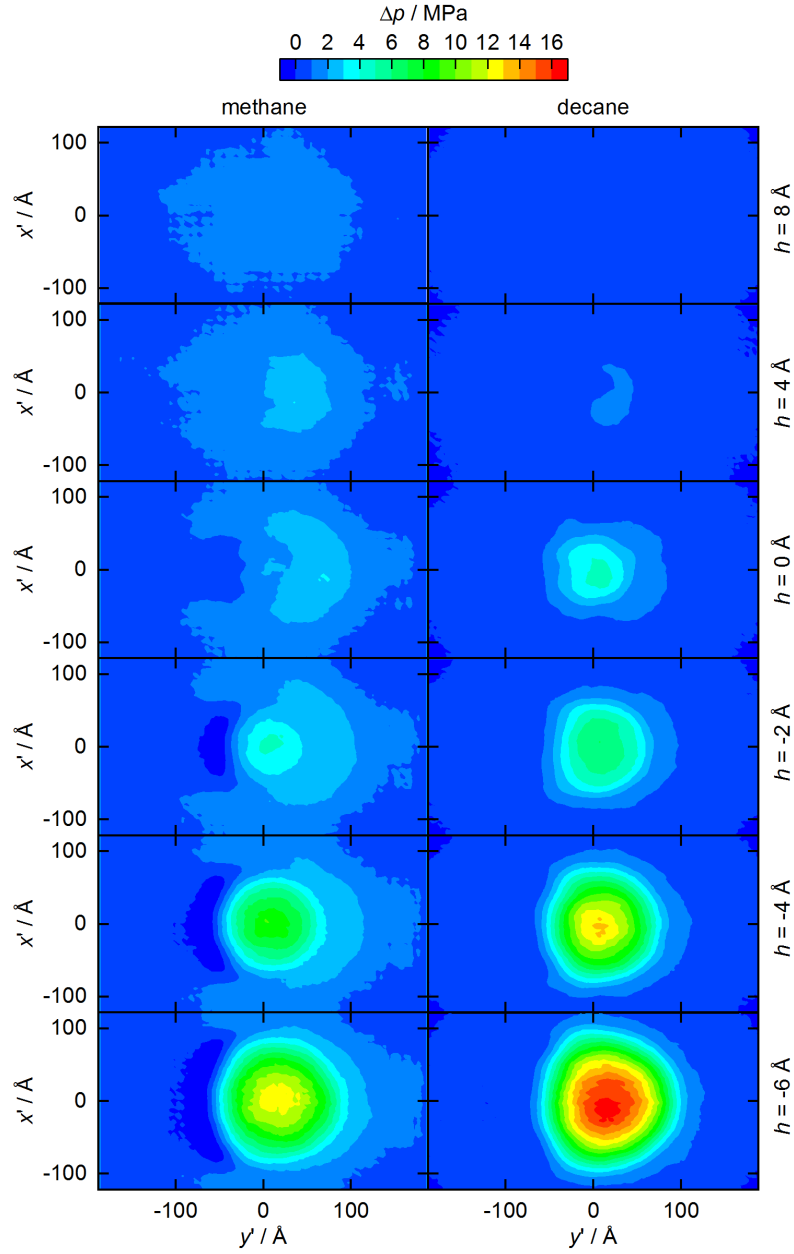


Figure 66: Pressure field of the fluid in the lubrication gap with respect to the moving coordinate system (cf. Fig. 53). The lubrication gap was determined by the slit between the alpha shape surface of the indenter and the substrate. Results shown for $h = 8, 4, 0, -2, -4, -6 \text{ \AA}$ (top to bottom). The left column shows the results for the methane simulations; the right column those for the decane simulations. Data was sampled during the quasi-stationary phase ($\tau_{\text{scratch}} \geq 400 \text{ ps}$). The color code is the same for all shown plots.

in the gap (cf. Fig. 65), which is in accordance with the dissipation behavior (cf. Fig. 64). Only a faint pressure increase Δp is observed in that regime – for the methane case (cf. Fig. 66). In the ML regime, a temperature increase of about $\Delta T \approx 25$ K is detected – which is similar for the two fluids. This is probably due to the fact that the thermodynamic properties in adsorbed fluid layers are very similar to the corresponding bulk phase behavior [219]. In the BL regime, both the temperature and the pressure in the gap are strongly increased compared to the bulk phase values, cf. Figs. 65 and 66.

The pressure fields for the methane cases (cf. Fig. 66) in the BL regime exhibit a significant pressure drop, i.e. the pressure at the rear side of the indenter (out-flow of the fluid) is smaller than the bulk phase pressure. This is due to the expansion of the fluid in the outlet of the rear side of the indenter, which led to the formation of a vapor phase.

The comparison between the methane and the decane cases provide additional insights in the contact process. Fig. 67 - top and bottom shows the maximum temperature and maximum pressure increase of the fluid in the gap as a function of the gap height during the quasi-stationary phase. The temperature of the fluid in the gap increases up to $\Delta T^{\max} \approx 100$ K; the pressure increases up to $\Delta p^{\max} \approx 16$ MPa. In the BL regime, the maximum temperature ΔT^{\max} in the fluid decreases linearly with increasing gap height h . Moreover, in the BL regime, both the temperature and pressure of the fluid in the gap increase more strongly during the lateral movement in the decane case. This is in line with the findings for the contact forces (cf. Fig. 56), the formation of the tribofilm (cf. Fig. 63), and the dissipated energy (cf. Fig. 64). For $h = -6$ Å, the temperature increases about 50 K more in contact zone in the case of decane in comparison to the methane case. Also in line with the dissipated heat removed by the thermostat, a cross-over between the methane and decane simulations is observed for ΔT^{\max} in the ML regime. In the HL regime, the temperature increase of the two fluids is essentially the same and hardly depends on the gap height.

The maximum pressure of the fluid in the gap Δp^{\max} (cf. Fig. 67 - bottom) overall shows a similar behavior as the maximum temperature (cf. Fig. 67 - top). The observable $\Delta p^{\max}(h)$ has a large gradient in the BL regime, then flattens in the ML regime, and finally converges in the HL regime. However, some differences in the ΔT^{\max} and Δp^{\max} behavior can be pointed out: The cross-over of the methane and decane results for ΔT^{\max} at $h \approx -1$ Å is in excellent agreement with the behavior of the dissipated heat removed from the system $\dot{Q}_{\text{thermostat}}$ (cf. Fig. 64). The cross-over of the methane and decane results for Δp^{\max} on the other hand at $h \approx -2$ Å is in excellent agreement with the behavior of the total normal force on the indenter F_N (cf. Fig. 56). This shows that for the thermodynamic properties of the fluid, the fluid pressure is dominated by the contact pressure imposed by the indenter, whereas the fluid temperature is a result

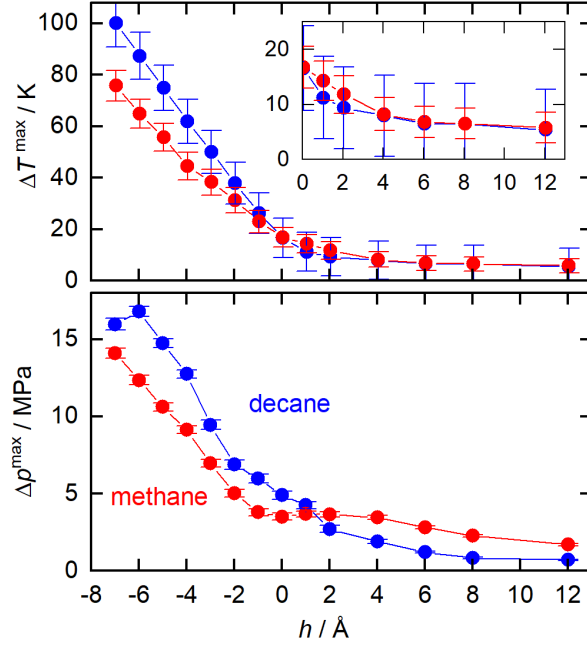


Figure 67: Maximum temperature (top) and pressure (bottom) of the fluid in the contact zone during the quasi-stationary phase of the lateral movement of the indenter as a function of the gap height. Results shown for the methane (red) and decane (blue) simulations. Lines are a guide for the eye.

of multiple simultaneous phenomena, e.g. the distortion of the adsorption layer, the formation of the tribofilm, and the elastic and plastic deformation of the substrate.

6.4 Conclusions

The atomistic mechanisms of the three main lubrication regimes of the Stribeck curve were studied using a simplified yet representative large-sized MD simulation setup. Thereby, the transition from boundary lubrication, to mixed lubrication, and hydrodynamic lubrication was elucidated. The behavior of two fluids in the system were studied: Methane (as a simple model fluid) and decane (as a model lubricant).

It is found that different mechanisms on the atomistic level dominate the different lubrication regimes. In the BL regime, the formation of a tribofilm, the squeeze-out, and the holding-up of the lubrication film are crucial. In the ML regime, the behavior of the adsorption layer in the gap is crucial – in particular a possible break-up of the adsorption layer structure. In the HL regime, the influence of the fluid bulk phase properties prevail – as expected. Yet, the gap height of the transition between the BL, ML, and HL regime depends on the studied system.

The simulation scenario used in this work can be favorably used to study different lubrication regimes. For future work, it would be interesting to study the effect of

different simulation parameters, e.g. to assess the influence of the periodic boundary conditions applied in x - and y -direction, which may in general affect the fluid flow and fluid pressure field. Moreover, it would be interesting to modify the scenario such that the normal load instead of the gap height is prescribed. Also, it would be interesting to study the relation of the formation of the tribofilm and the dislocation behavior as well as to consider the thermal effects of the substrate, i.e. the heat transfer in the bulk material, in more detail. Yet, a larger substrate size would have to be considered in the simulations. Moreover, it would be interesting to consider a reactive force field for the fluid to obtain more realistic predictions for the formation of the tribofilm.

Important insight was gained into the formation and influence of the tribofilm. If long chain molecules such as decane form a tribofilm, this formation requires a significant amount of energy as the surface structure of the substrate is distorted and the relatively large molecules are imprinted into the surface. Opposite to that, if small molecules such as methane form a tribofilm, this is found to require less energy as the lattice structure remains in most parts intact and the fluid particles substitute lattice atoms. Nevertheless, these energetic relations also result in the fact that the formation of a tribofilm occurs already at larger gap height for methane used as a fluid. The formation of a tribofilm with a decane fluid on the other hand requires larger forces, contact pressure etc.

7 Discussion and Outlook

7.1 Critical Discussion

Simplifications and assumptions in a model design in general influence the applicability and reliability of the results. Here, it is critically discussed, how the main findings obtained from the simulations carried out in this work might be influenced by simplifications of the model. The main findings to be critically discussed are: The imprinting of fluid molecules into the substrate surface and the formation of a tribofilm (cf. chapters 5 and 6); the alteration of the coefficient of friction by the presence of a fluid compared to a dry case (cf. chapters 3 and 4); the cooling of the contact zone by the presence of a fluid (cf. chapters 3 and 6); and the squeeze-out behavior of the fluid from the contact zone (cf. chapters 3 and 6). It should be noted that this section does not claim to provide a complete list of possible model factors that might influence the results.

The imprinting of fluid molecules into the substrate surface and the formation of a tribofilm is probably significantly influenced by assumptions and simplifications of the model. For example, this formation mechanism is probably influenced by the fact that a single crystal without any defects and grain boundaries in the initial state is considered. One would assume that the imprinting of fluid molecules can occur more easily if defects are already present in the crystal, e.g. a grain boundary at the substrate surface, cf. Fig. 3. The same essentially holds for the fact that a perfectly atomistically flat surface was considered in this work, i.e. irregularities of the surface topography would likely act as a favorable point of entry for imprinted fluid particles. Also the fact that no oxide and 'dirt' layer was considered in this work probably influences the imprinting mechanisms, i.e. a tribofilm would be formed of at least three component particles (substrate, fluid, and oxide) in such a case, which might influence the behavior of the tribosystem. Also, the fluid models used in the simulations, i.e. non-reactive united atom force fields, probably influence the tribofilm formation mechanisms.

The presence of a fluid in the tribosystem alters the coefficient of friction. The coefficient of friction is reduced by the presence of a fluid compared to a dry case in the starting phase of the contact, i.e. before the fluid is squeezed out of the contact. This

is found to be a results of the fluid particles being in the gap between the indenter and substrate in that phase. During that starting phase, the coefficient of friction is reduced, whereas it is slightly increased in a lubricated case in the (quasi-stationary) follow-up phase. Hence, there is a sequence of the contact being initially filled by fluid particles and then a direct contact between the two solid bodies. However, this sequence is likely a result of the model setup, which consists of an initially atomistically flat substrate surface. Real component surfaces, on the other hand, have to some extent a rough surface. It is hypothesized here that a surface roughness in such contact processes might cause a 're-filling' of the contact zone with fluid particles such that the contact becomes re-lubricated repetitively. Hence, the findings regarding the 'initially lubricated contact in the starting phase' and 'dry contact during the stationary phase' have to be seen in the context of an (idealized) atomistically flat surface.

The cooling effect of the contact zone by the presence of a fluid is mostly a result of providing an additional energy flux route. Hence, the dissipated energy can leave the contact zone not only via the indenter and the substrate, but additionally via the fluid phase. In the simulation model used in this work, no thermostat was used in the fluid phase that would reflect the heat flux into the bulk fluid material (opposite to the solid phases, cf. chapter 6). Hence, the fluid phase (artificially) continuously heats up during the simulation. Yet, this effect is not considered crucial since the fluid phase was relatively big in the simulations such that the overall temperature increase of the fluid probably does not have a critical influence on the other elementary processes (e.g. squeeze-out, tribofilm formation etc.).

Important insights were gained in this work on the behavior of the fluid in the contact zone and its squeeze-out. This is also related to the coefficient of friction behavior (discussed above). Additionally, the squeeze-out mechanism itself is likely influenced by simplifications of the simulation model such as the atomistically flat surface, the negligence of oxide and 'dirt' on the surface, and the choice of the solid-fluid interactions. In particular, a significant influence of a surface roughness on the squeeze-out behavior is expected.

The determination of the solid-fluid interaction model – and in particular the attraction energy of the potential – requires an independent critical discussion. It was shown in this work, that the attraction energy has an important influence on, for example, the squeeze-out behavior, cf. chapters 3 and 5 (which is not surprising). Yet, assigning an appropriate interaction model is a very difficult task (see also discussion in section 6.2.2) and there is no direct feedback loop indicating if the choice was physically appropriate or not. For the model systems (cf. chapters 3 and 4), this does inherently not pose a problem as the solid-fluid interaction energy is understood as a model parameter. For the real substance systems (cf. chapters 5 and 6), on the other hand, this parameter

is critical for the question how well the model reflects reality (see again discussion in section 6.2.2). Evidently, the question of the solid-fluid interaction model is also related to the question if an oxide/ 'dirt' layer should be considered on the solid surfaces. Moreover, the solid-fluid interaction model becomes increasingly important and influential the more fluid particles are imprinted into the substrate surface and a tribofilm is formed.

In summary, some features and simplifications of the simulation model have to be seen critical based on the results and findings of this work. The following model features are thereby suspected to be potentially significantly influential on the findings: Simplifying the substrate to be a single crystal, neglecting the surface roughness and assuming an atomistic flat substrate surface, and not considering the presence of adsorbed oxides and dirt on the substrate.

7.2 Possible Future Work

Based on the critical discussion of the results from this work (see above), multiple interesting steps for future work can be inferred:

- Using a more realistic surface topography instead of an atomistically flat surface, which might have important consequences for the lubrication state and the squeeze-out. Different geometrically well-defined surface structures (e.g. sinusoidal) could be studied as well as surface topographies obtained from real component surface measurement data [36]. This also comprises the shape of the indenter, which could be a cone or a *Berkovich* shape indenter (adapting nanoindentation experiment) [7, 124], which probably would have an influence on the squeeze-out behavior of the lubricant from the contact zone. Analogously, the radius of the (spherical) indenter may influence the squeeze-out behavior, which would be interesting to study in a future work.
- Considering a more detailed and realistic structure of the solid body surfaces regarding oxide layers and chemisorbed components ('dirt') – which will essentially always be present [51] in technical systems. This might also have important consequences for the formation of the tribofilm, the squeeze-out behavior, and the slip.
- Re-designing the simulation model such that no fluid flow above the indenter occurs, which might influence the pressure field in the fluid and thereby the squeeze-out behavior of the fluid.
- Adding a heat sink (thermostat) in the fluid phase for reflecting the heat flux into the bulk material, which evidently would influence the overall thermal balance.

- Using more realistic force field models for the fluid such as all-atom models (instead of united-atom models) that provide a more realistic molecular architecture. Also, reactive force fields for the fluid might provide a more realistic picture as thermal chemical degradation of the fluid molecules might occur under the extreme conditions, which might influence the squeeze-out behavior and the adsorption behavior of the fluid on the solid body surfaces. This might in particular have consequences for the mixed lubrication regime as well as for the formation of the tribofilm in the boundary lubrication regime.
- For the real substance systems, advanced machine learned force fields [393] for modeling the solid-fluid interactions might be an interesting approach. Alternatively, an intermediate step for getting a feedback for the applicability of the determined solid-fluid interaction model might help. Thus, EMD simulations could be carried out for determining simple adsorption isotherms for a given fluid on a given substrate surface using a solid-fluid interaction model. These results could be compared to adsorption isotherm experimental data, which would provide an independent assessment of the applicability of the solid-fluid interaction model.
- Studying the effect of defects and grain boundaries in the substrate crystal on the different lubrication elementary processes, i.e. the squeeze-out, the formation of the tribofilm, and the dissipation mechanisms. In this work, it was shown that the presence of a lubricant has no significant influence on the defect formation in the substrate; However, the effect of defects – in particular grain boundaries – (eventually present at the beginning of the contact process) on the lubrication mechanisms was not evaluated yet.

Also, the work presented here could be favorably extended for studying:

- Contact processes of amorphous (e.g. glass) solid phases. This might have important consequences for the imprinting of fluid particles and the formation of a tribofilm in the surfaces.
- Contact processes of surfaces that previously already experienced a scratching, i.e. studying the scratching process in a groove. This would be particularly interesting for cases, where a tribofilm was formed in the previous process.
- In this work, cases were studied, where the indenter and the substrate were different materials (e.g. iron and diamond), which has consequences for the formation of the tribofilm (cf. chapter 6). It would be interesting to study the special case, where the indenter and the substrate are the same material, e.g. both iron. In this case, the formation of a tribofilm in both surfaces is to be expected, which probably has consequences for the slip behavior and the coefficient of friction.

- Furthermore, it would be interesting to study the coupling of certain effects and mechanisms in more details. For example, fluid adsorption is influenced by the surface topography and the presence of dislocations and grain boundaries at the surface [176]. Hence, the presence of grain boundaries at a substrate surface (cf. Fig. 3) yields a perturbed adsorption layers [176] and perturbed wetting behavior [76], which probably also affects the fluid squeeze-out behavior.
- In this work, the fluid cooling was primarily established by increasing the internal energy of the fluid at homogeneous states, which is determined by the heat capacity. It would be interesting to study cases, where the fluid is in a vapor-liquid equilibrium state, i.e. the liquid phase co-exists with a vapor phase. In such a case, the heat flux to the fluid would result in an evaporation. This would be interesting since the enthalpy of vaporization is significantly larger than the liquid phase heat capacity. Hence, a significantly better cooling performance is expected, which is for example relevant in machining processes, where parts of the lubricant evaporate.
- Similarly, it would be interesting to study the effects of cavitation. Thereby, also a liquid and a vapor phase coexist – usually as a result of the pressure drop on the rear side of the indenter. The implosion of such vapor bubbles can, for example, cause significant wear on the solid body surfaces.
- In this work, pure component fluid lubricants were studied. In most real life application processes, e.g. machining in manufacturing and lubrication in machine parts, mixtures of multiple fluid components exist. In mixtures, additional phenomena occur, e.g. a selective/ competitive adsorption of components at interfaces and gas solubility effects of light-boiling components in the lubricants that can facilitate cavitation as well as complex transport property phenomena.

The developed methodology and simulation setup can be used and extended for addressing various research questions as outlined above.

8 Conclusions

This work contributes to the understanding of the fundamental processes of lubrication on the atomistic scale. Therefore, a simulation methodology that was well-established for studying dry contacts was extended for studying lubricated contact processes. Therein, a (relatively hard) solid body is fully submersed in a fluid lubricant. This solid body is called indenter and had in this work different (spherical) shapes. The kinematics are prescribed. Hence, the indenter carries out a lateral motion with respect to a second (relatively soft) solid body – called substrate. The model concept obtained from this route has some benefits compared to other tribological simulation concepts. Most importantly, the presence of a fluid bulk phase provides a realistic response to the perturbation imposed by the friction of the actual contact. This realistic fluid bulk phase response is crucial for elucidating the squeeze-out and disposition behavior of the fluid in the lubrication gap as well as for elucidating the cooling effect of the fluid. The presence of a fluid bulk phase has – besides these direct consequences – important indirect effects since these mechanisms couple with other mechanisms, e.g. the link of the squeeze-out and the formation of a tribofilm and the link of the cooling effects of the fluid on the elastic and plastic deformation. Moreover, the simulation setup brings the advantage, that different lubrication regimes can be easily studied by prescribing different gap heights.

Nevertheless, studying lubricated contact processes using MD simulation is a challenging modeling task. Both, the simulation setup as well as the molecular force field models have to be carefully selected since a large number of physical effects (e.g. elastic and plastic deformation, tribofilms, adsorption, wetting, cavitation, chemical degradation, heat conduction and energy balance, etc.) has to be covered appropriately. The number of physical effects relevant for lubricated contact processes is in fact too large such that considering them 'all' is (presently) not feasible – especially from a computational resource perspective. Hence, meaningful approximations and simplifications have to be applied such that the dominating effects are covered in the model setup in a meaningful way. In this work, the focus was on providing a realistic bulk fluid phase and studying its effects on the different tribological mechanisms (deformation, dissipation, dislocations, formation of tribofilm etc.).

This work provides several new insights into the atomistic mechanisms of lubrication such as: (i) the presence of a fluid lubricant reduces the coefficient of friction in the starting phase of a contact process; (ii) the fluid has an important effect on the thermal balance of the contact process, e.g. reduces the heat impact on the substrate by about 20%; (iii) all major lubrication regimes can be studied with the developed simulation setup and the well-known Stribeck curve is in fact retrieved from the computer experiment predictions; (iv) fluid particles are imprinted into the substrate surface, which can even lead to the formation of a tribofilm with a thickness of several atoms; (v) the main part (about 80%) of the work done by the indenter dissipates and is removed as heat from the system; (vi) an analysis of the reproducibility and the statistical uncertainties of the observables showed that these findings are significant (in a statistical sense); (vii) the presence of a lubricant reduces fluctuations of several observables, which is attributed to a mechanical coupling between the indenter and the substrate atoms via the lubricant, which balance and dampens force peaks; (viii) the presence of a lubricant slightly increases the groove and the chip, i.e. the plastic deformation, which is a result of fluid adsorption on the surfaces, which effectively increases the indenter size; (ix) the solid-fluid interaction energy has important effects on different aspects of the contact process, e.g. it influences the mobility of the fluid particles adsorbed on the surfaces, which influences the slip. Also, it influences the dissipation behavior since more energy is needed to break the adsorption bonds at high solid-fluid interaction energies; (x) the contact zone is essentially dry after a starting phase during which the fluid is squeezed out of the gap (in the scenario considered in this work, which has a planar substrate surface).

Based on the results and a critical discussion of the simplifications and assumptions applicable in the model, possible next steps for adapting the modeling approach were identified: The fluid particles being imprinted into the substrate surface and the formation of the tribofilm has important consequences for the entire contact process. Yet, no chemical degradation was captured in the model. The results indicate that fluid particles might be disrupted upon the formation of the tribofilm. Therefore, it would be interesting to use a reactive force field in the simulation scenario (which would, however, be computationally significantly more expensive).

A second interesting approach for adapting the simulation setup lies in the substrate surface topography. The results from this work indicate that the presence of the fluid has important effects in the starting phase of a scratching by decreasing the friction. After the vast majority of the fluid particles is squeezed out of the gap, the friction conditions during the ongoing steady state scratching process were not improved by the presence of the fluid. A steady state is established as a result of the atomistically flat substrate surface. Hence, it would be interesting to study the lubrication behavior and

squeeze-out in a modified setup using a rough substrate surface. The hypothesis is that the contact between the indenter and the substrate thereby becomes 're-lubricated' from passing valleys and hills of the surface topography.

Molecular dynamics simulation can be favorably used for studying tribological processes – especially since recent years, where system sizes with 10^6 particles can readily be simulated. Thereby, the big strength of MD simulation computer experiments – the strong physical basis of the framework – can be well exploited in tribology. The MD computer experiment approach required relatively few adjustable parameters (and none to be adjusted to tribological data) such that predictions are feasible, i.e. 'simulating physics' in the sense of *Feynman* [119]. Using MD computer experiments, this work provides novel insights into the inner workings and physical elementary processes of lubrication on the atomistic scale.

Literature

- [1] P. Abel, A. Szeri: Surface Physics in Tribology in 'Modern Tribology Handbook: Volume One: Principles of Tribology', 1 ed., CRC Press, Boca Raton, US, 2000.
- [2] M. Abraham, R. Apostolov, J. Barnoud, P. Bauer, C. Blau, A.M. Bonvin, M. Chavent, J. Chodera, K. Condic-Jurkic, L. Delemotte, H. Grubmueller, R.J. Howard, E.J. Jordan, E. Lindahl, O.H. Samuli Ollila, J. Selent, D.G. Smith, P.J. Stansfeld, J.K. Tiemann, M. Trellet, C. Woods, A. Zhmurov: Sharing data from molecular simulations, *Journal of Chemical Information and Modeling* 59 (2019) 4093–4099. doi:10.1021/acs.jcim.9b00665.
- [3] R. Aghababaei, D.H. Warner, J.F. Molinari: Critical length scale controls adhesive wear mechanisms, *Nature Communications* 7 (2016) 11816. doi:10.1038/ncomms11816.
- [4] J. Ahrens, B. Geveci, C. Law: ParaView: An end-user tool for large-data visualization, in: *Visualization Handbook*, Elsevier, 2005, pp. 717–731. doi:10.1016/B978-012387582-2/50038-1.
- [5] M. Aichele, M.H. Müser: Kinetic friction and atomistic instabilities in boundary-lubricated systems, *Physical Review E* 68 (2003) 016125. doi:10.1103/PhysRevE.68.016125.
- [6] B.J. Alder, T.E. Wainwright: Studies in molecular dynamics. i. general method, *The Journal of Chemical Physics* 31 (1959) 459–466. doi:10.1063/1.1730376.
- [7] I.A. Alhafez, A. Brodyanski, M. Kopnarski, H.M. Urbassek: Influence of tip geometry on nanoscratching, *Tribology Letters* 65 (2017) 26. doi:10.1007/s11249-016-0804-6.
- [8] I.A. Alhafez, H.M. Urbassek: Scratching of hcp metals: A molecular-dynamics study, *Computational Materials Science* 113 (2016) 187–197. doi:10.1016/j.commatsci.2015.11.038.

- [9] M.P. Allen, D.J. Tildesley: *Computer Simulation of Liquids*, Oxford University Press, Oxford, 1989.
- [10] R.J. Allen, D. Frenkel, P.R. ten Wolde: Forward flux sampling-type schemes for simulating rare events: Efficiency analysis, *The Journal of Chemical Physics* 124 (2006) 194111. doi:10.1063/1.2198827.
- [11] R. An, L. Huang, Y. Long, B. Kalanyan, X. Lu, K.E. Gubbins: Liquid–solid nanofriction and interfacial wetting, *Langmuir* 32 (2016) 743–750. doi:10.1021/acs.langmuir.5b04115.
- [12] I. Antolović, J. Staubach, S. Stephan, J. Vrabec: Phase equilibria of symmetric Lennard-Jones mixtures and a look at the transport properties near the upper critical solution temperature 25 (2023) 17627–17638. doi:10.1039/d3cp01434g.
- [13] H.D. Aristizabal, P.A. Parra, P. López, E. Restrepo-Parra: Atomic-scale simulations of material behaviors and tribology properties for BCC metal film, *Chinese Physics B* 25 (2016) 010204. doi:10.1088/1674-1056/25/1/010204.
- [14] N.W. Ashcroft, N.D. Mermin: *Solid state physics*, Cengage Learning, Dehli, 2022.
- [15] A. Bahadori: in: S. Mokhatab, J.Y. Mak, J.V. Valappil, D.A. Wood (Eds.), *Handbook of Liquefied Natural Gas*, Gulf Professional Publishing, Boston, 2014, pp. 147–183. doi:10.1016/B978-0-12-404585-9.00003-9.
- [16] V.G. Baidakov, S.P. Protsenko: Molecular-dynamics simulation of relaxation processes at liquid–gas interfaces in single- and two-component Lennard-Jones systems, *Colloid Journal* 81 (2019) 491–500. doi:10.1134/S1061933X19040021.
- [17] V.G. Baidakov, S.P. Protsenko, Z.R. Kozlova: Shear and bulk viscosity in stable and metastable states of a Lennard-Jones liquid, *Chemical Physics Letters* 517 (2011) 166–170. doi:10.1016/j.cplett.2011.10.041.
- [18] M. Baker: 1,500 scientists lift the lid on reproducibility, *Nature* 533 (2016) 452–454. doi:10.1038/533452a.
- [19] S. Banerjee, S. Naha, I.K. Puri: Molecular simulation of the carbon nanotube growth mode during catalytic synthesis, *Applied Physics Letters* 92 (2008) 233121. doi:10.1063/1.2945798.
- [20] M.S. Barhaghi, J.R. Mick, J.J. Potoff: Optimised Mie potentials for phase equilibria: Application to alkynes, *Molecular Physics* 115 (2017) 1378–1388. doi:10.1080/00268976.2017.1297862.

- [21] J.L. Barrat, F. Chiarutti: Kapitza resistance at the liquid-solid interface, *Molecular Physics* 101 (2003) 1605–1610. doi:10.1080/0026897031000068578.
- [22] T. Barth: On the propagation of statistical model parameter uncertainty in CFD calculations, *Theoretical and Computational Fluid Dynamics* 26 (2012) 435–457. doi:10.1007/s00162-011-0221-2.
- [23] S. Basten, L. Seis, M. Oehler, B. Kirsch, H. Hasse, J.C. Aurich: Tribological behaviour of AISI 4140 and WC-co carbides during dry condition, using cryogenic media, and sub-zero metalworking fluids at high contact stresses, *Wear* 512-513 (2023) 204525. doi:10.1016/j.wear.2022.204525.
- [24] F. Bauer: *Tribologie*, Springer Vieweg, Wiesbaden, 2021.
- [25] S. Becker, M. Kohns, H.M. Urbassek, M. Horsch, H. Hasse: Static and dynamic wetting behavior of drops on impregnated structured walls by molecular dynamics simulation, *The Journal of Physical Chemistry C* 121 (2017) 12669–12683. doi:10.1021/acs.jpcc.6b12741.
- [26] S. Becker, H.M. Urbassek, M. Horsch, H. Hasse: Contact angle of sessile drops in Lennard-Jones systems, *Langmuir* 30 (2014) 13606. doi:10.1021/la503974z.
- [27] S. Becker, S. Werth, M. Horsch, K. Langenbach, H. Hasse: Interfacial tension and adsorption in the binary system ethanol and carbon dioxide: Experiments, molecular simulation and density gradient theory, *Fluid Phase Equilibria* 427 (2016) 476. doi:10.1016/j.fluid.2016.08.007.
- [28] N. Beckmann, P.A. Romero, D. Linsler, M. Dienwiebel, U. Stolz, M. Moseler, P. Gumbsch: Origins of folding instabilities on polycrystalline metal surfaces, *Physical Review Applied* 2 (2014) 064004. doi:10.1103/PhysRevApplied.2.064004.
- [29] H.J. Berendsen, J.P. Postma, W.F. van Gunsteren, A. DiNola, J.R. Haak: Molecular dynamics with coupling to an external bath, *The Journal of Chemical Physics* 81 (1984) 3684–3690. doi:10.1063/1.448118.
- [30] G.O. Berim, E. Ruckenstein: Dependence of the macroscopic contact angle on the liquid-solid interaction parameters and temperature, *The Journal of Chemical Physics* 130 (2009) 184712. doi:10.1063/1.3133327.
- [31] H. Berro, N. Fillot, P. Vergne: Hybrid diffusion: An efficient method for kinetic temperature calculation in molecular dynamics simulations of confined lubricant films, *Tribology Letters* 37 (2009) 1. doi:10.1007/s11249-009-9484-9.

- [32] H. Berro, N. Fillot, P. Vergne: Molecular dynamics simulation of surface energy and ZDDP effects on friction in nano-scale lubricated contacts, *Tribology International* 43 (2010) 1811–1822. doi:10.1016/j.triboint.2010.02.011.
- [33] H. Berro, N. Fillot, P. Vergne, T. Tokumasu, T. Ohara, G. Kikugawa: Energy dissipation in non-isothermal molecular dynamics simulations of confined liquids under shear, *The Journal of Chemical Physics* 135 (2011) 134708. doi:10.1063/1.3644938.
- [34] D. Berthelot: Sur le mélange des gaz, *Comptes rendus hebdomadaires des séances de l'Académie des Sciences* 126 (1898) 1703–1706.
- [35] B. Bhushan (Ed.): *Modern Tribology Handbook: Volume One and Two*, 1 ed., CRC Press, Boca Raton, US, 2000.
- [36] B. Bhushan: *Surface Roughness Analysis and Measurement Techniques in 'Modern Tribology Handbook: Volume One: Principles of Tribology'*, 1 ed., CRC Press, Boca Raton, US, 2000.
- [37] B. Bhushan, J. Israelachvili, U. Landman: Nanotribology: Friction, wear and lubrication at the atomic scale, *Nature* 374 (1995) 607–616. doi:10.1038/374607a0.
- [38] R.C. Bill, D. Wisander: Recrystallization as a controlling process in the wear of some f.c.c. metals, *Wear* 41 (1977) 351–363. doi:10.1016/0043-1648(77)90013-8.
- [39] G. Binnig, C.F. Quate, C. Gerber: Atomic force microscope, *Physical Review Letters* 56 (1986) 930–933. doi:10.1103/physrevlett.56.930.
- [40] T.D. Blake: Slip between a liquid and a solid: D.M. Tolstoi's (1952) theory reconsidered, *Colloids and Surfaces* 47 (1990) 135–145. doi:10.1016/0166-6622(90)80068-F.
- [41] P.J. Blau: Scale effects in steady-state friction, *Tribology Transactions* 34 (1991) 335–342. doi:10.1080/10402009108982042.
- [42] P.J. Blau: *Friction Science and Technology*, 2 ed., CRC Press, Boca Raton, 2009. doi:10.1201/9781420054101.
- [43] R. Boehler: The phase diagram of iron to 430 kbar, *Geophysical Research Letters* 13 (1986) 1153–1156. doi:10.1029/g1013i011p01153.

- [44] K. Bolton, S. Bosio, W.L. Hase, W.F. Schneider, K.C. Hass: Comparison of explicit and united atom models for alkane chains physisorbed on α -Al₂O₃ (0001), *The Journal of Physical Chemistry B* 103 (1999) 3885–3895. doi:10.1021/jp9840026.
- [45] E. Bonaccorso, H.J. Butt, V.S.J. Craig: Surface roughness and hydrodynamic boundary slip of a Newtonian fluid in a completely wetting system, *Physical Review Letters* 90 (2003) 144501. doi:10.1103/PhysRevLett.90.144501.
- [46] F. Bowden, D. Tabor: *Reibung und Schmierung fester Körper*, Springer, Berlin, 1957.
- [47] G.R. Bowman: Improved coarse-graining of Markov state models via explicit consideration of statistical uncertainty, *The Journal of Chemical Physics* 137 (2012) 134111. doi:10.1063/1.4755751.
- [48] C. Braga, J. Muscatello, G. Lau, E.A. Müller, G. Jackson: Nonequilibrium study of the intrinsic free-energy profile across a liquid-vapour interface, *The Journal of Chemical Physics* 144 (2016) 044703. doi:10.1063/1.4940137.
- [49] O. Braun, A. Naumovets: *Nanotribology: Microscopic mechanisms of friction*, *Surface Science Reports* 60 (2006) 79–158. doi:10.1016/j.surfrep.2005.10.004.
- [50] E. Brinksmeier, J. Aurich, E. Govekar, C. Heinzl, H.W. Hoffmeister, F. Klocke, J. Peters, R. Rentsch, D. Stephenson, E. Uhlmann, K. Weinert, M. Wittmann: Advances in modeling and simulation of grinding processes, *CIRP Annals – Manufacturing Technology* 55 (2006) 667–696. doi:10.1016/j.cirp.2006.10.003.
- [51] D.H. Buckley: *Surface Effects in Adhesion, Friction, Wear, and Lubrication*, Elsevier, Amsterdam, 1981.
- [52] G. Bussi, D. Donadio, M. Parrinello: Canonical sampling through velocity rescaling, *The Journal of Chemical Physics* 126 (2007) 014101. doi:10.1063/1.2408420.
- [53] F. Cailliez, P. Pernot: Statistical approaches to forcefield calibration and prediction uncertainty in molecular simulation, *The Journal of Chemical Physics* 134 (2011) 054124. doi:10.1063/1.3545069.
- [54] *Cambridge Dictionary*: 4 ed., Cambridge University Press, Cambridge, UK, 2020.
- [55] F. Cao, J.D. Deetz, H. Sun: Free energy-based coarse-grained force field for binary mixtures of hydrocarbons, nitrogen, oxygen, and carbon dioxide, *Journal of*

- Chemical Information and Modeling 57 (2017) 50–59. doi:10.1021/acs.jcim.6b00685.
- [56] H. Cárdenas, E. Müller: Molecular simulation of the adsorption and diffusion in cylindrical nanopores: Effect of shape and fluid–solid interactions, *Molecules* 24 (2019) 608. doi:10.3390/molecules24030608.
- [57] R.W. Carpick: Measurement of interfacial shear (friction) with an ultrahigh vacuum atomic force microscope, *Journal of Vacuum Science & Technology B* 14 (1996) 1289. doi:10.1116/1.589083.
- [58] R.W. Carpick, M. Salmeron: Scratching the surface: Fundamental investigations of tribology with atomic force microscopy, *Chemical Reviews* 97 (1997) 1163–1194. doi:10.1021/cr960068q.
- [59] L. Casalino, Z. Gaieb, J.A. Goldsmith, C.K. Hjorth, A.C. Dommer, A.M. Harbison, C.A. Fogarty, E.P. Barros, B.C. Taylor, J.S. McLellan, et al.: Beyond shielding: the roles of glycans in the SARS-CoV-2 spike protein, *ACS Central Science* 6 (2020) 1722–1734. doi:10.1021/acscentsci.0c01056.
- [60] W. Castle: Air separation and liquefaction: Recent developments and prospects for the beginning of the new millennium, *International Journal of Refrigeration* 25 (2002) 158–172. doi:10.1016/S0140-7007(01)00003-2.
- [61] E. Ceretti, L. Filice, D. Umbrello, F. Micari: ALE simulation of orthogonal cutting: a new approach to model heat transfer phenomena at the tool-chip interface, *CIRP Annals* 56 (2007) 69–72. doi:10.1016/j.cirp.2007.05.019.
- [62] M. Chandross, C.D. Lorenz, M.J. Stevens, G.S. Grest: Simulations of nanotribology with realistic probe tip models, *Langmuir* 24 (2008) 1240–1246. doi:10.1021/la702323y.
- [63] W.Y. Chang, T.H. Fang, C.N. Fang: Molecular dynamics on interface and nano-scratch mechanisms of alkanethiol self-assembled monolayers, *The Journal of Physical Chemistry B* 113 (2009) 14994–15001. doi:10.1021/jp905389w.
- [64] G.A. Chapela, L.E. Scriven, H.T. Davis: Molecular dynamics for discontinuous potential. IV. Lennard-Jonesium, *The Journal of Chemical Physics* 91 (1989) 4307–4313. doi:10.1063/1.456811.
- [65] B. Chen, J.J. Potoff, J.I. Siepmann: Monte Carlo calculations for alcohols and their mixtures with alkanes. transferable potentials for phase equilibria. 5. united-atom description of primary, secondary, and tertiary alcohols, *Journal of Physical Chemistry B* 105 (2001) 3093–3104. doi:10.1021/jp003882x.

- [66] B. Chen, J.I. Siepmann: Transferable potentials for phase equilibria. 3. explicit-hydrogen description of normal alkanes, *The Journal of Physical Chemistry B* 103 (1999) 5370–5379. doi:10.1021/jp990822m.
- [67] B. Chen, J.I. Siepmann, M.L. Klein: Direct Gibbs Ensemble Monte Carlo simulations for solid-vapor phase equilibria: Applications to Lennard-Jonesium and carbon dioxide, *The Journal of Physical Chemistry B* 105 (2001) 9840–9848. doi:10.1021/jp011950p.
- [68] R. Chen, M. Liang, J. Luo, H. Lei, D. Guo, X. Hu: Comparison of surface damage under the dry and wet impact: Molecular dynamics simulation, *Applied Surface Science* 258 (2011) 1756–1761. doi:10.1016/j.apsusc.2011.10.035.
- [69] Y. Chen, H. Han, F. Fang, X. Hu: MD simulation of nanometric cutting of copper with and without water lubrication, *Science China Technological Sciences* 57 (2014) 1154–1159. doi:10.1007/s11431-014-5519-z.
- [70] Chetan, S. Ghosh, P. Rao: Specific cutting energy modeling for turning nickel-based nimonic 90 alloy under MQL condition, *International Journal of Mechanical Sciences* 146-147 (2018) 25–38. doi:10.1016/j.ijmecsci.2018.07.033.
- [71] H. Childs, E. Brugger, B. Whitlock, J. Meredith, S. Ahern, D. Pugmire, K. Bigas, M. Miller, C. Harrison, G.H. Weber, H. Krishnan, T. Fogal, A. Sanderson, C. Garth, E.W. Bethel, D. Camp, O. Rübel, M. Durant, J.M. Favre, P. Navrátil: VisIt: An End-User Tool For Visualizing and Analyzing Very Large Data, in: *High Performance Visualization—Enabling Extreme-Scale Scientific Insight*, CRC Press, Boca Raton, USA, 2012, pp. 357–372.
- [72] M. Cho, S. Kim, D.S. Lim, H. Jang: Atomic scale stick-slip caused by dislocation nucleation and propagation during scratching of a Cu substrate with a nanoindenter: A molecular dynamics simulation, *Wear* 259 (2005) 1392–1399. doi:10.1016/j.wear.2005.01.002.
- [73] J.D. Chodera, F. Noé: Probability distributions of molecular observables computed from Markov models. II. uncertainties in observables and their time-evolution, *The Journal of Chemical Physics* 133 (2010) 105102. doi:10.1063/1.3463406.
- [74] M. Cieplak, E.D. Smith, M.O. Robbins: Molecular origins of friction: The force on adsorbed layers, *Science* 265 (1994) 1209–1212. doi:10.1126/science.265.5176.1209.

- [75] E. Cihan, S. İpek, E. Durgun, M.Z. Baykara: Structural lubricity under ambient conditions, *Nature Communications* 7 (2016) 12055. doi:10.1038/ncomms12055.
- [76] D. Clarke, M. Gee: Weeting of surfaces and grain boundaries, in: D. Wolf, S. Yip (Eds.), *Materials Interfaces – Atomic-Level Structure and Properties*, Chapman & Hall, London, 1992.
- [77] J. Collins, E. Hurlbert, K. Romig, J. Melcher, A. Hobson, P. Eaton: Sea-level flight demonstration and altitude characterization of a LO₂/LCH₄ based ascent propulsion lander, 45th AIAA/ASME/SAE/ASEE Joint Propulsion Conference proceedings 45 (2009) 4948. doi:10.2514/6.2009-4948.
- [78] K. Condic-Jurkic, N. Subramanian, A.E. Mark, M.L. O'Mara: The reliability of molecular dynamics simulations of the multidrug transporter P-glycoprotein in a membrane environment, *Plos One* 13 (2018) 1–24. doi:10.1371/journal.pone.0191882.
- [79] W.D. Cornell, P. Cieplak, C.I. Bayly, I.R. Gould, K.M. Merz, D.M. Ferguson, D.C. Spellmeyer, T. Fox, J.W. Caldwell, P.A. Kollman: A second generation force field for the simulation of proteins, nucleic acids, and organic molecules, *Journal of the American Chemical Society* 117 (1995) 5179–5197. doi:10.1021/ja00124a002.
- [80] M. Cuesta, P. Aristimuño, A. Garay, P. Arrazola: Heat transferred to the work-piece based on temperature measurements by IR technique in dry and lubricated drilling of Inconel 718, *Applied Thermal Engineering* 104 (2016) 309–318. doi:10.1016/j.applthermaleng.2016.05.040.
- [81] D. Cui, K. Mylvaganam, L. Zhang, W. Liu: Some critical issues for a reliable molecular dynamics simulation of nano-machining, *Computational Materials Science* 90 (2014) 23–31. doi:10.1016/j.commatsci.2014.03.063.
- [82] H. Czichos: Tribosystems, in: T. Mang (Ed.), *Encyclopedia of Lubricants and Lubrication*, Springer, Berlin, 2014, pp. 2178–2183. doi:10.1007/978-3-642-22647-2_303.
- [83] H. Czichos, K.H. Habig (Eds.): *Tribologie-Handbuch*, 5 ed., Springer Vieweg, Berlin, 2020.
- [84] H. Czichos, M. Woydt: Tribological testing and presentation of data, in: *Friction, Lubrication, and Wear Technology*, ASM International, 2017, pp. 16–32. doi:10.31399/asm.hb.v18.a0006402.

- [85] L. Dai, V. Sorkin, Y.W. Zhang: Effect of surface chemistry on the mechanisms and governing laws of friction and wear, *ACS Applied Materials & Interfaces* 8 (2016) 8765–8772. doi:10.1021/acsami.5b10232.
- [86] W. Damm, A. Frontera, J. Tirado-Rives, W.L. Jorgensen: OPLS all-atom force field for carbohydrates, *Journal of Computational Chemistry* 18 (1997) 1955–1970. doi:10.1002/(SICI)1096-987X(199712)18:16<1955::AID-JCC1>3.0.CO;2-L.
- [87] P. Dauber-Osguthorpe, V.A. Roberts, D.J. Osguthorpe, J. Wolff, M. Genest, A.T. Hagler: Structure and energetics of ligand binding to proteins: Escherichia coli dihydrofolate reductase-trimethoprim, a drug-receptor system, *Proteins: Structure, Function, and Bioinformatics* 4 (1988) 31–47. doi:10.1002/prot.340040106.
- [88] M.S. Daw, M.I. Baskes: Embedded-atom method: Derivation and application to impurities, surfaces, and other defects in metals, *Physical Review B* 29 (1984) 6443–6453. doi:10.1103/physrevb.29.6443.
- [89] M.S. Daw, S.M. Foiles, M.I. Baskes: The embedded-atom method: A review of theory and applications, *Materials Science Reports* 9 (1993) 251–310. doi:10.1016/0920-2307(93)90001-u.
- [90] X. Deng, X. Xu, X. Song, Q. Li, C. Liu: Boiling heat transfer of CO₂/lubricant on structured surfaces using molecular dynamics simulations, *Applied Thermal Engineering* 219 (2023) 119682. doi:10.1016/j.applthermaleng.2022.119682.
- [91] B. Derjaguin: Molekulartheorie der äußeren Reibung, *Zeitschrift für Physik* 88 (1934) 661–675. doi:10.1007/bf01333114.
- [92] F. Diewald, M. Lautenschlaeger, S. Stephan, K. Langenbach, C. Kuhn, S. Seckler, H.J. Bungartz, H. Hasse, R. Müller: Molecular dynamics and phase field simulations of droplets on surfaces with wettability gradient, *Computer Methods in Applied Mechanics and Engineering* 361 (2020) 112773. doi:10.1016/j.cma.2019.112773.
- [93] S. Domínguez-García, C.E. Aguilar-Ramírez, L. Béjar-Gómez, R. Maya-Yescas: Mass balance of the tribofilm in lubricated systems, *Tribology International* 155 (2021) 106757. doi:10.1016/j.triboint.2020.106757.
- [94] X. Dong, S. Jahanmir, L. Ives: Wear transition diagram for silicon carbide, *Tribology International* 28 (1995) 559–572. doi:10.1016/0301-679X(96)85544-7.

- [95] Y. Dong, Q. Li, A. Martini: Molecular dynamics simulation of atomic friction: A review and guide, *Journal of Vacuum Science & Technology A: Vacuum, Surfaces, and Films* 31 (2013) 030801. doi:10.1116/1.4794357.
- [96] D. Dowson: *History of tribology*, 2 ed., Wiley, London, 1998.
- [97] T. Dreher, C. Lemarchand, L. Soulard, E. Bourasseau, P. Malfreyt, N. Pineau: Calculation of a solid/liquid surface tension: A methodological study, *The Journal of Chemical Physics* 148 (2018) 034702. doi:10.1063/1.5008473.
- [98] H. Edelsbrunner, D. Kirkpatrick, R. Seidel: On the shape of a set of points in the plane, *IEEE Transactions on Information Theory* 29 (1983) 551–559. doi:10.1109/TIT.1983.1056714.
- [99] S. Eder, D. Bianchi, U. Cihak-Bayr, A. Vernes, G. Betz: An analysis method for atomistic abrasion simulations featuring rough surfaces and multiple abrasive particles, *Computer Physics Communications* 185 (2014) 2456–2466. doi:10.1016/j.cpc.2014.05.018.
- [100] S. Eder, A. Vernes, G. Betz: On the Derjaguin offset in boundary-lubricated nanotribological systems, *Langmuir* 29 (2013) 13760–13772. doi:10.1021/la4026443.
- [101] S. Eder, A. Vernes, G. Vorlaufer, G. Betz: Molecular dynamics simulations of mixed lubrication with smooth particle post-processing, *Journal of Physics: Condensed Matter* 23 (2011) 175004. doi:10.1088/0953-8984/23/17/175004.
- [102] B.L. Eggimann, A.J. Sunnarborg, H.D. Stern, A.P. Bliss, J.I. Siepmann: An online parameter and property database for the TraPPE force field, *Molecular Simulation* 40 (2014) 101–105. doi:10.1080/08927022.2013.842994.
- [103] S. Emrich, T. Lohner, A. Ziegltrum, A. Brodyanski, R. Merz, M. Kopnarski, K. Stahl: Charakterisierung von triboinduzierten Schichten in Abhängigkeit des Schmierstoffs bei Verzahnungen, *Tribologie und Schmierungstechnik* 64 (2017) 25–32. URL: <https://elibrary.narr.digital/article/99.125005/tus201750025>.
- [104] F. Ercolessi, J.B. Adams: Interatomic potentials from first-principles calculations: The force-matching method, *Europhysics Letters (EPL)* 26 (1994) 583–588. doi:10.1209/0295-5075/26/8/005.
- [105] D.J. Evans: Homogeneous NEMD algorithm for thermal conductivity – application of non-canonical linear response theory, *Physics Letters A* 91 (1982) 457–460. doi:10.1016/0375-9601(82)90748-4.

- [106] D.J. Evans, P.T. Cummings: Non-equilibrium molecular dynamics algorithm for the calculation of thermal diffusion in simple fluid mixtures, *Molecular Physics* 72 (1991) 893–898. doi:10.1080/00268979100100621.
- [107] D.J. Evans, G. Morriss: *Statistical Mechanics of Nonequilibrium Liquids*, 2 ed., Cambridge University Press, Cambridge, UK, 2008.
- [108] D.J. Evans, G. Morriss, L. Hood: On the number dependence of viscosity in three dimensional fluids, *Molecular Physics* 68 (1989) 637–646. doi:10.1080/00268978900102421.
- [109] J.P. Ewen, H. Gao, M.H. Müser, D. Dini: Shear heating, flow, and friction of confined molecular fluids at high pressure, *Physical Chemistry Chemical Physics* 21 (2019) 5813–5823. doi:10.1039/C8CP07436D.
- [110] J.P. Ewen, C. Gattinoni, F.M. Thakker, N. Morgan, H.A. Spikes, D. Dini: A comparison of classical force-fields for molecular dynamics simulations of lubricants, *materials* 9 (2016) 1–17. doi:10.3390/ma9080651.
- [111] J.P. Ewen, C. Gattinoni, J. Zhang, D.M. Heyes, H.A. Spikes, D. Dini: On the effect of confined fluid molecular structure on nonequilibrium phase behaviour and friction, *Physical Chemistry Chemical Physics* 19 (2017) 17883–17894. doi:10.1039/C7CP01895A.
- [112] J.P. Ewen, D.M. Heyes, D. Dini: Advances in nonequilibrium molecular dynamics simulations of lubricants and additives, *Friction* 6 (2018) 349–386. doi:10.1007/s40544-018-0207-9.
- [113] J.P. Ewen, S.K. Kannam, B.D. Todd, D. Dini: Slip of alkanes confined between surfactant monolayers adsorbed on solid surfaces, *Langmuir* 34 (2018) 3864–3873. doi:10.1021/acs.langmuir.8b00189.
- [114] J.P. Ewen, S.E. Restrepo, N. Morgan, D. Dini: Nonequilibrium molecular dynamics simulations of stearic acid adsorbed on iron surfaces with nanoscale roughness, *Tribology International* 107 (2017) 264–273. doi:10.1016/j.triboint.2016.11.039.
- [115] J.P. Ewen, H.A. Spikes, D. Dini: Contributions of molecular dynamics simulations to elastohydrodynamic lubrication, *Tribology Letters* 69 (2021) 24. doi:10.1007/s11249-021-01399-w.
- [116] D. Fertig, H. Hasse, S. Stephan: Transport properties of binary Lennard-Jones mixtures: Insights from entropy scaling and conformal solution theory, *Journal of Molecular Liquids* 367 (2022) 120401. doi:10.1016/j.molliq.2022.120401.

- [117] D. Fertig, S. Stephan: Influence of dispersive long-range interactions on transport and excess properties of simple mixtures, *Molecular Physics* 121 (2023) e2162993. doi:10.1080/00268976.2022.2162993.
- [118] R.P. Feynman: Forces in molecules, *Physical Review* 56 (1939) 340–343. doi:10.1103/physrev.56.340.
- [119] R.P. Feynman: Simulating physics with computers, *International Journal of Theoretical Physics* 21 (1982) 467–488. doi:10.1007/BF02650179.
- [120] R.P. Feynman, R.B. Leighton, M. Sands: *The Feynman Lectures on Physics*, Addison-Wesley Publishing, Reading, Massachusetts, 1966.
- [121] N. Fillot, H. Berro, P. Vergne: From continuous to molecular scale in modelling elastohydrodynamic lubrication: Nanoscale surface slip effects on film thickness and friction, *Tribology Letters* 43 (2011) 257–266. doi:10.1007/s11249-011-9804-8.
- [122] J. Fischer, M. Wendland: On the history of key empirical intermolecular potentials, *Fluid Phase Equilibria* 573 (2023) 113876. doi:10.1016/j.fluid.2023.113876.
- [123] A.C. Fischer-Cripps: *Nanoindentation*, 2 ed., Springer, New York, 2004.
- [124] A.C. Fischer-Cripps: Nanoindentation testing, in: *Nanoindentation*, Springer New York, 2011, pp. 21–37. doi:10.1007/978-1-4419-9872-9_2.
- [125] D. Frenkel, B. Smit: *Understanding Molecular Simulation: From Algorithms to Applications*, 2nd ed., Academic Press, Orlando, FL, USA, 2002.
- [126] G. Galliéro, C. Boned, A. Baylaucq: Molecular dynamics study of the Lennard-Jones fluid viscosity: Application to real fluids, *Industrial & Engineering Chemistry Research* 44 (2005) 6963–6972. doi:10.1021/ie050154t.
- [127] J. Gao, W. Luedtke, U. Landman: Friction control in thin-film lubrication, *The Journal of Physical Chemistry B* 102 (1998) 5033–5037. doi:10.1021/jp982150q.
- [128] J. Gao, W.D. Luedtke, D. Gourdon, M. Ruths, J.N. Israelachvili, U. Landman: Frictional forces and Amontons' law: From the molecular to the macroscopic scale, *The Journal of Physical Chemistry B* 108 (2004) 3410–3425. doi:10.1021/jp036362l.

- [129] J. Gao, W.D. Luedtke, U. Landman: Nano-elastohydrodynamics: Structure, dynamics, and flow in nonuniform lubricated junctions, *Science* 270 (1995) 605–608. doi:10.1126/science.270.5236.605.
- [130] J. Gao, W.D. Luedtke, U. Landman: Layering transitions and dynamics of confined liquid films, *Physical Review Letters* 79 (1997) 705–708. doi:10.1103/physrevlett.79.705.
- [131] Y. Gao, A. Brodyanski, M. Kopnarski, H.M. Urbassek: Nanoscratching of iron: A molecular dynamics study of the influence of surface orientation and scratching direction, *Computational Materials Science* 103 (2015) 77–89. doi:10.1016/j.commatsci.2015.03.011.
- [132] Y. Gao, C. Lu, N. Huynh, G. Michal, H. Zhu, A. Tieu: Molecular dynamics simulation of effect of indenter shape on nanoscratch of Ni, *Wear* 267 (2009) 1998–2002. doi:10.1016/j.wear.2009.06.024.
- [133] Y. Gao, C.J. Ruestes, D.R. Tramontina, H.M. Urbassek: Comparative simulation study of the structure of the plastic zone produced by nanoindentation, *Journal of the Mechanics and Physics of Solids* 75 (2015) 58–75. doi:10.1016/j.jmps.2014.11.005.
- [134] Y. Gao, C.J. Ruestes, H.M. Urbassek: Nanoindentation and nanoscratching of iron: Atomistic simulation of dislocation generation and reactions, *Computational Materials Science* 90 (2014) 232–240. doi:10.1016/j.commatsci.2014.04.027.
- [135] Y. Gao, H.M. Urbassek: Evolution of plasticity in nanometric cutting of Fe single crystals, *Applied Surface Science* 317 (2014) 6–10. doi:10.1016/j.apsusc.2014.08.020.
- [136] Y. Gao, H.M. Urbassek: Scratching of nanocrystalline metals: A molecular dynamics study of Fe, *Applied Surface Science* 389 (2016) 688–695. doi:10.1016/j.apsusc.2016.07.139.
- [137] E.J. Garcia, D. Bhandary, M.T. Horsch, H. Hasse: A molecular dynamics simulation scenario for studying solvent-mediated interactions of polymers and application to thermoresponse of poly(n-isopropylacrylamide) in water, *Journal of Molecular Liquids* 268 (2018) 294–302. doi:10.1016/j.molliq.2018.07.025.
- [138] J.W. Gibbs: *The Scientific Papers of J. W. Gibbs*, Dover Publications, 1961.

- [139] C.L. Giusca, R.K. Leach, F. Helary, T. Gutauskas, L. Nimishakavi: Calibration of the scales of areal surface topography-measuring instruments: part 1. measurement noise and residual flatness, *Measurement Science and Technology* 23 (2012) 035008. doi:10.1088/0957-0233/23/3/035008.
- [140] E. Gnecco, E. Meyer: *Elements of Friction Theory and Nanotribology*, Cambridge University Press, Cambridge, 2015. doi:10.1017/CBO9780511795039.
- [141] J. Gore, F. Ritort, C. Bustamante: Bias and error in estimates of equilibrium free-energy differences from nonequilibrium measurements, *Proceedings of the National Academy of Sciences* 100 (2003) 12564–12569. doi:10.1073/pnas.1635159100.
- [142] N.N. Gosvami, S.J. O’Shea: Nanoscale trapping and squeeze-out of confined alkane monolayers, *Langmuir* 31 (2015) 12960–12967. doi:10.1021/acs.langmuir.5b03133.
- [143] H. Graben, J.R. Ray: Eight physical systems of thermodynamics, statistical mechanics, and computer simulations, *Molecular Physics* 80 (1993) 1183–1193. doi:10.1080/00268979300102971.
- [144] M.S. Green: Markoff random processes and the statistical mechanics of time-dependent phenomena. II. irreversible processes in fluids, *The Journal of Chemical Physics* 22 (1954) 398–413. doi:10.1063/1.1740082.
- [145] C. Greiner, J.R. Felts, Z. Dai, W.P. King, R.W. Carpick: Controlling nanoscale friction through the competition between capillary adsorption and thermally activated sliding, *ACS Nano* 6 (2012) 4305–4313. doi:10.1021/nn300869w.
- [146] A. Grossfield, D.M. Zuckerman: Chapter 2: Quantifying uncertainty and sampling quality in biomolecular simulations, volume 5 of *Annual Reports in Computational Chemistry*, Elsevier, 2009, pp. 23–48. doi:10.1016/S1574-1400(09)00502-7.
- [147] W. Grzesik: *Advanced Machining Processes of Metallic Materials*, 2 ed., Elsevier, Amsterdam, Netherlands, 2016. doi:10.1016/B978-0-444-63711-6.00021-1.
- [148] G. Guevara-Carrion, T. Janzen, Y.M. Muñoz Muñoz, J. Vrabec: Mutual diffusion of binary liquid mixtures containing methanol, ethanol, acetone, benzene, cyclohexane, toluene, and carbon tetrachloride, *The Journal of Chemical Physics* 144 (2016) 124501. doi:10.1063/1.4943395.

- [149] G. Guevara-Carrion, C. Nieto-Draghi, J. Vrabec, H. Hasse: Prediction of transport properties by molecular simulation: Methanol and ethanol and their mixture, *The Journal of Physical Chemistry B* 112 (2008) 16664–16674. doi:10.1021/jp805584d.
- [150] E.A. Guggenheim, N.K. Adam: The thermodynamics of adsorption at the surface of solutions, *Proceedings of the Royal Society of London. Series A, Containing Papers of a Mathematical and Physical Character* 139 (1933) 218–236. doi:10.1098/rspa.1933.0015.
- [151] W.F. van Gunsteren, A.E. Mark: Validation of molecular dynamics simulation, *The Journal of Chemical Physics* 108 (1998) 6109–6116. doi:10.1063/1.476021.
- [152] N.G. Hadjiconstantinou, A.L. Garcia, M.Z. Bazant, G. He: Statistical error in particle simulations of hydrodynamic phenomena, *Journal of Computational Physics* 187 (2003) 274–297. doi:10.1016/S0021-9991(03)00099-8.
- [153] T. Halicioglu, G.M. Pound: Calculation of potential energy parameters from crystalline state properties, *Physica Status Solidi* 30 (1975) 619–623. doi:10.1002/pssa.2210300223.
- [154] J.P. Hansen, I. McDonald: *Theory of Simple Liquids*, 4 ed., Academic Press, Oxford, 2013.
- [155] H. Hasegawa, D.G. Pettifor: Microscopic theory of the temperature-pressure phase diagram of iron, *Physical Review Letters* 50 (1983) 130–133. doi:10.1103/physrevlett.50.130.
- [156] M. Hassan, M. Walter, M. Moseler: Interactions of polymers with reduced graphene oxide: van der Waals binding energies of benzene on graphene with defects, *Physical Chemistry Chemical Physics* 16 (2014) 33–37. doi:10.1039/C3CP53922A.
- [157] H. Hasse, J. Lenhard: Boon and bane: On the role of adjustable parameters in simulation models, in: J. Lenhard, M. Carrier (Eds.), *Mathematics as a Tool: Tracing New Roles of Mathematics in the Sciences*, Springer International Publishing, 2017, pp. 93–115. doi:10.1007/978-3-319-54469-4_6.
- [158] X. He, Z. Liu, L.B. Ripley, V.L. Swensen, I.J. Griffin-Wiesner, B.R. Gulner, G.R. McAndrews, R.J. Wieser, B.P. Borovsky, Q.J. Wang, S.H. Kim: Empirical relationship between interfacial shear stress and contact pressure in micro- and macro-scale friction, *Tribology International* 155 (2021) 106780. doi:10.1016/j.triboint.2020.106780.

- [159] G.S. Heffelfinger, F. van Swol: Diffusion in Lennard-Jones fluids using dual control volume grand canonical molecular dynamics simulation (DCV-GCMD), *The Journal of Chemical Physics* 100 (1994) 7548–7552. doi:10.1063/1.466849.
- [160] M. Heier, F. Diewald, M.T. Horsch, K. Langenbach, R. Müller, H. Hasse: Molecular dynamics study of adsorption of the Lennard-Jones truncated and shifted fluid on planar walls, *Journal of Chemical & Engineering Data* 64 (2019) 386–394. doi:10.1021/acs.jced.8b00927.
- [161] M. Heier, F. Diewald, R. Müller, K. Langenbach, H. Hasse: Adsorption of binary mixtures of the Lennard-Jones truncated and shifted fluid on planar walls, *Journal of Chemical & Engineering Data* 66 (2021) 3722–3734. doi:10.1021/acs.jced.1c00350.
- [162] M. Heier, S. Stephan, F. Diewald, R. Müller, K. Langenbach, H. Hasse: Molecular dynamics study of wetting and adsorption of binary mixtures of the Lennard-Jones truncated and shifted fluid on a planar wall, *Langmuir* 37 (2021) 7405–7419. doi:10.1021/acs.langmuir.1c00780.
- [163] M. Heier, S. Stephan, J. Liu, W.G. Chapman, H. Hasse, K. Langenbach: Equation of state for the Lennard-Jones truncated and shifted fluid with a cut-off radius of 2.5σ based on perturbation theory and its applications to interfacial thermodynamics, *Molecular Physics* 116 (2018) 2083–2094. doi:10.1080/00268976.2018.1447153.
- [164] M. Heinen, M. Hoffmann, F. Diewald, S. Seckler, K. Langenbach, J. Vrabec: Droplet coalescence by molecular dynamics and phase-field modeling, *Physics of Fluids* 34 (2022) 042006. doi:10.1063/5.0086131.
- [165] A. Henderson: Paraview guide, a parallel visualization application, Kitware Inc., 2007. URL: <http://www.paraview.org>, <http://www.paraview.org>.
- [166] D.M. Heyes: The Lennard-Jones fluid in the liquid-vapour critical region, *Computational Methods in Science and Technology* 21 (2015) 169. doi:10.12921/cmst.2015.21.04.001.
- [167] D.M. Heyes, E.R. Smith, D. Dini, H.A. Spikes, T.A. Zaki: Pressure dependence of confined liquid behavior subjected to boundary-driven shear, *The Journal of Chemical Physics* 136 (2012) 134705. doi:10.1063/1.3698601.
- [168] T.L. Hill: *Statistical Mechanics*, McGraw-Hill Book, New York, 1956.

- [169] H. Hoang, G. Galliero: Grand canonical-like molecular dynamics simulations: Application to anisotropic mass diffusion in a nanoporous medium, *The Journal of Chemical Physics* 136 (2012) 184702. doi:10.1063/1.4712139.
- [170] A. Hocquet, F. Wieber: Epistemic issues in computational reproducibility: Software as the elephant in the room, *European Journal for Philosophy of Science* 11 (2021). doi:10.1007/s13194-021-00362-9.
- [171] S. Homes, M. Heinen, J. Vrabec, J. Fischer: Evaporation driven by conductive heat transport, *Molecular Physics* 119 (2021) e1836410. doi:10.1080/00268976.2020.1836410.
- [172] M. Horsch, J. Vrabec, H. Hasse: Modification of the classical nucleation theory based on molecular simulation data for surface tension, critical nucleus size, and nucleation rate, *Physical Review E* 78 (2008) 011603. doi:10.1103/PhysRevE.78.011603.
- [173] M.T. Horsch, S.K. Miroshnichenko, J. Vrabec, C.W. Glass, C. Niethammer, M.F. Bernreuther, E.A. Mueller, G. Jackson: Static and dynamic properties of curved vapour-liquid interfaces by massively parallel molecular dynamics simulation, in: *Competence in High Performance Computing*, 1 ed., Springer-Verlag, Berlin Heidelberg, 2010, pp. 73–84. doi:10.1007/978-3-642-24025-6_7.
- [174] H. Hou, Y. Zhang, Z. Li, T. Jiang, J. Zhang, C. Xu: Numerical analysis of entropy production on a LNG cryogenic submerged pump, *Journal of Natural Gas Science and Engineering* 36 (2016) 87–96. doi:10.1016/j.jngse.2016.10.017.
- [175] S. Hsu, R. Gates: *Boundary Lubrication and Boundary Lubricating Films in 'Modern Tribology Handbook: Volume One: Principles of Tribology'*, 1 ed., CRC Press, Boca Raton, US, 2000.
- [176] H. Ibach: *Physics of Surfaces and Interfaces*, Springer, Berlin, 2010. doi:10.1007/3-540-34710-0.
- [177] K.K. Irikura, R.D. Johnson III, R.N. Kacker: Uncertainty associated with virtual measurements from computational quantum chemistry models, *Metrologia* 41 (2004) 369. doi:10.1088/0026-1394/41/6/003.
- [178] J. Israelachvili: *Intermolecular and Surface Forces*, 3 ed., Academic Press, San Diego, 2011. doi:10.1016/C2009-0-21560-1.
- [179] A. Jabbarzadeh, J.D. Atkinson, R.I. Tanner: Effect of the wall roughness on slip and rheological properties of hexadecane in molecular dynamics simulation

- of couette shear flow between two sinusoidal walls, *Physical Review E* 61 (2000) 690–699. doi:10.1103/physreve.61.690.
- [180] T. Janzen, J. Vrabec: Diffusion coefficients of a highly nonideal ternary liquid mixture: Cyclohexane-toluene-methanol, *Industrial & Engineering Chemistry Research* 57 (2018) 16508–16517. doi:10.1021/acs.iecr.8b04385.
- [181] I. Jawahir, H. Attia, D. Biermann, J. Duflou, F. Klocke, D. Meyer, S. Newman, F. Pusavec, M. Putz, J. Rech, V. Schulze, D. Umbrello: Cryogenic manufacturing processes, *CIRP Annals* 65 (2016) 713–736. doi:10.1016/j.cirp.2016.06.007.
- [182] B. Jelinek, S. Groh, M.F. Horstemeyer, J. Houze, S.G. Kim, G.J. Wagner, A. Moitra, M.I. Baskes: Modified embedded atom method potential for Al, Si, Mg, Cu, and Fe alloys, *Physical Review B* 85 (2012) 245102. doi:10.1103/physrevb.85.245102.
- [183] Y.R. Jeng, P.C. Tsai, Y.H. Liu: Adsorbed multilayer effects on the mechanical properties in nanometer indentation depth, *Materials Research Bulletin* 44 (2009) 1995–1999. doi:10.1016/j.materresbull.2009.06.005.
- [184] K. Johnson, J. Woodhouse: Stick-slip motion in the atomic force microscope, *Tribology Letters* 5 (1998) 155–160. doi:10.1023/a:1019106127794.
- [185] W.L. Jorgensen, D.S. Maxwell, J. Tirado-Rives: Development and testing of the OPLS all-atom force field on conformational energetics and properties of organic liquids, *Journal of the American Chemical Society* 118 (1996) 11225–11236. doi:10.1021/ja9621760.
- [186] W.L. Jorgensen, N.A. McDonald: Development of an all-atom force field for heterocycles. properties of liquid pyridine and diazenes, *Journal of Molecular Structure: THEOCHEM* 424 (1998) 145–155. doi:10.1016/S0166-1280(97)00237-6.
- [187] H.P. Jost: Tribology: How a word was coined 40 years ago, *Tribology & Lubrication Technology* 62 (2006) 24–28.
- [188] N. Juristo, O.S. Gomez: Replications of software engineering experiments, in: B. Meyer, M. Nordio (Eds.), *Empirical Software Engineering and Verification*, Springer, 2014. doi:10.1007/978-3-642-25231-0_2.
- [189] S. Kajita, A. Pacini, G. Losi, N. Kikkawa, M.C. Righi: Accurate multiscale simulation of frictional interfaces by quantum mechanics/Green’s function molecular

- dynamics, *Journal of Chemical Theory and Computation* (2023). doi:10.1021/acs.jctc.3c00295.
- [190] G. Kanagalingam, S. Schmitt, F. Fleckenstein, S. Stephan: Data scheme and data format for transferable forcefields for molecular simulation, *scientific data* 10 (2023) 495. doi:10.1038/s41597-023-02369-8.
- [191] T. Kanda, M. Sato, T. Kimura, H. Asakawa: Expander and coolant-bleed cycles of methane-fueled rocket engines, *Transactions of the Japan Society for Aeronautical and Space Sciences* 61 (2018) 106–118. doi:10.2322/tjsass.61.106.
- [192] P. Kapitza: The study of heat transfer in helium II, *Journal of Physics (USSR)* 4 (1941) 181–210.
- [193] R.W. Katz: Techniques for estimating uncertainty in climate change scenarios and impact studies, *Climate Research* 20 (2002) 167. doi:10.3354/cr020167.
- [194] M.C. Kennedy, A. O’Hagan: Bayesian calibration of computer models, *Journal of the Royal Statistical Society: Series B (Statistical Methodology)* 63 (2001) 425–464. doi:10.1111/1467-9868.00294.
- [195] B.H. Kim, A. Beskok, T. Cagin: Molecular dynamics simulations of thermal resistance at the liquid-solid interface, *The Journal of Chemical Physics* 129 (2008) 174701. doi:10.1063/1.3001926.
- [196] B.H. Kim, A. Beskok, T. Cagin: Viscous heating in nanoscale shear driven liquid flows, *Microfluidics and Nanofluidics* 9 (2010) 31–40. doi:10.1007/s10404-009-0515-5.
- [197] C. Kim, O. Borodin, G.E. Karniadakis: Quantification of sampling uncertainty for molecular dynamics simulation: Time-dependent diffusion coefficient in simple fluids, *Journal of Computational Physics* 302 (2015) 485–508. doi:10.1016/j.jcp.2015.09.021.
- [198] H.J. Kim, P. Ehret, D. Dowson, C.M. Taylor: Thermal elastohydrodynamic analysis of circular contacts Part 1: Newtonian model, *Proceedings of the Institution of Mechanical Engineers, Part J: Journal of Engineering Tribology* 215 (2001) 339–352. doi:10.1243/1350650011543583.
- [199] K.S. Kim, M.H. Han, C. Kim, Z. Li, G.E. Karniadakis, E.K. Lee: Nature of intrinsic uncertainties in equilibrium molecular dynamics estimation of shear viscosity for simple and complex fluids, *The Journal of Chemical Physics* 149 (2018) 044510. doi:10.1063/1.5035119.

- [200] B. Kirsch, M. Bohley, P. Arrabiyeh, J. Aurich: Application of ultra-small micro grinding and micro milling tools: Possibilities and limitations, *Micromachines* 8 (2017) 261. doi:10.3390/mi8090261.
- [201] C. Kittel: Introduction to solid state physics, 8 ed., John Wiley & Sons, Singapore, 2005.
- [202] D.A. Kofke, J.I. Siepmann, R.D. Chirico, M. Kroon, P.M. Mathias, G. Sadowski, J. Wu, J.F. Brennecke: Editorial: Molecular modeling and simulation in JCED, *Journal of Chemical & Engineering Data* 61 (2016) 1–2. doi:10.1021/acs.jced.5b01054.
- [203] R. Komanduri, N. Chandrasekaran, L. Raff: Orientation effects in nanometric cutting of single crystal materials: An MD simulation approach, *CIRP Annals – Manufacturing Technology* 48 (1999) 67–72. doi:10.1016/s0007-8506(07)63133-3.
- [204] R. Komanduri, N. Chandrasekaran, L.M. Raff: Molecular dynamics simulation of atomic-scale friction, *Physical Review B* 61 (2000) 14007–14019. doi:10.1103/physrevb.61.14007.
- [205] R. Komanduri, L.M. Raff: A review on the molecular dynamics simulation of machining at the atomic scale, *Proceedings of the Institution of Mechanical Engineers, Part B: Journal of Engineering Manufacture* 215 (2001) 1639–1672. doi:10.1177/095440540121501201.
- [206] N.D. Kondratyuk, V.V. Pisarev: Calculation of viscosities of branched alkanes from 0.1 to 1000 MPa by molecular dynamics methods using COMPASS force field, *Fluid Phase Equilibria* 498 (2019) 151–159. doi:10.1016/j.fluid.2019.06.023.
- [207] L.T. Kong, C. Denniston, M.H. Müser: The crucial role of chemical detail for slip-boundary conditions: Molecular dynamics simulations of linear oligomers between sliding aluminum surfaces, *Modelling and Simulation in Materials Science and Engineering* 18 (2010) 034004. doi:10.1088/0965-0393/18/3/034004.
- [208] L.T. Kong, C. Denniston, M.H. Müser, Y. Qi: Non-bonded force field for the interaction between metals and organic molecules: A case study of olefins on aluminum, *Physical Chemistry Chemical Physics* 11 (2009) 10195–10203. doi:10.1039/B906874K.
- [209] J. Krim: Friction and energy dissipation mechanisms in adsorbed molecules and molecularly thin films, *Advances in Physics* 61 (2012) 155–323. doi:10.1080/00018732.2012.706401.

- [210] L.C. Kröger, W.A. Kopp, M. Döntgen, K. Leonhard: Assessing statistical uncertainties of rare events in reactive molecular dynamics simulations, *Journal of Chemical Theory and Computation* 13 (2017) 3955–3960. doi:10.1021/acs.jctc.7b00524.
- [211] R. Kubo: Statistical-mechanical theory of irreversible processes. i. general theory and simple applications to magnetic and conduction problems, *Journal of the Physical Society of Japan* 12 (1957) 570–586. doi:10.1143/jpsj.12.570.
- [212] T. Kuwahara, G. Moras, M. Moseler: Friction regimes of water-lubricated diamond (111): Role of interfacial ether groups and tribo-induced aromatic surface reconstructions, *Physical Review Letters* 119 (2017) 096101. doi:10.1103/PhysRevLett.119.096101.
- [213] T. Kuwahara, G. Moras, M. Moseler: Role of oxygen functional groups in the friction of water-lubricated low-index diamond surfaces, *Physical Review Materials* 2 (2018) 073606. doi:10.1103/PhysRevMaterials.2.073606.
- [214] U. Landman, W. Luedtke, J. Gao: Atomic-scale issues in tribology: Interfacial junctions and nano-elastohydrodynamics, *Langmuir* 12 (1996) 4514–4528. doi:10.1021/la950890+.
- [215] U. Landman, W. Luedtke, E.M. Ringer: Atomistic mechanisms of adhesive contact formation and interfacial processes, *Wear* 153 (1992) 3–30. doi:10.1016/0043-1648(92)90258-a.
- [216] I. Langmuir: The mechanism of the surface phenomena of flotation, *Transactions of the Faraday Society* 15 (1920) 62. doi:10.1039/tf9201500062.
- [217] I. Langmuir: Mechanical properties of monomolecular films, *Journal of the Franklin Institute* 218 (1934) 143–171. doi:10.1016/s0016-0032(34)90284-2.
- [218] M.P. Lautenschlaeger, H. Hasse: Transport properties of the Lennard-Jones truncated and shifted fluid from non-equilibrium molecular dynamics simulations, *Fluid Phase Equilibria* 482 (2019) 38–47. doi:10.1016/j.fluid.2018.10.019.
- [219] M.P. Lautenschlaeger, H. Hasse: Thermal, caloric and transport properties of the Lennard-Jones truncated and shifted fluid in the adsorbed layers at dispersive solid walls, *Molecular Physics* 118 (2020) e1669838. doi:10.1080/00268976.2019.1669838.

- [220] M.P. Lautenschlaeger, S. Stephan, M. Horsch, B. Kirsch, J. Aurich, H. Hasse: Effects of lubrication on the friction and heat transfer in machining processes on the nanoscale: A molecular dynamics approach, *Procedia CIRP* 67 (2018) 296–301. doi:10.1016/j.procir.2017.12.216.
- [221] M.P. Lautenschlaeger, S. Stephan, H.M. Urbassek, B. Kirsch, J.C. Aurich, M.T. Horsch, H. Hasse: Effects of lubrication on the friction in nanometric machining processes: A molecular dynamics approach, *Applied Mechanics and Materials* 869 (2017) 85–93. doi:10.4028/www.scientific.net/AMM.869.85.
- [222] I. Lazoglu, B. Bugdayci: Thermal modelling of end milling, *CIRP Annals* 63 (2014) 113 – 116. doi:10.1016/j.cirp.2014.03.072.
- [223] A.R. Leach: *Molecular modelling: principles and applications*, 2, Pearson, Edinburgh, 2001.
- [224] R. Leach (Ed.): *Optical Measurement of Surface Topography*, Springer Berlin Heidelberg, 2011. doi:10.1007/978-3-642-12012-1.
- [225] B.J. Lee, W.S. Ko, H.K. Kim, E.H. Kim: The modified embedded-atom method interatomic potentials and recent progress in atomistic simulations, *Calphad* 34 (2010) 510–522. doi:10.1016/j.calphad.2010.10.007.
- [226] S.H. Lee, W. Chen: A comparative study of uncertainty propagation methods for black-box-type problems, *Structural and Multidisciplinary Optimization* 37 (2008) 239. doi:10.1007/s00158-008-0234-7.
- [227] W.J. Lee, S.P. Ju, C.H. Cheng: A molecular dynamics study of nanoindentation on a methyl methacrylate ultrathin film on a Au(111) substrate: Interface and thickness effects, *Langmuir* 24 (2008) 13440–13449. doi:10.1021/la801786u.
- [228] K. Lejaeghere, G. Bihlmayer, T. Björkman, P. Blaha, S. Blügel, V. Blum, D. Caliste, I.E. Castelli, S.J. Clark, A. Dal Corso, S. de Gironcoli, T. Deutsch, J.K. Dewhurst, I. Di Marco, C. Draxl, M. Dułak, O. Eriksson, J.A. Flores-Livas, K.F. Garrity, L. Genovese, P. Giannozzi, M. Giantomassi, S. Goedecker, X. Gonze, O. Grånäs, E.K. Gross, A. Gulans, F. Gygi, D.R. Hamann, P.J. Hasnip, N.A. Holzwarth, D. Iuşan, D.B. Jochym, F. Jollet, D. Jones, G. Kresse, K. Koepnik, E. Küçükbenli, Y.O. Kvashnin, I.L. Locht, S. Lubeck, M. Marsman, N. Marzari, U. Nitzsche, L. Nordström, T. Ozaki, L. Paulatto, C.J. Pickard, W. Poelmans, M.I. Probert, K. Refson, M. Richter, G.M. Rignanese, S. Saha, M. Scheffler, M. Schlipf, K. Schwarz, S. Sharma, F. Tavazza, P. Thunström, A. Tkatchenko, M. Torrent, D. Vanderbilt, M.J. van Setten, V. Van Speybroeck, J.M. Wills, J.R. Yates, G.X.

- Zhang, S. Cottenier: Reproducibility in density functional theory calculations of solids, *Science* 351 (2016) 1394. doi:10.1126/science.aad3000.
- [229] J. Lenhard: *Calculated Surprises. A Philosophy of Computer Simulation*, Oxford University Press, New York, 2019.
- [230] J. Lenhard, H. Hasse: Traveling with TARDIS. parameterization and transferability in molecular modeling and simulation, *Synthese* 201 (2023). doi:10.1007/s11229-023-04116-3.
- [231] J. Lenhard, U. Küster: Reproducibility and the concept of numerical solution, *Minds and Machines* 29 (2019) 19–36. doi:10.1007/s11023-019-09492-9.
- [232] J.E. Lennard-Jones: Cohesion, *Proceedings of the Physical Society* 43 (1931) 461–482. doi:10.1088/0959-5309/43/5/301.
- [233] J. Leong, T. Reddyhoff, S. Sinha, A. Holmes, H. Spikes: Hydrodynamic friction reduction in a MAC–hexadecane lubricated MEMS contact, *Tribology Letters* 49 (2013) 217–225. doi:10.1007/s11249-012-0056-z.
- [234] J. Li, J. Huang, S. Tan, Z. Cheng, C. Ding: Tribological properties of silicon carbide under water-lubricated sliding, *Wear* 218 (1998) 167–171. doi:10.1016/S0043-1648(98)00217-8.
- [235] K. Li, T. Amann, M. Walter, M. Moseler, A. Kailer, J. Rühle: Ultralow friction induced by tribochemical reactions: A novel mechanism of lubrication on steel surfaces, *Langmuir* 29 (2013) 5207–5213. doi:10.1021/la400333d.
- [236] Y. Li, A. Goyal, A. Chernatynski, J. Jayashanker, M. Kautzky, S. Sinnott, S. Phillpot: Nanoindentation of gold and gold alloys by molecular dynamics simulations, *Materials Science & Engineering A* 651 (2016) 346–357. doi:10.1016/j.msea.2015.10.081.
- [237] E.Q. Lin, L.S. Niu, H.J. Shi, Z. Duan: Molecular dynamics simulation of nano-scale interfacial friction characteristic for different tribopair systems, *Applied Surface Science* 258 (2012) 2022–2028. doi:10.1016/j.apsusc.2011.04.117.
- [238] P. Linstrom: *NIST Chemistry WebBook*, NIST Standard Reference Database 69, 1997. URL: <http://webbook.nist.gov/chemistry/>.
- [239] H. Liu, H. Xu, P.J. Ellison, Z. Jin: Application of computational fluid dynamics and fluid-structure interaction method to the lubrication study of a rotor-bearing system, *Tribology Letters* 38 (2010) 325–336. doi:10.1007/s11249-010-9612-6.

- [240] Z.Y. Liu, N. Wei, C. Wang, H. Zhou, L. Zhang, Q. Liao, L. Zhang: Interfacial assignment of branched-alkyl benzene sulfonates: A molecular simulation, *AIP Advances* 5 (2015) 117203. doi:10.1063/1.4935339.
- [241] H.H. Loeffler, S. Bosisio, G. Duarte Ramos Matos, D. Suh, B. Roux, D.L. Mobley, J. Michel: Reproducibility of free energy calculations across different molecular simulation software packages, *Journal of Chemical Theory and Computation* 14 (2018) 5567–5582. doi:10.1021/acs.jctc.8b00544.
- [242] H.A. Lorentz: Über die Anwendung des Satzes vom Virial in der kinetischen Theorie der Gase, *Annalen Der Physik* 248 (1881) 127–136. doi:10.1002/andp.18812480110.
- [243] J. Lu, Q.J. Wang, N. Ren, F.E. Lockwood: Correlation between pressure-viscosity coefficient and traction coefficient of the base stocks in traction lubricants: A molecular dynamic approach, *Tribology International* 134 (2019) 328–334. doi:10.1016/j.triboint.2019.02.013.
- [244] X. Lu, M.M. Khonsari, E.R. Gelinck: The Stribeck Curve: Experimental Results and Theoretical Prediction, *Journal of Tribology* 128 (2006) 789–794. doi:10.1115/1.2345406.
- [245] L. Ma, J. Luo: Thin film lubrication in the past 20 years, *Friction* 4 (2016) 280–302. doi:10.1007/s40544-016-0135-5.
- [246] K. Maekawa, A. Itoh: Friction and tool wear in nano-scale machining – a molecular dynamics approach, *Wear* 188 (1995) 115–122. doi:10.1016/0043-1648(95)06633-0.
- [247] H.A. Maier, P.A. Bopp, M.J. Hampe: Non-equilibrium molecular dynamics simulation of the thermocapillary effect, *The Canadian Journal of Chemical Engineering* 90 (2012) 833–842. doi:10.1002/cjce.21659.
- [248] T. Mang, W. Dresel: *Lubricants and lubrication*, John Wiley & Sons, Weinheim, 2007.
- [249] M.G. Martin, J.I. Siepmann: Transferable potentials for phase equilibria. 1. united-atom description of n-alkanes, *Journal of Physical Chemistry B* 102 (1998) 2569–2577. doi:10.1021/jp972543+.
- [250] M.G. Martin, J.I. Siepmann: Novel configurational-bias Monte Carlo method for branched molecules. transferable potentials for phase equilibria. 2. united-atom description of branched alkanes, *The Journal of Physical Chemistry B* 103 (1999) 4508–4517. doi:10.1021/jp984742e.

- [251] M. Mate: *Tribology on the Small Scale – A Bottom Up Approach to Friction, Lubrication, and Wear*, Oxford University Press, Oxford, 2008.
- [252] L. Mathelin, M.Y. Hussaini, T.A. Zang: Stochastic approaches to uncertainty quantification in CFD simulations, *Numerical Algorithms* 38 (2005) 209–236. doi:10.1007/BF02810624.
- [253] S.L. Mayo, B.D. Olafson, W.A. Goddard: DREIDING: A Generic Force Field for Molecular Simulations, *Journal of Physical Chemistry* 94 (1990) 8897–8909. doi:10.1021/j100389a010.
- [254] S. Makowiak, D.M. Heyes, D. Dini, A.C. Braka: Non-equilibrium phase behavior and friction of confined molecular films under shear: A non-equilibrium molecular dynamics study, *The Journal of Chemical Physics* 145 (2016) 164704. doi:10.1063/1.4965829.
- [255] C. McCabe, S. Cui, P.T. Cummings: Characterizing the viscosity–temperature dependence of lubricants by molecular simulation, *Fluid Phase Equilibria* 183–184 (2001) 363–370. doi:10.1016/s0378-3812(01)00448-4.
- [256] D.A. McQuarrie: *Statistical Mechanics*, Harper & Row, New York, 1976.
- [257] K. Meier, A. Laesecke, S. Kabelac: A molecular dynamics simulation study of the self-diffusion coefficient and viscosity of the Lennard-Jones fluid, *International Journal of Thermophysics* 22 (2001) 161–173. doi:10.1023/A:1006715921252.
- [258] M.I. Mendeleev, S. Han, D.J. Srolovitz, G.J. Ackland, D.Y. Sun, M. Asta: Development of new interatomic potentials appropriate for crystalline and liquid iron, *Philosophical Magazine* 83 (2003) 3977–3994. doi:10.1080/14786430310001613264.
- [259] Y. Meng, J. Xu, Z. Jin, B. Prakash, Y. Hu: A review of recent advances in tribology, *Friction* 8 (2020) 221–300. doi:10.1007/s40544-020-0367-2.
- [260] T. Merker, J. Vrabec, H. Hasse: Engineering molecular models: Efficient parameterization procedure and cyclohexanol as case study, *Soft Materials* 10 (2012) 3–25. doi:10.1080/1539445X.2011.599695.
- [261] K. Merz, R. Amaro, Z. Cournia, M. Rarey, T. Soares, A. Tropsha, H. Wahab, R. Wang: Editorial: Method and data sharing and reproducibility of scientific results, *Journal of Chemical Information and Modeling* 60 (2020) 5868–5869. doi:10.1021/acs.jcim.0c01389.

- [262] N. Metropolis, A.W. Rosenbluth, M.N. Rosenbluth, A.H. Teller, E. Teller: Equation of state calculations by fast computing machines, *The Journal of Chemical Physics* 21 (1953) 1087–1092. doi:10.1063/1.1699114.
- [263] P. Metzner, F. Noé, C. Schütte: Estimating the sampling error: Distribution of transition matrices and functions of transition matrices for given trajectory data, *Physical Review E* 80 (2009) 021106. doi:10.1103/PhysRevE.80.021106.
- [264] J. Mick, E. Hailat, V. Russo, K. Rushaidat, L. Schwiebert, J. Potoff: GPU-accelerated Gibbs ensemble Monte Carlo simulations of Lennard-Jonesium, *Computer Physics Communications* 184 (2013) 2662–2669. doi:10.1016/j.cpc.2013.06.020.
- [265] J. Mick, M. Soroush Barhaghi, B. Jackman, L. Schwiebert, J.J. Potoff: Optimized Mie potentials for phase equilibria: Application to branched alkanes, *Journal of Chemical & Engineering Data* 62 (2017) 1806–1818. doi:10.1021/acs.jced.6b01036.
- [266] G. Mie: Zur kinetischen Theorie der einatomigen Körper, *Annalen der Physik* 316 (1903) 657–697. doi:10.1002/andp.19033160802.
- [267] A. Mir, X. Luo, I. Llavori, A. Roy, D.L. Zlatanovic, S.N. Joshi, S. Goel: Challenges and issues in continuum modelling of tribology, wear, cutting and other processes involving high-strain rate plastic deformation of metals, *Journal of the Mechanical Behavior of Biomedical Materials* 130 (2022) 105185. doi:10.1016/j.jmbbm.2022.105185.
- [268] M. Mishra, P. Egberts, R. Bennewitz, I. Szlufarska: Friction model for single-asperity elastic-plastic contacts, *Physical Review B* 86 (2012). doi:10.1103/physrevb.86.045452.
- [269] A. Mondelin, C. Claudin, J. Rech, F. Dumont: Effects of lubrication mode on friction and heat partition coefficients at the toolwork material interface in machining, *Tribology Transactions* 54 (2011) 247–255. doi:10.1080/10402004.2010.538489.
- [270] G. Morard, S. Boccato, A.D. Rosa, S. Anzellini, F. Miozzi, L. Henry, G. Garbarino, M. Mezouar, M. Harmand, F. Guyot, E. Boulard, I. Kantor, T. Irifune, R. Torchio: Solving controversies on the iron phase diagram under high pressure, *Geophysical Research Letters* 45 (2018). doi:10.1029/2018gl1079950.
- [271] G.P. Morriss, D.J. Evans: Application of transient correlation functions to shear flow far from equilibrium, *Physical Review A* 35 (1987) 792–797. doi:10.1103/PhysRevA.35.792.

- [272] A. Morsali, S.A. Beyramabadi, M.R. Bozorgmehr: Evaluation of P–V–T differential properties of the Lennard-Jones fluid using radial distribution functions and molecular dynamics, *Chemical Physics* 335 (2007) 194–200. doi:10.1016/j.chemphys.2007.04.019.
- [273] A. Morsali, E.K. Goharshadi, A.G. Mansoori, M. Abbaspour: An accurate expression for radial distribution function of the Lennard-Jones fluid, *Chemical Physics* 310 (2005) 11–15. doi:10.1016/j.chemphys.2004.09.027.
- [274] N.J. Mosey, M.H. Müser, T.K. Woo: Molecular mechanisms for the functionality of lubricant additives, *Science* 307 (2005) 1612–1615. doi:10.1126/science.1107895.
- [275] E.A. Müller, G. Jackson: Force-field parameters from the SAFT- γ equation of state for use in coarse-grained molecular simulations, *Annual Review of Chemical and Biomolecular Engineering* 5 (2014) 405–427. doi:10.1146/annurev-chembioeng-061312-103314.
- [276] E.A. Müller, A. Mejía: Comparison of united-atom potentials for the simulation of vapor-liquid equilibria and interfacial properties of long-chain n-alkanes up to n-C100, *The Journal of Physical Chemistry B* 115 (2011) 12822–12834. doi:10.1021/jp203236q.
- [277] M.H. Müser: Theory and simulation of friction and lubrication, in: *Computer Simulations in Condensed Matter Systems: From Materials to Chemical Biology Volume 2*, Springer Berlin Heidelberg, 2006, pp. 65–104. doi:10.1007/3-540-35284-8_4.
- [278] M.H. Müser, W.B. Dapp, R. Bugnicourt, P. Sainsot, N. Lesaffre, T.A. Lubrecht, B.N.J. Persson, K. Harris, A. Bennett, K. Schulze, S. Rohde, P. Ifju, W.G. Sawyer, T. Angelini, H. Ashtari Esfahani, M. Kadkhodaei, S. Akbarzadeh, J.J. Wu, G. Vorlaufer, A. Vernes, S. Solhjoo, A.I. Vakis, R.L. Jackson, Y. Xu, J. Streater, A. Rostami, D. Dini, S. Medina, G. Carbone, F. Bottiglione, L. Afferrante, J. Monti, L. Pastewka, M.O. Robbins, J.A. Greenwood: Meeting the contact-mechanics challenge, *Tribology Letters* 65 (2017) 118. doi:10.1007/s11249-017-0900-2.
- [279] S. O’Shea, N. Gosvami, L. Lim, W. Hofbauer: Liquid atomic force microscopy: Solvation forces, molecular order, and squeeze-out, *Japanese Journal of Applied Physics* 49 (2010) 08LA01. doi:10.1143/JJAP.49.08LA01.
- [280] R.M. Overney, E. Meyer, J. Frommer, D. Brodbeck, R. Lüthi, L. Howald, H.J. Giintherodt, M. Fujihira, H. Takano, Y. Gotoh: Friction measurements on phase-

- separated thin films with a modified atomic force microscope, *Nature* 359 (1992) 133–135. doi:10.1038/359133a0.
- [281] Oxford Dictionary of English: Oxford University Press, 2010. doi:10.1093/acref/9780199571123.001.0001.
- [282] E. Pakyuz-Charrier, M. Lindsay, V. Ogarko, J. Giraud, M. Jessell: Monte Carlo simulation for uncertainty estimation on structural data in implicit 3-D geological modeling, a guide for disturbance distribution selection and parameterization, *Solid Earth* 9 (2018) 385–402. doi:10.5194/se-9-385-2018.
- [283] J.Y. Park, M. Salmeron: Fundamental aspects of energy dissipation in friction, *Chemical Reviews* 114 (2014) 677–711. doi:10.1021/cr200431y.
- [284] R.S. Payal, S. Balasubramanian, I. Rudra, K. Tandon, I. Mahlke, D. Doyle, R. Cracknell: Shear viscosity of linear alkanes through molecular simulations: quantitative tests for *n*-decane and *n*-hexadecane, *Molecular Simulation* 38 (2012) 1234–1241. doi:10.1080/08927022.2012.702423.
- [285] B.N.T. Persson: History of tribology, in: T. Mang (Ed.), *Encyclopedia of Lubricants and Lubrication*, Springer, Berlin, 2014, pp. 791–797. doi:10.1007/978-3-642-22647-2_80.
- [286] O. Pinkus: *Thermal Aspects of Fluid Film Tribology*, ASME Press, New York, 1990.
- [287] V. Pisarev, N. Kondratyuk: Prediction of viscosity-density dependence of liquid methane+n-butane+n-pentane mixtures using the molecular dynamics method and empirical correlations, *Fluid Phase Equilib.* 501 (2019) 112273. doi:10.1016/j.fluid.2019.112273.
- [288] S. Plimpton: Fast parallel algorithms for short-range molecular dynamics, *Journal of Computational Physics* 117 (1995) 1–19. doi:10.1006/jcph.1995.1039.
- [289] V.L. Popov: *Kontaktmechanik und Reibung*, 3 ed., Springer Vieweg, Berlin, 2015.
- [290] J.J. Potoff, D.A. Bernard-Brunel: Mie potentials for phase equilibria calculations: Application to alkanes and perfluoroalkanes, *The Journal of Physical Chemistry B* 113 (2009) 14725–14731. doi:10.1021/jp9072137.
- [291] J.J. Potoff, G. Kamath: Mie potentials for phase equilibria: Application to alkenes, *Journal of Chemical & Engineering Data* 59 (2014) 3144–3150. doi:10.1021/je500202q.

- [292] D.K. Prajapati, D. Ahmad, J.K. Katiyar, C. Prakash, R.M. Ajaj: A numerical study on the impact of lubricant rheology and surface topography on heavily loaded non-conformal contacts, *Surface Topography: Metrology and Properties* 11 (2023) 035006. doi:10.1088/2051-672x/ace6c2.
- [293] J.H. Prinz, H. Wu, M. Sarich, B. Keller, M. Senne, M. Held, J.D. Chodera, C. Schütte, F. Noé: Markov models of molecular kinetics: Generation and validation, *The Journal of Chemical Physics* 134 (2011) 174105. doi:10.1063/1.3565032.
- [294] F. Pusavec, T. Lu, C. Courbon, J. Rech, U. Aljancic, J. Kopac, I. Jawahir: Analysis of the influence of nitrogen phase and surface heat transfer coefficient on cryogenic machining performance, *Journal of Materials Processing Technology* 233 (2016) 19–28. doi:10.1016/j.jmatprotec.2016.02.003.
- [295] C. Race: Quantifying uncertainty in molecular dynamics simulations of grain boundary migration, *Molecular Simulation* 41 (2015) 1069–1073. doi:10.1080/08927022.2014.935774.
- [296] A. Rahman: Correlations in the motion of atoms in liquid argon, *Physical Review* 136 (1964) A405–A411. doi:10.1103/PhysRev.136.A405.
- [297] D.C. Rapaport: *The Art of Molecular Dynamics Simulation*, Cambridge University Press, 2004. doi:10.1017/cbo9780511816581.
- [298] J. Rech, P. Arrazola, C. Claudin, C. Courbon, F. Pusavec, J. Kopac: Characterisation of friction and heat partition coefficients at the tool-work material interface in cutting, *CIRP Annals* 62 (2013) 79–82. doi:10.1016/j.cirp.2013.03.099.
- [299] J. Ren, J. Zhao, Z. Dong, P. Liu: Molecular dynamics study on the mechanism of AFM-based nanoscratching process with water-layer lubrication, *Applied Surface Science* 346 (2015) 84–98. doi:10.1016/j.apsusc.2015.03.177.
- [300] R. Rentsch, I. Inasaki: Effects of fluids on the surface generation in material removal processes, *CIRP Annals – Manufacturing Technology* 55 (2006) 601–604. doi:10.1016/s0007-8506(07)60492-2.
- [301] M. Robbins, M. Müser: Computer simulations of friction, lubrication, and wear in 'Modern Tribology Handbook: Volume One: Principles of Tribology', 1 ed., CRC Press, Boca Raton, US, 2000.
- [302] T.D. Romo, A. Grossfield: Unknown unknowns: The challenge of systematic and statistical error in molecular dynamics simulations, *Biophysical Journal* 106 (2018) 1553. doi:10.1016/j.bpj.2014.03.007.

- [303] J.S. Rowlinson, B. Widom: *Molecular Theory of Capillarity*, Dover Publications, New York, 1982.
- [304] C.J. Ruestes, I.A. Alhafez, H.M. Urbassek: Atomistic studies of nanoindentation – a review of recent advances, *Crystals* 7 (2017) 293. doi:10.3390/cryst7100293.
- [305] G. Rutkai, A. Köster, G. Guevara-Carrion, T. Janzen, M. Schappals, C.W. Glass, M. Bernreuther, A. Wafai, S. Stephan, M. Kohns, S. Reiser, S. Deublein, M. Horsch, H. Hasse, J. Vrabec: ms2: A molecular simulation tool for thermodynamic properties, release 3.0, *Computer Physics Communications* 221 (2017) 343–351. doi:10.1016/j.cpc.2017.07.025.
- [306] G. Rutkai, M. Thol, R. Span, J. Vrabec: How well does the Lennard-Jones potential represent the thermodynamic properties of noble gases?, *Molecular Physics* 115 (2017) 1104–1121. doi:10.1080/00268976.2016.1246760.
- [307] J. Ryu, T. Oda, H. Tanigawa: Comparison and validation of the lattice thermal conductivity formulas used in equilibrium molecular dynamics simulations for binary systems, *Computational Materials Science* 178 (2020) 109615. doi:10.1016/j.commatsci.2020.109615.
- [308] B. Saager, J. Fischer: Predictive power of effective intermolecular pair potentials: MD simulation results for methane up to 1000 MPa, *Fluid Phase Equilibria* 57 (1990) 35–46. doi:10.1016/0378-3812(90)80011-Y.
- [309] J. Sacks, W.J. Welch, T.J. Mitchell, H.P. Wynn: Design and analysis of computer experiments, *Statistical Science* 4 (1989) 409–423. doi:10.1214/ss/1177012413.
- [310] V.N. Samoilov, I.M. Sivebaek, B.N.J. Persson: The effect of surface roughness on the adhesion of solid surfaces for systems with and without liquid lubricant, *The Journal of Chemical Physics* 121 (2004) 9639–9647. doi:10.1063/1.1806814.
- [311] S. Sarman, D.J. Evans: Heat flow and mass diffusion in binary Lennard-Jones mixtures, *Physical Review A* 45 (1992) 2370–2379. doi:10.1103/PhysRevA.45.2370.
- [312] S.S. Sarman, D.J. Evans, P.T. Cummings: Recent developments in non-newtonian molecular dynamics, *Physics Reports* 305 (1998) 1–92. doi:10.1016/s0370-1573(98)00018-0.

- [313] N. Sasaki, K. Kobayashi, M. Tsukada: Atomic-scale friction image of graphite in atomic-force microscopy, *Physical Review B* 54 (1996) 2138–2149. doi:10.1103/physrevb.54.2138.
- [314] D. Savio, N. Fillot, P. Vergne: A molecular dynamics study of the transition from ultra-thin film lubrication toward local film breakdown, *Tribology Letters* 50 (2013) 207–220. doi:10.1007/s11249-013-0113-2.
- [315] D. Savio, N. Fillot, P. Vergne, H. Hetzler, W. Seemann, G. Morales-Espejel: A multiscale study on the wall slip effect in a ceramicsteel contact with nanometer-thick lubricant film by a nano-to-elastohydrodynamic lubrication approach, *Journal of Tribology* 137 (2015) 031502. doi:10.1115/1.4029937.
- [316] D. Savio, N. Fillot, P. Vergne, M. Zaccheddu: A model for wall slip prediction of confined n-alkanes: Effect of wall-fluid interaction versus fluid resistance, *Tribology Letters* 46 (2012) 11–22. doi:10.1007/s11249-011-9911-6.
- [317] R. Scalco, A. Caffisch: Equilibrium distribution from distributed computing (simulations of protein folding), *The Journal of Physical Chemistry B* 115 (2011) 6358–6365. doi:10.1021/jp2014918.
- [318] D. Schaefer, S. Stephan, K. Langenbach, M.T. Horsch, H. Hasse: Mass transfer through vapor-liquid interfaces studied by nonstationary molecular dynamics simulations, *The Journal of Physical Chemistry B* 127 (2023) 2521–2533. doi:10.1021/acs.jpcc.2c08752.
- [319] M. Schappals, A. Mecklenfeld, L. Kröger, V. Botan, A. Köster, S. Stephan, E.J. García, G. Rutkai, G. Raabe, P. Klein, K. Leonhard, C.W. Glass, J. Lenhard, J. Vrabec, H. Hasse: Round robin study: Molecular simulation of thermodynamic properties from models with internal degrees of freedom, *Journal of Chemical Theory and Computation* 13 (2017) 4270–4280. doi:10.1021/acs.jctc.7b00489.
- [320] M. Scherge, A. Brink, D. Linsler: Tribofilms forming in oil-lubricated contacts, *Lubricants* 4 (2016). doi:10.3390/lubricants4030027.
- [321] J.R. Schmidt, K. Yu, J.G. McDaniel: Transferable next-generation force fields from simple liquids to complex materials, *Accounts of Chemical Research* 48 (2015) 548–556. doi:10.1021/ar500272n.
- [322] S. Schmitt, F. Fleckenstein, H. Hasse, S. Stephan: Comparison of force fields for the prediction of thermophysical properties of long linear and branched alkanes, *The Journal of Physical Chemistry B* 127 (2023) 1789–1802. doi:10.1021/acs.jpcc.2c07997.

- [323] S. Schmitt, S. Stephan, B. Kirsch, J.C. Aurich, E. Kerscher, H.M. Urbassek, H. Hasse: Molecular simulation study on the influence of the scratching velocity on nanoscopic contact processes, in: Proceedings of the 2nd International Conference on Physical Modeling for Virtual Manufacturing (iPMVM 2020), volume 89, Schloss Dagstuhl – Leibniz-Zentrum für Informatik, 2021, pp. 17:1–17:16. doi:10.4230/OASICS.iPMVM.2020.17.
- [324] S. Schmitt, S. Stephan, B. Kirsch, J.C. Aurich, H.M. Urbassek, H. Hasse: Molecular dynamics simulation of cutting processes: The influence of cutting fluids at the atomistic scale, in: Proceedings of the 3rd Conference on Physical Modeling for Virtual Manufacturing Systems and Processes, Springer International Publishing, 2023, pp. 260–280. doi:10.1007/978-3-031-35779-4_14.
- [325] S. Schmitt, T. Vo, M.P. Lautenschlaeger, S. Stephan, H. Hasse: Molecular dynamics simulation study of heat transfer across solid-fluid interfaces in a simple model system, *Molecular Physics* 120 (2022) e2057364. doi:10.1080/00268976.2022.2057364.
- [326] F. Schneider, J. Das, B. Kirsch, B. Linke, J.C. Aurich: Sustainability in ultra precision and micro machining: A review, *International Journal of Precision Engineering and Manufacturing-Green Technology* 6 (2019) 601–610. doi:10.1007/s40684-019-00035-2.
- [327] A.J. Schultz, D.A. Kofke: Comprehensive high-precision high-accuracy equation of state and coexistence properties for classical Lennard-Jones crystals and low-temperature fluid phases, *The Journal of Chemical Physics* 149 (2018) 204508. doi:10.1063/1.5053714.
- [328] J. Shi, Y. Zhang, K. Sun, L. Fang: Effect of water film on the plastic deformation of monocrystalline copper, *RSC Advances* 6 (2016) 96824–96831. doi:10.1039/c6ra17126e.
- [329] K. Shi, E.E. Santiso, K.E. Gubbins: Conformal sites theory for adsorbed films on energetically heterogeneous surfaces, *Langmuir* 36 (2020) 1822–1838. doi:10.1021/acs.langmuir.9b03633.
- [330] B. Shiari, R.E. Miller, D.D. Klug: Multiscale simulation of material removal processes at the nanoscale, *Journal of the Mechanics and Physics of Solids* 55 (2007) 2384–2405. doi:10.1016/j.jmps.2007.03.018.
- [331] G.C.Q. da Silva, G.M. Silva, F.W. Tavares, F.P. Fleming, B.A.C. Horta: Are all-atom any better than united-atom force fields for the description of liquid

- properties of alkanes?, *Journal of Molecular Modeling* 26 (2020) 296. doi:10.1007/s00894-020-04548-5.
- [332] M. Singh, P. Ilg, R. Espinosa-Marzal, N. Spencer, M. Kröger: Influence of chain stiffness, grafting density and normal load on the tribological and structural behavior of polymer brushes: A nonequilibrium-molecular-dynamics study, *Polymers* 8 (2016) 254. doi:10.3390/polym8070254.
- [333] M. Singh, P. Ilg, R.M. Espinosa-Marzal, M. Kröger, N. Spencer: Polymer brushes under shear: Molecular dynamics simulations compared to experiments, *Langmuir* 31 (2015) 4798–4805. doi:10.1021/acs.langmuir.5b00641.
- [334] M. Singh, P. Ilg, R.M. Espinosa-Marzal, M. Kröger, N.D. Spencer: Effect of crosslinking on the microtribological behavior of model polymer brushes, *Tribology Letters* 63 (2016) 17. doi:10.1007/s11249-016-0705-8.
- [335] I.M. Sivebaek, B.N. Persson: The effect of surface nano-corrugation on the squeeze-out of molecular thin hydrocarbon films between curved surfaces with long range elasticity, *Nanotechnology* 27 (2016) 445401. doi:10.1088/0957-4484/27/44/445401.
- [336] I.M. Sivebaek, V.N. Samoilov, B.N. Persson: Squeezing molecular thin alkane lubrication films between curved solid surfaces with long-range elasticity: Layering transitions and wear, *The Journal of Chemical Physics* 119 (2003) 2314–2321. doi:10.1063/1.1582835.
- [337] A. Smith, J. Klosek: A review of air separation technologies and their integration with energy conversion processes, *Fuel Processing Technology* 70 (2001) 115–134. doi:10.1016/S0378-3820(01)00131-X.
- [338] C. Snyder, L. Gschwender, S. Sharma, D. Kramer, B. Lok, M. Sztenderowicz, R. Krug: *Liquid Lubricants and Lubrication in 'Modern Tribology Handbook: Volume One: Principles of Tribology'*, 1 ed., CRC Press, Boca Raton, US, 2000.
- [339] W. Song, J. Zhang, S. Campen, J. Yan, H. Ji, J.S.S. Wong: Lubrication mechanism of a strong tribofilm by imidazolium ionic liquid, *Friction* 11 (2022) 425–440. doi:10.1007/s40544-022-0614-9.
- [340] M.R. Sorensen, K.W. Jacobsen, P. Stoltze: Simulations of atomic-scale sliding friction, *Physical Review B* 53 (1996) 2101–2113. doi:10.1103/PhysRevB.53.2101.
- [341] H. Spikes: Boundary lubrication and boundary films, in: D. Dowson, C. Taylor, T. Childs, M. Godet, G. Dalmaz (Eds.), *Thin Films in Tribology*, volume 25 of

- Tribology Series*, Elsevier, 1993, pp. 331–346. doi:10.1016/S0167-8922(08)70389-4.
- [342] D.A. Stainforth, T. Aina, C. Christensen, M. Collins, N. Faull, D.J. Frame, J.A. Kettleborough, S. Knight, A. Martin, J.M. Murphy, C. Piani, D. Sexton, L.A. Smith, R.A. Spicer, A.J. Thorpe, M.R. Allen: Uncertainty in predictions of the climate response to rising levels of greenhouse gases, *Nature* 433 (2005) 403. doi:10.1038/nature03301.
- [343] S. Stephan: Vapor-Liquid Interfaces: Molecular Simulation, Density Gradient Theory, and Experiments, Phd thesis, Laboratory of Engineering Thermodynamics, Technische Universität Kaiserslautern, Kaiserslautern, 2020.
- [344] S. Stephan, S. Becker, K. Langenbach, H. Hasse: Vapor-liquid interfacial properties of the binary system cyclohexane + CO₂: Experiment, molecular simulation and density gradient theory, *Fluid Phase Equilibria* 518 (2020) 112583. doi:10.1016/j.fluid.2020.112583.
- [345] S. Stephan, H. Cardenas, A. Mejia, E.A. Mueller: The monotonicity behavior of density profiles at vapor-liquid interfaces of mixtures, *Fluid Phase Equilibria* 564 (2023) 113596. doi:10.1016/j.fluid.2022.113596.
- [346] S. Stephan, U.K. Deiters: Characteristic curves of the Lennard-Jones fluid, *International Journal of Thermophysics* 41 (2020) 147. doi:10.1007/s10765-020-02721-9.
- [347] S. Stephan, M. Dyga, I.A. Alhafez, J. Lenhard, H.M. Urbassek, H. Hasse: Reproducibility of atomistic friction computer experiments: A molecular dynamics simulation study, *Molecular Simulation* 47 (2021) 1509–1521. doi:10.1080/08927022.2021.1987430.
- [348] S. Stephan, M. Dyga, H. Urbassek, H. Hasse: The influence of lubrication and the solid-fluid interaction on thermodynamic properties in a nanoscopic scratching process, *Langmuir* 35 (2019) 16948–16960. doi:10.1021/acs.langmuir.9b01033.
- [349] S. Stephan, H. Hasse: Enrichment at vapour-liquid interfaces of mixtures: Establishing a link between nanoscopic and macroscopic properties, *International Reviews in Physical Chemistry* 39 (2020) 319–349. doi:10.1080/0144235X.2020.1777705.
- [350] S. Stephan, H. Hasse: Influence of dispersive long-range interactions on properties of vapour-liquid equilibria and interfaces of binary Lennard-Jones mixtures, *Molecular Physics* 118 (2020) e1699185. doi:10.1080/00268976.2019.1699185.

- [351] S. Stephan, H. Hasse: Interfacial properties of binary mixtures of simple fluids and their relation to the phase diagram, *Physical Chemistry Chemical Physics* 22 (2020) 12544–12564. doi:10.1039/d0cp01411g.
- [352] S. Stephan, H. Hasse: Molecular interactions at vapor-liquid interfaces: Binary mixtures of simple fluids, *Physical Review E* 101 (2020) 012802. doi:10.1103/PhysRevE.101.012802.
- [353] S. Stephan, M. Horsch, J. Vrabec, H. Hasse: MolMod - an open access database of force fields for molecular simulations of fluids, *Molecular Simulation* 45 (2019) 806–814. doi:10.1080/08927022.2019.1601191.
- [354] S. Stephan, K. Langenbach, H. Hasse: Enrichment of components at vapour-liquid interfaces: A study by molecular simulation and density gradient theory, *Chemical Engineering Transactions* 69 (2018) 295–300. doi:10.3303/CET1869050.
- [355] S. Stephan, K. Langenbach, H. Hasse: Interfacial properties of binary Lennard-Jones mixtures by molecular simulations and density gradient theory, *The Journal of Chemical Physics* 150 (2019) 174704. doi:10.1063/1.5093603.
- [356] S. Stephan, M.P. Lautenschlaeger, I.A. Alhafez, M.T. Horsch, H.M. Urbassek, H. Hasse: Molecular dynamics simulation study of mechanical effects of lubrication on a nanoscale contact process, *Tribology Letters* 66 (2018) 126. doi:10.1007/s11249-018-1076-0.
- [357] S. Stephan, J. Liu, K. Langenbach, W.G. Chapman, H. Hasse: Vapor-liquid interface of the Lennard-Jones truncated and shifted fluid: Comparison of molecular simulation, density gradient theory, and density functional theory, *Journal of Physical Chemistry C* 122 (2018) 24705–24715. doi:10.1021/acs.jpcc.8b06332.
- [358] S. Stephan, D. Schaefer, K. Langenbach, H. Hasse: Mass transfer through vapour-liquid interfaces: A molecular dynamics simulation study, *Molecular Physics* 119 (2021) e1810798. doi:10.1080/00268976.2020.1810798.
- [359] S. Stephan, S. Schmitt, H. Hasse, H.M. Urbassek: Molecular dynamics simulation of the stribeck curve: Boundary lubrication, mixedlubrication, and hydrodynamic lubrication on the atomistic level, *Friction* 11 (2023) 2342–2366. doi:10.1007/s40544-023-0745-y.
- [360] S. Stephan, J. Staubach, H. Hasse: Review and comparison of equations of state for the Lennard-Jones fluid, *Fluid Phase Equilibria* 523 (2020) 112772. doi:10.1016/j.fluid.2020.112772.

- [361] S. Stephan, M. Thol, J. Vrabc, H. Hasse: Thermophysical properties of the Lennard-Jones fluid: Database and data assessment, *Journal of Chemical Information and Modeling* 59 (2019) 4248–4265. doi:10.1021/acs.jcim.9b00620.
- [362] S. Stephan, W. Uffrecht, M. Raddatz: Development of a sensor concept for a non-invasive measurement of the steam fraction by vibrational spectroscopy, *Technisches Messen* 84 (2017) 719–733. doi:10.1515/teme-2017-0058.
- [363] M.J. Stevens, M. Mondello, G.S. Grest, S.T. Cui, H.D. Cochran, P.T. Cummings: Comparison of shear flow of hexadecane in a confined geometry and in bulk, *The Journal of Chemical Physics* 106 (1997) 7303–7314. doi:10.1063/1.473692.
- [364] P. Stoyanov, R. Merz, P.A. Romero, F.C. Wählich, O.T. Abad, R. Gralla, P. Stemmer, M. Kopnarski, M. Moseler, R. Bennewitz, M. Dienwiebel: Surface softening in metal - ceramic sliding contacts: an experimental and numerical investigation, *ACS Nano* 9 (2015) 1478. doi:10.1021/nn505968m.
- [365] P. Stoyanov, P.A. Romero, R. Merz, M. Kopnarski, M. Stricker, P. Stemmer, M. Dienwiebel, M. Moseler: Nanoscale sliding friction phenomena at the interface of diamond-like carbon and tungsten, *Acta Materialia* 67 (2014) 395–408. doi:10.1016/j.actamat.2013.12.029.
- [366] P. Stoyanov, P. Stemmer, T.T. Järvi, R. Merz, P.A. Romero, M. Scherge, M. Kopnarski, M. Moseler, A. Fischer, M. Dienwiebel: Friction and wear mechanisms of tungstencarbon systems: A comparison of dry and lubricated conditions, *ACS Applied Materials & Interfaces* 5 (2013) 6123–6135. doi:10.1021/am4010094.
- [367] T. Straatsma, H. Berendsen, A. Stam: Estimation of statistical errors in molecular simulation calculations, *Molecular Physics* 57 (1986) 89–95. doi:10.1080/00268978600100071.
- [368] R.H. Stribeck: Die wesentlichen Eigenschaften der Gleit- und Rollenlager, *Zeitschrift des Vereins Deutscher Ingenieure* 46 (1902) 1341, 1432, 1463.
- [369] J.M. Strubbs, J.J. Potoff, J.I. Siepmann: Transferable potentials for phase equilibria. 6. united-atom description for ethers, glycols, ketones, and aldehydes, *Journal of Physical Chemistry B* 108 (2004) 17596–17605. doi:10.1021/jp049459w.
- [370] A. Stukowski: Visualization and analysis of atomistic simulation data with OVITO - the open visualization tool, *Modelling and Simulation in Materials Science and Engineering* 18 (2010) 015012. URL: <http://www.ovito.org/>. doi:10.1088/0965-0393/18/1/015012, <http://www.ovito.org/>.

- [371] A. Stukowski, K. Albe: Extracting dislocations and non-dislocation crystal defects from atomistic simulation data, *Modelling and Simulation in Materials Science and Engineering* 18 (2010) 085001. URL: <http://www.ovito.org/>. doi:10.1088/0965-0393/18/1/015012.
- [372] H. Sun, S.J. Mumby, J.R. Maple, A.T. Hagler: An ab initio CFF93 all-atom force field for polycarbonates, *Journal of the American Chemical Society* 116 (1994) 2978–2987. doi:10.1021/ja00086a030.
- [373] A. Szeri: *Hydrodynamic and Elastohydrodynamic Lubrication in 'Modern Tribology Handbook: Volume One: Principles of Tribology'*, 1 ed., CRC Press, Boca Raton, US, 2000.
- [374] I. Szlufarska: Atomistic simulations of nanoindentation, *Materials Today* 9 (2006) 42–50. doi:10.1016/s1369-7021(06)71496-1.
- [375] I. Szlufarska, M. Chandross, R.W. Carpick: Recent advances in single-asperity nanotribology, *Journal of Physics D: Applied Physics* 41 (2008) 123001. doi:10.1088/0022-3727/41/12/123001.
- [376] T.D. Ta, A.K. Tieu, H. Zhu, B. Kosasih: Adsorption of normal-alkanes on Fe(110), FeO(110), and Fe₂O₃(0001): Influence of iron oxide surfaces, *The Journal of Physical Chemistry C* 119 (2015) 12999–13010. doi:10.1021/acs.jpcc.5b01847.
- [377] C.Y. Tang, L.C. Zhang: A molecular dynamics analysis of the mechanical effect of water on the deformation of silicon monocrystals subjected to nano-indentation, *Nanotechnology* 16 (2005) 15–20. doi:10.1088/0957-4484/16/1/004.
- [378] U. Tartaglino, I.M. Sivebaek, B.N.J. Persson, E. Tosatti: Impact of molecular structure on the lubricant squeeze-out between curved surfaces with long range elasticity, *The Journal of Chemical Physics* 125 (2006) 014704. doi:10.1063/1.2210008.
- [379] N. Tchipev, S. Seckler, M. Heinen, J. Vrabc, F. Gratl, M. Horsch, M. Bernreuther, C.W. Glass, C. Niethammer, N. Hammer, B. Krischok, M. Resch, D. Kranzlmüller, H. Hasse, H.J. Bungartz, P. Neumann: Twetris: Twenty trillion-atom simulation, *The International Journal of High Performance Computing Applications* 33 (2019) 838–854. doi:10.1177/1094342018819741.
- [380] C. Tebaldi, R.L. Smith, D. Nychka, L.O. Mearns: Quantifying uncertainty in projections of regional climate change: A Bayesian approach to the analysis of multimodel ensembles, *Journal of Climate* 18 (2005) 1524–1540. doi:10.1175/JCLI3363.1.

- [381] J. Tersoff: New empirical approach for the structure and energy of covalent systems, *Physical Review B* 37 (1988) 6991–7000. doi:10.1103/physrevb.37.6991.
- [382] J. Tersoff: Modeling solid-state chemistry: Interatomic potentials for multicomponent systems, *Physical Review B* 39 (1989) 5566–5568. doi:10.1103/physrevb.39.5566.
- [383] M.W. Thompson, J.B. Gilmer, R.A. Matsumoto, C.D. Quach, P. Shamaprasad, A.H. Yang, C.R. Iacovella, C. McCabe, P.T. Cummings: Towards molecular simulations that are transparent, reproducible, usable by others, and extensible (true), *Molecular Physics* 118 (2020) e1742938. doi:10.1080/00268976.2020.1742938.
- [384] P.A. Thompson, M.O. Robbins: Origin of stick-slip motion in boundary lubrication, *Science* 250 (1990) 792–794. doi:10.1126/science.250.4982.792.
- [385] P.A. Thompson, M.O. Robbins: Shear flow near solids: Epitaxial order and flow boundary conditions, *Physical Review A* 41 (1990) 6830–6837. doi:10.1103/PhysRevA.41.6830.
- [386] P.A. Thompson, S.M. Troian: A general boundary condition for liquid flow at solid surfaces, *Nature* 389 (1997) 360–362. doi:10.1038/38686.
- [387] B.D. Todd, P.J. Daivis: Nonequilibrium molecular dynamics: theory, algorithms and applications, Cambridge University Press, 2017. doi:10.1017/9781139017848.
- [388] M. Torbacke, A.K. Rudolphi, E. Kassfeldt: *Lubricants: Introduction to Properties and Performance*, John Wiley & Sons, Chichester, 2014.
- [389] A. Travasset: Phase diagram of power law and Lennard-Jones systems: Crystal phases, *The Journal of Chemical Physics* 141 (2014) 164501. doi:10.1063/1.4898371.
- [390] K.P. Travis, P.J. Daivis, D.J. Evans: Thermostats for molecular fluids undergoing shear flow: Application to liquid chlorine, *The Journal of Chemical Physics* 103 (1995) 10638–10651. doi:10.1063/1.469850.
- [391] K.P. Travis, K.E. Gubbins: Poiseuille flow of Lennard-Jones fluids in narrow slit pores, *The Journal of Chemical Physics* 112 (2000) 1984–1994. doi:10.1063/1.480758.

- [392] S. Tromp, L. Joly, M. Cobian, N. Fillot: Tribological performance of the R1233zd refrigerant in extreme confinement at the nanoasperity level: A molecular dynamics study using an ab initio-based force field, *Tribology Letters* 67 (2019) 67. doi:10.1007/s11249-019-1180-9.
- [393] O.T. Unke, S. Chmiela, H.E. Sauceda, M. Gastegger, I. Poltavsky, K.T. Schuett, A. Tkatchenko, K. Mueller: Machine learning force fields, *Chemical Reviews* 121 (2021) 10142–10186. doi:10.1021/acs.chemrev.0c01111.
- [394] M. Urschel, S. Stephan: Determining Browns characteristic curves using molecular simulation, *Journal of Chemical Theory and Computation* 5 (2023) 1537–1552. doi:10.1021/acs.jctc.2c01102.
- [395] A. Vakis, V. Yastrebov, J. Scheibert, L. Nicola, D. Dini, C. Minfray, A. Almqvist, M. Paggi, S. Lee, G. Limbert, J. Molinari, G. Anciaux, R. Aghababaei, S.E. Restrepo, A. Papangelo, A. Cammarata, P. Nicolini, C. Putignano, G. Carbone, S. Stupkiewicz, J. Lengiewicz, G. Costagliola, F. Bosia, R. Guarino, N. Pugno, M. Müser, M. Ciavarella: Modeling and simulation in tribology across scales: An overview, *Tribology International* 125 (2018) 169–199. doi:10.1016/j.triboint.2018.02.005.
- [396] W.F. van Gunsteren, X. Daura, N. Hansen, A.E. Mark, C. Oostenbrink, S. Riniker, L.J. Smith: Validation of molecular simulation: An overview of issues, *Angewandte Chemie International Edition* 57 (2017) 884–902. doi:10.1002/anie.201702945.
- [397] A. Vanossi, N. Manini, M. Urbakh, S. Zapperi, E. Tosatti: Modeling friction: From nanoscale to mesoscale, *Reviews of Modern Physics* 85 (2013) 512–552. doi:10.1103/RevModPhys.85.529.
- [398] L. Verlet: Computer 'experiments' on classical fluids. I. thermodynamical properties of Lennard-Jones molecules, *Physical Review* 159 (1967) 98–103. doi:10.1103/PhysRev.159.98.
- [399] A. Vernes, S. Eder, G. Vorlauffer, G. Betz: On the three-term kinetic friction law in nanotribological systems, *Faraday Discussions* 156 (2012) 173. doi:10.1039/c2fd00120a.
- [400] M. Vohra, A.Y. Nobakht, S. Shin, S. Mahadevan: Uncertainty quantification in non-equilibrium molecular dynamics simulations of thermal transport, *International Journal of Heat and Mass Transfer* 127 (2018) 297–307. doi:10.1016/j.ijheatmasstransfer.2018.07.073.

- [401] J. Vrabec, M. Bernreuther, H.J. Bungartz, W.L. Chen, W. Cordes, R. Fingerhut, C.W. Glass, J. Gmehling, R. Hamburger, M. Heilig, M. Heinen, M.T. Horsch, C.M. Hsieh, M. Hülsmann, P. Jäger, P. Klein, S. Knauer, T. Köddermann, A. Köster, K. Langenbach, S.T. Lin, P. Neumann, J. Rarey, D. Reith, G. Rutkai, M. Schappals, M. Schenk, A. Schedemann, M. Schönherr, S. Seckler, S. Stephan, K. Stöbener, N. Tchipev, A. Wafai, S. Werth, H. Hasse: Skasim – skalierbare HPC-software für molekulare simulationen in der chemischen industrie, *Chemie Ingenieur Technik* 90 (2018) 295–306. doi:10.1002/cite.201700113.
- [402] J. Vrabec, G.K. Kedia, G. Fuchs, H. Hasse: Comprehensive study of the vapour-liquid coexistence of the truncated and shifted Lennard-Jones fluid including planar and spherical interface properties, *Molecular Physics* 104 (2006) 1509–1527. doi:10.1080/00268970600556774.
- [403] J. Vrabec, J. Stoll, H. Hasse: A set of molecular models for symmetric quadrupolar fluids, *The Journal of Physical Chemistry B* 105 (2001) 12126–12133. doi:10.1021/jp012542o.
- [404] F.C. Wang, Y.P. Zhao: Slip boundary conditions based on molecular kinetic theory: The critical shear stress and the energy dissipation at the liquid-solid interface, *Soft Matter* 7 (2011) 8628–8634. doi:10.1039/C1SM05543G.
- [405] X. Wang, S. Ramírez-Hinestrosa, J. Dobnikar, D. Frenkel: The Lennard-Jones potential: When (not) to use it, *Physical Chemistry Chemical Physics* 22 (2020) 10624–10633. doi:10.1039/C9CP05445F.
- [406] Z. Wang, L. Li: Boiling heat transfer of nanofluids on the graphene membrane: A molecular dynamics simulation, *Applied Thermal Engineering* 213 (2022) 118708. doi:10.1016/j.applthermaleng.2022.118708.
- [407] Z. Wang, S. Safarkhani, G. Lin, X. Ruan: Uncertainty quantification of thermal conductivities from equilibrium molecular dynamics simulations, *International Journal of Heat and Mass Transfer* 112 (2017) 267–278. doi:10.1016/j.ijheatmasstransfer.2017.04.077.
- [408] J.D. Weeks, D. Chandler, H.C. Andersen: Role of repulsive forces in determining the equilibrium structure of simple liquids, *The Journal of Chemical Physics* 54 (1971) 5237–5247. doi:10.1063/1.1674820.
- [409] A. Weidner, J. Seewig, E. Reithmeier: 3D roughness evaluation of cylinder liner surfaces based on structure-oriented parameters, *Measurement Science and Technology* 17 (2006) 477. doi:10.1088/0957-0233/17/3/S03.

- [410] S.J. Weiner, P.A. Kollman, D.T. Nguyen, D.A. Case: An all Atom Force Field for Simulations of Proteins and Nucleic Acids, *Journal of Computational Chemistry* 7 (1986) 230–252. doi:10.1002/jcc.540070216.
- [411] C.D. Wick, M.G. Martin, J.I. Siepmann: Transferable potentials for phase equilibria. 4. united-atom description of linear and branched alkenes and alkylbenzenes, *Journal of Physical Chemistry B* 104 (2000) 8008–8016. doi:10.1021/jp001044x.
- [412] R.R. Wilcox: *Applying Contemporary Statistical Techniques*, Academic Press, Burlington, 2003. doi:10.1016/B978-012751541-0/50021-3.
- [413] D.W. Wisander: Friction and wear of selected metals and alloys in sliding contact with AISI 440c stainless steel in liquid methane and in liquid natural gas, NASA Technical Report 1150 (1978) 1–20.
- [414] M. Wolloch, G. Feldbauer, P. Mohn, J. Redinger, A. Vernes: Ab initio friction forces on the nanoscale: A density functional theory study of fcc Cu(111), *Physical Review B* 90 (2014) 195418. doi:10.1103/physrevb.90.195418.
- [415] B. Wu, Y. Sun: Normal contact analysis between two self-affine fractal surfaces at the nanoscale by molecular dynamics simulations, *Tribology Letters* 71 (2023). doi:10.1007/s11249-023-01705-8.
- [416] C.D. Wu, T.H. Fang, J.F. Lin: Atomic-scale simulations of material behaviors and tribology properties for FCC and BCC metal films, *Materials Letters* 80 (2012) 59–62. doi:10.1016/j.matlet.2012.04.079.
- [417] R. Wäsche, M. Woydt: Stribeck curve, in: *Encyclopedia of Lubricants and Lubrication*, Springer, Berlin, 2014, pp. 1998–2005. doi:10.1007/978-3-642-22647-2_274.
- [418] L. Xu, D. Kirvassilis, Y. Bai, M. Mavrikakis: Atomic and molecular adsorption on Fe(110), *Surface Science* 667 (2018) 54–65. doi:10.1016/j.susc.2017.09.002.
- [419] F. Yang, R.W. Carpick, D.J. Srolovitz: Mechanisms of contact, adhesion, and failure of metallic nanoasperities in the presence of adsorbates: Toward conductive contact design, *ACS Nano* 11 (2017) 490–500. doi:10.1021/acsnano.6b06473.
- [420] J. Yang, J. Zhang, J. Qiao: Molecular dynamics simulations of atomic diffusion during the Al-Cu ultrasonic welding process, *Materials* 12 (2019) 2306. doi:10.3390/ma12142306.

- [421] C. Yi, C. Hu, L. Shi, M. Bai, Y. Li, D. Tang: Frictional properties of MoS₂ on a multi-level rough wall under starved lubrication, *Physical Chemistry Chemical Physics* 25 (2023) 14348–14358. doi:10.1039/d3cp01288c.
- [422] Y. Yildiz, M. Nalbant: A review of cryogenic cooling in machining processes, *International Journal of Machine Tools and Manufacture* 48 (2008) 947–964. doi:10.1016/j.ijmachtools.2008.01.008.
- [423] X. Yong, L.T. Zhang: Slip in nanoscale shear flow: Mechanisms of interfacial friction, *Microfluidics and Nanofluidics* 14 (2013) 299–308. doi:10.1007/s10404-012-1048-x.
- [424] C. Zhang: Research on thin film lubrication: State of the art, *Tribology International* 38 (2005) 443–448. doi:10.1016/j.triboint.2004.10.011.
- [425] J. Zhang, Y. Meng: Boundary lubrication by adsorption film, *Friction* 3 (2015) 115–147. doi:10.1007/s40544-015-0084-4.
- [426] J. Zhang, T. Sun, Y. Yan, Y. Liang: Molecular dynamics study of scratching velocity dependency in AFM-based nanometric scratching process, *Materials Science and Engineering: A* 505 (2009) 65–69. doi:10.1016/j.msea.2008.10.049.
- [427] L. Zhang, H. Zhao, Y. Yang, H. Huang, Z. Ma, M. Shao: Evaluation of repeated single-point diamond turning on the deformation behavior of monocrystalline silicon via molecular dynamic simulations, *Applied Physics A* 116 (2014) 141–150. doi:10.1007/s00339-014-8243-4.
- [428] Y. Zhang, A. Otani, E.J. Maginn: Reliable viscosity calculation from equilibrium molecular dynamics simulations: A time decomposition method, *Journal of Chemical Theory and Computation* 11 (2015) 3537–3546. doi:10.1021/acs.jctc.5b00351.
- [429] S. Zhen, G.J. Davies: Calculation of the Lennard-Jones n-m potential energy parameters for metals, *Physica Status Solidi (a)* 78 (1983) 595–605. doi:10.1002/pssa.2210780226.
- [430] X. Zheng, H. Zhu, B. Kosasih, A.K. Tieu: A molecular dynamics simulation of boundary lubrication: The effect of n-alkanes chain length and normal load, *Wear* 301 (2013) 62–69. doi:10.1016/j.wear.2013.01.052.
- [431] X. Zheng, H. Zhu, A.K. Tieu, B. Kosasih: A molecular dynamics simulation of 3D rough lubricated contact, *Tribology International* 67 (2013) 217–221. doi:10.1016/j.triboint.2013.07.015.

-
- [432] J. Zhong, J.B. Adams, L.G. Hector: Molecular dynamics simulations of asperity shear in aluminum, *Journal of Applied Physics* 94 (2003) 4306–4314. doi:10.1063/1.1558966.

Appendix

A The Lennard-Jones Model System

The Lennard-Jones model is a simple molecular model and a modeling system. The Lennard-Jones system is a generic system that captures the basic features of matter, e.g. describing different phases, interfaces, equilibrium, and dynamic properties. The Lennard-Jones system is based on the Lennard-Jones potential, which can be written as

$$u_{\text{LJ}}(r) = 4\varepsilon \left[\left(\frac{\sigma}{r} \right)^{12} - \left(\frac{\sigma}{r} \right)^6 \right], \quad (74)$$

where ε , σ , and r indicate the energy parameter, the size parameter, and the distance between two particles, respectively. The Lennard-Jones potential can be considered as the archetype for intermolecular interactions. It is the simplest interaction potential that captures the two basic atomistic interaction features (repulsion and attraction) in a principally realistic way. Moreover, matter described by the Lennard-Jones potential captures the vast majority of material behavior and properties known from macroscopic experience, e.g. phase equilibria, criticality, transport properties etc. The (virtual) material described by the Lennard-Jones potential is called the *Lennard-Jones substance* – sometimes even referred to as *Lennard-Jonesium* [64, 67, 264], suggesting that it is viewed as a chemical element. The Lennard-Jones system can also be used for modeling mixtures or co-existing components by adapting the size and energy parameter of the two (or more) components. The Lennard-Jones potential is often used in molecular physics as it is known to describe the thermodynamic properties of simple substances well – especially for fluids [172, 306, 353, 402] – and still gives a reasonable description for some solid crystals [153, 381, 429]. The Lennard-Jones model system brings several advantages. It can be therefore favorably used:

- For learning and investigating the fundamentals of thermophysical properties of matter [12, 154].
- For the development and testing of new simulation methods due to its simplicity and computational efficiency [318, 379, 394].
- For studying complex processes and phenomena on the atomistic scale [16, 159, 164, 171, 346, 379].
- For the development of theories and approaches based on statistical mechanics for describing matter based atomistic interactions. The aim is then to cast these theories into analytical mathematically simple models. The Lennard-Jones potential is well-defined and can be evaluated exactly in certain limits, e.g. ideal lattice structures of inert gases [201] and the zero-density limit for computing virial coefficients [154, 168]. Theories using that approach and describe matter in a quasi-analytical way are then based on the Lennard-Jones substance, i.e. data and properties of the Lennard-Jones substance obtained from molecular simulation computer experiments.
- For mapping results to real systems in an approximate way, e.g. using a corresponding states principle and dimensionless variables (see below).
- For benchmarking simulation results. A large number of high-quality thermophysical property data of the Lennard-Jones system is available in the literature [361], for both atomistic structural properties as well as macroscopic properties of the Lennard-Jonesium. This is not limited to simple thermodynamic equilibrium properties, but also includes transport and interfacial properties.

The advantages of these use cases of the Lennard-Jones model system reinforce each other in a holistic way. Therefore, new simulation methods as well as new theories can be well tested using a system, which provides a wealth of high-accurate benchmark data. Also, studying fundamentals of thermophysical properties is beneficially supported by a good availability of theories, models, and computer experiment data.

The Lennard-Jones model system is today well-understood regarding its thermophysical properties – for both the atomistic structure and its macroscopic properties. The structure of the Lennard-Jones system has been studied for both homogeneous bulk phases [272, 273] and heterogeneous systems [26, 27, 160, 325, 357]. Both, thermodynamic equilibrium bulk phase properties [348, 350, 361], transport properties [17, 92, 116, 126, 218, 257, 325], and interfacial properties [26, 162, 357] have been systematically investigated in the literature.

The Lennard-Jones potential has proven a valuable tool for modeling intermolecular interactions in fluids [122, 306, 353]. Yet, it was early noticed that the Lennard-Jones

potential gives only a relatively rough description of the interactions in metal solids [429]. This is probably the main drawback from using the Lennard-Jones potential in tribological contact process simulations.

Results from the Lennard-Jones system can be interpreted in a general way and transferred to real substance problems. The advantage is that this transferability manifests in a straightforward computable way. Thereby, the Lennard-Jones units system can be used for scaling its model system results to more complex problems. This scaling is similar to the approach using dimensionless properties often used in engineering. This feature underlines the general applicability and transferability of the system. Evidently, this scaling goes in hand with severe approximations, which, at the same time, limit the transferability. The Lennard-Jones scaling is based on the Lennard-Jones units system. This units base system is defined based on the energy parameter ε , the size parameter σ , the Boltzmann constant k_B , and the mass of the Lennard-Jones particle M [9]. Thereby, practically all relevant physical properties for soft matter physics and solid state physics (with some exceptions) can be described. The results for a given Lennard-Jones system simulation can be scaled to a real substance problem by converting the units to the SI units system using values for ε and σ that represent the system. Table A.1 provides the reduced units definitions of some exemplaric physical properties. The reduced properties are referred to by an asterisk. The Lennard-Jones units system is used for presenting the results of the model system studies, cf. chapters 3 and 4. It should be noted, that this scaling method has limitations when multiple components are involved. As a side note, the Lennard-Jones scaling based on the Lennard-Jones units system can also be used for the parametrization of force field models [260].

Table A.1: The definition of physical properties in reduced units based on the Lennard-Jones parameters ε , σ , and the particle mass M .

property	definition	property	definition
Length	$l^* = \frac{l}{\sigma}$	Pressure	$p^* = \frac{p}{\varepsilon/\sigma^3}$
Time	$\tau^* = \frac{\tau}{\sigma\sqrt{M/\varepsilon}}$	Diffusion coefficient	$D^* = \frac{D}{\sqrt{\varepsilon/M}/\sigma}$
Density	$\rho^* = \rho\sigma^3$	Shear viscosity	$\eta^* = \frac{\eta}{\sqrt{\varepsilon M}/\sigma^2}$
Temperature	$T^* = \frac{T}{\varepsilon/k_B}$	Thermal conductivity	$\lambda^* = \frac{\lambda}{k_B\sqrt{\varepsilon/M}/\sigma^2}$
Velocity	$\underline{v}^* = \frac{v}{\sqrt{\varepsilon/M}}$	Energy flux	$\underline{J}_q^* = \frac{J_q}{\varepsilon\sqrt{\varepsilon/M}/\sigma^3}$
Energy	$u^* = \frac{u}{\varepsilon}$	Entropy	$s^* = \frac{s}{k_B}$

The Lennard-Jones potential has been frequently used in tribological MD simulations. It has been successfully used for the modeling of dispersive and repulsive interactions of simple spherically shaped fluid molecules [166, 167, 254, 300, 314] and interactions between chain molecules [62, 314–316, 430, 431] as well as for the modeling of the solid-

fluid interactions [11, 69, 114, 299, 300, 314–316, 328, 377, 392, 430, 431]. In this work, the Lennard-Jones system was used for studying lubricated contact processes (cf. chapters 3 and 4). Thereby, several of the above-listed advantages are used, e.g. for testing a new approach for determining the statistical uncertainties in contact process simulations and benefiting from the computational efficiency for carrying out a comprehensive parameter study on the influence of the solid-fluid interaction energy. Moreover, specific aspects from the knowledge on thermophysical properties of the system (e.g. the wetting behavior) were comprised in the evaluation and interpretation of the results.

B Details on Influence of Fluid with Respect to Statistical Uncertainty Analysis

This Appendix provides details on the results presented in chapters 3 and 4. It contains details on the computation of local thermodynamic properties presented therein. Moreover, an additional comparison of the results from chapters 3 and 4 is presented.

B.1 Calculation of Local Thermodynamic Properties

The fluid temperature, density, and pressure were calculated locally during the scratching process. All three properties were calculated as per-atom values by averaging the respective property over the particles within the cut-off radius of each particle. The average aligned velocity from each per-atom collective was subtracted from the total average kinetic energy for the computation of the local temperature by the thermal motion. The fluid region was divided into bins with a square cross section with the size 1.34σ and reaching over the entire box length in x -direction. The density, pressure, and temperature were averaged over all molecules in a bin over 5,000 time steps. Moreover, the state point of the fluid was evaluated in the direct vicinity of the chip. The temperature, density, and pressure of the fluid were therefore averaged radially as a function of the distance R^* from the instantaneous chip surface, which was computed using an alpha shape algorithm. The radial averaging was carried out with respect to the center of mass of the chip. The profiles were determined over the angle α with an increment of 2° between α_{\min} and α_{\max} . The angle α_{\min} is specified as the angle where the radius R^* tangentially touches the cylindrical indenter. The angle α_{\max} is specified as the angle where the distance $R^* = 65$ touches the unpenetrated substrate surface in positive y -direction. All individual profiles at different angles α were shifted such that the distance R^* has its origin $R^* = 0$ at the surface of the chip before the averaging of all profiles.

B.2 Comparison of Uncertainty Analysis to Results from Chapter 3

The results presented in chapter 3 and chapter 4 are based on the same setup, e.g. the domain sizes, indenter velocity, simulation time etc. were kept the same for both studies. In the study presented in chapter 3, the contact process simulation was performed 18 times with a varying energy of the solid-fluid interaction $\tilde{\varepsilon}^*$. The influence of $\tilde{\varepsilon}^*$ on various mechanical and thermodynamic properties were thereby investigated. Since the simulation scenarios (kinematics, geometry etc.) of chapter 3 and chapter 4 are equal (besides the solid-fluid interaction energy) for both the indentation and the scratching process, the results of the two chapters can be compared. Hence, the effect of the variation of several physical observables upon varying $\tilde{\varepsilon}^*$ is compared in this Appendix with the respective standard deviation obtained from the statistical analysis presented in chapter 4. The outcome of this comparison is an assessment on whether the effect of the variation of $\tilde{\varepsilon}^*$ is significant regarding statistical uncertainties.

Therefore, a measure for this significance is introduced as

$$\Delta_Z(\tau^*) = \frac{2\sigma_Z(\tau^*)}{Z_{\max.\text{Lit}}(\tau^*) - Z_{\min.\text{Lit}}(\tau^*)}, \quad (75)$$

where $\sigma_Z(\tau^*)$ is the standard deviation of the observable Z according to Eq. (56) of the main part of this work. $Z_{\max.\text{Lit}}(\tau^*)$ and $Z_{\min.\text{Lit}}(\tau^*)$ are the maximum and minimum values of the observable Z at a specific time τ^* of the 18 simulations from chapter 3 as a result of the variation of $\tilde{\varepsilon}^*$. The numerator of Eq. (75) is a measure for the uncertainty of a property Z (taken from chapter 4); the denominator on the other side is a measure for the interval that arises from the influence of a variation of the energy of the solid-fluid interaction $\tilde{\varepsilon}^*$ (taken from chapter 3). For Δ_Z being a value of unity indicates that the range of the observable Z from ' $\bar{Z}(\tau^*) - \sigma_Z(\tau^*)$ ' to ' $\bar{Z}(\tau^*) + \sigma_Z(\tau^*)$ ' is just as large as the effect of the variation of $\tilde{\varepsilon}^*$. Values of Δ_Z smaller than unity indicate that trends of an observable Z as a result of the variation of $\tilde{\varepsilon}^*$ are significant regarding the statistical uncertainties. Values of Δ_Z larger than unity indicate that the statistical uncertainties of an observable exceed the effect of the variation of $\tilde{\varepsilon}^*$. In this case, any trends of Z due to the effect of the variation of $\tilde{\varepsilon}^*$ cannot be measured reliably. It should be noted that small values of Δ_Z do not indicate that the observable Z shows a clear trend with respect to $\tilde{\varepsilon}^*$, but rather that a trend could potentially be identified in the presence of the inevitable statistical uncertainties.

In the following, the general trends of the measured observables and their physical origin are not discussed, as this is done in chapter 3. The emphasis of this Appendix lies

in the evaluation of whether trends of observables due to the variation of $\tilde{\varepsilon}^*$ could be measured reliably regarding the statistical uncertainties determined in chapter 4. Trends of the investigated observables with respect to $\tilde{\varepsilon}^*$ reported in chapter 3 are assessed here by the corresponding statistical uncertainties obtained from a simulation ensemble.

Fig. B.1 shows the results for the total normal force F_n^* on the indenter from both chapter 3 and chapter 4. For the normal force, $\Delta_{F_n^*}$ ranges between 0.02 and 0.4 during the indentation ($\tau^* < 142$). Therefore, trends due to the variation of $\tilde{\varepsilon}^*$ are significant during this phase. This supports the findings reported in chapter 3 that the energy of the solid-fluid interaction has a strong influence during the indentation. At the end of the indentation and during the scratching, $\Delta_{F_n^*}$ steadily increases reaching values up to unity. This indicates that the statistical uncertainties exceed most effects of the variation of $\tilde{\varepsilon}^*$. This holds especially during the main phase of the scratching ($300 < \tau^* < 625$).

Fig. B.2 shows the results for the total tangential force F_t^* on the indenter from both chapter 3 and chapter 4. During the indentation, trends of the tangential force due a varying $\tilde{\varepsilon}^*$ are significant with values of $\Delta_{F_t^*}$ well below 0.5. During the scratching process, $\Delta_{F_t^*}$ fluctuates around 0.6. Therefore, trends in the tangential force are less significant in this phase. This was also estimated in chapter 3.

Fig. B.3 shows the results for the coefficient of friction μ from both chapter 3 and chapter 4. Δ_μ shows a slightly increasing trend throughout the scratching phase, which indicates, that differences due to the variation of $\tilde{\varepsilon}^*$ become less significant during the main phase of the scratching, which is in line with the results discussed for the tangential force above.

Fig. B.4 shows the results for the chip volume V_{chip}^* from both chapter 3 and chapter 4. The chip volume is only measured during the scratching process. At about $\tau^* = 200$, $\Delta_{V_{\text{chip}}^*}$ reaches a steady state with small fluctuations around the mean value of 0.36. Therefore, trends due to the variation of $\tilde{\varepsilon}^*$ have a relatively high statistical weight.

Fig. B.5 shows the results for the chip temperature T_{chip}^* from both chapter 3 and chapter 4. As for the chip volume, the chip temperature is only measured during the scratching process. $\Delta_{T_{\text{chip}}^*}$ quickly reaches a steady state superimposed by fluctuations and a mean value of about 0.6. The variation of the chip temperature due to the variation of $\tilde{\varepsilon}^*$ exceeds the fluctuations from the lubricated set of replica. This supports the findings reported in chapter 3 that the chip temperature during the scratching process depends on the energy of the solid-fluid interaction.

Fig. B.6 shows the results for the cumulative energy balance from both chapter 3 and chapter 4. For the cumulative work of the indenter during the indentation, $\Delta_{W_1^*}$ starts at values below 0.4, which is simply due the fact the numeric values of W_1^* fluctuate around zero at the beginning of the indentation. Until the beginning of the scratching,

$\Delta_{W_I^*}$ fluctuates around values of 0.02. Therefore, trends due to the varying of $\tilde{\varepsilon}^*$ on the work done by the indenter in this phase are reliable observations. This supports the findings from chapter 3 that the work done by the indenter in this phase strongly depends on the energy of the solid-fluid interaction. During the scratching process, $\Delta_{W_I^*}$ increases to values of up to 0.4.

Fig. B.7 shows the results for the temperature, density, and pressure of the fluid around the chip during the scratching process from both chapter 3 and chapter 4. For the temperature and the density of the fluid around the chip during the scratching, Δ lies below 0.5. For the temperature, Δ_{T^*} is steady at a value of about 0.4, while for the density, Δ_{ρ^*} shows small fluctuations around a mean value of about 0.3. For both properties, a clear trend due to the variation of $\tilde{\varepsilon}^*$ can be observed reliably. For the fluid pressure, Δ_{p^*} lies above 0.5 with extreme values of up to 0.9. Therefore, clear trends with respect to $\tilde{\varepsilon}^*$ cannot be identified – the statistical uncertainty exceeds a possible variation due to different energies of the solid-fluid interaction.

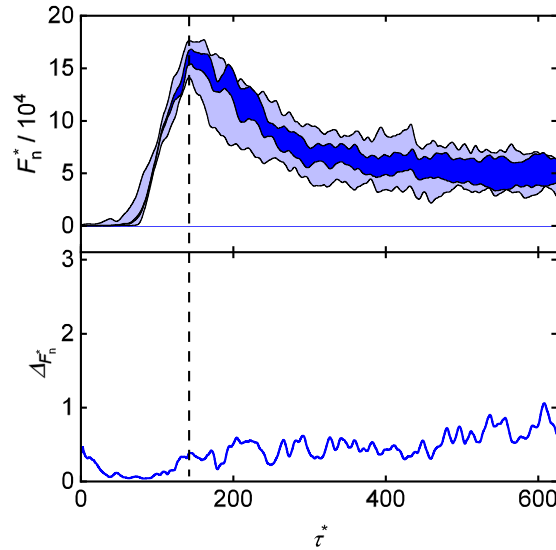


Figure B.1: Normal force on the indenter during the contact process (top) and the corresponding significance measure Δ of the effect of the variation of the solid-fluid interaction energy $\tilde{\varepsilon}^*$ (bottom). The dark blue shaded area indicates the range between the positive and the negative standard deviation of the set of replica with lubrication as defined in Eq. (56). The light blue shaded area indicates the range of the maximum and minimum values of the normal force as a result of the variation of $\tilde{\varepsilon}^*$. The dashed vertical line indicates the beginning of the scratching process.

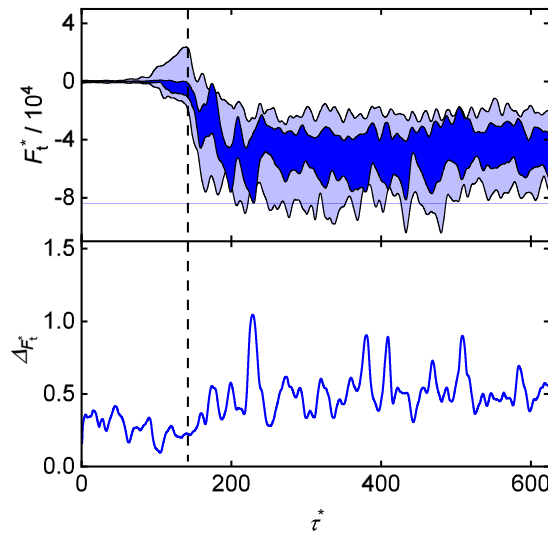


Figure B.2: Tangential force on the indenter during the contact process (top) and the corresponding significance measure Δ of the effect of the variation of the solid-fluid interaction energy $\tilde{\varepsilon}^*$ (bottom). The dark blue shaded area indicates the range between the positive and the negative standard deviation of the set of replica with lubrication as defined in Eq. (56). The light blue shaded area indicates the range of the maximum and minimum values of the tangential force as a result of the variation of $\tilde{\varepsilon}^*$. The dashed vertical line indicates the beginning of the scratching process.

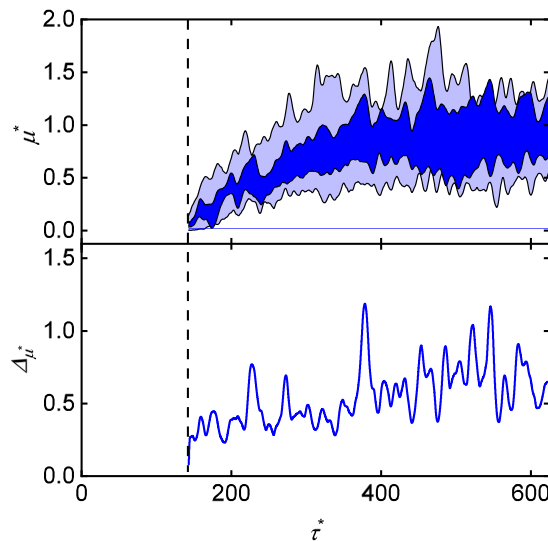


Figure B.3: Coefficient of friction during the contact process (top) and the corresponding significance measure Δ of the effect of the variation of the solid-fluid interaction energy $\tilde{\varepsilon}^*$ (bottom). The dark blue shaded area indicates the range between the positive and the negative standard deviation of the set of replica with lubrication as defined in Eq. (56). The light blue shaded area indicates the range of the maximum and minimum values of the COF as a result of the variation of $\tilde{\varepsilon}^*$. The dashed vertical line indicates the beginning of the scratching process.

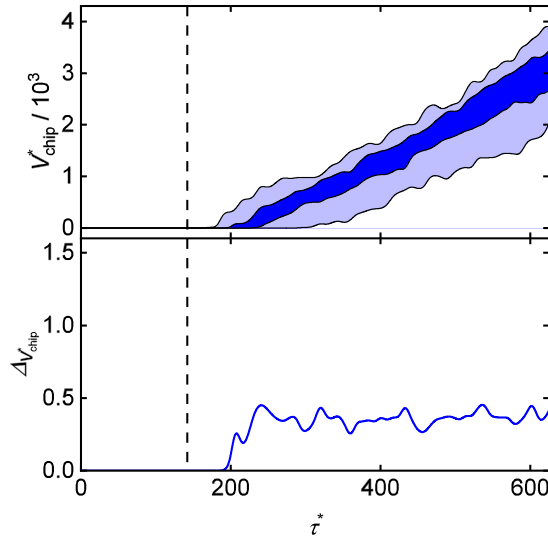


Figure B.4: Chip volume during the contact process (top) and the corresponding significance measure Δ of the effect of the variation of the solid-fluid interaction energy $\tilde{\varepsilon}^*$ (bottom). The dark blue shaded area indicates the range between the positive and the negative standard deviation of the set of replica with lubrication as defined in Eq. (56). The light blue shaded area indicates the range of the maximum and minimum values of the chip volume as a result of the variation of $\tilde{\varepsilon}^*$. The dashed vertical line indicates the beginning of the scratching process.

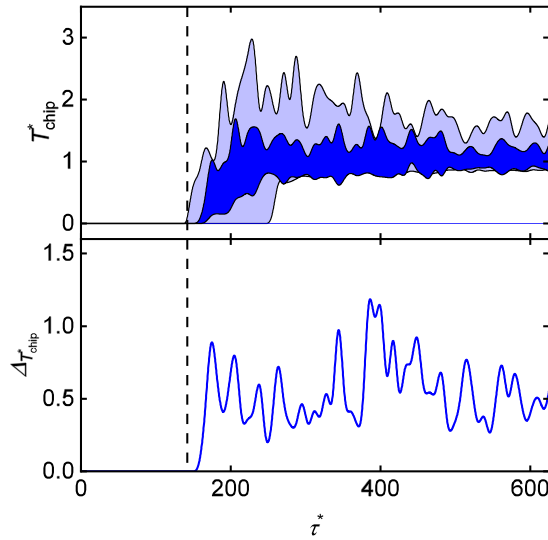


Figure B.5: Chip temperature during the contact process (top) and the corresponding significance measure Δ of the effect of the variation of the solid-fluid interaction energy $\tilde{\varepsilon}^*$ (bottom). The dark blue shaded area indicates the range between the positive and the negative standard deviation of the set of replica with lubrication as defined in Eq. (56). The light blue shaded area indicates the range of the maximum and minimum values of the chip temperature as a result of the variation of $\tilde{\varepsilon}^*$. The dashed vertical line indicates the beginning of the scratching process.

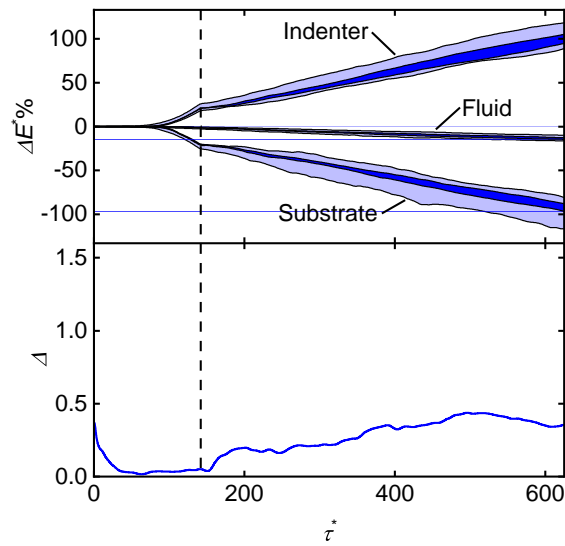


Figure B.6: Cumulative energy balance during the contact process (top) and the corresponding significance measure Δ of the effect of the variation of the solid-fluid interaction energy $\tilde{\epsilon}^*$ on the cumulative work (bottom). The dark blue shaded area indicates the range between the positive and the negative standard deviation of the set of replica with lubrication as defined in Eq. (56). The light blue shaded area indicates the range of the maximum and minimum values of the respective cumulative energies as a result of the variation of $\tilde{\epsilon}^*$. The dashed vertical line indicates the beginning of the scratching process.

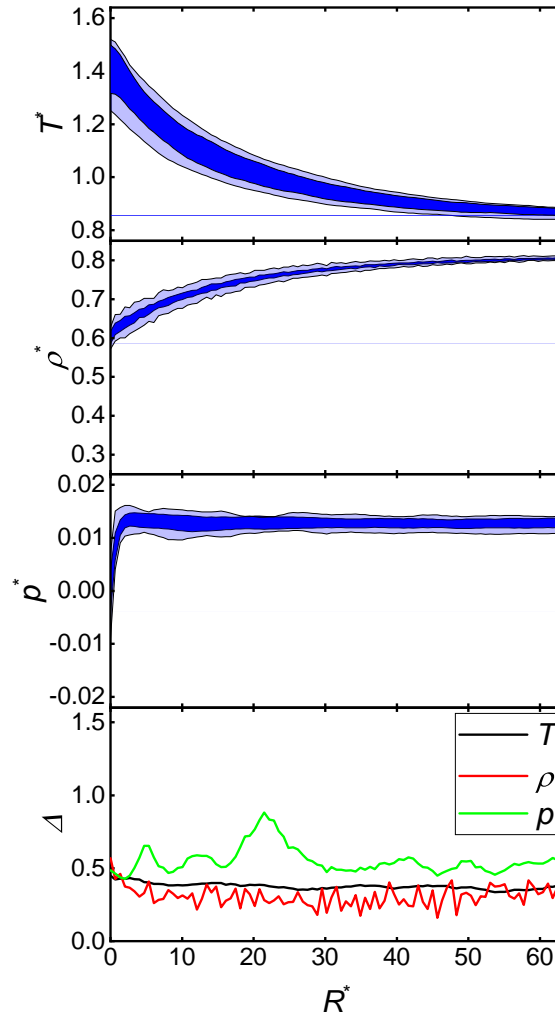


Figure B.7: Temperature, density, and pressure profile of the fluid during the scratching process (top) and the corresponding significance measure Δ of the effect of the variation of the solid-fluid interaction energy $\tilde{\varepsilon}^*$ (bottom). The dark blue shaded area indicates the range between the positive and the negative standard deviation of the set of replica with lubrication as defined in Eq. (56). The light blue shaded area indicates the range of the maximum and minimum values of the respective fluid property as a result of the variation of $\tilde{\varepsilon}^*$. The dashed vertical line indicates the beginning of the scratching process.

C Details on Stribeck Curve Simulations

C.1 Model for Solid-Fluid Interactions

The solid-fluid interaction model has a significant influence on tribological systems studied by molecular dynamics simulations. There is a large variety of different interaction parameters and potentials used in the literature, even for a single substance combination of a fluid and a substrate, e.g. for systems with iron surface and alkanes as fluid [32, 179, 315, 376, 418, 431]. Often the solid-fluid interaction is calculated based on simple combination rules whereby the solid interaction itself is modeled by another potential, e.g. by a complex multi-body potential [431]. Comparing the solid-fluid interaction energy modeled by *Mie*-type potentials [266] yields values from $\varepsilon^* = 1.5$ [315] up to $\varepsilon^* = 10.5$ [32] in tribological simulations (each brought to dimensionless form by the energy parameter ε_{FF} of the respective fluid-fluid interaction). Higher solid-fluid interaction energies were used in conjunction with the *Morse* potential, e.g. *Chang et al.* [63] used a cohesion energy of $\varepsilon^* = 28.87$.

For the simulations presented and discussed in chapter 6, a model for the solid-fluid interaction was derived from quantum mechanical (QM) data that was taken from *Xu et al.* [418] for the systems $\text{CH}_2\text{-Fe}$ and $\text{CH}_3\text{-Fe}$. The data of the system $\text{CH}_2\text{-Fe}$ were used for the interaction between the surface particles and the chain particles in the middle (excluding end-groups) of the LJ chain fluid. The solid-fluid parameters for the end-groups of the LJ chain fluid as well as for the LJ fluid were calculated from the system $\text{CH}_3\text{-Fe}$. *Xu et al.* [418] report interaction energies as well as corresponding configurational data, which were used here to adjust the parameters σ and ε of a LJ 9-6 potential.

For this purpose, a single particle of each type was placed above a (100) surface of a bcc structured solid. This configuration was used to adjust the parameters σ^* and ε^* such that a single fluid particle on a surface has the same potential energy as given by *Xu et al.* [418]. This procedure follows the force matching method [104], which

has been applied for mapping of solid-fluid interaction energies as iterative procedure with multiple QM calculations [208] or with single QM calculations [44] (as done in the present work in a simplified form). The LJ 9-6 potential has been used as potential for solid-fluid interactions in the literature [376] and was favored here over the LJ 12-6 potential due to better fitting of the QM data. The final values used in the simulations are reported in Table C.1.

Table C.1: Reduced solid-fluid interaction parameters (with respect to the fluid-fluid interaction parameters) used with the 9-6 Lennard-Jones potential.

	methane	decane middle group	decane end group
σ^*	0.56	0.58	0.67
ε^*	35.86	17.28	7.17

C.2 Computational Aspects of Simulations

The simulations presented and discussed in chapter 6 were carried out on the Elwe supercomputer at the RHRK of the TU Kaiserslautern (today RPTU). For the simulations, Intel E5-2670 processors with a memory of 64 GB were used. Each simulation ran on 16 CPUs with 16 cores each (total: 256 cores). The simulations were computationally expensive due to the large number of particles and, which is also important, due to complexity of the interaction potentials. In particular, the EAM potential requires significant amounts of computational resources. As only a single equilibration and indentation had to be carried out for each considered fluid, the bulk part of the computer time was spent on the scratching simulations. Each simulation at a given gap height, required around 22×103 CPUh. The decane simulations were computationally slightly more expensive due to the larger number of interaction sites and, in particular, the smaller time step. Here, each simulation required around 50×103 CPUh.

C.3 Force Contributions

Fig. C.1 shows the results for the contributions to the total force on the indenter, i.e. the contribution from the indenter-substrate interactions.

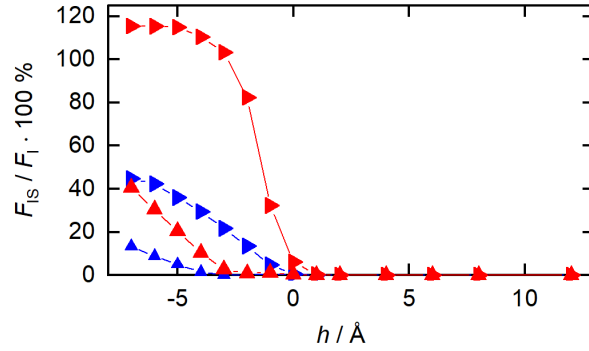


Figure C.1: Ratio of the force contribution to the forces on the indenter sampled in the quasi-stationary regime as a function of the gap heights h : Forces in z - (up-triangles) and y -direction (right-triangles). The quantity F_{IS}/F_I indicates the contribution of the indenter-substrate interactions of the total force on the indenter. Results for both lubricated cases: Methane (red) and decane (blue). Lines are a guide for the eye.

C.4 Temperature and Pressure in the Lubrication Gap

Fig. C.2 shows the results for the temperature and pressure profiles in the lubrication gap.

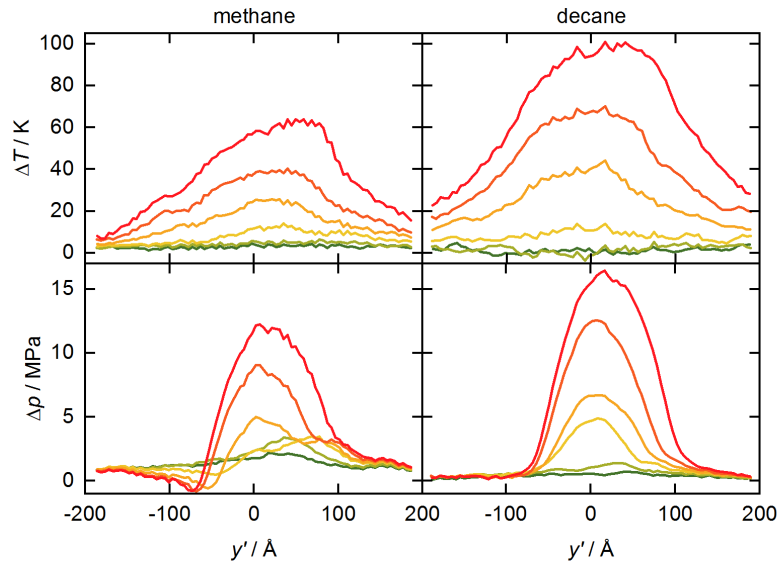


Figure C.2: Temperature and pressure profiles of the fluid in the lubrication gap with respect to the moving coordinate system y' (cf. Fig. 54): Temperature profiles (top); pressure profiles (bottom). Results shown for $h = -6, -4, -2, 0, 4, 8 \text{ \AA}$ (graphs top to bottom). The left column gives the results for the methane simulations; the right column gives the results for the decane simulations. Data was sampled during the quasi-stationary phase (cf. Fig. 55).

Authorship Declaration

This dissertation contains material that has been published in four papers [347, 348, 356, 359] in peer-reviewed journals. In the following, these publications are listed together with a statement on the contributions of the author of the this dissertation (Si. St.).

- S. Stephan, M. Dyga, H.M. Urbassek, H. Hasse: The Influence of Lubrication and the Solid-Fluid Interaction on Thermodynamic Properties in a Nanoscopic Scratching Process, *Langmuir* 35, 51 (2019) 16948-16960, DOI: 10.1021/acs.langmuir.9b01033.
The author Si. St. carried out the simulations, developed the post-processing routines, carried out the post-processing and data analysis, and wrote the manuscript. Carrying out the simulations was supported by the student assistant M. Dyga.
- S. Stephan, M. Dyga, I. Alabad Alhafez, J. Lenhard, H.M. Urbassek, H. Hasse: Reproducibility of Atomistic Friction Computer Experiments: A Molecular Dynamics Simulation Study, *Molecular Simulation* 47, 18 (2021) 1509-1521, DOI: 10.1080/08927022.2021.1987430.
The author Si. St. designed the research, carried out the simulations, the post-processing, and the data analysis and wrote the manuscript. The dislocation analysis was carried out by I. Alabad Alhafez. Carrying out the simulations was supported by the student assistant M. Dyga.
- S. Stephan, M.P. Lautenschlaeger, I. Alabad Alhafez, M. Horsch, H.M. Urbassek, H. Hasse: Molecular Dynamics Simulation Study of Mechanical Effects of Lubrication on a Nanoscale Contact Process. *Tribology Letters* 66 (2018) 126, DOI: 10.1007/s11249-018-1076-0.
The author Si. St. carried out the simulations and the post-processing. Si. St. carried out the data analysis – supported by M.P. Lautenschlaeger. Si. St. wrote the manuscript. The dislocation analysis was carried out by I. Alabad Alhafez.
- S. Stephan, S. Schmitt, H. Hasse, H.M. Urbassek: Molecular Dynamics Simulation of the Stribeck curve: Boundary Lubrication, Mixed Lubrication, and Hydrodynamic Lubrication on the Atomistic Level, *Friction* 11 (2023) 23422366,

DOI: 10.1007/s40544-023-0745-y.

The author Si. St. designed the research. Si. St. carried out the simulations and post-processing together with S. Schmitt. The author carried out the data analysis and wrote the manuscript.

The content of these four papers [348, 356, 358, 359] corresponds to the content of the chapters 3 - 6 of this dissertation. Therein, essentially, only typographical and minor editorial changes were applied with respect to the versions published in the journals. The chapters 1, 2, 7, and 8 were written for this dissertation specifically.

Furthermore, the author contributed to the following publications [92, 116, 117, 162, 220, 221, 319, 325, 353] that are relevant for this thesis:

- M. Schappals, A. Mecklenfeld, L. Kröger, V. Botan, A. Köster, S. Stephan, E.J. Garcia, G. Rutkai, G. Raabe, P. Klein, K. Leonhard, C. Glass, J. Lenhard, J. Vrabec, H. Hasse: Round Robin Study: Molecular Simulation of Thermodynamic Properties from Models with Internal Degrees of Freedom, *Journal of Chemical Theory Computation* 13 (2017) 4270, DOI: 10.1021/acs.jctc.7b00489.
- M.P. Lautenschlaeger, S. Stephan, H.M. Urbassek, B. Kirsch, J.C. Aurich, M. Horsch, H. Hasse: Effects of Lubrication on the Friction in Nanometric Machining Processes: A Molecular Dynamics Approach, *Applied Mechanics and Materials* 869 (2017) 85, DOI: 10.4028/www.scientific.net/AMM.869.85.
- M.P. Lautenschlaeger, S. Stephan, M. Horsch, B. Kirsch, J.C. Aurich, H. Hasse: Effects of Lubrication on Friction and Heat Transfer in Machining Processes on the Nanoscale: A Molecular Dynamics Approach, *Procedia CIRP*, 67 (2018) 296, DOI: 10.1016/j.procir.2017.12.216.
- S. Stephan, M. Horsch, J. Vrabec, H. Hasse: MolMod – an Open Access Database of Force Fields for Molecular Simulations of Fluids, *Molecular Simulation* 45, 10 (2019) 806-814, DOI: 10.1080/08927022.2019.1601191.
- F. Diewald, M.P. Lautenschlaeger, S. Stephan, K. Langenbach, C. Kuhn, S. Seckler, H.-J. Bungartz, H. Hasse, R. Müller: Molecular Dynamics and Phase Field Simulations of Droplets on Surfaces with Wettability Gradient, *Computer Methods in Applied Mechanics and Engineering* 361 (2020) 112773, DOI: 10.1016/j.cma.2019.112773.
- D. Fertig, H. Hasse, S. Stephan: Transport Properties of Binary Lennard-Jones Mixtures: Insights from Entropy Scaling and Conformal Solution Theory, *Journal*

- of Molecular Liquids 367 (2022) 120401,
DOI: 10.1016/j.molliq.2022.120401.
- D. Fertig, S. Stephan: Influence of Dispersive Long-Range Interactions on Transport and Excess Properties of Binary Mixtures of Simple Fluids, *Molecular Physics* 121, 19-20 (2023) e2162993,
DOI: 10.1080/00268976.2022.2162993.
 - M. Heier, S. Stephan, F. Diewald, R. Müller, K. Langenbach, H. Hasse: Molecular Dynamics Study of Wetting and Adsorption of Binary Mixtures of the Lennard-Jones Truncated and Shifted Fluid on a Planar Wall, *Langmuir* 37, 24, 7405-7419 (2021),
DOI: 10.1021/acs.langmuir.1c00780.
 - S. Schmitt, S. Stephan, B. Kirsch, J.C. Aurich, H.M. Urbassek, H. Hasse: Molecular Dynamics Simulation of Cutting Processes: The Influence of Cutting Fluids at the Atomistic Scale, *Physical Modeling for Virtual Manufacturing (iPMVM 2023)* (2023) 260280,
DOI: 10.1007/978-3-031-35779-4_14.
 - S. Schmitt, S. Stephan, B. Kirsch, J.C. Aurich, E. Kerscher, H.M. Urbassek, H. Hasse: Molecular Simulation Study on the Influence of the Scratching Velocity on Nanoscopic Contact Processes, *Physical Modeling for Virtual Manufacturing (iPMVM 2020)* 89 (2021) 17:1-17:16,
DOI: 10.4230/OASIs.iPMVM.2020.17.
 - S. Schmitt, T. Vo, M.P. Lautenschlaeger, S. Stephan, H. Hasse: Molecular Dynamics Simulation Study of Heat Transfer Across SolidFluid Interfaces in a Simple Model System, *Molecular Physics* 120, 10 (2022) e2057364,
DOI: 10.1080/00268976.2022.2057364.

The author has successfully submitted a PhD dissertation to the faculty of Mechanical and Chemical Engineering of the TU Kaiserslautern in June 2020 [343] on vapor-liquid interfacial properties. These results were published in Refs. [163, 344, 346, 349–352, 354, 355, 357, 360, 361]. These are fully disjunct from the present work (see above).

Supervised Student Theses

The following student theses that are related to this work were prepared under the supervision of the author of the this dissertation:

- M. Weber: Untersuchung des Einflusses der Kettenlänge von Alkanen auf deren Schmierwirkung in einem nanotribologischen System. Bachelor thesis, TU Kaiserslautern (2018).
- S. Schmitt: Untersuchung des Einflusses der Kettenlänge linearer Alkane auf deren Schmierwirkung in einem nanotribologischen System. Master thesis, TU Kaiserslautern (2018).

Curriculum Vitae – Simon Stephan

Education

1995 – 1999	Elementary school in Roth, Germany
1999 – 2008	Gymnasium Wilhel-Löhe Schule in Nuremberg, Germany Degree: Allgemeine Hochschulreife
2009 – 2015	Diplomstudium at TU Dresden Program: mechanical engineering (Maschinenbau) Degree: Dipl.-Ing.
2020	Dissertation at TU Kaiserslautern (Faculty for Mechanical and Process Engineering) Degree: Dr.-Ing.

Professional

08/2008 – 04/2009	Civil service at Jugendbildungsstätte Asel/Ostfriesland
03/2015 – 08/2015	University of Reading, Academic visitor
02/2016 – 05/2019	TU Kaiserslautern, PhD student and member of the International Research Training Group "Physical Modeling for Virtual Manufacturing Systems and Processes" (IRTG 2057)
01/2017 – 03/2017	Rice University, Research stay
08/2020 – 01/2021	Imperial College London, UK, Researcher
02/2021 – 06/2021	TU Berlin, Researcher
07/2022 – 09/2022	University of Berkeley, USA, Research stay
since 07/2021	RPTU Kaiserslautern (Faculty for Mechanical and Process Engineering), Junior Professor for Molecular Thermodynamics

Acknowledgment

I want to express my sincere gratitude to my supervisor Herbert Urbassek, who supported this work with great interest, experience, patience, friendly guidance, and constructive criticism. My special thanks go to Michael Kopnarski for committing time by serving as the second reviewer for this thesis.

I would like to thank Jan Aurich and Hans Hasse who provided continuous input from an engineering perspective on tribology and for co-supervising as well as cooperating in the IRTG 2057. I am sincerely grateful for financial support by the IRTG 2057 – Physical Modeling for Virtual Manufacturing Systems and Processes and the people therein, firstly Jan Aurich, Benjamin Kirsch, and Marion Teubner for their friendly collaborative support. The IRTG 2057 was a true enabler for this thesis. I am also very thankful for the possibility to spent a research stay in the summer 2022 at the University of Berkeley under the auspicious of the IRTG 2057. Moreover, I want to thank Sebastian Schmitt, Martin Lautenschlaeger, and Iyad Alabad Alhafez for the inspiring and constructive collaboration within the IRTG 2057 in the area of nanotribology.